

University of Windsor

## Scholarship at UWindor

---

Electronic Theses and Dissertations

Theses, Dissertations, and Major Papers

---

1995

### Elevated temperature wear of an aluminum matrix composite Al6061-20 percent aluminum(2) oxygen(3) intermetallic alloy titanium(50) nickel(47) iron(3).

Jugraj. Singh  
*University of Windsor*

Follow this and additional works at: <https://scholar.uwindsor.ca/etd>

---

#### Recommended Citation

Singh, Jugraj., "Elevated temperature wear of an aluminum matrix composite Al6061-20 percent aluminum(2) oxygen(3) intermetallic alloy titanium(50) nickel(47) iron(3)." (1995). *Electronic Theses and Dissertations*. 1912.

<https://scholar.uwindsor.ca/etd/1912>

This online database contains the full-text of PhD dissertations and Masters' theses of University of Windsor students from 1954 forward. These documents are made available for personal study and research purposes only, in accordance with the Canadian Copyright Act and the Creative Commons license—CC BY-NC-ND (Attribution, Non-Commercial, No Derivative Works). Under this license, works must always be attributed to the copyright holder (original author), cannot be used for any commercial purposes, and may not be altered. Any other use would require the permission of the copyright holder. Students may inquire about withdrawing their dissertation and/or thesis from this database. For additional inquiries, please contact the repository administrator via email ([scholarship@uwindsor.ca](mailto:scholarship@uwindsor.ca)) or by telephone at 519-253-3000ext. 3208.



National Library  
of Canada

Acquisitions and  
Bibliographic Services Branch

395 Wellington Street  
Ottawa, Ontario  
K1A 0N4

Bibliothèque nationale  
du Canada

Direction des acquisitions et  
des services bibliographiques

395, rue Wellington  
Ottawa (Ontario)  
K1A 0N4

*Your file    Votre référence*

*Our file    Notre référence*

## NOTICE

The quality of this microform is heavily dependent upon the quality of the original thesis submitted for microfilming. Every effort has been made to ensure the highest quality of reproduction possible.

If pages are missing, contact the university which granted the degree.

Some pages may have indistinct print especially if the original pages were typed with a poor typewriter ribbon or if the university sent us an inferior photocopy.

Reproduction in full or in part of this microform is governed by the Canadian Copyright Act, R.S.C. 1970, c. C-30, and subsequent amendments.

## AVIS

La qualité de cette microforme dépend grandement de la qualité de la thèse soumise au microfilmage. Nous avons tout fait pour assurer une qualité supérieure de reproduction.

S'il manque des pages, veuillez communiquer avec l'université qui a conféré le grade.

La qualité d'impression de certaines pages peut laisser à désirer, surtout si les pages originales ont été dactylographiées à l'aide d'un ruban usé ou si l'université nous a fait parvenir une photocopie de qualité inférieure.

La reproduction, même partielle, de cette microforme est soumise à la Loi canadienne sur le droit d'auteur, SRC 1970, c. C-30, et ses amendements subséquents.

**Canada**

**ELEVATED TEMPERATURE WEAR**  
**OF**  
**AN ALUMINUM MATRIX COMPOSITE Al6061-20%Al<sub>2</sub>O<sub>3</sub>**  
**AND**  
**AN INTERMETALLIC ALLOY Ti<sub>50</sub>Ni<sub>47</sub>Fe<sub>3</sub>**

**by**  
**Jugraj Singh**

**A Thesis**

**Submitted to the Faculty of Graduate Studies and Research  
through the Engineering Materials Program of the  
Department of Mechanical Engineering in partial  
fulfilment of the requirements for the  
Degree of Master of Applied Science at the  
University of Windsor**

**Windsor, Ontario, Canada**

**1995**

**© 1995 Jugraj Singh**



National Library  
of Canada

Acquisitions and  
Bibliographic Services Branch

395 Wellington Street  
Ottawa, Ontario  
K1A 0N4

Bibliothèque nationale  
du Canada

Direction des acquisitions et  
des services bibliographiques

395, rue Wellington  
Ottawa (Ontario)  
K1A 0N4

Your file    Votre référence

Our file    Notre référence

THE AUTHOR HAS GRANTED AN  
IRREVOCABLE NON-EXCLUSIVE  
LICENCE ALLOWING THE NATIONAL  
LIBRARY OF CANADA TO  
REPRODUCE, LOAN, DISTRIBUTE OR  
SELL COPIES OF HIS/HER THESIS BY  
ANY MEANS AND IN ANY FORM OR  
FORMAT, MAKING THIS THESIS  
AVAILABLE TO INTERESTED  
PERSONS.

L'AUTEUR A ACCORDE UNE LICENCE  
IRREVOCABLE ET NON EXCLUSIVE  
PERMETTANT A LA BIBLIOTHEQUE  
NATIONALE DU CANADA DE  
REPRODUIRE, PRETER, DISTRIBUER  
OU VENDRE DES COPIES DE SA  
THESE DE QUELQUE MANIERE ET  
SOUS QUELQUE FORME QUE CE SOIT  
POUR METTRE DES EXEMPLAIRES DE  
CETTE THESE A LA DISPOSITION DES  
PERSONNE INTERESSEES.

THE AUTHOR RETAINS OWNERSHIP  
OF THE COPYRIGHT IN HIS/HER  
THESIS. NEITHER THE THESIS NOR  
SUBSTANTIAL EXTRACTS FROM IT  
MAY BE PRINTED OR OTHERWISE  
REPRODUCED WITHOUT HIS/HER  
PERMISSION.

L'AUTEUR CONSERVE LA PROPRIETE  
DU DROIT D'AUTEUR QUI PROTEGE  
SA THESE. NI LA THESE NI DES  
EXTRAITS SUBSTANTIELS DE CELLE-  
CI NE DOIVENT ETRE IMPRIMES OU  
AUTREMENT REPRODUITS SANS SON  
AUTORISATION.

ISBN 0-612-01488-6

Canada

Name JUGRAJ SINGH

Dissertation Abstracts International is arranged by broad, general subject categories. Please select the one subject which most nearly describes the content of your dissertation. Enter the corresponding four-digit code in the spaces provided.

MATERIALS SCIENCE

SUBJECT TERM

0794

U·M·I

SUBJECT CODE

## Subject Categories

### THE HUMANITIES AND SOCIAL SCIENCES

#### COMMUNICATIONS AND THE ARTS

Architecture ..... 0729  
Art History ..... 0377  
Cinema ..... 0900  
Dance ..... 0378  
Fine Arts ..... 0357  
Information Science ..... 0723  
Journalism ..... 0391  
Library Science ..... 0399  
Mass Communications ..... 0708  
Music ..... 0413  
Speech Communication ..... 0459  
Theater ..... 0465

#### EDUCATION

General ..... 0515  
Administration ..... 0514  
Adult and Continuing ..... 0516  
Agricultural ..... 0517  
Art ..... 0273  
Bilingual and Multicultural ..... 0282  
Business ..... 0688  
Community College ..... 0275  
Curriculum and Instruction ..... 0727  
Early Childhood ..... 0518  
Elementary ..... 0524  
Finance ..... 0277  
Guidance and Counseling ..... 0519  
Health ..... 0680  
Higher ..... 0745  
History of ..... 0520  
Home Economics ..... 0278  
Industrial ..... 0521  
Language and Literature ..... 0279  
Mathematics ..... 0280  
Music ..... 0522  
Philosophy of ..... 0998  
Physical ..... 0523

Psychology ..... 0525  
Reading ..... 0535  
Religious ..... 0527  
Sciences ..... 0714  
Secondary ..... 0533  
Social Sciences ..... 0534  
Sociology of ..... 0340  
Special ..... 0529  
Teacher Training ..... 0530  
Technology ..... 0710  
Tests and Measurements ..... 0288  
Vocational ..... 0747

#### LANGUAGE, LITERATURE AND LINGUISTICS

Language ..... 0679  
General ..... 0289  
Ancient ..... 0290  
Linguistics ..... 0291  
Modern ..... 0401  
General ..... 0294  
Classical ..... 0295  
Comparative ..... 0297  
Medieval ..... 0298  
Modern ..... 0316  
African ..... 0591  
American ..... 0305  
Asian ..... 0352  
Canadian (English) ..... 0355  
Canadian (French) ..... 0593  
English ..... 0311  
Germanic ..... 0312  
Latin American ..... 0315  
Middle Eastern ..... 0313  
Romance ..... 0314  
Slavic and East European ..... 0314

#### PHILOSOPHY, RELIGION AND THEOLOGY

Philosophy ..... 0422  
Religion ..... 0318  
General ..... 0321  
Biblical Studies ..... 0319  
Clergy ..... 0320  
History of ..... 0322  
Philosophy of ..... 0469  
Theology ..... 0323

#### SOCIAL SCIENCES

American Studies ..... 0323  
Anthropology ..... 0324  
Archaeology ..... 0326  
Cultural ..... 0327  
Physical ..... 0310  
Business Administration ..... 0272  
General ..... 0770  
Accounting ..... 0454  
Banking ..... 0338  
Management ..... 0385  
Canadian Studies ..... 0501  
Economics ..... 0503  
General ..... 0505  
Agricultural ..... 0503  
Commerce-Business ..... 0503  
Finance ..... 0509  
History ..... 0510  
Labor ..... 0511  
Theory ..... 0358  
Folklore ..... 0366  
Geography ..... 0351  
Gerontology ..... 0578  
History ..... 0578

Ancient ..... 0579  
Medieval ..... 0581  
Modern ..... 0582  
Black ..... 0328  
African ..... 0331  
Asia, Australia and Oceania ..... 0332  
Canadian ..... 0334  
European ..... 0335  
Latin American ..... 0336  
Middle Eastern ..... 0337  
United States ..... 0585  
History of Science ..... 0398  
Law ..... 0615  
Political Science ..... 0616  
General ..... 0617  
International Law and Relations ..... 0814  
Public Administration ..... 0452  
Recreation ..... 0626  
Social Work ..... 0627  
Criminology and Penology ..... 0938  
Demography ..... 0631  
Ethnic and Racial Studies ..... 0628  
Individual and Family Studies ..... 0629  
Industrial and Labor Relations ..... 0630  
Public and Social Welfare ..... 0700  
Social Structure and Development ..... 0344  
Theory and Methods ..... 0709  
Transportation ..... 0999  
Urban and Regional Planning ..... 0453  
Women's Studies ..... 0453

### THE SCIENCES AND ENGINEERING

#### BIOLOGICAL SCIENCES

Agriculture ..... 0473  
General ..... 0285  
Agronomy ..... 0475  
Animal Culture and Nutrition ..... 0476  
Animal Pathology ..... 0359  
Food Science and Technology ..... 0478  
Forestry and Wildlife ..... 0479  
Plant Culture ..... 0480  
Plant Pathology ..... 0817  
Plant Physiology ..... 0777  
Range Management ..... 0746  
Wood Technology ..... 0306

Biology ..... 0287  
General ..... 0308  
Anatomy ..... 0309  
Biostatistics ..... 0379  
Botany ..... 0329  
Cell ..... 0353  
Ecology ..... 0369  
Entomology ..... 0793  
Genetics ..... 0410  
Limnology ..... 0307  
Microbiology ..... 0317  
Molecular ..... 0416  
Neuroscience ..... 0433  
Oceanography ..... 0821  
Physiology ..... 0778  
Radiation ..... 0472  
Veterinary Science ..... 0786  
Zoology ..... 0760

#### EARTH SCIENCES

Biogeochemistry ..... 0425  
Geochemistry ..... 0996

Geodesy ..... 0370  
Geology ..... 0372  
Geophysics ..... 0373  
Hydrology ..... 0388  
Mineralogy ..... 0411  
Paleobotany ..... 0345  
Paleoecology ..... 0426  
Paleontology ..... 0418  
Paleozoology ..... 0985  
Palynology ..... 0427  
Physical Geography ..... 0368  
Physical Oceanography ..... 0415

#### HEALTH AND ENVIRONMENTAL SCIENCES

Environmental Sciences ..... 0768  
Health Sciences ..... 0566  
General ..... 0300  
Audiology ..... 0992  
Chemotherapy ..... 0567  
Dentistry ..... 0350  
Education ..... 0769  
Hospital Management ..... 0758  
Human Development ..... 0982  
Immunology ..... 0564  
Medicine and Surgery ..... 0347  
Mental Health ..... 0569  
Nursing ..... 0570  
Nutrition ..... 0380  
Obstetrics and Gynecology ..... 0354  
Occupational Health and Therapy ..... 0381  
Ophthalmology ..... 0571  
Pathology ..... 0419  
Pharmacology ..... 0572  
Pharmacy ..... 0382  
Physical Therapy ..... 0573  
Public Health ..... 0574  
Radiology ..... 0575  
Recreation ..... 0460

Speech Pathology ..... 0383  
Toxicology ..... 0386  
Home Economics ..... 0405

#### PHYSICAL SCIENCES

Pure Sciences ..... 0485  
Chemistry ..... 0485  
General ..... 0749  
Agricultural ..... 0486  
Analytical ..... 0487  
Biochemistry ..... 0488  
Inorganic ..... 0738  
Nuclear ..... 0490  
Organic ..... 0491  
Pharmaceutical ..... 0494  
Physical ..... 0495  
Polymer ..... 0754  
Radiation ..... 0405  
Mathematics ..... 0605  
Physics ..... 0986  
General ..... 0606  
Acoustics ..... 0608  
Astronomy and Astrophysics ..... 0748  
Atmospheric Science ..... 0607  
Atomic ..... 0607  
Electronics and Electricity ..... 0798  
Elementary Particles and High Energy ..... 0759  
Fluid and Plasma ..... 0609  
Molecular ..... 0610  
Nuclear ..... 0752  
Optics ..... 0756  
Radiation ..... 0611  
Solid State ..... 0463  
Statistics ..... 0346  
Applied Mechanics ..... 0984  
Computer Science ..... 0984

Engineering ..... 0537  
General ..... 0538  
Aerospace ..... 0539  
Agricultural ..... 0540  
Automotive ..... 0541  
Biomedical ..... 0542  
Chemical ..... 0543  
Civil ..... 0544  
Electronics and Electrical ..... 0348  
Heat and Thermodynamics ..... 0545  
Hydraulic ..... 0546  
Industrial ..... 0547  
Marine ..... 0794  
Materials Science ..... 0548  
Mechanical ..... 0743  
Metallurgy ..... 0551  
Mining ..... 0552  
Nuclear ..... 0549  
Packaging ..... 0765  
Petroleum ..... 0554  
Sanitary and Municipal ..... 0790  
System Science ..... 0428  
Geotechnology ..... 0796  
Operations Research ..... 0795  
Plastics Technology ..... 0994  
Textile Technology ..... 0994

#### PSYCHOLOGY

General ..... 0621  
Behavioral ..... 0384  
Behavioral ..... 0622  
Clinical ..... 0620  
Developmental ..... 0623  
Experimental ..... 0624  
Industrial ..... 0625  
Personality ..... 0989  
Physiological ..... 0349  
Psychobiology ..... 0632  
Psychometrics ..... 0451  
Social ..... 0451



## ABSTRACT

Wear at high temperatures is technologically important in components which function at elevated temperatures and are subjected to sliding or erosive wear. Examples include components in combustion engines, brake components and turbine blades and rotors in jet engines. No quantitative wear equations for material selection and design against high temperature wear are presently available. It is therefore important to understand the physical mechanisms involved in the wear process and to determine wear rates under different operating conditions such as sliding speed and applied load at elevated temperatures. Mechanisms of debris formation and effect of these variables on the wear mechanisms at elevated temperatures have not been investigated in new engineering materials. Aluminum matrix composites, with high strength and high thermal stability, are replacing cast iron in automotive engine and brake components where temperature exceeds 200°C. Intermetallic materials are designated high temperature materials and considerable progress has been made in improving their ductility. Thus two materials, representing each class of materials with potential tribological application prospects, have been selected for this work. Sliding wear of Al6061, Al6061-20%Al<sub>2</sub>O<sub>3</sub> and Ti<sub>50</sub>Ni<sub>47</sub>Fe<sub>3</sub> was studied in the temperature range 25-520°C against a SAE52100 steel counterface. A new wear machine was constructed to operate in the temperature range 25-1000°C. Both wear rates and coefficient of friction ( $\mu$ ) were measured. Detailed analysis of wear debris and worn materials was carried out.

Al6061 and Al6061-20%Al<sub>2</sub>O<sub>3</sub> showed transitions from mild wear to severe wear at a critical temperature which depended on the applied load. The transition was delayed in Al6061-20%Al<sub>2</sub>O<sub>3</sub> to 230°C as compared to 150°C for Al6061 at 10 N load due to a higher flow strength of the composite at elevated temperatures. Al6061-20%Al<sub>2</sub>O<sub>3</sub> showed better severe wear resistance than Al6061 due to formation of hard surface layers containing a fine distribution of comminuted Al<sub>2</sub>O<sub>3</sub> particles. During mild wear at low temperatures, wear resistance of Al6061 was slightly better than the composite and improved (along with  $\mu$ ) with temperature due to formation of iron (oxide) transfer layer on the sliding surfaces.

The  $\text{Ti}_{50}\text{Ni}_{47}\text{Fe}_3$  alloy demonstrated excellent wear resistance at room temperature. Despite having lower hardness of  $300 \text{ kg.mm}^{-2}$ ,  $\text{Ti}_{50}\text{Ni}_{47}\text{Fe}_3$  alloy showed only 2-5% as much wear as hard SAE52100 (hardness  $870 \text{ kg.mm}^{-2}$ ). This could be attributed to formation (on the surface of  $\text{Ti}_{50}\text{Ni}_{47}\text{Fe}_3$ ) of transfer layers of compacted oxide debris which were supported by hard mechanically mixed layer below. A sliding speed dependent transition from mild to severe wear was observed on increasing the sliding speed above  $2.6 \text{ m.s}^{-1}$ .  $\text{Ti}_{50}\text{Ni}_{47}\text{Fe}_3$  alloy showed mild to severe wear transition on increasing the test temperature above  $350^\circ\text{C}$ . The wear rates and  $\mu$  decreased with increase of temperature in the mild wear regime. The  $\text{Ti}_{50}\text{Ni}_{47}\text{Fe}_3$  show extremely low wear rates in the temperature range  $200\text{-}350^\circ\text{C}$ . At elevated temperatures, the intermetallic softened and suffered extensive sliding wear damage.

The effect of an increase in temperature was similar for all the three materials investigated. The wear rates decreased with temperature up to a critical temperature above which the wear rates increased sharply. At low temperatures, formation of iron rich layers on the sliding surfaces and solid lubrication by the steel wear debris, both helped to decrease the wear rates and  $\mu$ . At high temperatures, low flow strength and loss of work hardening ability resulted in extensive damage to sliding surface as a result of gross plastic deformations and macroscopic material transfer to the counterface.

**To my wife Sandeep**



## **ACKNOWLEDGMENTS**

I would like to express my sincere thanks to Dr. A.T. Alpas for his supervision, interest, encouragement and friendship. The technical expertise of Mr. J.W. Robinson is appreciated.

The financial support from NSERC and an Industrial Consortium of Alcan, INCO, Ontario Hydro, Sherrit-Gordon, Pratt and Whitney and ComDev is gratefully acknowledged.

## TABLE OF CONTENTS

|   |       |
|---|-------|
| Abstract  | iii   |
| Dedication  | v     |
| Acknowledgements  | vi    |
| List of Tables  | x     |
| List of Figures   | xi    |
| Nomenclature  | xvi   |
| <br>Chapter 1. INTRODUCTION                             | <br>1 |
| <br>Chapter 2. LITERATURE SURVEY                        |       |
| 2.1. Sliding Wear                                       | 4     |
| 2.2. Factors Effecting Sliding Wear                     | 6     |
| 2.3. Frictional Heating                                 | 8     |
| 2.4. Effect of Temperature on Sliding Wear              | 9     |
| 2.5. High Temperature wear of Metallic Materials        | 10    |
| 2.6. Sliding Wear of Aluminum Matrix Composites         | 12    |
| 2.7. Sliding Wear of Intermetallic Alloys               | 13    |
| 2.8. Mechanical Behaviour of Aluminum Matrix Composites | 14    |
| 2.9. $\text{Ti}_{50}\text{Ni}_{47}\text{Fe}_3$ alloy    | 17    |
| <br>Chapter 3. EXPERIMENTAL METHODS                     |       |
| 3.1. Test and Counterface Materials                     | 19    |
| 3.2. Wear Testing                                       | 25    |
| 3.3. Analyses of Worn Materials                         | 37    |
| 3.4. Mechanical Testing                                 | 38    |

## Chapter 4. Al6061 AND Al6061-20%Al<sub>2</sub>O<sub>3</sub>

### A. EXPERIMENTAL RESULTS

|   |    |
|---|----|
| 4.1. Volume Loss vs Sliding Distance Curves | 40 |
| 4.2. Wear Rates vs Temperature              | 44 |
| 4.3. Wear Rates vs Applied Load             | 47 |
| 4.4. Counterface Wear                       | 49 |
| 4.5. Friction Measurements                  | 49 |
| 4.6. Characterization of Worn Surfaces      | 56 |
| 4.7. Subsurface Characterization            | 66 |
| 4.8. Debris Analysis                        | 69 |
| 4.9. Mechanical Behaviour                   | 70 |
| 4.10 Summary of the Results                 | 92 |

### B. DISCUSSION OF THE RESULTS

|   |     |
|---|-----|
| 4.11. Role of Plastic Deformation During Severe Wear  | 96  |
| 4.12. Modelling of Severe Wear  | 98  |
| 4.13. Changes in Subsurface Microstructural and Mechanical<br>Properties During Severe Wear | 105 |
| 4.15. Effect of Temperature on Mild Wear  | 108 |

## Chapter 5. Ti<sub>50</sub>Ni<sub>47</sub>Fe<sub>3</sub> INTERMETALLIC ALLOY

### A. EXPERIMENTAL RESULTS

|  |     |
|--|-----|
| 5.1. Thermo-mechanical Treatment         | 112 |
| 5.2. Wear Rates at Room Temperature      | 116 |
| 5.3. Wear Rates at Elevated Temperatures | 122 |
| 5.4. Friction Measurements               | 124 |
| 5.5. Wear Debris                         | 124 |
| 5.6. Worn Surfaces                       | 131 |

|  |         |
|--|---------|
| 5.7. Subsurfaces Characterization              | 143     |
| 5.8. Summary of Observations                   | 153     |
| <br><u>B. DISCUSSION OF THE RESULTS</u>        |         |
| 5.9. Room Temperature Wear                     | 158     |
| 5.10. Effect of Temperature                    | 163     |
| 5.11. Formation of Tribo-Layers                | 165     |
| <br>Chapter 6. CONCLUSIONS AND RECOMMENDATIONS | <br>169 |
| <br>References                                 | <br>174 |
| Vita Auctoris                                  | 180     |

## LIST OF TABLES

### Table

|  |     |
|--|-----|
| 3.1. Hardness and densities of specimen and counterface materials.   | 23  |
| 4.1. Transition loads for Al6061 and Al6061-20%Al <sub>2</sub> O <sub>3</sub> .  | 48  |
| 4.2. Summary of observations on wear of Al6061 and Al6061-20%Al <sub>2</sub> O <sub>3</sub> .                                | 93  |
| 4.3. Summary of important findings on sliding high temperature wear of Al6061 and Al6061-20%Al <sub>2</sub> O <sub>3</sub> . | 110 |
| 5.1. Effect of thermo-mechanical treatment on mechanical properties of Ti <sub>50</sub> Ni <sub>47</sub> Fe <sub>3</sub> .   | 114 |
| 5.2. Summary of results on sliding wear of Ti <sub>50</sub> Ni <sub>47</sub> Fe <sub>3</sub> alloy.                          | 155 |

## LIST OF FIGURES

|   |    |
|---|----|
| Fig.  |    |
| 3.1. Optical micrographs of (a) unreinforced Al6061, (b) Al6061-20%Al <sub>2</sub> O <sub>3</sub> .   | 21 |
| 3.2. X-ray diffraction analysis (XRD) of Ti <sub>50</sub> Ni <sub>47</sub> Fe <sub>3</sub> alloy after melting and homogenization at 950°C for two hours.                                   | 22 |
| 3.3. Optical micrograph of fully annealed Ti <sub>50</sub> Ni <sub>47</sub> Fe <sub>3</sub> intermetallic alloy.  | 23 |
| 3.4. Optical micrographs of SAE52100 steel, (a) spherodized and (b) quenched and tempered.  | 24 |
| 3.5. High temperature wear machine (a) photograph and (b) schematic.  | 27 |
| 3.6. A schematic showing principle of friction force measurement.   | 30 |
| 3.7. Specimen and counterface geometries employed for high temperature wear of Al6061-20%Al <sub>2</sub> O <sub>3</sub> .   | 33 |
| 3.8. Pin on disc wear geometry employed for high temperature wear of Ti <sub>50</sub> Ni <sub>47</sub> Fe <sub>3</sub> .  | 34 |
| 3.9. Block on ring wear machine used for room temperature sliding wear of Ti <sub>50</sub> Ni <sub>47</sub> Fe <sub>3</sub> .   | 35 |
| 4.1. Plots of volumetric wear loss (a) Al6061, (b) Al6061-20%Al <sub>2</sub> O <sub>3</sub> under 10 N load at different test temperatures.   | 41 |
| 4.2. Wear rates of both Al6061 and Al6061-20%Al <sub>2</sub> O <sub>3</sub> plotted against temperature. Wear rates obtained from specimen height change.                                   | 45 |
| 4.3. Wear rates obtained from weight loss measurements plotted against test temperature.  | 46 |
| 4.4. Effect of load on the sliding wear behaviour of Al6061-20%Al <sub>2</sub> O <sub>3</sub> at different test temperatures. Wear rates obtained from specimen height change measurements. | 51 |
| 4.5. Wear rates vs applied load plots for Al6061-20%Al <sub>2</sub> O <sub>3</sub> determined at different temperatures. Wear rates obtained from weight measurements.                      | 52 |

|   |    |
|---|----|
| 4.6. Wear rates of SAE52100 counterface plotted against test temperature.   | 53 |
| 4.7. Wear rates vs applied load plots for SAE52100 counterface determined at different temperatures.  | 54 |
| 4.8. Frictional trace during sliding of Al6061-20%Al <sub>2</sub> O <sub>3</sub> against SAE 52100 at different temperatures.                                 | 55 |
| 4.9. Effect of temperature on coefficient of friction for Al6061 and Al6061-20%Al <sub>2</sub> O <sub>3</sub> .   | 57 |
| 4.10. Optical micrographs of worn surfaces of Al6061 and Al6061-20%Al <sub>2</sub> O <sub>3</sub> after sliding at room temperatures at 10 N load.            | 59 |
| 4.11. Electron micrographs from worn surfaces of Al6061 after sliding at room temperature at 10 N load.   | 60 |
| 4.12. Al6061 specimen worn at 150°C under 10 N load (a)-(c) electron micrographs and (d) EDS of the iron rich region in (b).                                  | 61 |
| 4.13. Electron micrographs of worn surfaces of Al6061-20%Al <sub>2</sub> O <sub>3</sub> after sliding at room temperature at 10 N load.                       | 63 |
| 4.14. Optical micrographs of worn surfaces of Al6061 and Al6061-20%Al <sub>2</sub> O <sub>3</sub> specimen after sliding at room temperature under 10 N load. | 64 |
| 4.15. Electron micrographs of worn surfaces of Al6061 slid at 200°C and Al6061-20%Al <sub>2</sub> O <sub>3</sub> slid at 350°C at 10 N load.                  | 65 |
| 4.16. Longitudinal cross-sections of Al6061 and Al6061-20%Al <sub>2</sub> O <sub>3</sub> after sliding at room temperature under 10 N load.                   | 70 |
| 4.17. Longitudinal cross-section of Al6061 worn at 350°C at 10 N load depicting recrystallised grains.  | 71 |
| 4.18. Longitudinal cross-section of Al6061 after sliding at room temperature under 250N load.   | 72 |
| 4.19. Longitudinal cross-section of Al6061-20%Al <sub>2</sub> O <sub>3</sub> after sliding at 300°C at 10 N load.   | 73 |
| 4.20. Transverse tapered section of Al6061-Al <sub>2</sub> O <sub>3</sub> after sliding at 350°C at 10 N load.  | 74 |
| 4.21. Optical micrographs indicating particle comminution after sliding   |    |

|   |     |
|---|-----|
| at elevated temperatures.   | 75  |
| 4.22. Plots of subsurface hardness (Vickers) vs depth below the surface for Al6061 and Al6061-20%Al <sub>2</sub> O <sub>3</sub> after sliding at different temperatures.                                  | 76  |
| 4.23. XRD analysis of debris generated during Al6061 sliding at room temperature and 150°C at 10 N load.  | 77  |
| 4.24. Stress-strain curves obtained from compression tests at elevated temperatures for Al6061 and Al6061-20%Al <sub>2</sub> O <sub>3</sub> .   | 82  |
| 4.25. Comparison of flow curves (a), and work-hardening rates (b), for Al6061 and Al6061-20%Al <sub>2</sub> O <sub>3</sub> at room temperature.   | 84  |
| 4.26. Comparison of flow curves (a), and work-hardening rates (b), for Al6061 and Al6061-20%Al <sub>2</sub> O <sub>3</sub> at 300°C.  | 85  |
| 4.27. Plots of flow strength of both unreinforced Al6061 and Al6061-20%Al <sub>2</sub> O <sub>3</sub> at plastic strain of 1%, and 20% ( $\epsilon_p=0.01$ , and 0.2) against temperature of compression. | 86  |
| 4.28. Rate of decrease of flow strength vs temperature for Al6061 and Al6061-20%Al <sub>2</sub> O <sub>3</sub> .  | 87  |
| 4.29. Effect of temperature on the work hardening behaviour of Al6061 and Al606-20%Al <sub>2</sub> O <sub>3</sub> .   | 88  |
| 4.30. Electron-micrograph of Al6061-20%Al <sub>2</sub> O <sub>3</sub> compressed to 50% strain at room temperature.   | 89  |
| 4.31. Electron micrographs and an optical micrograph of Al6061-20%Al <sub>2</sub> O <sub>3</sub> specimen compressed at room temperature to 50% strain depicting particulate damage.                      | 90  |
| 4.32. Flow strength and wear rates of both Al6061 and Al6061-20%Al <sub>2</sub> O <sub>3</sub> plotted against test temperature.  | 100 |
| 4.33. Wear rates of Al6061 and Al6061-20%Al <sub>2</sub> O <sub>3</sub> plotted against 1/T. The wear rates measured from specimen height change at 10 N load.  | 104 |
| 5.1. Effect of cold work on yield strength (YS), tensile strength (TS), and ductility (% el.) of Ti <sub>50</sub> Ni <sub>47</sub> Fe <sub>3</sub> .  | 113 |



|  |     |
|--|-----|
| 5.2. Outline of the thermo-mechanical treatment given to $\text{Ti}_{50}\text{Ni}_{47}\text{Fe}_3$ prior to wear testing.  | 115 |
| 5.3. Volumetric wear plots of (a) $\text{Ti}_{50}\text{Ni}_{47}\text{Fe}_3$ alloy and (b) SAE52100 steel at various applied loads at a sliding speed of $0.4 \text{ m.s}^{-1}$ .                   | 117 |
| 5.4. Effect of load on wear rates of $\text{Ti}_{50}\text{Ni}_{47}\text{Fe}_3$ and SAE52100 steel at room temperature.   | 119 |
| 5.5. Effect of sliding speed on wear rates of $\text{Ti}_{50}\text{Ni}_{47}\text{Fe}_3$ and SAE52100.  | 121 |
| 5.6. Effect of temperature on the sliding wear of $\text{Ti}_{50}\text{Ni}_{47}\text{Fe}_3$ and SAE52100.  | 123 |
| 5.7. Friction trace during wear run of $\text{Ti}_{50}\text{Ni}_{47}\text{Fe}_3$ alloy sliding against SAE52100 at different temperatures.   | 126 |
| 5.8. Plot of average coefficient of friction against test temperature during sliding of $\text{Ti}_{50}\text{Ni}_{47}\text{Fe}_3$ against SAE52100.  | 128 |
| 5.9. XRD analysis of wear debris produced during sliding of $\text{Ti}_{50}\text{Ni}_{47}\text{Fe}_3$ against SAE52100 at (a) 10 N load, and (b) 400 N load.                                       | 129 |
| 5.10. XRD analysis of wear debris at sliding speed of $4.2 \text{ m.s}^{-1}$ under 20N load.   | 130 |
| 5.11. Optical micrographs of worn surfaces of $\text{Ti}_{50}\text{Ni}_{47}\text{Fe}_3$ alloy at (a) 10 N load, (b) 400 N load, at sliding speed of $0.4 \text{ m.s}^{-1}$ .                       | 133 |
| 5.12. (a) Electron micrograph of the worn surface of $\text{Ti}_{50}\text{Ni}_{47}\text{Fe}_3$ alloy at 10 N load, (b)EDS performed on the wear tracks.  | 134 |
| 5.13. (a) Electron micrograph of the worn surface $\text{Ti}_{50}\text{Ni}_{47}\text{Fe}_3$ alloy at 400 N load, and (b) EDS results. (sliding speed of $0.4 \text{ m.s}^{-1}$ ).                  | 135 |
| 5.14. XRD analysis performed on the worn surface of $\text{Ti}_{50}\text{Ni}_{47}\text{Fe}_3$ after sliding at 400 N load (sliding speed $0.4 \text{ m.s}^{-1}$ ).                                 | 136 |
| 5.15. Surface morphology of SAE 521000 steel ring after sliding at 400 N load.   | 137 |
| 5.16. Optical micrograph of the worn surface of $\text{Ti}_{50}\text{Ni}_{47}\text{Fe}_3$ after sliding at sliding speed of $4.2 \text{ m.s}^{-1}$ (load 20 N).                                    | 137 |
| 5.17. Optical micrographs of worn surfaces of $\text{Ti}_{50}\text{Ni}_{47}\text{Fe}_3$ after sliding at different loads.  | 138 |
| 5.18. Electron micrograph and EDS analysis of worn surface of $\text{Ti}_{50}\text{Ni}_{47}\text{Fe}_3$ after sliding at $520^\circ\text{C}$ . (load 15 N, sliding speed $0.4 \text{ m.s}^{-1}$ ). | 139 |

|   |     |
|---|-----|
| 5.19. XRD analysis performed on wear track of $\text{Ti}_{50}\text{Ni}_{47}\text{Fe}_3$ slid at 520°C.  | 140 |
| 5.20. Optical micrographs of wear tracks on the surface of SAE52100 after sliding at (a) 200°C and (b) 480°C.   | 141 |
| 5.21. Wear track on the surface of SAE52100 after sliding at 520°C, (b) EDS analysis done inside the wear track, and (c) outside the wear track.  | 142 |
| 5.22. Longitudinal cross-section through the worn surface of $\text{Ti}_{50}\text{Ni}_{47}\text{Fe}_3$ at 400 N load.   | 146 |
| 5.23. Longitudinal tapered section of $\text{Ti}_{50}\text{Ni}_{47}\text{Fe}_3$ tested under 400 N load depicting (a) finger type morphology below the contact surface; (b) microhardness values obtained at various locations. | 147 |
| 5.24. Detailed morphology of hard fingers and oxide layer present on the wear track.  | 148 |
| 5.25. Cross-section (transverse) through $\text{Ti}_{50}\text{Ni}_{47}\text{Fe}_3$ worn at 400 N load.  | 149 |
| 5.26. Longitudinal section of $\text{Ti}_{50}\text{Ni}_{47}\text{Fe}_3$ after sliding at a speed of 4.2 m.s <sup>-1</sup> at 20 N load, (a) optical, (b) electron micrograph.   | 150 |
| 5.27. Longitudinal cross-section of $\text{Ti}_{50}\text{Ni}_{47}\text{Fe}_3$ after sliding at 520°C (unetched).  | 151 |
| 5.28. Longitudinal cross-section of $\text{Ti}_{50}\text{Ni}_{47}\text{Fe}_3$ after sliding at 520°C (etched).  | 152 |
| 5.29. Subsurface changes in $\text{Ti}_{50}\text{Ni}_{47}\text{Fe}_3$ after sliding against SAE52100 at room temperature (schematic). (sliding speed 0.4 m.s <sup>-1</sup> ).   | 160 |
| 5.30. A model for development of transfer layer on the surface of $\text{Ti}_{50}\text{Ni}_{47}\text{Fe}_3$ during sliding against SAE52100.  | 167 |

## NOMENCLATURE

|                     |                                  |
|---------------------|----------------------------------|
| $e$                 | Engineering strain               |
| $\varepsilon$       | True strain                      |
| $S$                 | Engineering stress               |
| $\sigma$            | True stress                      |
| $\dot{\varepsilon}$ | Strain rate                      |
| $t$                 | Time                             |
| $D$                 | Diameter                         |
| $h, H$              | Height                           |
| $L$                 | Length                           |
| $s$                 | Sliding distance                 |
| $v$                 | Sliding speed                    |
| $w$                 | Volumetric wear loss             |
| $\dot{w}$           | Volumetric wear rate             |
| $P$                 | Applied normal load              |
| $T$                 | Tagential load                   |
| $\mu$               | Coefficient of friction          |
| CTE                 | Coefficient of thermal expansion |
| $Q$                 | Activation energy                |

## Chapter 1

# INTRODUCTION

Many components subjected to sliding wear or erosion are also required to operate at high temperatures. Erosion of turbine-blades made from super alloys occur at about 800°C. Cast iron liners in combustion engines are required to operate at 200°C. For the development of materials subjected to high temperature wear, the wear mechanisms have to be known. This is important because at elevated temperature the wear mechanisms are completely different from those observed at room temperature and often result in large unexpected changes in friction and wear of materials. Frictional heating itself plays important role during ambient temperature wear [1,2] and varies with load and speed. External heating, therefore, can be used to vary the temperature of sliding bodies in a more controlled fashion to understand its significance more clearly. This work aims to examine the high temperature wear of two technologically important groups of materials: metal matrix composites, and intermetallics.

Aluminum alloys are now increasingly being favoured for applications in the automobile industry to reduce the weight of passenger cars and to improve fuel efficiency in order to satisfy emission standards [3]. Reinforcing these alloys with ceramic particulate to achieve superior mechanical properties have opened new applications [4]. Heat treatable aluminum alloys reinforced with discontinuous particulate or fibres are presently the most commonly available and easily produced metal matrix composites [5].

Recent research has focused on the room temperature tribological and mechanical behaviour of aluminum matrix composites [5-7]. However, their high temperature properties have only recently started being considered [5,8]. Many of the current and potential applications of aluminum matrix composites involve components which are required to operate under sliding contact conditions at elevated temperatures. Examples

include piston and cylinder liners in automotive engines where traditionally cast iron liners have been used. Aluminum matrix composites are being tested for brake rotors in cars as well as brake discs for high speed railway vehicles [9]. The operating temperature can reach 0.5 to 0.8 times the melting point of the matrix alloy under these conditions.

The study of elevated temperature wear mechanisms is relevant to the hot extrusion of aluminum matrix composites. Extensive die wear and surface cracking of composites during extrusion remains outstanding problems in the processing of these materials. Joining of metal matrix composites is difficult and frictional welding is being tried [10]. For this purpose, understanding of frictional behaviour and subsurface damage accumulation during sliding under high contact pressures at elevated temperatures is needed.

Alloys of both nickel and titanium are often used for applications at elevated temperatures which require oxidation resistance and high temperature strength. Intermetallics are known for their better mechanical properties as well as oxidation resistance at elevated temperatures. These alloys are marred by very low ductility at low temperatures. Titanium-Nickel alloys based on the intermetallic alloy TiNi, however, exhibit unusually high room temperature ductility, good impact resistance as well as good corrosion resistance. These alloys are better known for their exotic two-way shape memory properties[11]. These alloys are being commercially produced and used for hydraulic fittings. They show excellent bio-compatibility and are often used for body implants.

Ti<sub>50</sub>Ni<sub>47</sub>Fe<sub>3</sub> alloy, has an Ms temperature well below 0°C. High temperature B2 phase possesses very good ductility because plastic deformation occurs through a combination of twinning and dislocation slip. Work of Moberly et al. [12] has shown that thermo-mechanical strengthening can be used to obtain a high strength high ductility alloy. The intermetallic shows good fatigue resistance as cyclic loading results in large strain hardening of the alloy. With these properties, this alloy can be expected to possess

good wear resistance. The alloy is being considered for structural applications such as rim for locomotive wheels due to its superior tribological behaviour.

Two different classes of materials, which have the potential for improved wear resistance at elevated temperatures, have been investigated in this study. An aluminum matrix composite, Al6061 reinforced with 20%  $\text{Al}_2\text{O}_3$  has been investigated for its dry sliding wear behaviour up to 500°C. Unreinforced 6061 alloy was investigated for comparison. Studies on the mechanical behaviour of both the alloys were carried out in order to understand the high temperature wear behaviour. Elevated temperature dry sliding characteristics of a ternary  $\text{Ti}_{50}\text{Ni}_{47}\text{Fe}_3$  intermetallic alloy were also studied. Mechanical testing was undertaken to characterize the intermetallic alloy and to understand its response to thermo-mechanical treatments. Effort was also made to understand the room temperature wear of the alloy due to lack of information on the sliding wear of this alloy in the open literature.

This thesis is divided into six chapters. The relevant literature on the mechanical and tribological behaviour of the two materials is reviewed (Chapter 2). Experimental procedure which applies to both the materials is given in Chapter 3. The experimental results and discussion are divided according to the materials studied. The Al6061-20% $\text{Al}_2\text{O}_3$  including unreinforced 6061 alloy are dealt with in Chapter 4 while Chapter 5 is dedicated to the intermetallic alloy. Conclusions and suggestions for further work are given in Chapter 6.

## Chapter 2

# LITERATURE SURVEY

### 2.1. Sliding Wear

Wear is defined as damage to a solid surface, generally involving progressive loss of material, due to relative motion between that surface and a contacting substance or substances (ASTM Standard G40 [13]). The wear classification most widely used at the present time is the one based on the ideas of Burwall and Stran [14] with four principal wear mechanisms: abrasion, adhesion, corrosion and fatigue. In any one set of imposed sliding conditions, particle detachment and debris frequently result from a mixture of two or more of the above processes operating either simultaneously or successively for limited periods of time.

Sliding wear can be classified based on two broad types of wear phenomena encountered [15] and described as severe and mild wear. The characteristic features of the severe wear are high wear rates, extensive plastic deformation in metals, transfer to harder counterface and metallic wear debris. Mild wear, in contrast, involves low wear rates, oxidised wear debris and surface film formation.

One of the very first and most commonly cited wear models is accredited to Archard [16,17], who gave an expression that predicted that the wear rate is proportional to the load and independent of the nominal contact area[16],

$$W=k.(P/P_m).s \quad \dots\dots\dots (2.1)$$

where, W is the volumetric loss during wear, k is proportionality constant, P is the applied

load,  $P_m$  is the flow stress of the material and  $s$  is the sliding distance. The coefficient,  $k$ , is known as wear coefficient or Archard's wear coefficient. According to Archard,  $k$  indicates the probability of forming a debris particle during interaction among contacting asperities. The flow stress is often obtained from the indentation hardness of the material.

Flake type wear debris and cracks parallel to the wear surface are frequently encountered in sliding wear and is often described as delamination wear [18-26]. Suh [18,19] postulated a wear model based on dislocation dynamics in which wear is thought to occur by the coalescence of voids or cracks. The cracks form at a critical distance below the surface and lead to the delamination of sheets of metal from the surface. Suh [18] proposed that dislocations in a thin layer near the surface were eliminated through migration to the surface under the image force which arise due to the proximity to the free surface. The dislocation pileups would form at a certain distance below the surface by the interaction of the hard slider against a softer material. Voids can nucleate with continued sliding as a result of high dislocation density. Second phase particles would provide a boundary where dislocations could pile-up leading to enhanced void nucleation. Heilmann and his co-workers [20] have suggested that subsurface cracks would develop parallel to the dislocation cell boundaries which form under large plastic strains. Fracture mechanics has been applied to the problem and microscopic ideas based on cell structure has been invoked to explain the size of the wear fragments [20].

Flemming and Suh [21], Kimura [22], and Ritchie [23] have proposed wear models based on fatigue process due to the cyclic nature of the asperity loading. Many workers have applied linear elastic fracture mechanics to the phenomenon of subsurface crack growth which assumes that the plasticity exists only at the crack tip. Most ductile metals, however, exhibit large subsurface deformation during sliding wear which makes the basis of these models suspect.

In ductile alloys, subsurface deformation is often localized in shear bands[24-26]. Alpas and Embury[25] demonstrated that strain localization in the subsurface led to crack



nucleation and growth through the shear bands. Rosenfield [26] has put forth a shear instability model for the sliding wear. According to his theory, a crack once nucleated, grows under Mode-II loading. The depth at which crack nucleates is determined by the local flow strength of the material and the stress intensity due to asperity loading. Since, the flow strength decreases with increasing depth (work-hardening gradient) while the stress intensity has a maximum below the surface, there may be a point where the stress intensity exceeds the local flow stress resulting in shear instability and crack propagation.

Zhang and Alpas [27] have developed a model based on the damage gradient observed below the worn surface. The damage gradient exists due to competition between the surface plastic strain, which leads to crack nucleation at second phase particles, and the hydrostatic stress which opposes the crack formation. Using an equation developed by Rice and Tracy [28] for void growth during ductile fracture, the problem of subsurface plasticity which limits linear elastic fracture mechanics approach, was overcome. The model indicated that an increase in hydrostatic stress results in an increase in crack depth but a reduction in the crack growth rate.

Development of wear mechanism maps [29] has marked significant progress in understanding the complex problem of wear. Normalized load and normalized velocity are taken as independent variables and form, respectively, the abscissa and the ordinate axis of the map. The normalized load is obtained by dividing the applied load by the product of nominal area of contact and the room temperature hardness while velocity is normalized by dividing it with the pin radius and the thermal diffusivity of the material. Lines of constant wear rate are scribed on the map as well as boundaries between dominant wear mechanisms are outlined. These maps are not yet developed to the point where they could be used for the design purposes.

## 2.2. Factors Effecting Wear

Material variables play important role during sliding wear. Material composition,

microstructural properties such as grain size, number of phases, phase distribution, anisotropy as well as mechanical properties such as strength, hardness and ductility of both contacting bodies affect the wear behaviour[30,31]. The presence of second phase particles for instance has important influence on the operating wear mechanisms[29]. Studies on the effect of grain size have reported conflicting results. Decreasing the grain size, which increases the strength and hardness, resulted in an increase in wear resistance as well as in seizure resistance[32]. Many of the factors listed above are however interrelated. A change in one factor often result in change of other properties as well. Therefore, appropriate reporting of microstructural and mechanical properties is important.

Environmental variables exert important influence in the process of wear. Testing in vacuum produces entirely different results than testing in air [33]. The coefficient of friction is often much higher in vacuum than in air. During testing in air, the surface is contaminated with an absorbed layer containing gases, hydrocarbons and moisture. Most metals oxidize in air. Oxides and nitride products are often form a thin layer, about 10 nm thick, on the surface of metals [34-35]. During sliding, these layers can act as lubricants and are effective in preventing metal to metal contact at low loads [34]. The influence of environmental humidity on the friction and wear of materials has been reviewed by Lancaster[35].

Testing method and test conditions also plays important role in the sliding wear of materials. During a wear test, the factors that affect wear include applied load, sliding speed, sliding distance, ambient temperature, environment, counterface material, surface geometry and oscillating versus unidirectional sliding [34]. Less obvious factors are machine stiffness and its damping capacity. Increasing damping capacity lowers wear rates. Increasing machine stiffness yields results similar to increasing the load. The geometry of the wear couple has significant influence on the friction and wear in any wear set up. Drastically different results are often obtained when the pin and disk materials are interchanged [36]. The ability of the debris to exit from the contact surface has been identified as a critical factor. Close control of the testing variables is therefore

necessary if comparison with the published data is desired.

### 2.3. Frictional Heating

When two surfaces slide together, most of the work done against friction turns into heat. The resulting temperature rise may modify the mechanical and metallurgical properties of the sliding materials, it may oxidize or even melt them and therefore greatly influence the wear rates [2,29,37-46]. Increase of sliding speed increases the temperature and often has the same effect on wear as increasing the ambient temperature. However, the predominant effect of increasing the applied load is to increase the plastic damage in the subsurface [38]. Oxidational wear of steels has been studied by many workers and transition from mild oxidation wear to severe oxidation wear has been attributed to the frictional heating during sliding. Lancaster [35] has observed similar transitions dependent on sliding speed during wear of copper based alloys. Quinn [40,41] has reviewed the oxidational wear of steel recently.

The frictional heat is generated at tiny contact areas (asperities), where, the local or flash temperature could be much higher than the average or bulk temperature [42-44]. The heat generated during the sliding process depends on the coefficient of friction ( $\mu$ ), applied load ( $P$ ) and the sliding speed. The heat generated per unit area per second is [26],

$$q = \mu P v / A_n \quad \dots\dots\dots (2.2)$$

where,  $A_n$  is nominal area of contact between the sliding bodies. This heat is shared by the contacting bodies depending upon the contact geometry as well as their thermal conductivity values. The value of  $\mu$  is often dependent upon sliding speed,  $v$ . Lim and Ashby [29] have analyzed the case of pin on disc sliding geometry for steel and generated temperature maps for both bulk and flash temperature, with normalized load and normalized speed making the abscissa and the ordinate, respectively. Ashby et al. [42] have similarly generated friction heating maps and applied them to the friction welding

of various materials.

## 2.4. Effect of Temperature on Sliding Wear

Temperature plays an important role in sliding wear of metallic materials and the wear mechanisms at high temperature are completely different from those operating at ambient temperature [46-49]. As the temperature is raised, any single-phase materials, including those with martensitic structures, will become softer and more ductile; rate of oxidation will increase and the type of oxide formed may change; hard precipitates may be dissolved or grow and become less effective; crystal structure may change; and mutual solubility may increase [49].

The effect of temperature on the oxidative wear of materials has been well documented [50,51]. Friction heating also plays important role in the oxidative wear. Oxidation kinetics during sliding wear have been found to be much greater than the static oxidation on account of higher defect concentration and therefore higher diffusion rates[35,37,38].

In the oxidative wear of steels, the predominant oxide present in the debris changes with sliding speed and ambient temperature. At low temperatures  $\alpha$ -Fe<sub>2</sub>O<sub>3</sub> dominates, with FeO forming at higher speeds and temperatures and Fe<sub>3</sub>O<sub>4</sub> at intermediate conditions [35]. It is clear that oxide growth during sliding, like thermal oxidation during static conditions, obeys an Arrhenius equation [40,41]:

$$k_p = A \exp (-Q/RT) \quad \text{.....} \quad (2.3)$$

where,  $k_p$  is the parabolic rate constant for growth of the oxide film,  $T$  is the absolute temperature and  $R$  is the gas constant.  $A$  is the pre-exponential factor or Arrhenius constant and  $Q$  is the activation energy which determines the temperature dependence of the growth rate. Value of  $A$  in sliding wear has been found to be much higher than

observed for the static oxidation of steel, while the values of  $Q$  was similar for both and dynamic oxidation [41]. However, more recent results of the same author [50] suggest that the  $Q$  for oxidation during sliding wear is almost half the magnitude of static oxidation.

Temperature dependent wear transitions have been reported by many workers in the case of high temperature alloys of nickel, iron and cobalt [51,52]. These alloys have been shown to form a protective glaze of oxides on the surface resulting in large drop in wear rates.

At elevated temperature ( $>0.5T_m$ , where,  $T_m$  is the melting temperature) the time dependent microstructural changes may dominate the wear properties of the material. High recovery kinetics will lower the flow stress of the material. Recrystallization at high temperature can result in total loss of the work hardening ability of the material [43,44].

The effect of change of crystal structure has been demonstrated in the case of cobalt which undergoes allotropic change from CPH to FCC at 417°C which results in a dramatic increase in friction and wear [49].

## 2.5. High Temperature Wear of Metallic Materials

Alloys of iron, nickel, cobalt and titanium are often used in high temperature applications where strength and oxidation resistance are important. Their wear behaviour has been studied by many workers [51-55]. High temperature fretting and wear of metallic materials has been reviewed recently by Waterhous and Taylor [53].

Earles and Fenwick [51] studied the sliding wear of nickel based alloy (Nimonic 75) using pin on disc tests at temperatures up to 810°C and found that the friction and wear rates were high below 600°C. Above 600°C, at low loads the sliding was smooth and wear rates were low due to formation of a layer of oxide on the pin. Prolonged sliding distances or increase of load resulted in removal of the oxide and increase in wear rates.

For a constant value of applied load both the wear rate and the friction coefficient decreased rapidly between 750 and 800°C, a transition which appears to be related to large increase in oxidation rate in this temperature range.

Buckley and Johnson [52] have reported wear data in the temperature from 25-540°C for a series of binary silicon-nickel alloys. They found that wear decreased by an order of magnitude on increasing the temperature over the above range. X-ray diffraction analysis of the wear debris from the 2.5% silicon-nickel run in air at 540°C indicated that the debris was essentially silicon dioxide ( $\text{SiO}_2$ ) or metallic nickel. Even relatively small additions of silicon reduced the wear rates markedly and the wear rates of the 7.5% silicon-nickel remained only one third of that of a ternary Ni-Cr-Fe alloy which showed higher oxidation resistance. The improved wear resistance of the binary alloys was ascribed to the greater affinity of the silicon for oxygen at high temperatures.

Reciprocating sliding wear of nickel based alloys have been investigated by Stott et al. [54] on commercial as well as specially prepared nickel based alloys with up to 40% chromium. These alloys showed a transition temperature above which a low coefficient of friction and usually low wear rates are observed. Below this temperature, these parameters remain high. These transitions have often been attributed to the formation of protective oxide layers at elevated temperatures. Frequently, due to appearance as a shiny, glassy looking film, the layer has been termed as surface "glaze".

Elevated temperature sliding wear of brass has been studied by Lancaster [55] against hard tool steel up to 500°C using a pin on ring wear machine. At low temperatures, brass suffered severe wear and the wear rates increased with temperature due to thermal softening. Above a critical temperature, however, the rate of wear suddenly decreased into the regime of mild wear. The severe to mild transition temperature decreased with decrease in normal load. This transition could be ascribed to the formation of hardened oxide film on the surface of brass pin. Temperature dependent severe to mild wear transitions have been investigated by Clark et al. [56] in steels and by Dunkley et

al. [54] in cobalt based alloys.

## 2.6. Sliding Wear of Aluminum Matrix composites

Sliding wear of aluminum alloys and aluminum matrix composites has been studied [3,4,58-70]. Improvement in sliding wear resistance of the reinforced alloy has been reported by the addition of discontinuous fibres of  $\text{Al}_2\text{O}_3$  or SiC [58,59]. Lee et al. [58] have shown that the wear resistance of Al6061 increased with volume fraction and size of the reinforcement at sliding speed of  $0.94 \text{ m.s}^{-1}$  at 15 N load. The composite showed higher wear rates than the unreinforced alloy at lower sliding speeds ( $<0.5 \text{ m.s}^{-1}$ ). Similar results have been reported by Park [59]. The composite showed improvement over the unreinforced alloy only at sliding speeds above  $0.4 \text{ m.s}^{-1}$  [63].

Zhang and Alpas [64,65,68] found the wear rates of the reinforced aluminum alloys similar to the unreinforced alloy in the intermediate (5 N-50 N) load range. At low loads ( $<5 \text{ N}$ ) the composite showed lower wear rates than the unreinforced alloy. At higher loads, the wear rates of the composite were close to that of the unreinforced alloy, due to the ease of subsurface crack nucleation and growth in the reinforced alloy. The decohesion along the matrix-particle interface leads to high delamination wear rates. The unreinforced alloy also showed delamination with cracks nucleating at the second phase particles [64-66,68]. The wear resistance of copper decreased after reinforced with  $\text{Al}_2\text{O}_3$  particles [66]. Poor interface bonding resulted in large increase in delamination wear and the reinforced alloy recorded five times higher wear rates than the unreinforced alloy.

Ceramic particles have been shown to increase the load required for the onset of severe wear or seizure with respect to the unreinforced alloy [64-66,68]. Alpas and Zhang have proposed that the severe wear transition will occur once the surfaces reach a critical temperature due to frictional heating [64,65,68]. The critical temperatures were found to be typically between 390-420°K (about  $0.4T_m$ ) for the unreinforced aluminum alloys. Al6061 reinforced with 20%  $\text{Al}_2\text{O}_3$  particles demonstrated higher transition temperature

of  $440 \pm 10^\circ\text{K}$  [64,68].

At very low loads the particles can support the load and result in better wear resistance [64,68]. The counterface often shows higher wear rates due to abrasion by the particles. Debris containing counterface material and the fractured particles transfers and forms a layer on the surface with better wear properties [64-66,68,70]. At high loads, during severe wear, a layer of broken ceramic particles form near the contact surface [8,64-70]. The particle fracturing is often attributed to the large plastic strain beneath the contact surfaces [64,65,68].

Very few studies have been done to understand the wear and friction behaviour of aluminum alloys and aluminum matrix composites at elevated temperatures. Martinez and his co-workers [8] have investigated the dry sliding behaviour of an Al-20Si alloy as well as an Al-7Si alloy reinforced with SiC particles at temperatures from room temperature to  $200^\circ\text{C}$  at load of 25 N. The Al-20Si alloy contained large Si particles. Both the alloys showed mild to severe wear transitions at elevated temperatures. The transition temperature was found to be  $110^\circ\text{C}$  for the unreinforced alloy and  $150^\circ\text{C}$  for the Al-7Si/SiC alloy. Severe wear leads to large subsurface plastic strains and extensive fracture of the reinforcing particles. Friction coefficient values were similar at room temperature and at high temperatures but were lower for the SiC reinforced alloy in the intermediate temperature range.

## 2.7 Wear of Intermetallic Alloys

Tribological properties of the alloys based on ordered TiNi shape memory alloy have been investigated due to their industrial importance. Suzuki and Kuroyanagi [72] showed that the equiatomic TiNi alloy exhibits very good slurry erosion resistance under corrosive environments. Shida and Sugimoto [73] have studied the water jet erosion behaviour of Ti-Ni binary alloys containing 54-60 wt.% nickel. The equiatomic TiNi alloy showed the best erosion resistance and could be attributed to the pseudo-elastic behaviour



of the alloy. Alloys with high or low nickel contents showed poor behaviour due to precipitation of brittle phases.

Moine et al. [74] investigated the dry sliding wear of NiTi alloys after implanting the surface with N<sup>+</sup> ions. The austenitic alloy had better wear and friction resistance than the martensitic alloy. However, after implantation, which formed an amorphous layer on the surface, the sliding behaviour of the martensitic alloy exhibited much more improvement. Sliding wear of a ternary (TiNiFe) alloy has been studied by Clayton [75]. The intermetallic alloy demonstrated good wear resistance under rolling/sliding contact conditions which was attributed to the hardening of the alloy under the application of cyclic stresses generated during the sliding wear process.

Dry sliding wear of ordered Fe-Al alloys have been investigated [76]. The wear resistance of the intermetallic was found to be comparable to the hard steels. No significant difference was observed between ordered and disordered alloys.

## 2.8. Mechanical Behaviour of Aluminum Matrix Composites

There has been a profound interest in the development of metal matrix composites in the last two decades. The addition of high modulus ceramic particles, fibres or whiskers to metallic materials offers a marked increase in stiffness and in many cases tensile strength over monolithic alloys. Particle reinforced light metals, with their potential as low cost, high modulus and strength, better wear resistance, and easily fabricated materials, are reaching the commercial production stage. Considerable research effort has been made to understand the influence of ceramic reinforcement on the mechanical and microstructural properties of aluminum alloys.

The first extensive study of the strength of discontinuously reinforced aluminum alloys was carried out by McDanel [77], who investigated the stress-strain behaviour of various aluminum alloys reinforced with SiC whiskers and particles. He reported up to

60% increase in yield and tensile strengths, depending upon the volume fraction, type of alloy and the matrix temper. The strengthening mechanisms which may operate in particle reinforced MMCs have been considered in many recent publications, and the behaviour has been extensively modeled mathematically [78,79]. Improvement in mechanical response depends on the matrix strength as well as damage accumulation during plastic deformation [80]. Formation of finer substructure during plastic deformation and higher dislocation density on cooling due to large difference in coefficient of thermal expansion between matrix and the reinforcing ceramic particles leads to increased strength of the MMCs [81].

High temperature mechanical behaviour of particle reinforced aluminum matrix composites has been studied only recently [7,82-85]. It has been shown that, while the presence of particles improves the modulus at high temperatures, they do not add significantly to the high temperature strength [82]. The reason for this is that the strengthening mechanisms operating in composites at lower temperatures are relaxed at higher temperatures, and the composite strength is primarily controlled by the high temperature strength of the matrix. Lloyd [5] has, however, indicated that a small improvement in the strength of the composite over the unreinforced alloy is retained at high temperatures. The composite (A356-15%SiC) had 10 MPa higher strength than the matrix alloy (A356) at 300°C. Incorporation of higher volume fraction of the particles (up to 60 vol.%) leads to significant improvement of the high temperature strength but at the cost of ductility [82]. Alternatively, powder processing of rapidly solidified alloys is needed to achieve high strength at elevated temperatures. The ductility of aluminum matrix composites has been shown to increase with temperature [5]. At low temperatures particle fracture controls the tensile elongation. However, at elevated temperatures, general cavitation becomes the predominant failure mechanism.

Recent studies on hot deformation have indicated that the composites have higher recovery and recrystallization rates at elevated temperatures [84,85]. Xiaoxin [84] et al. have shown that the recrystallization occurred during hot torsion specimens of Al6061-

15 vol.% SiC<sub>p</sub> strained at 300-500°C at strain rates between 0.1 and 4 s<sup>-1</sup>.

Strength and ductility of particulate reinforced alloys is significantly effected by the particle damage during plastic deformation, and therefore, has received considerable attention. Early work [86] on weakly bonded reinforcements showed that fracture is dominated by interfacial failure. However, the composites of present commercial interest have good bonding between matrix and the particles and fracture of particles is more important [87-89]. This fracturing of particles starts very early in deformation and continues with increasing strain [89]. Areas of clustered particles are more sensitive to the early damage. At room temperature, tensile strains fracture the particles which lead to high density of void initiation in comparison to the unreinforced alloy. The probability of fracture of particles increases with increase in particle size [5,89]. Brechet et al. [90] have shown that, in tension, the average particle size ( $D$ ) decreased with strain,  $\epsilon$ , as

$$\epsilon = 10^3 \times (D^3 - D_0^3) \quad \text{.....} \quad (2.4)$$

where,  $D_0$  is the initial average particle size.

Results of Zhao, Tuler and Lloyd [8] on high temperature tensile loading of 2014 aluminum alloy with Al<sub>2</sub>O<sub>3</sub> particles indicate that the particle fracture tendency diminishes while propensity to void formation is enhanced at elevated temperatures. At high temperatures the matrix softens and the local stress at the particles does not exceed their fracture stress. Cai et al. [92] carried out hot torsion tests under superimposed large hydrostatic pressure and showed that large decrease in particle size can occur as a result of particle fracture.

## 2.9. Ti<sub>50</sub>Ni<sub>47</sub>Fe<sub>3</sub> Alloy

Intermetallics (intermetallic compounds) are based on integral ratios of metallic

atoms of at least two species. They show long range order with each species occupying a particular sublattice. Many intermetallics show lower symmetry than cubic and have fewer slip systems operating near room temperature, and therefore, are brittle. At elevated temperatures additional slip systems are activated, but dislocation mobility is hindered by the need to maintain order and thus show high strength at elevated temperatures [93]. Intermetallic compound TiNi is an exception in that it shows good room temperature ductility [12].

Titanium-Nickel alloys based on the intermetallic compound TiNi are well known for their excellent shape memory properties [11,94,95]. On cooling, the high temperature ordered phase B2 (CsCl type) undergo a reversible, diffusionless shear transformation to a distorted monoclinic structure, B19' [94]. The shape memory effect has been widely investigated and can be attributed to the self-accommodating nature of the thermoelastic martensite [94-96]. The transformation temperature of TiNi alloys can be varied between -100°C to +100°C with the help of ternary additions [97]. Substituting 3 at.% Fe for Ni lowers the  $M_s$  temperature to -140°C [97]. Apart from the shape memory effect, TiNi alloys exhibit high room temperature ductility, good impact resistance, vibration damping properties as well as good corrosion resistance and bio-compatibility [94,95].

Mechanical properties of  $Ti_{50}Ni_{47}Fe_3$  alloy has received considerable attention due to the stability of the alloy against stress induced martensitic transformation near room temperature. Twinning in ordered intermetallic alloys is not expected as it will destroy the long range order. However, recent TEM investigations have indicated twinning in ordered B2 and DO<sub>3</sub> structures through complex twinning mode [98,99]. Goo et al. [98] have shown that the room temperature deformation TiNi (B2) alloy involves extensive mechanical twinning. complex twinning, requiring shear and shuffle, occurred on planes {112} and {114}.

The B2 phase, with ordered B2 structure, is not expected to show good ductility due to only three active independent slip systems (ISS). Moberly and co-workers [12]

have shown that the twinning within a grain occurs on only one set of parallel planes and provides fourth ISS which is responsible for significant ductility in this intermetallic at room temperature. Cold working produces a very high density of fine twins and post work annealing causes dislocation recovery within these twins resulting in a fine stable subgrain structure and an improved combination of yield strength and ductility [12]. Under cyclic loading, the alloy work hardens appreciably and shows an endurance limit close to 0.7 of its tensile strength [100].

# EXPERIMENTAL METHODS

### 3.1. Specimen and Counterface Materials for the Wear Tests

#### 3.1.1 Al6061-20%Al<sub>2</sub>O<sub>3</sub>

The aluminum matrix composite studied was an Al6061 alloy reinforced with 20% by volume Al<sub>2</sub>O<sub>3</sub> particulate (Duralcan W6A.20A). Unreinforced Al6061 alloy was also investigated for comparison. The matrix alloy had a composition (in wt.%): Mg 1.0%, Si 0.6%, Cu 0.3%, Zn 0.3%, Cr 0.2%, Fe 0.7% and balance aluminum. These materials were supplied by Alcan International (Kingston, Ontario) as extruded round bars in the T6 (peak aged) condition.

Optical microscopy was done to characterize the microstructure of both the alloys. Conventional metallographic sample preparation techniques were used for Al6061, but special metallographic treatment was needed to obtain satisfactory surface finish for microscopy of Al6061-20%Al<sub>2</sub>O<sub>3</sub> : Specimens were cold mounted in epoxy resin and wet-ground to 600 grit SiC paper. Care was taken to reduce the excessive fragmentation of the Al<sub>2</sub>O<sub>3</sub> particles by applying low contact pressure on the grinding surface. This was followed by polishing over 6 $\mu$ m and then 1 $\mu$ m size diamond paste. Final polishing was done, against a wet cloth sprayed with 0.05  $\mu$ m alumina suspension, for a short time. This process assured minimum surface relief of the hard particles on the matrix. Etching was performed with an aqueous solution of 5 ml HF and 10ml H<sub>2</sub>SO<sub>4</sub> in 85 ml of H<sub>2</sub>O.

The optical micrographs of the unreinforced Al6061 as well as Al6061-20%Al<sub>2</sub>O<sub>3</sub> alloy are given in Figs. 3.1(a) and 3.1(b), respectively. Grain size of Al6061 is 31 $\pm$ 6  $\mu$ m. Grain size of Al6061-20%Al<sub>2</sub>O<sub>3</sub> is 22 $\pm$ 6  $\mu$ m. Al<sub>2</sub>O<sub>3</sub> particles have a mean particle size of 15  $\mu$ m and an aspect ratio of 2. Microhardness values measured using Vickers indenter

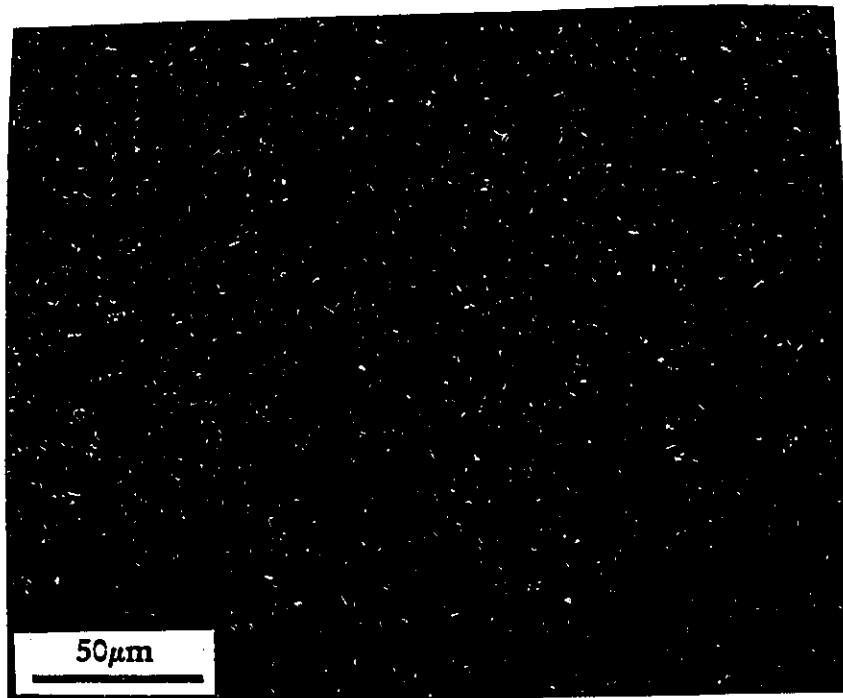
and 1000 g load for the unreinforced Al6061 and Al6061-20%Al<sub>2</sub>O<sub>3</sub> were 118 kg.mm<sup>-2</sup> and 135 kg.mm<sup>-2</sup>, respectively. The hardness values and densities [68] of both the alloys are listed in Table 3.1.

### 3.1.2 Ti<sub>50</sub>Ni<sub>47</sub>Fe<sub>3</sub> alloy

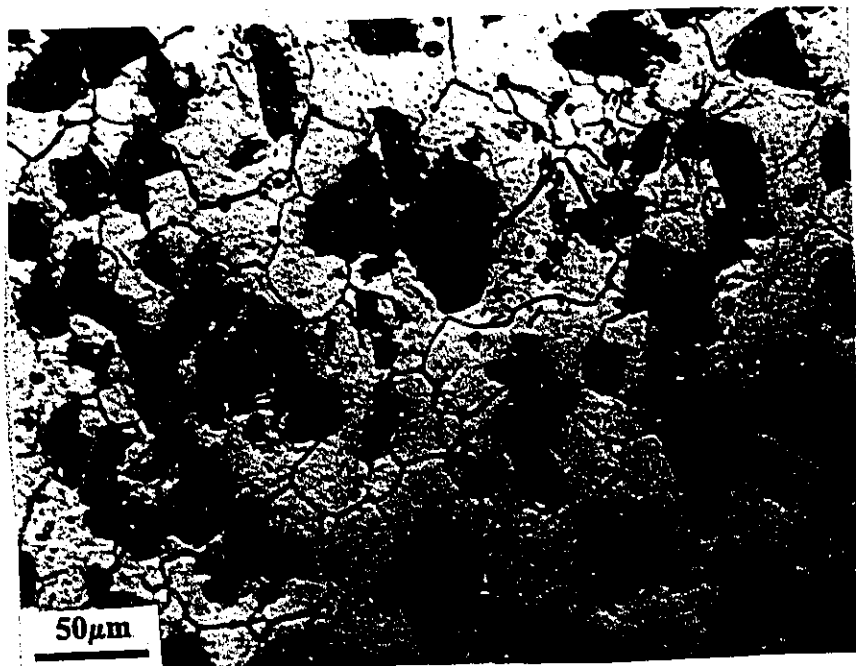
A ternary alloy of composition Ti<sub>50</sub>Ni<sub>47</sub>Fe<sub>3</sub> was produced and studied for its wear properties. Substitution of up to 3 atomic percent Fe for Ni in the binary TiNi alloy is known to lower the martensitic transformation temperature (Ms) to -140°C [33]. The starting materials were titanium sponge (99.9%), nickel pellets (99.9%) and iron lumps (99.98%). These materials were weighed in a proportion to yield a nominal composition of the charge as 50 at.% Ti, 47 at.% Ni and 3 at.% Fe. Buttons, approximately 50 g in weight, were melted in an arc furnace in a water cooled copper mould. Melting was done in an argon atmosphere to prevent oxidation of the constituents. The buttons were turned upside down and remelted 7-8 times to ensure chemical homogeneity. The XRD analysis of Ti<sub>50</sub>Ni<sub>47</sub>Fe<sub>3</sub> buttons after the homogenization treatment (Fig. 3.2) showed the existence of a single B2 phase with a lattice parameter of 0.3027 nm. The buttons were repeatedly cold rolled, with intermediate anneals at 850°C for one hour under an argon atmosphere, until the thickness was reduced either to 2 mm sheet for the tensile test specimens or 7 mm for the wear specimens. The optical microscopy revealed that the final grain size of the annealed alloy was about 6±1 µm (Fig. 3.3). The annealed alloy had the hardness (Vickers) of 205 kg.mm<sup>-2</sup>. The annealed alloy was given 45% cold work and annealed at 450°C for 10 min. This heat treatment will be explained in section 5.1.

### 3.1.3 Counterface Material

Wear is a system property and wear resistances of the materials tested vary with the type of materials used as counterface. In this investigation, all the materials were tested against a hardenable high strength steel, SAE52100, of nominal composition (by weight) 1%C, 0.35% Mn, 1.45% Cr, 0.25% Si, 0.04% max S, 0.035% max P and the balance iron. The steel was used in two different states. Both ambient temperature and elevated temperature wear of Al6061 and Al6061-20%Al<sub>2</sub>O<sub>3</sub> was studied against



(a)



(b)

Fig. 3.1. Optical micrographs of (a) Al6061, (b) Al6061-20%Al<sub>2</sub>O<sub>3</sub>.



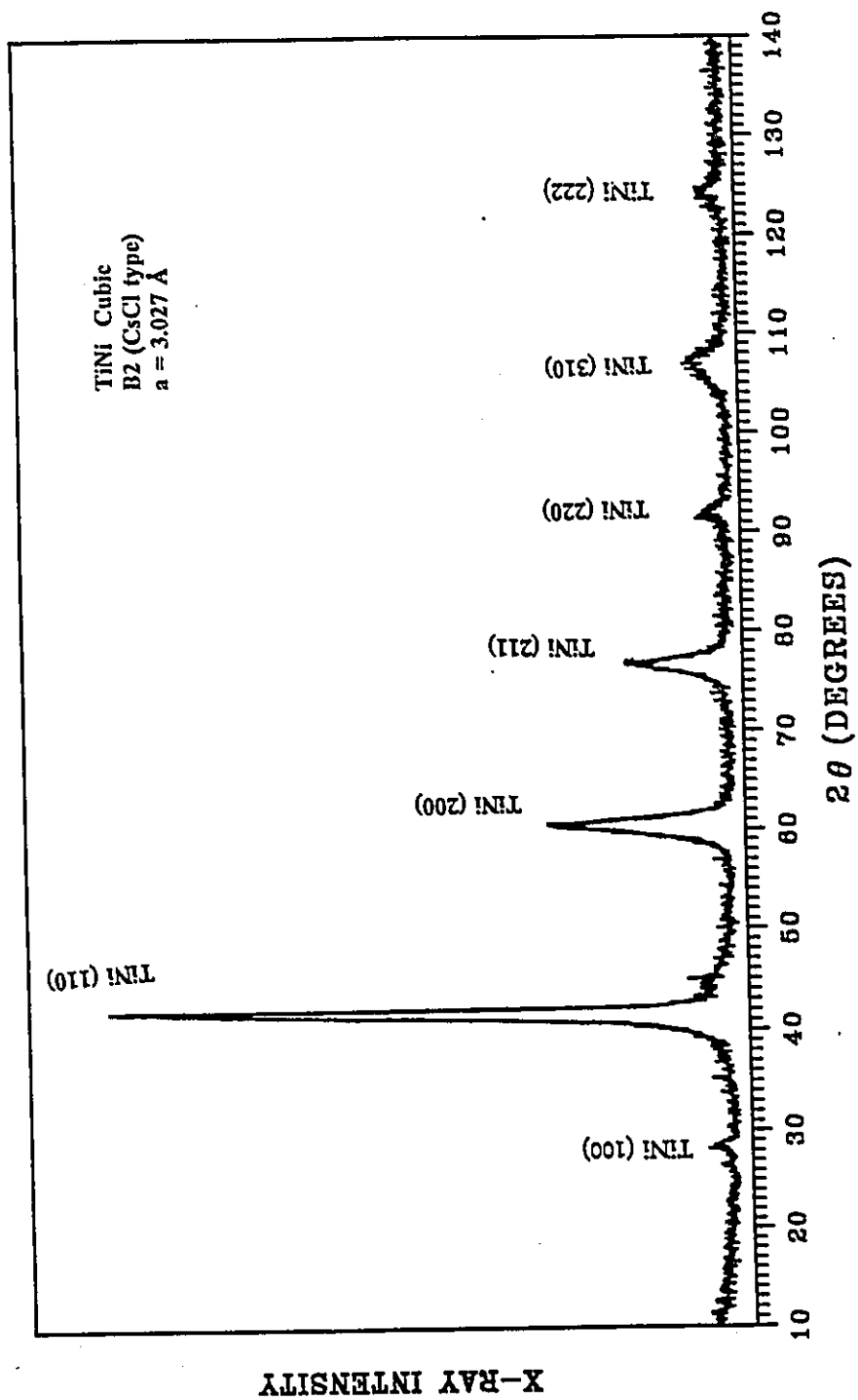


Fig. 3.2. X-ray diffraction analysis (XRD) of  $\text{Ti}_{50}\text{Ni}_{47.5}\text{Fe}_3$  alloy after homogenization at  $950^\circ\text{C}$  for two hours.

**Table 3.1 Hardnesses and densities of the specimen and counterface materials used in wear tests.**

| Property ►<br>Material ▼                                  | Microhardness<br>(Vickers, 1000g)<br>(kg.mm <sup>-2</sup> ) | Density<br>(g <sup>-3</sup> ×10 <sup>3</sup> ) |
|---|---|--|
| Al6061 (T6)*  | 118±4   | 2.71   |
| Al6061-20%Al <sub>2</sub> O <sub>3</sub><br>(T6)*         | 134±8   | 2.96   |
| Ti <sub>50</sub> Ni <sub>47</sub> Fe <sub>3</sub> (TMT)** | 300±5   | 6.55   |
| SAE 52100<br>(spherodized)                                | 290±4   | 7.88   |
| SAE 52100<br>(Q & T)                                      | 870±6   | 7.88   |

\* T6 (Peak aged) :Solutionized 530°C, water quenched, aged 16 h. at 175°C.

\* TMT: 45% cold work, annealed 450°C, 10 min.

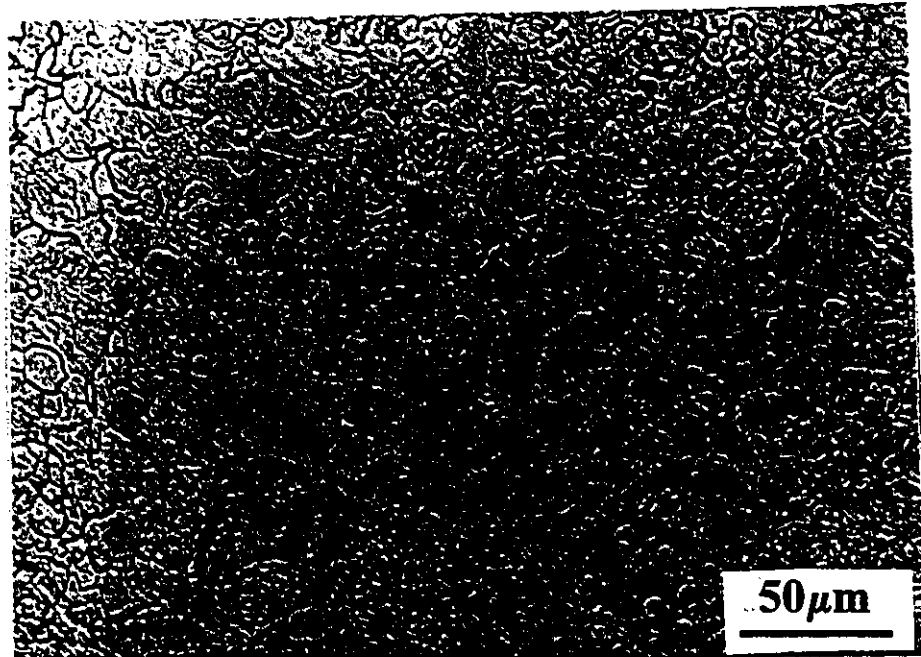


**Fig. 3.3. Microstructure of annealed (850°C, 2hrs.) Ti<sub>50</sub>Ni<sub>47</sub>Fe<sub>3</sub> alloy.**

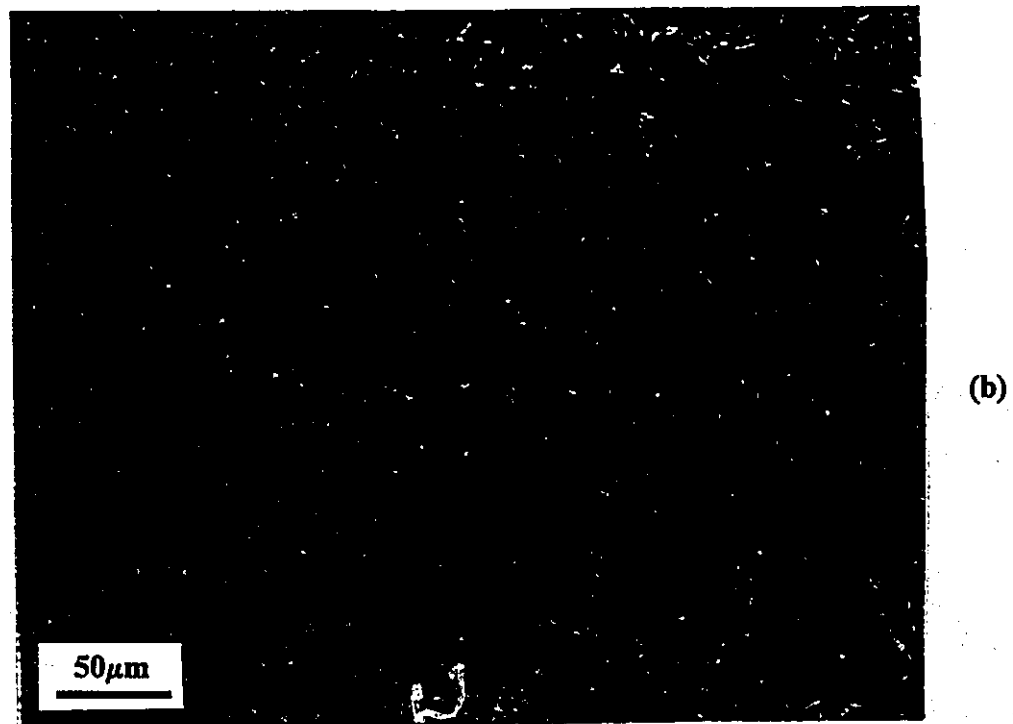
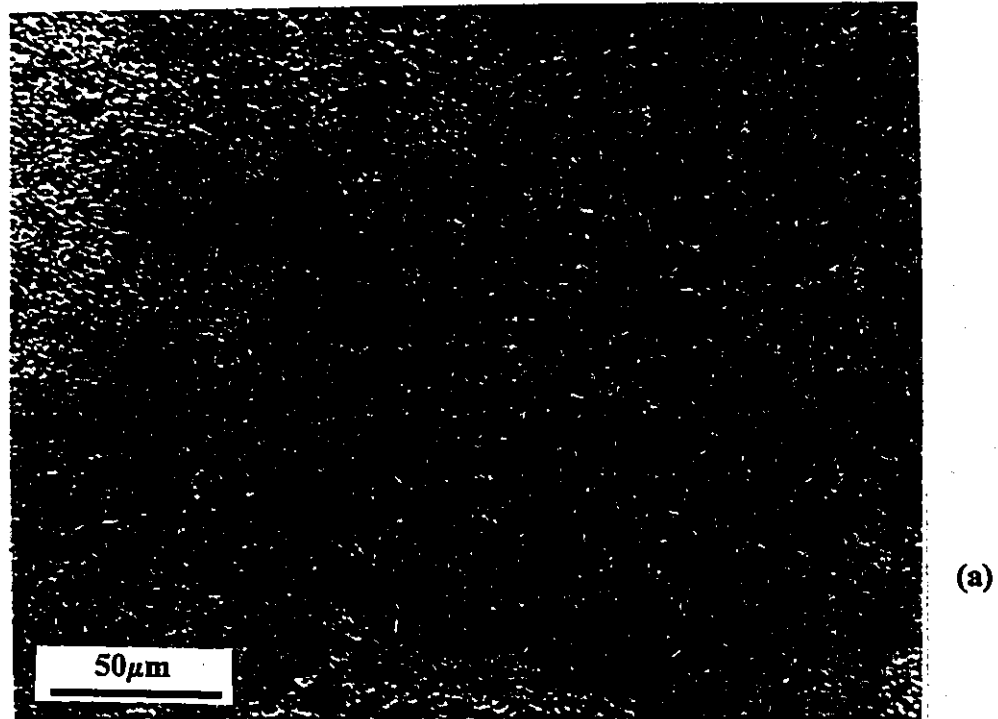


**Fig. 3.4. Optical micrographs of SAE52100 steel. (a) Spherodized and (b) Tempered martensite (Q & T).**

SAE52100 which was spherodized (Fig. 3.4(a)) to a low hardness of  $290 \pm 4 \text{ kg.mm}^{-2}$ . This stabilization treatment was given to SAE52100 to avoid large drop in counterface hardness during sliding tests at high temperatures.  $\text{Ti}_{50}\text{Ni}_{47}\text{Fe}_3$  sliding wear tests were done against quenched and tempered (Q&T) SAE52100. The steel was homogenized at  $850^\circ\text{C}$  for 30 min., quenched in oil at room temperature and tempered at  $200^\circ\text{C}$  for 4 h. The surface microhardness after the tempering treatment was  $870 \pm 6 \text{ kgmm}^{-2}$ . Optical micrograph of the hardened steel is shown in Fig. 3.4(b).

## 3.2 High Temperature Wear Tests

### 3.2.1 High Temperature Wear Machine

High temperature wear tests were performed using a high temperature wear machine (Fig. 3.5(a)). The machine was specially built at the University of Windsor to carry out the elevated temperature wear tests. The machine was designed to carry out tests at temperatures up to  $1000^\circ\text{C}$  and could be operated within a load range of 5N to 500N. A schematic drawing of the equipment is shown in Fig. 3.5(b) depicting its essential components. The machine consists of the following parts:

(i) An upper vertical shaft (see item 1 in Fig 3.5(b)) which carries the specimen holder (item 2) at the bottom end. The weight of the shaft and the specimen holder is balanced through counter weights (item 3) hanging from a pulley system. Normal load on the samples could be applied by dead weights (item 4) placed in a pan which is mounted at the top of the shaft. The shaft, supported by ceramic linear motion bearings, does not rotate but is free to move vertically up and down and serves to apply the normal load on to the specimen.

(ii) A lower vertical shaft (item 5), carrying the counterface holder (item 6) at its top end. The holder is in the form of a cylindrical block with a concentric cylindrical cavity in which the counterface could be tight fitted with the help of set screws.

(iii) The lower shaft is rotated by a variable speed motor (item 7) attached to its bottom end. This 735 watt DC (direct current) motor can achieve maximum rotation speed of 1750 rpm. The speed of the motor was controlled through a variac which also supplied the DC power to the motor. The motor itself is supported by bearings and is free to rotate.

(iii) A high temperature furnace (item 8) equipped with a temperature controller is used to heat the wear couple and the holders to the desired test temperature. The furnace carries kanthal super 33 elements (item 9) for rapid radiation heating and can reach up to a maximum temperature of 1540°C. The furnace temperature could be controlled to  $\pm 1^\circ\text{C}$ .

(iv) A linear variable differential transducer, LVDT, (item 10) for wear measurements. The LVDT, with a displacement range of 5 mm ( $\pm 2.5$  mm), measures displacements with a least count of 2.5  $\mu\text{m}$ . The core of the LVDT is secured to the upper shaft with the help of a connecting rod while the outer coil is fixed to the supporting structure. The LVDT measures the loss of the height of the wear couple as indicated by the downward movement of the upper shaft.

(v) A torsion type load cell (item 11), 10N capacity, connected to the body of the motor to measure the frictional force during sliding.

Both upper and lower shafts were firmly attached to a rigid steel platform which in turn was secured to the wall as well as to the floor to reduce vibrations.

Care was taken to avoid error from thermal expansion of steel shaft and fixtures which could otherwise effect the LVDT measurements. For this reason, the wear machine was equilibrated for one hour at the test temperature before the start of the wear run. Both upper and lower shafts were water cooled (item 14) during high temperature tests to help maintain thermal equilibrium and to protect the LVDT as well as the electric motor from heating up.



**Fig. 3.5(a). High temperature wear tester.**

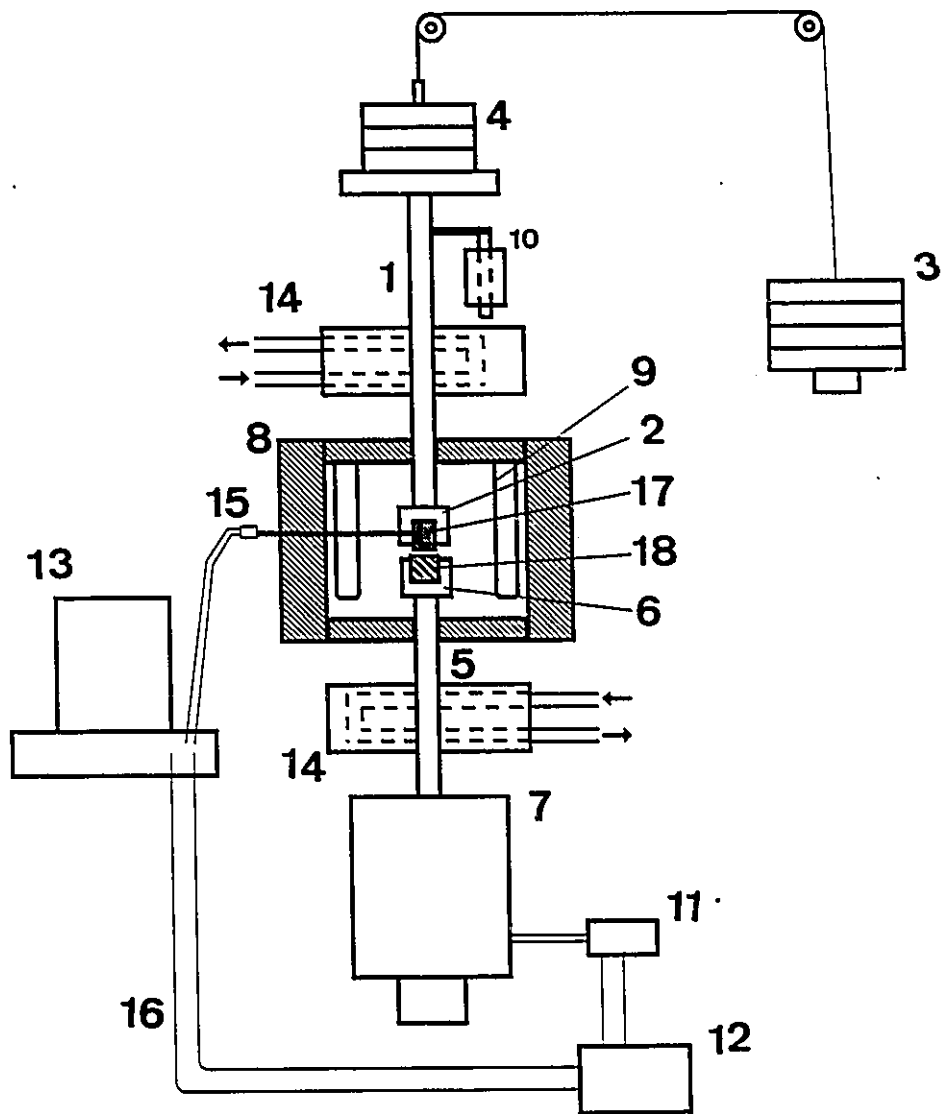


**Fig. 3.5(b). High temperature wear tester (schematic, not to scale).**

- |                             |                                |                               |
|-----------------------------|--------------------------------|-------------------------------|
| <b>1. Upper shaft</b>       | <b>2. Specimen holder</b>      | <b>3. Counter-weights</b>     |
| <b>4. Dead weights</b>      | <b>5. Lower shaft</b>          | <b>6. Counterface Holder</b>  |
| <b>7. Electric motor</b>    | <b>8. Heating furnace</b>      | <b>9. Heating elements</b>    |
| <b>10. LVDT</b>             | <b>11. Friction Load Cell</b>  | <b>12. Load cell meter</b>    |
| <b>13. PC with A/D card</b> | <b>14. Water cooled Blocks</b> | <b>15. Thermocouple wires</b> |
| <b>16. Connection cable</b> | <b>17. Test specimen</b>       | <b>18. Counterface</b>        |

A schematic given in Fig. 3.6. explains the method to determine friction coefficient during sliding. The frictional torque acting on the counterface is measured through a loading arm which is connected to the load cell at a distance of 305 mm. The distance,  $L_1$ , from the central line at which the friction torque acts is measured as radius of the circular wear track on the counterface. The tangential load ( $T_1$ ) then can be calculated from the load,  $T_2$ , indicated by the load cell as,

$$T_1 = T_2 \times 305/L_1 \quad \text{.....} \quad (3.1)$$

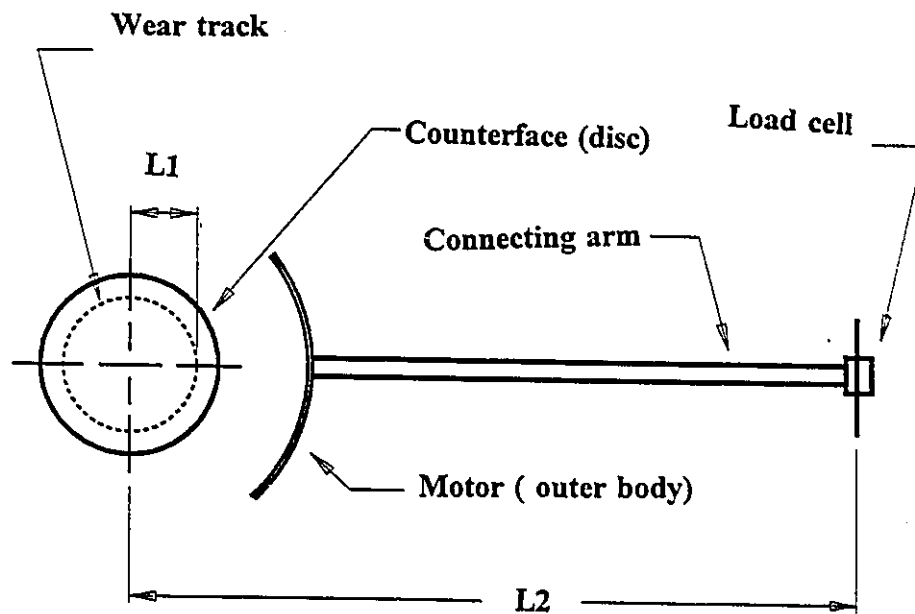
The friction coefficient ( $\mu$ ) is then calculated as a ratio  $T_1/N$ , where,  $N$  is the applied normal load.

The specimen temperature was measured by inserting a thin ungrounded chromel-alumel thermocouple into the body of the specimen. The ungrounded thermocouple (thermocouple wires insulated from the outer stainless steel (316 SS) protective sheath) avoided the interference from stray electric current from the machine. The thermocouple was inserted at a distance of about 2 mm from the contact surface. The specimen temperature differed from the temperature indicated by furnace thermocouple (connected to temperature controller) by more than 50°C at elevated temperatures. The specimen bulk temperature has been reported as the test temperature throughout this work.

The specimen temperature as well as friction force were recorded continuously in the course of the wear test by a personal computer (486SX) equipped with an analog to digital conversion card and a data acquisition/storage system.

The sliding speed of the sample during wear tests was controlled by varying the rotational speed of the motor. The speed of rotation could be varied from 0 to 1750 rpm (rotations per minute). The rotational speed,  $n$ , was measured using a tachometer after pasting a 2mm wide reflective tape on the lower shaft. The sliding speed,  $v$ , could be determined as a product  $nxL$ , where,  $L (= \pi D)$ ,  $D$  being the average diameter of the





$$L1 = 4 \text{ mm}$$

$$L2 = 305 \text{ mm}$$

Friction force acting at the sliding surface =  $T1$

Friction force measured by the load cell =  $T2$

$$L1.T1 = L2.T2$$

or,

$$T1 = T2(L2/L1)$$

$$= 76.25 T2$$

**Fig. 3.6. A schematic illustrating the principle of friction force measurement during high temperature wear tests.**

circular wear track generated on the counterface) is the distance slid in one rotation. The sliding distance,  $S$ , was obtained by multiplying the sliding speed with the elapsed time.

### 3.2.2 Wear Sample Geometries

Wear of the Al6061-20%Al<sub>2</sub>O<sub>3</sub> and the unreinforced Al6061 at elevated temperatures was studied using a ring on disc wear configuration as shown in Fig.3.7. The specimen was a 15 mm long cylinder with 10 mm in diameter. One end of the cylinder was made hollow to a depth of 5 mm with inner diameter of 6mm. The solid end was held in the specimen holder cavity with the help of set screws. The hollow end, the wear face, was forced against a rotating counterface disc. The counterface was a solid cylinder of SAE52100, 15 mm long and 13 mm in diameter. Both the specimen and the steel counterface were concentrically held, respectively, by the holders on the upper and lower shaft of the high temperature wear machine. The contacting surfaces were polished with 600 grit SiC paper prior to wear tests.

High Temperature wear of the Ti<sub>50</sub>Ni<sub>47</sub>Fe<sub>3</sub> was studied using a pin on disc type wear geometry which is depicted in Fig. 3.8. The ring on disk setup used for the aluminum alloys was readily converted into pin on disk configuration. The SAE52100 counterface disc in this case had a larger diameter of 25 mm. The counterface holder was similar to the one used for aluminum alloys but with a cavity of bigger diameter. Pins with 5 mm diameter and 12 mm in height were machined from Ti<sub>50</sub>Ni<sub>47</sub>Fe<sub>3</sub> alloy. The sliding end of the specimen was reduced to 3mm diameter. The pin holder was a solid cylinder of stainless steel with a hole of 5mm diameter and 10mm depth located at a distance of 10 mm from the centre of rotation of the counterface. The pin holder was secured to the shaft by the specimen holder used for the aluminum specimens. Both the pin and the disc surfaces were polished with 600 grit paper.

### 3.2.3. Wear Measurements

The wear rates were measured in two ways:

- i) Measurement of specimen height: Change in height of the wear couple ( $\Delta H$ ) was

recorded continuously during the test run through an LVDT. The height measured was converted to the volumetric wear loss (W) from the original contact area (A) being worn out as  $W = \Delta H \cdot A$ . The method used to calculate wear rate of the specimen from the total wear loss (W) is explained in section 4.1.

ii) Weight loss measurements: The test specimens were weighed before and after the sliding run from which volumetric wear rates were computed using the known densities of the alloys (Table 3.1 ). The weight loss from counterface was also recorded simultaneously.

Sliding tests were conducted in three separate sets of experiments:

(a) Constant Load Tests at Different Temperatures

In the first set, the tests were done at fixed load, 10N or 50N, while the test temperature was systematically varied from room temperature to 500°C. A constant sliding speed of  $0.2 \text{ m} \cdot \text{s}^{-1}$  was used. For the tests on Al6061-20%Al<sub>2</sub>O<sub>3</sub>, sliding distance was about  $6 \times 10^3 \text{ m}$  for the tests at low temperatures but was  $10^3 \text{ m}$  or less at elevated temperature due to very high wear rates. The wear rates were determined both from height reduction and weight loss measurements.

High temperature wear of the Ti<sub>50</sub>Ni<sub>47</sub>Fe<sub>3</sub> was also studied using the high temperature wear machine but with a pin on disc sliding configuration described in section 3.2.2. The sliding speed used was  $0.4 \text{ m} \cdot \text{s}^{-1}$  and a constant applied load employed was 15N. Sliding was continued to total distance of  $10^4 \text{ m}$ . The wear rates were determined from weight loss measurements.

(b) Wear Tests at Constant Temperature

In the second set, three sliding temperatures, room temperature, 150°C, and 200°C were selected and the applied load was varied independently from 10N to 450N. Sliding speed used was  $0.2 \text{ m} \cdot \text{s}^{-1}$ . In this set of experiments the wear rates were determined as weight loss measurements.

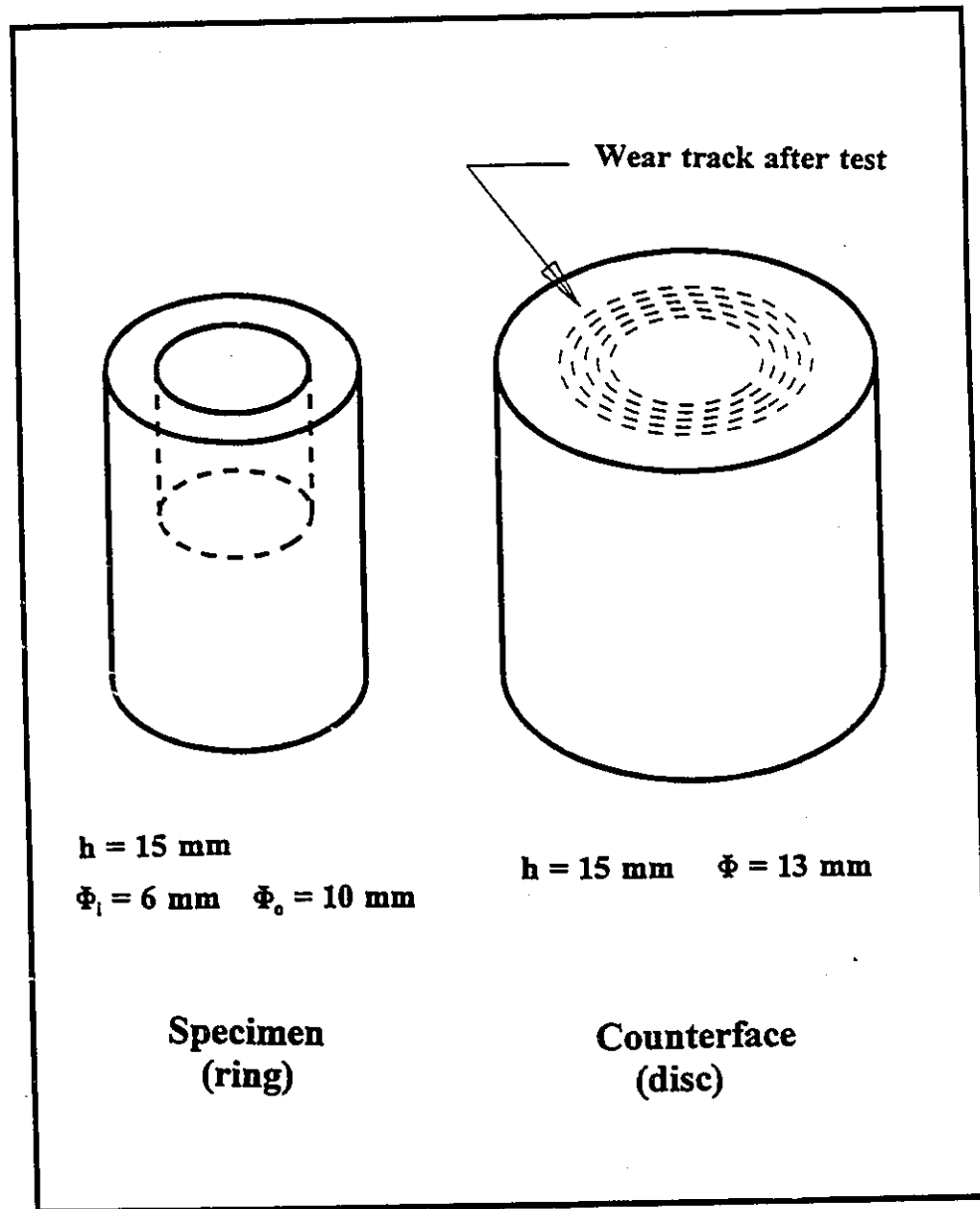


**Fig. 3.7. Specimen (ring) and counterface (disc) geometries employed for high temperature wear testing of Al6061 and Al6061-20%Al<sub>2</sub>O<sub>3</sub>.**

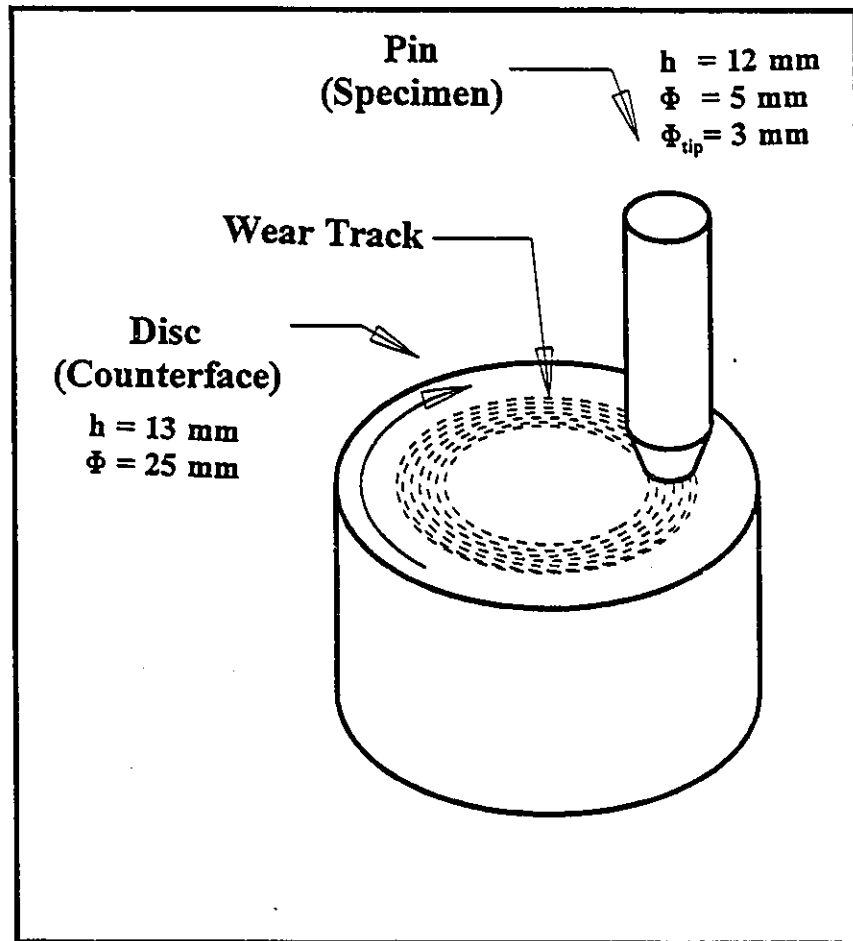
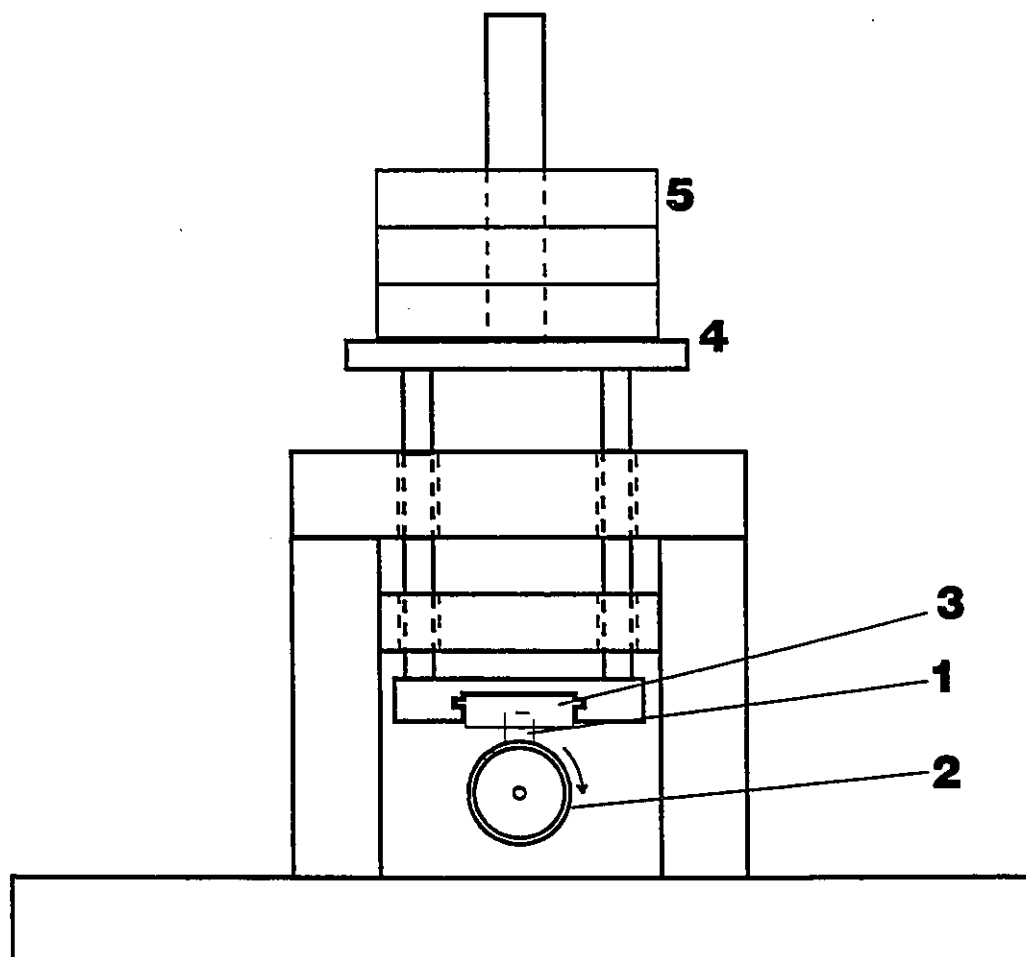


Fig. 3.8. Pin on disc wear geometry employed for high temperature wear testing of  $\text{Ti}_{50}\text{Ni}_{47}\text{Fe}_3$ .



- |                   |                                |                    |
|-------------------|--------------------------------|--------------------|
| 1. Specimen Block | 2. Counterface (rotating ring) | 3. Specimen Holder |
| 4. Load Tray      | 5. Dead Weights                |                    |

Fig. 3.9. Block on ring wear machine employed for room temperature sliding wear study of  $\text{Ti}_{50}\text{Ni}_{47}\text{Fe}_3$ .

### (c) Ambient Temperature Wear Tests

Data for room temperature wear of Al6061-20%Al<sub>2</sub>O<sub>3</sub> was already available through work of Zhang and Alpas [65] who performed room temperature tests on this material (and unreinforced Al6061) using a block on ring machine. However, for the Ti<sub>50</sub>Ni<sub>47</sub>Fe<sub>3</sub> alloy, it was essential to generate room temperature wear data prior to high temperature studies. The ambient temperature wear of the Ti<sub>50</sub>Ni<sub>47</sub>Fe<sub>3</sub> was studied using the same block on ring machine used by Zhang and Alpas [65]. A schematic of the block-on-ring machine is shown in Fig. 3.9.

Rectangular blocks of 10mmx10mmx5mm were machined from the Ti<sub>50</sub>Ni<sub>47</sub>Fe<sub>3</sub> alloy and slid against SAE 52100 steel rings with outer diameter of 38mm. Following experiments were carried out to understand the ambient temperature wear characteristics of the intermetallic alloy:

- (i) The effect of applied load was in the load range 2N to 400N. The sliding speed was kept constant at 0.4m.s<sup>-1</sup>. The weight of both the specimen and the counterface was measured prior to the wear test. During the wear run, the test was interrupted at regular intervals to take weight measurements to determine weight loss as a function of sliding distance.
- (ii) In another set of experiments, the effect of sliding speed on the wear resistance of the intermetallic was investigated. The sliding speed was varied between 0.04m.s<sup>-1</sup> and 6m.s<sup>-1</sup> while keeping the applied load constant at 20N.

### 3.3. Analysis of Worn Materials

A low power microscope was used to record the general morphology of worn surfaces. Subsequently secondary electron images were obtained employing a Semco Nanolab 7 Scanning Electron Microscope (SEM). The microscope was equipped with a Kevex-Ray 5100C X-Ray Energy Spectrometer (EDS) capable of detecting elements with

atomic numbers greater than 12. Compositional variations were recorded both on the worn surfaces as well as in the subsurface region.

Subsurface metallography was done on both transverse and longitudinal cross-sections below the worn surfaces. The worn specimen was carefully cut normal to the sliding surface using a slow speed diamond saw. The specimens were coated in an acetone soluble lacquer and then mounted in a cold epoxy mount in order to improve edge retention and reduce damage to the wear surface during polishing. Metallographic polishing was carried out using a diamond polishing cloth as explained in section 3.1. Etching was done only to reveal the extent of plastic deformation in the subsurface. Etching of aluminum alloys was done with an acid solution: 5ml HF, 10 ml  $H_2SO_4$ , and 85 ml water. For the intermetallic alloy the etching solution was: 5 ml HF, 10 ml  $HNO_3$ , and 85 ml water.

Microscopy on the tapered sections was done to investigate thin tribo-layers on the worn tracks. The specimens were held in a specially designed holder and mechanically ground and polished to metallographic finish with the worn surface at about  $7^\circ$  to the flat surface of the holder. This would "enlarge" a subsurface region of  $10\ \mu m$  depth to  $82\ \mu m$ . The exact value of the taper angle was determined accurately under the optical microscopy with a graduated lens (accuracy of  $0.1\ \mu m$ ) in a micro-hardness tester. These tapered sections were employed for the investigation of hardness changes below the contact surface using a Buehler Micromet II Vickers Hardness Tester.

X-Ray diffraction studies were performed on the wear debris and the worn surfaces. A Rigaku X-ray diffractometer with  $Cu-K\alpha$  radiations was used.

### 3.4. Mechanical Testing

#### 3.4.1. Compression Testing $Al6061-20\%Al_2O_3$

Compression testing of Al6061 as well as  $Al6061-20\%Al_2O_3$  alloy was done to



understand the mechanical property changes during the high temperature sliding wear of these alloys. Severe wear of these alloys at elevated temperature involved gross plastic deformation at the sliding surfaces and extrusion of the material out of the contact area. Compression tests were performed in the temperature range of 25-500°C. Both the alloys were given the same heat treatment: They were solutionized at 530°C, water quenched and artificially aged at 175°C for 16 h (T6). The specimens were machined as solid cylinders of 8mm diameter and 8 mm in length. The height to diameter ratio (h/d) was kept low (h/d=1) to avoid buckling of the specimen.

The specimens were compressed between two hardened steel platens. These platens were machined from tool steel. The platens after machining were heat treated (oil quench from 850°C and tempered for 30 min. at 350°C) to 50 Rc.

Compression testing was done using a microprocessor controlled servo-hydraulic Instron 8562 model testing machine. A high temperature three zone furnace, equipped with a self adaptive temperature control and a water cooling system for protecting the load cell and machine stability, was used to heat the compression samples. During the tests, the test temperature was held within  $\pm 0.5^\circ\text{C}$  and the specimen was kept at the test temperature for one hour prior to the tests to equilibrate the temperature of the furnace and the specimen.

Specimens were deformed at a constant engineering strain rate,  $\dot{\epsilon}$ , of  $0.05\text{s}^{-1}$ . calculated as;

$$\dot{\epsilon} = \frac{de}{dt} = -\frac{dh}{h_o} \frac{1}{dt} = -\frac{v}{h_o} \dots\dots\dots (3.2)$$

where,  $h_o$  and  $d_o$  are initial height and diameter respectively and  $h$  and  $d$  are the instantaneous values of height and diameter during compression and  $t$  is the elapsed time during compression test. Cross-head speed of the machine,  $v$ , was set at  $0.4\text{ mm.s}^{-1}$ . The true strain rate increases continuously during compression and was  $0.05\text{ s}^{-1}$  at the

beginning of the compression and  $0.1 \text{ s}^{-1}$  at the end of compression. This corresponds to a mean true strain rate,  $\dot{\epsilon} = 0.7 \text{ s}^{-1}$ , calculated as;

$$\dot{\epsilon} = v_o \frac{\ln h_o/h}{h_o - h} \quad \text{.....} \quad (3.3)$$

The specimens were compressed to a total engineering strain of 0.5. The load and strain data was recorded to a personal computer with the help of a 16 bit A/D (analog to digital) conversion card.

### 3.4.2. Tensile Testing of $\text{Ti}_{50}\text{Ni}_{47}\text{Fe}_3$ Alloy

Tensile testing was done to investigate the effect of cold working and the thermo-mechanical treatment on the strength and ductility of the alloy. Annealing of the intermetallic was carried out in argon atmosphere.  $\text{Ti}_{50}\text{Ni}_{47}\text{Fe}_3$  sheets were annealed at  $850^\circ\text{C}$  for 1 hour and cold-rolled to give different percentages of cold-work up to 45% reduction in thickness. Tensile test specimens with reduced gage section of 0.8 mm thick, 5 mm wide and 20 mm in length were machined from cold worked sheets. The tensile tests were performed using an Instron (floor model) mechanical testing machine. A clip-on extensometer fixed on the reduced gage section of the specimen was used for strain measurements. The load cell was calibrated by hanging dead weights in a pan while the extensometer calibration was performed by a micrometer available for this purpose. The specimens were strained to fracture at a constant engineering strain rate of  $4 \times 10^{-4} \text{ s}^{-1}$ . In a second set of experiments, cold-worked sheets after 40% reduction in thickness were given a short time anneal at  $450^\circ\text{C}$  and  $500^\circ\text{C}$  before carrying out tensile tests with the objective of determining the optimum combination of yield strength and ductility.

## Chapter 4

### Al6061 and Al6061-20%Al<sub>2</sub>O<sub>3</sub>

The results on high temperature sliding wear of Al6061 and Al6061-20%Al<sub>2</sub>O<sub>3</sub> are presented in this chapter. Both materials showed "mild wear" and "severe wear" during sliding at elevated temperatures. Wear rates were low during the mild wear at low temperatures and benefitted from oxidation of the specimen and counterface surfaces. At high temperatures, the severe wear occurred through plastic displacement of the subsurface material out of the contact area and material transfer to the counterface. Compression testing at elevated temperatures was carried out to understand the role of subsurface softening on the high temperature sliding wear.

#### A. EXPERIMENTAL RESULTS

##### 4.1. Volume Loss vs Sliding Distance Curves

The volumetric wear loss of Al6061 as well as Al6061-20%Al<sub>2</sub>O<sub>3</sub> obtained from LVDT data are plotted against sliding distance in Fig. 4.1. Fig. 4.1.(a) and (b) show the effect of temperature on the wear losses at 10N load for Al6061 and Al6061-20%Al<sub>2</sub>O<sub>3</sub>, respectively. The volumetric wear loss vs sliding distance plots for the Al6061-20%Al<sub>2</sub>O<sub>3</sub> at 50N load are given in Fig. 4.1(c).

At low temperatures (e.g. at 25°C) the wear loss increases linearly with sliding distance. However, at elevated temperatures ( $T > 150^{\circ}\text{C}$ ), the irregular shape of the wear plots indicates that occasionally changes in wear rates in the course of the wear tests took place. The extent of these variations and their frequency varies widely with temperature and loads employed. It can be observed that the initial high wear rates decreased and reached a steady state in several samples tested. For example, this is evident for the test at 200°C on Al6061 (Fig. 4.2(a)) as well as for Al6061-20%Al<sub>2</sub>O<sub>3</sub> tested at 300°C at 50N

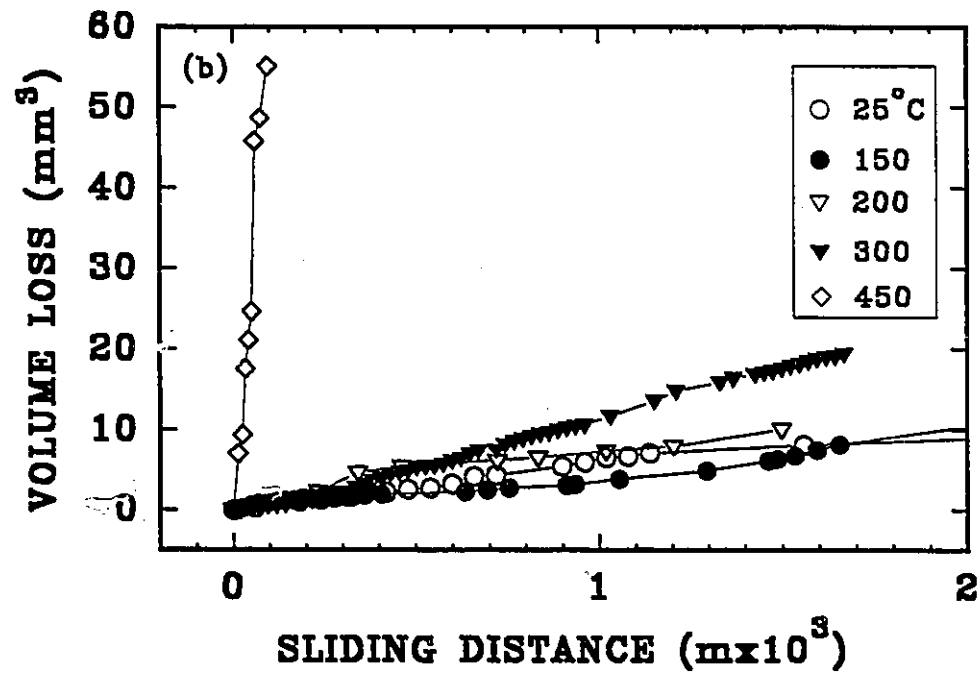
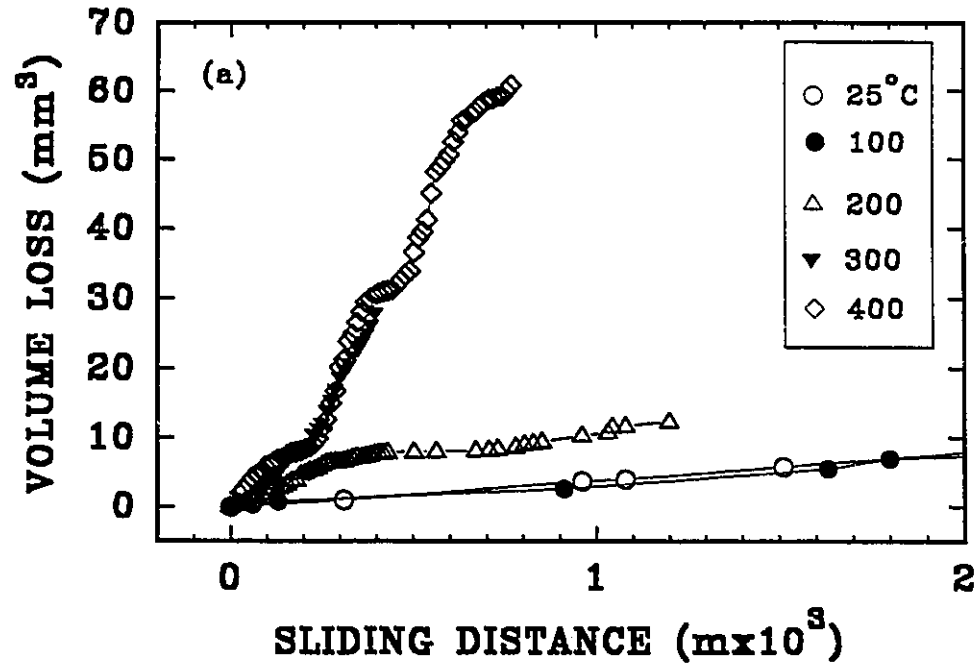


Fig. 4.1. Plots of volumetric wear loss (a) Al6061 at 10N, (b) Al6061-20%Al<sub>2</sub>O<sub>3</sub> at 10 N and (c) Al6061-20%Al<sub>2</sub>O<sub>3</sub> at 50N at different test temperatures.

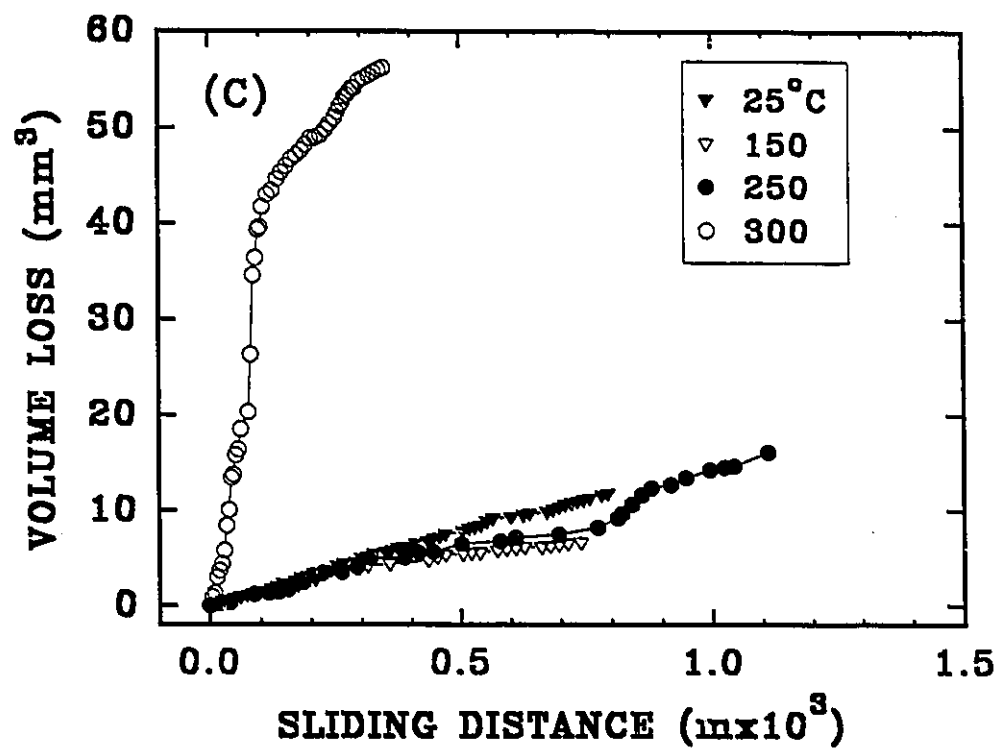


Fig. 4.1. Continued...

load (Fig. 4.2(c)).

At high temperatures "S" type curves were also frequently observed e.g. test at 230°C for Al6061-Al6061-20%Al<sub>2</sub>O<sub>3</sub> (Fig 4.1(c)). The low wear rates at the onset rose sharply after a few minutes, the wear run becoming more noisy, again decreased to stable low rates of wear at higher sliding distances. This appears to reflect the dynamic and continuing modification of the tribo-surfaces as well as the microstructural changes below the contact surface.

The wear rates of the wear couple at a given temperature were determined as a slope of the volume loss versus sliding distance curves in the steady state. At elevated temperatures, since no steady state was reached, an average slope of the entire plot was used. These apparent wear rates ( $W_a$ ) were corrected as follows: (i) when the counterface wear occurred, the weight loss of the counterface was converted to volumetric wear rate by dividing with density of steel and the sliding distance. This counterface wear rate was subtracted from those obtained from LVDT ( $W_a$ ) to yield the wear rates for the aluminum specimens. (ii) When the counterface showed weight gain because of material transfer, the LVDT data underestimated the specimen wear rates. In this situation, the weight gain was converted to volumetric wear rate using density of the specimen material and was added into  $W_a$ . These corrected wear rates are plotted in Fig. 4.2 and are described in the next section.

## 4.2 Wear Rates vs Temperature

### 4.2.1. Wear Rates From Height Reduction Measurement

The wear rates of Al6061 show a decrease when temperature is increased from room temperature to 150°C. The wear rates at 25°C at 10 N load are of the order of  $4 \times 10^{-3} \text{ mm}^3 \text{ m}^{-1}$  and they are  $2 \times 10^{-3} \text{ mm}^3 \text{ m}^{-1}$  at 150°C (Fig. 4.2). However, the wear rates rise sharply on further increase in temperature. For example, the wear rates at 400°C are

about  $1.5 \times 10^{-1} \text{ mm}^3\text{m}^{-1}$ . This transition from mild wear to severe wear is apparent from the change in slope of W vs T curves. The transition temperature ( $T_1$  on Fig. 4.2) is estimated to be about  $150^\circ\text{C}$ .

In the case of Al6061-20%Al<sub>2</sub>O<sub>3</sub>, a similar wear rate versus temperature behaviour is observed during sliding at 10N load. The wear rates of Al6061-20%Al<sub>2</sub>O<sub>3</sub> are comparable to those of unreinforced alloys at room temperature, and are about  $3 \times 10^{-3} \text{ mm}^3\text{m}^{-1}$ . Unlike, the unreinforced alloy, the wear rates in the mild wear do not decrease with temperature. At  $150^\circ\text{C}$ , the composite wear rates are about 50% higher than the unreinforced alloy. The transition to severe wear in the composite occurs at a higher temperature marked as  $T_2$  (Fig. 4.2) which corresponds to about  $230^\circ\text{C}$ . The wear rates of the composite increase from  $5 \times 10^{-3} \text{ mm}^3\text{m}^{-1}$  at  $230^\circ\text{C}$  to  $1.5 \times 10^{-2} \text{ mm}^3\text{m}^{-1}$  at  $300^\circ\text{C}$ . The wear rates of Al6061-20%Al<sub>2</sub>O<sub>3</sub> become  $2 \times 10^{-1} \text{ mm}^3\text{m}^{-1}$  at  $450^\circ\text{C}$ . The wear rates of the Al6061-20%Al<sub>2</sub>O<sub>3</sub> remain lower than the unreinforced 6061 alloy at temperatures higher than  $200^\circ\text{C}$ .

The results of wear tests done at 50N load on Al6061-20%Al<sub>2</sub>O<sub>3</sub> are also shown in Fig. 4.2. The wear rates at 50N are higher than those observed at 10N at the same test temperature. The transition to severe wear now occurs at a lower temperature of  $200^\circ\text{C}$  indicated as  $T_3$ . Moreover, the wear rates in the severe wear regime increase at a faster rate with increase in temperature at 50N than at 10N load.

#### 4.2.2. Wear Rates From Weight Loss Measurements

The results of wear rates determined from weight loss are depicted in Fig. 4.3. The rate of weight loss of the specimen was converted into volumetric wear rate using the density of the materials listed in Table 3.1. The mild to severe wear transition is evident for both Al6061 and Al6061-20%Al<sub>2</sub>O<sub>3</sub>. The transition temperatures indicated by these plots are  $200^\circ\text{C}$  and  $270^\circ\text{C}$  for the unreinforced alloy and the composite, respectively, as compared to  $150^\circ\text{C}$  and  $230^\circ\text{C}$  indicated by the height change measurements. The wear rates of both alloys decrease with temperature on increasing the temperature above room

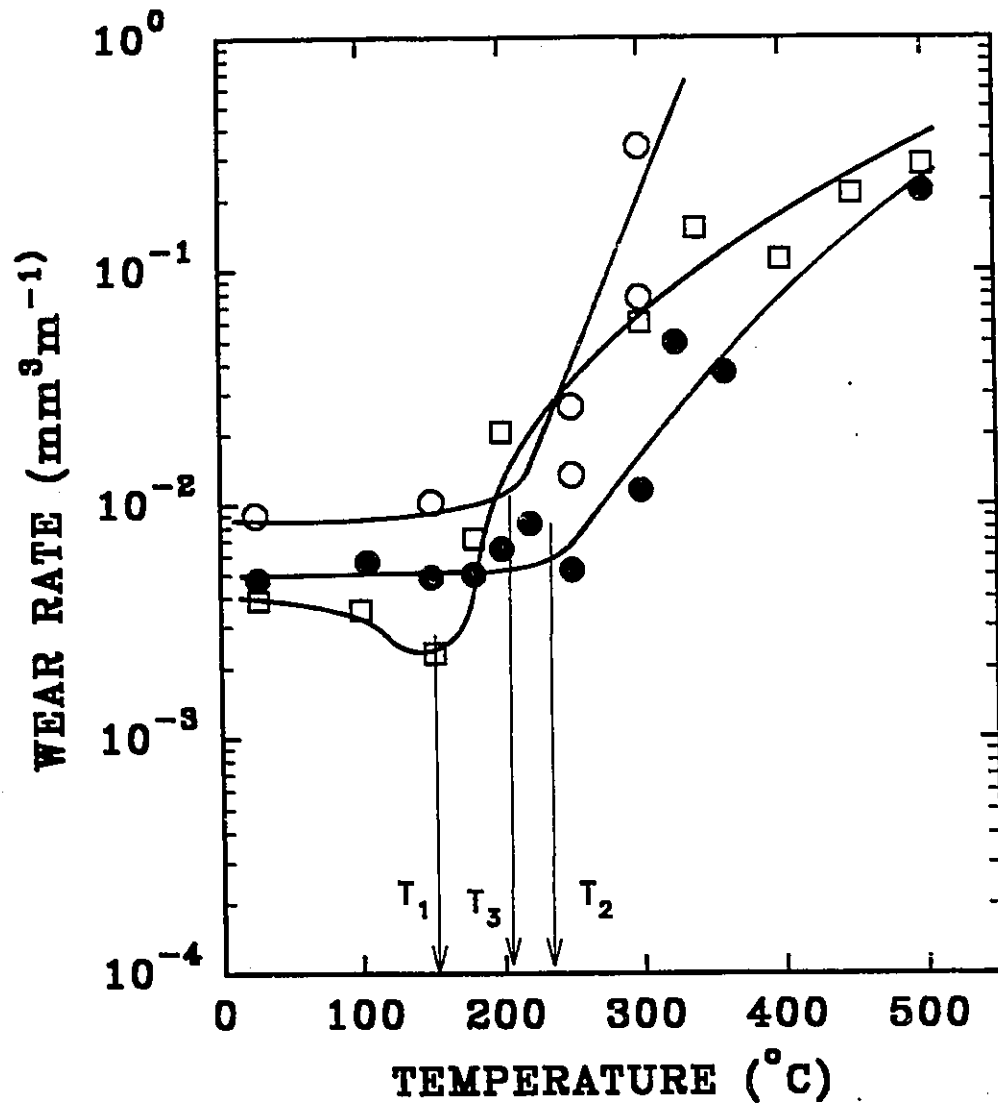


Fig. 4.2. Plots of wear rates for Al6061 at 10N load ( □ ) and Al6061-20% Al<sub>2</sub>O<sub>3</sub> at 10N ( ● ) and 50N ( ○ ) load. Wear rates determined through specimen hight change measurements and corrected for counterface wear.



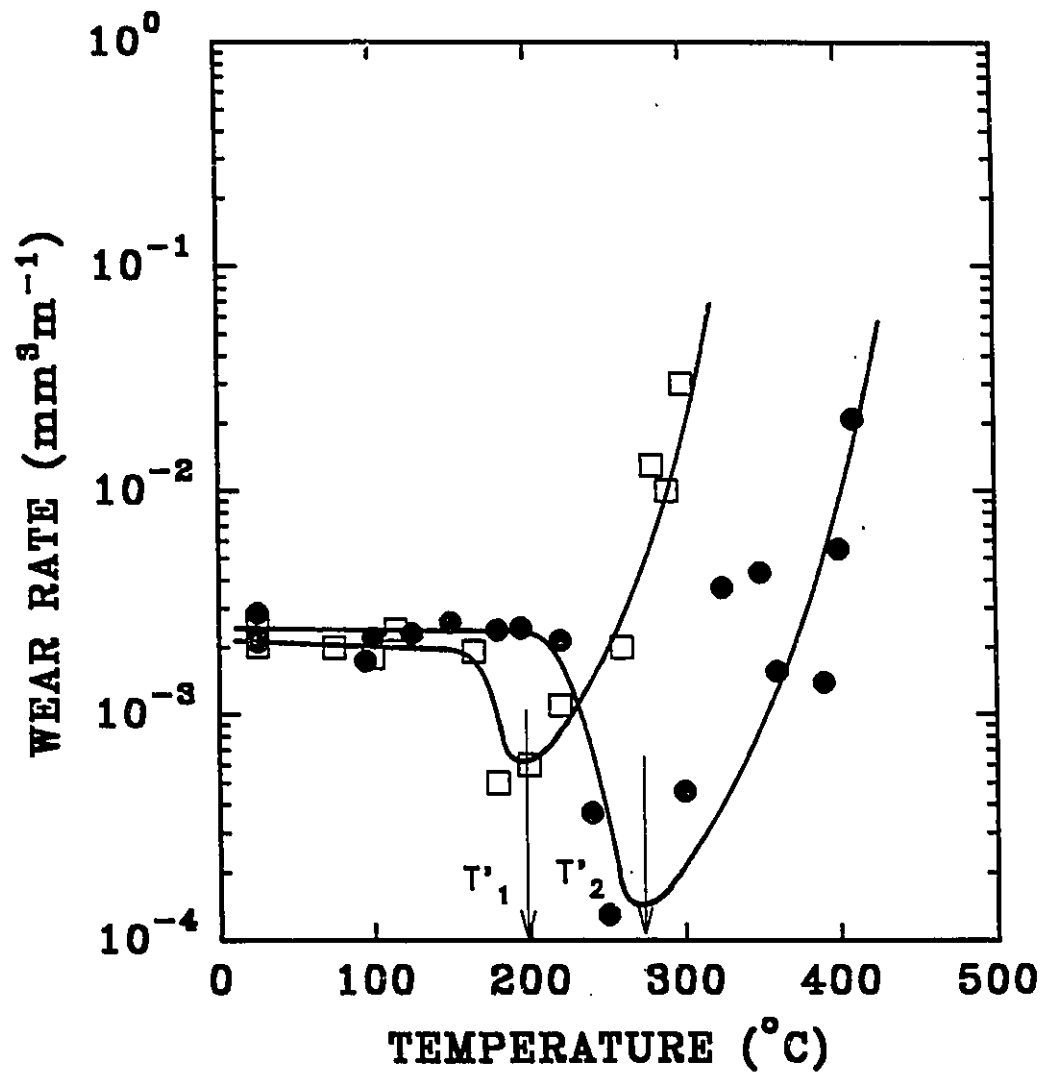


Fig. 4.3. Wear rate plots for Al6061 ( □ ) and Al6061-20%Al<sub>2</sub>O<sub>3</sub> ( ● ) at 10N load. Wear rates obtained from weight loss measurements and converted to volume loss by dividing it with the density of the specimen material.

temperature similar to wear rates obtained from height measurements. Near the transition temperature a significant drop in wear rates is evident. The wear rates decrease sharply as the test temperature approaches near the transition temperature. This is the main difference between height change measurements and weight loss measurements. At temperatures beyond the transition temperature, the wear rates increase rapidly with temperature as the severe wear sets in. Thus, there appears to be a weight loss "well" at the transition temperature where the alloy show a minimum in wear rates. This well is more pronounced in the case of the Al6061-20%Al<sub>2</sub>O<sub>3</sub> as compared to the unreinforced alloy. In the mild wear regime, the Al6061 alloy has slightly lower wear rates than the Al6061-20%Al<sub>2</sub>O<sub>3</sub>. However, in the severe wear regime the composite shows much better wear resistance than the unreinforced alloy.

The wear rates of Al6061 obtained from weight loss measurements are lower than those obtained from height change measurements all temperatures. The difference is about 40% near room temperature. The Al6061-20%Al<sub>2</sub>O<sub>3</sub> alloy similarly show lower wear rates from weight loss measurements when compared to those obtained from height change measurements. The difference in the wear rates from the two techniques is dramatic near the transition temperature where the wear rates from weight loss show a well. For example, for the Al6061-20%Al<sub>2</sub>O<sub>3</sub> alloy at 270°C, the wear rates measured through weight loss are only about 5% of those obtained from height change measurements. Similarly, the weight loss of Al6061 indicates only 10% as much wear as shown by the height change of the specimen. The difference in the wear rates obtained from the two techniques appear to indicate difference in the wear mechanisms in the two regimes and will be discussed later.

#### 4.3. Wear Rates vs Applied Load

The wear behaviour of Al6061-20%Al<sub>2</sub>O<sub>3</sub> alloy was studied as a function of applied load at different test temperatures viz. 25°C, 150°C and 200°C. The results of wear rates determined from measurements from the change in the specimen height are depicted

in Fig. 4.4 The mild to severe wear transition is evident at higher loads. The transition loads are marked as  $L_1$ ,  $L_2$ ,  $L_3$  on the Fig. 4.4 and can be seen to decrease with increase in test temperature. The transition occurs at about 350N at room temperature (25°C), 150N at 150°C and 50N at 200°C. The transition is less clear at lower temperatures, 25°C and 150°C due to limitation of the maximum load (450N) which can be applied on the high temperature wear machine.

The wear rates increase slowly with load in the load range for the mild wear. The wear rates of the Al6061-20%Al<sub>2</sub>O<sub>3</sub> are slightly lower at 150°C as compared to those at room temperature in the intermediate (20 to 100N) load range. However, the wear rates at 150°C are higher than those for the room temperature tests in the severe wear regime because of lower transition load in the former case. The wear rates at 200°C are higher as compared to the wear rates at room temperature (25°C ) and 150°C in both mild and severe wear regimes.

**Table 4.1. Transition loads for Al6061-20%Al<sub>2</sub>O<sub>3</sub> at different test temperatures.**

| Test temperature  | 25°C  | 150°C | 200°C | 230°<br>C |
|---|-------|-------|-------|-----------|
| Transition Load ( $L_c$ )<br>(from height change<br>measurements) | 300 N | 150 N | 40 N  | 10N       |
| Transition Load ( $l_c$ )<br>(from weight loss measurements)      | 300 N | 140 N | 50 N  | --        |

The wear rates of both the composite and the counterface were determined through weight loss as well and the results are plotted in Fig. 4.5 The wear behaviour indicated by these plots is similar to that indicated by Fig. 4.4, except that the wear rates of the composite now show a slight decrease at loads near the transition load for the tests carried out at 25°C and 150°C. This decrease is quite similar to but not as striking as seen in the wear rates from weight loss plotted as a function of temperature (Fig. 4.3) The decrease in wear is not seen at 200°C in the temperature range of mild wear and could be attributed to the paucity of data near the transition load. The transition loads from weight loss wear data (from Fig. 4.5) are compared to the transition loads indicated by the wear rates measured from change in sample height (from Fig. 4.4) in Table 4.1 and show similar values of transition load for the two different techniques. It can be seen from the Table 4.1 that the transition load decreases rapidly above 150°C.

#### 4.4. Counterface Wear

The behaviour of the counterface studied through weight loss at 10N is depicted in Fig. 4.6 Considerable wear of the counterface SAE 52100 steel took place near room temperature. The wear rates of SAE52100 steel (weight loss per unit sliding distance) increase with increase in ambient temperatures in the mild wear regime of Al6061, that is up to 150°C. At higher temperatures the steel wear rates decrease with temperature as the specimen material undergoes transition to severe wear. The weight gain of the counterface during high temperature tests is due to the transfer of aluminum to the SAE52100 counterface steel.

The counterface shows higher weight loss against the Al6061-20%Al<sub>2</sub>O<sub>3</sub> alloy at all temperatures. During mild wear at 10N at low temperatures, the counterface wear rates against Al6061-20%Al<sub>2</sub>O<sub>3</sub> show little dependence on the test temperature. With the onset of severe wear of the composite at 230°C, the counterface wear decreases sharply with temperature. Weight gain of the counterface is again evident above 320°C as a result of gross material transfer to the counterface surface.

Counterface wear rates measured during constant temperature tests of Al6061-20%Al<sub>2</sub>O<sub>3</sub> through weight loss are given in Fig. 4.7 The wear rates of the steel are lower at 150°C as compared to those at 25°C. However, 30N load test at 200°C shows higher wear of the steel than at lower temperatures (25°C and 150°C). The wear of counterface decreases once the composite starts to exhibit severe wear at higher loads. At 200°C the counterface shows weight gain due to extensive specimen material transfer to its surface.

#### 4.5. Friction Measurements

Coefficient of friction was determined as a ratio of tangential force (T) to the applied normal load (P) (see section 3.2). Three typical friction trace curves obtained during sliding under 10N load are shown in Fig 4.8 The wear runs at low temperatures (mild wear regime) were smooth and the friction trace, therefore, shows relatively narrow spread. The coefficient of friction, in the mild wear regime, was often high in the beginning but stabilized to a steady low value at higher sliding distances. However, fluctuations in friction force are evident at high sliding distances during tests at room temperature in both Al6061-20%Al<sub>2</sub>O<sub>3</sub> and the unreinforced alloy (Fig. 4.8). During severe wear at elevated temperatures, the coefficient of friction showed larger fluctuations during the wear run and the friction trace was much more spread out.

Average value of coefficient of friction as well as its maximum and minimum values are plotted against test temperature for both the alloys in Fig 4.9 The coefficient of friction of Al6061 decreased with increasing temperature in the mild wear regime. For example, the value of coefficient of friction at room temperature was 0.56 and reduced to 0.35 at 150°C. On the other hand, the coefficient of friction increased sharply with temperature during sliding in the severe wear regime. At room temperature the Al6061-20%Al<sub>2</sub>O<sub>3</sub> alloy showed slightly lower coefficient of friction ( $\mu=0.48$ ) than the unreinforced 6061 alloy. Coefficient of friction for Al6061-20%Al<sub>2</sub>O<sub>3</sub>, however did not change much with temperature up to about 230°C and stayed around 0.45 throughout the

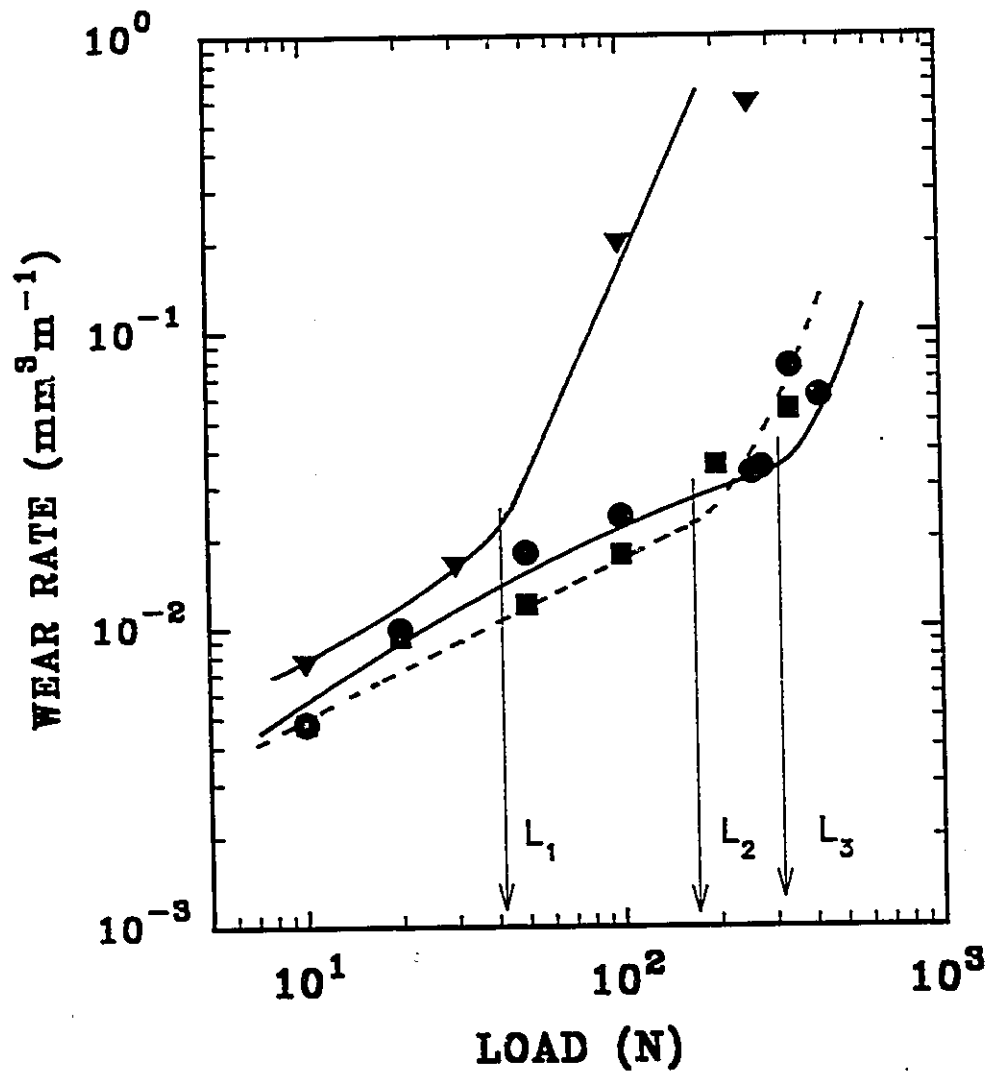


Fig. 4.4. Effect of load on the sliding wear behaviour of Al6061-20%Al<sub>2</sub>O<sub>3</sub> at 25°C ( ● ), 150°C ( ■ ) and 200°C. ( ▼ ). Wear rates determined from specimen height change measurements.

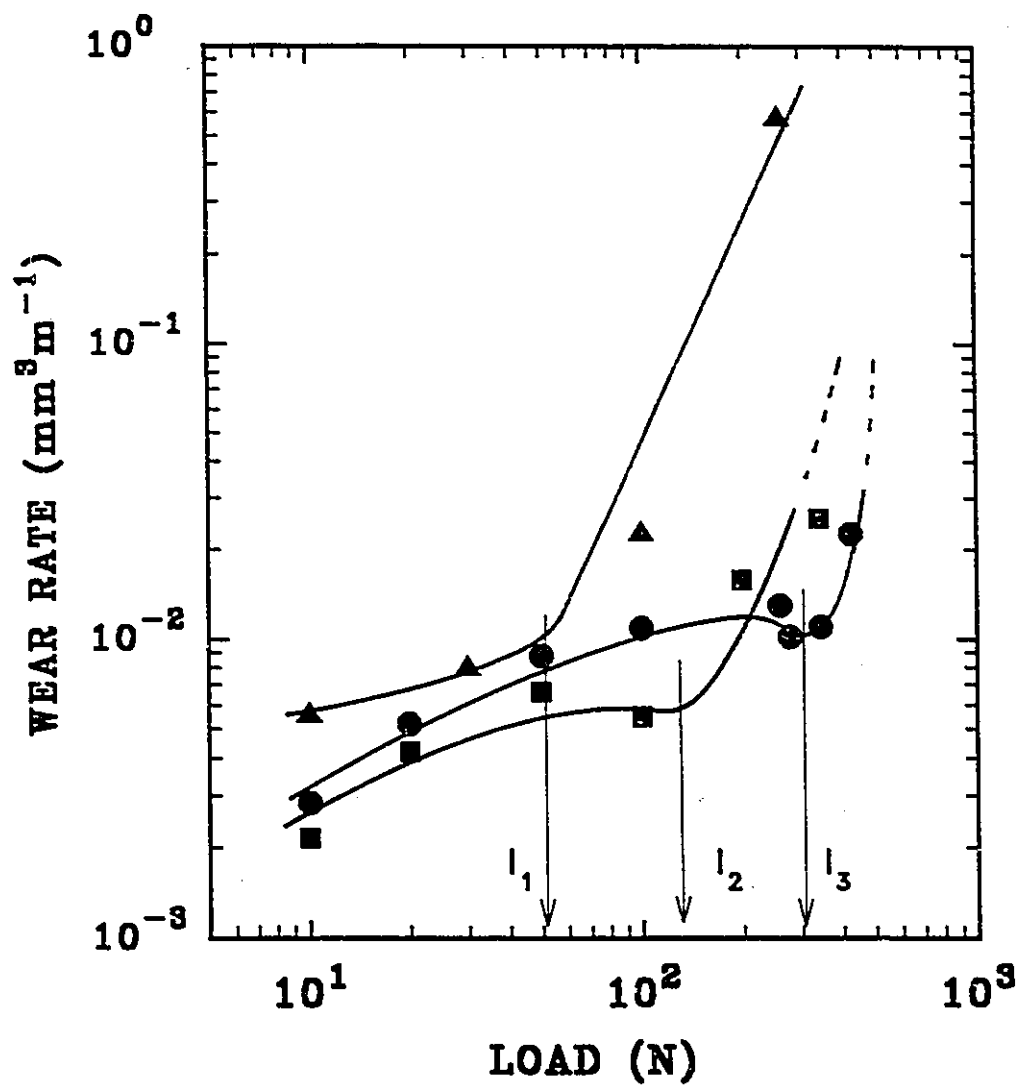


Fig. 4.5. Wear rate vs load plots for Al6061-20%Al<sub>2</sub>O<sub>3</sub> at 25°C ( ● ), 150°C ( ■ ) and 200°C ( ▲ ). The wear rates were obtained from weight loss measurements.

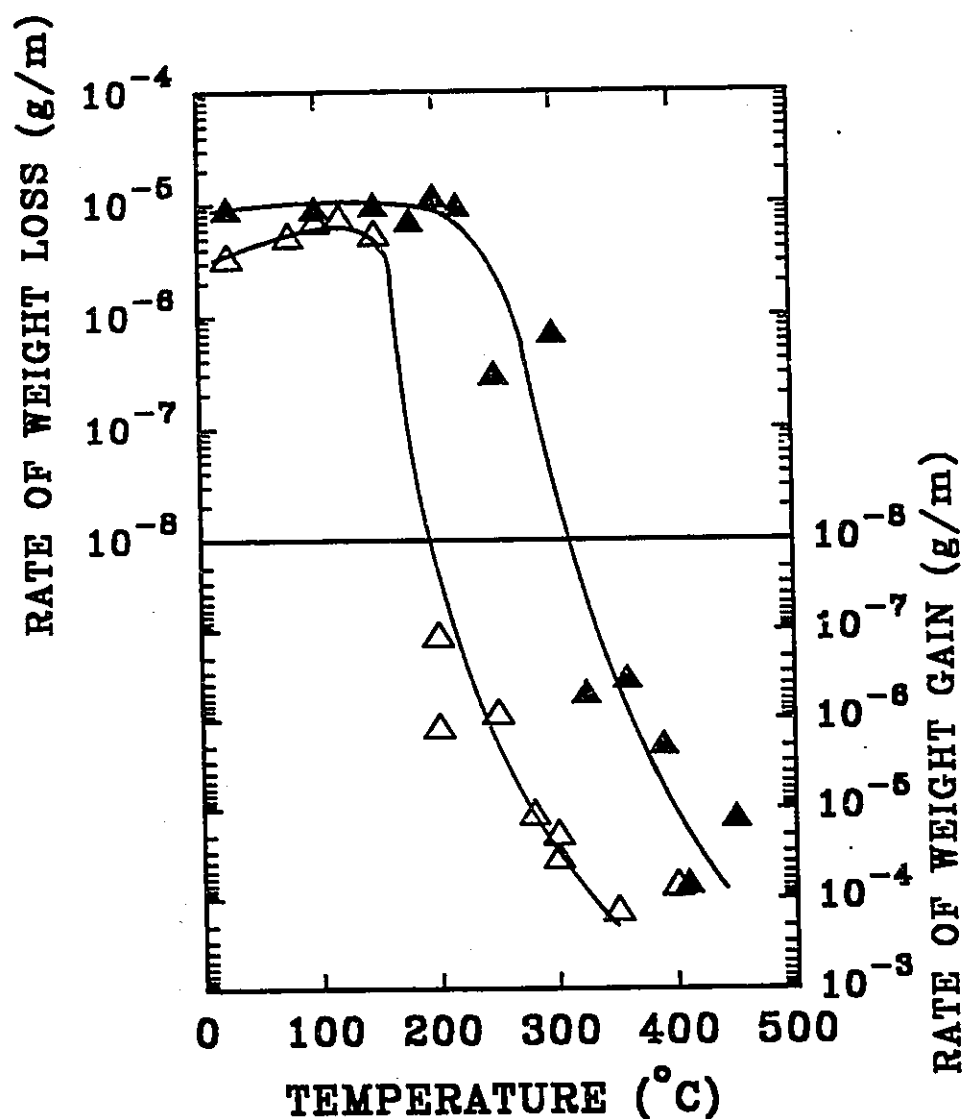


Fig. 4.6. Changes in the weight of SAE52100 counterface sliding against Al6061 (  $\triangle$  ) and Al6061-20%Al<sub>2</sub>O<sub>3</sub> (  $\blacktriangle$  ) at elevated temperatures. Top half shows the weight loss accompanying steel wear and the bottom half indicates weight gain due to aluminum transfer to the counterface surface. (applied load = 10N)



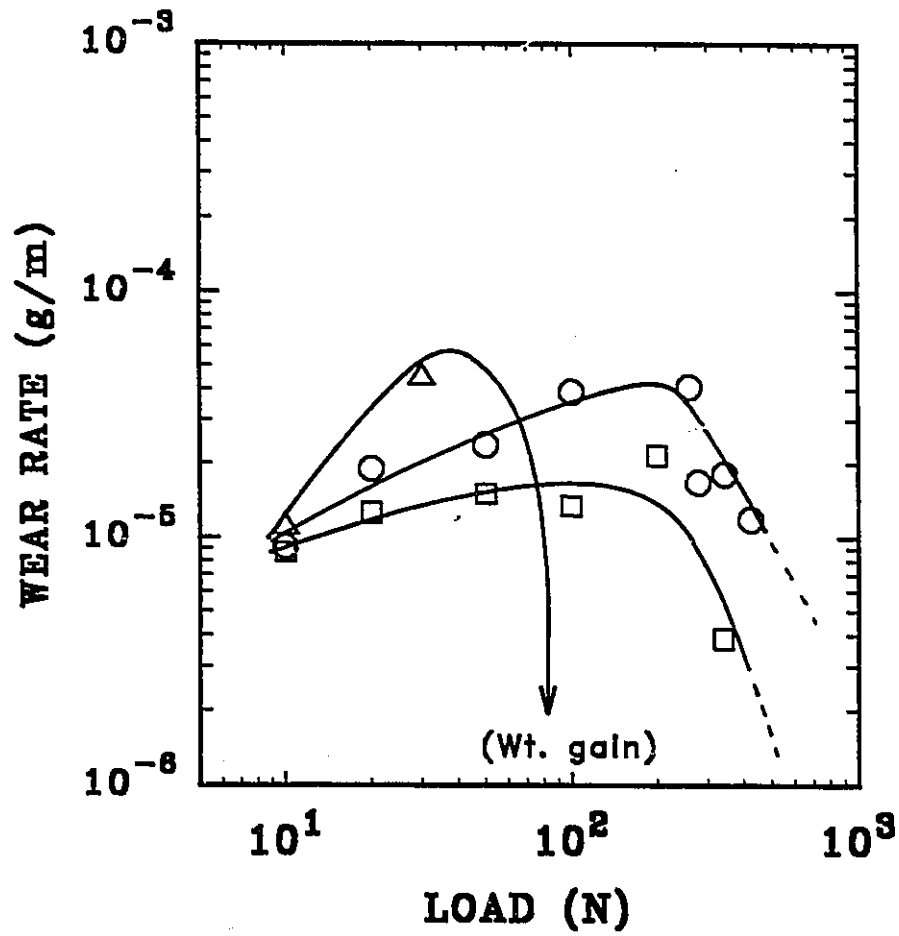


Fig. 4.7. Counterface (SAE52100) wear behaviour during sliding against Al6061-20%Al<sub>2</sub>O<sub>3</sub> at 25°C ( O ), 150°C ( □ ) and 200°C ( Δ ).

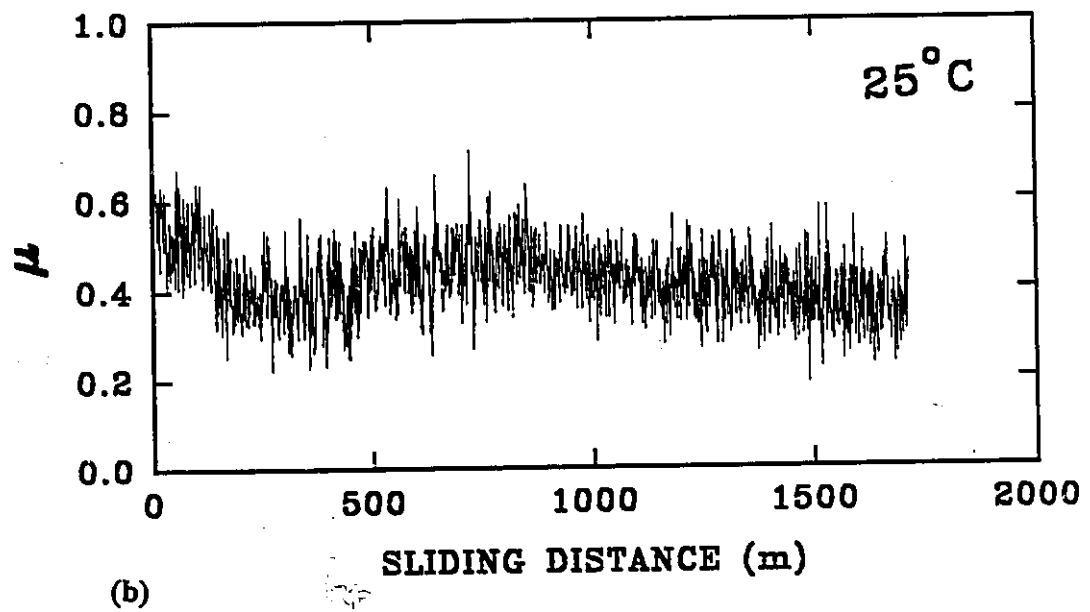
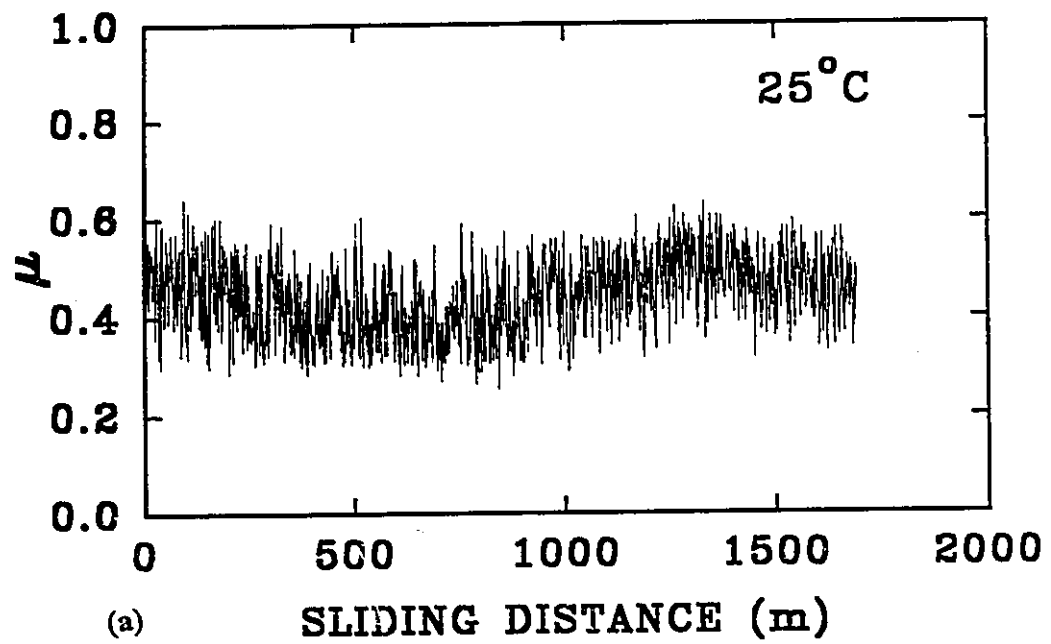


Fig. 4.8. Friction trace during sliding of Al6061 at 25°C (a); Al6061-20%Al<sub>2</sub>O<sub>3</sub> at 25°C (b), 120°C (c), and 350°C (d).

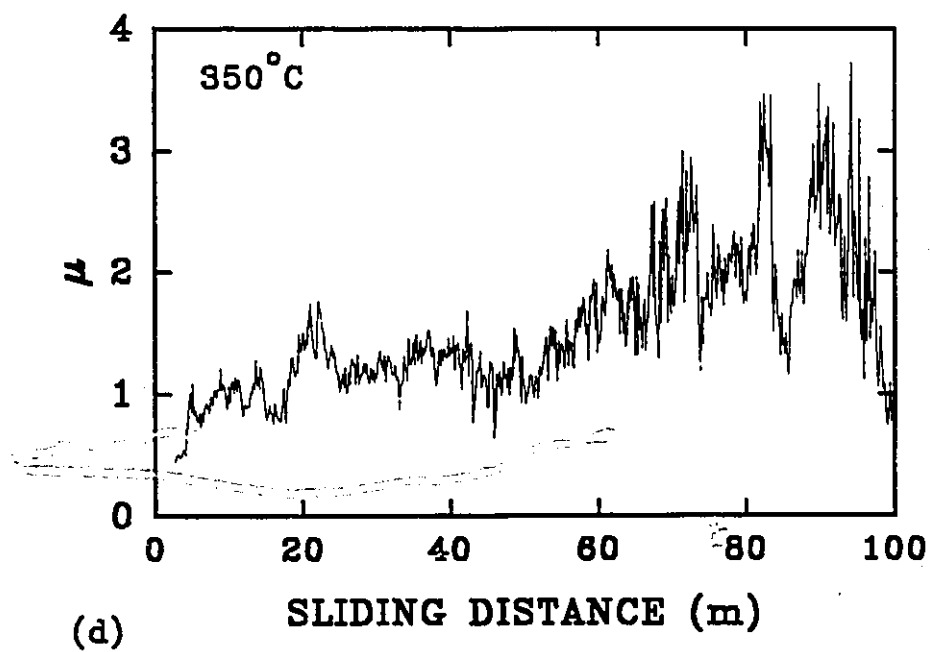
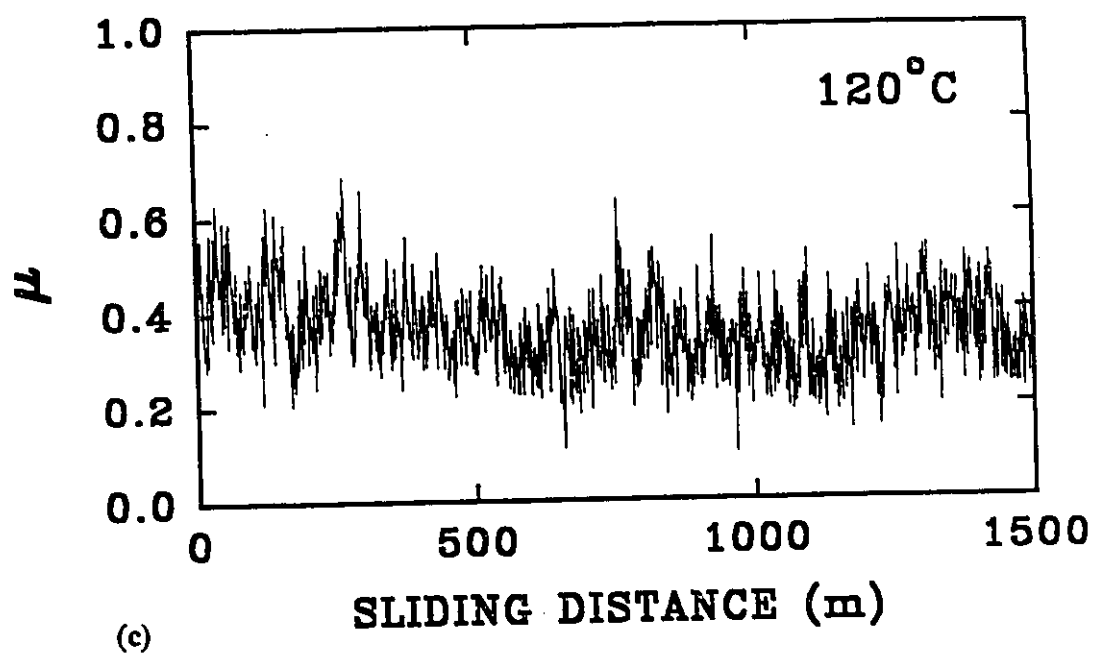


Fig. 4.8. Continued.

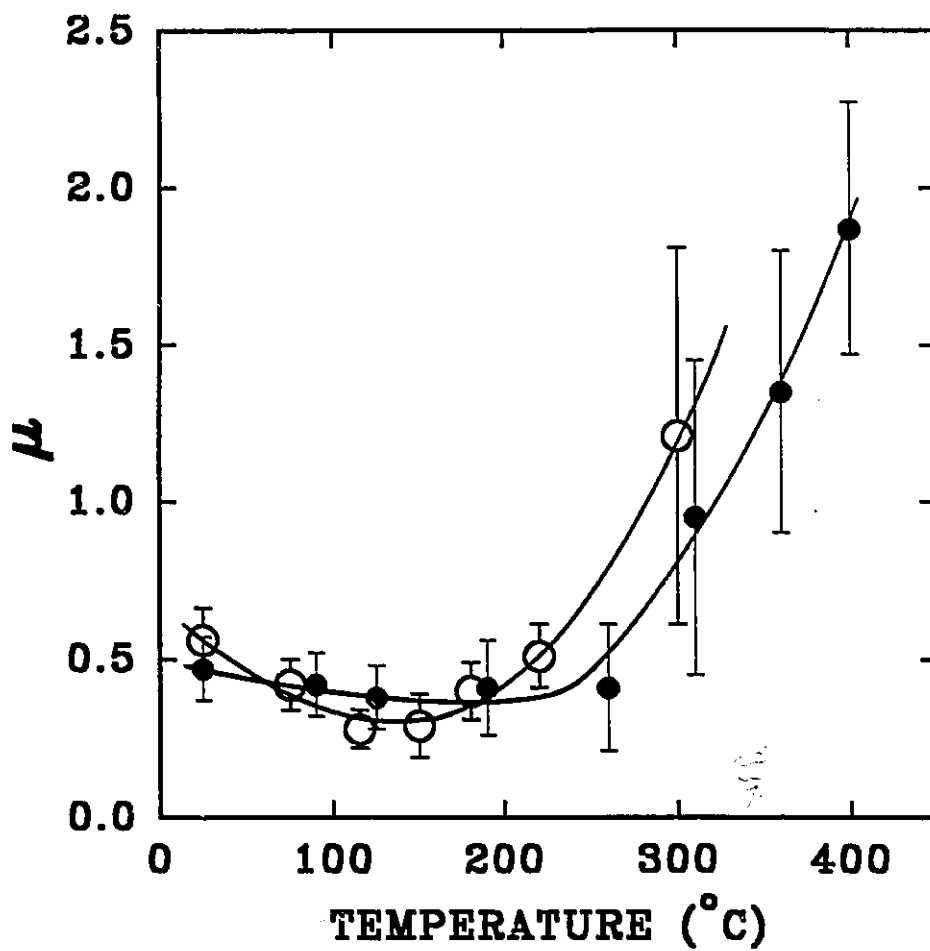


Fig. 4.9. Effect of temperature on the coefficient of friction of Al6061 (  $\bigcirc$  ) and Al6061-20%Al<sub>2</sub>O<sub>3</sub> (  $\bullet$  ) against SAE 52100. The bars represent the maximum and minimum of the spread of friction trace.

mild wear regime. At higher temperatures, the coefficient of friction increased rapidly to 1.0 at 300°C and to 2.0 at 400°C.

## 4.6. Characterization of Worn Surfaces

### 4.6.1. Mild Wear

The worn surfaces were first examined visually and then through optical as well as scanning electron microscopy (SEM). The worn surfaces after testing in the mild wear regime appeared black to the unaided eye. Fig. 4.10 shows the worn surfaces of Al6061 and Al6061-20%Al<sub>2</sub>O<sub>3</sub> specimens tested at room temperature at 10N load and are typical of the specimens worn at temperatures within the mild wear regime. The specimen wear surfaces are flat and have sharp edges. The specimens had polished surfaces prior to wear test and after the sliding showed increase in surface roughness. The composite surface appears to have higher surface roughness as compared to the unreinforced alloy and is covered with patches of black layer. The counterface surfaces are smooth as compared to the specimen surfaces.

Electron micrograph in Fig. 4.11. shows abrasion marks as well as formation of shallow pits (indicated by arrows) on the worn surface of Al6061 after sliding at low loads (10 N) at room temperature. Worn surface at temperatures near 150°C, where minimum in the wear rates of the Al6061 alloy occurred (see Fig. 4.3.), the specimens were found to be covered with an oxide layer (Fig. 4.12. (a) and (b)). The parts of worn surfaces that appear white on these photographs were found to be rich in iron. Higher magnification photograph in 4.12(c) indicates the presence of small debris particles which according to EDS results (Fig. 4.12(d)) are iron oxide and aluminum oxide. Thus the layer seen in Fig. 4.12(b) is most likely to be the iron oxide debris (transferred from the counterface) particles adhered and compacted on to the worn surface. Ultrasonic cleaning of the surface in alcohol did not dislodge the layer.

SEM observations on the worn surface of the Al6061-20%Al<sub>2</sub>O<sub>3</sub> alloy after sliding at room temperature at 10N load is given in Fig. 4.13(a). The raised plateaus on the

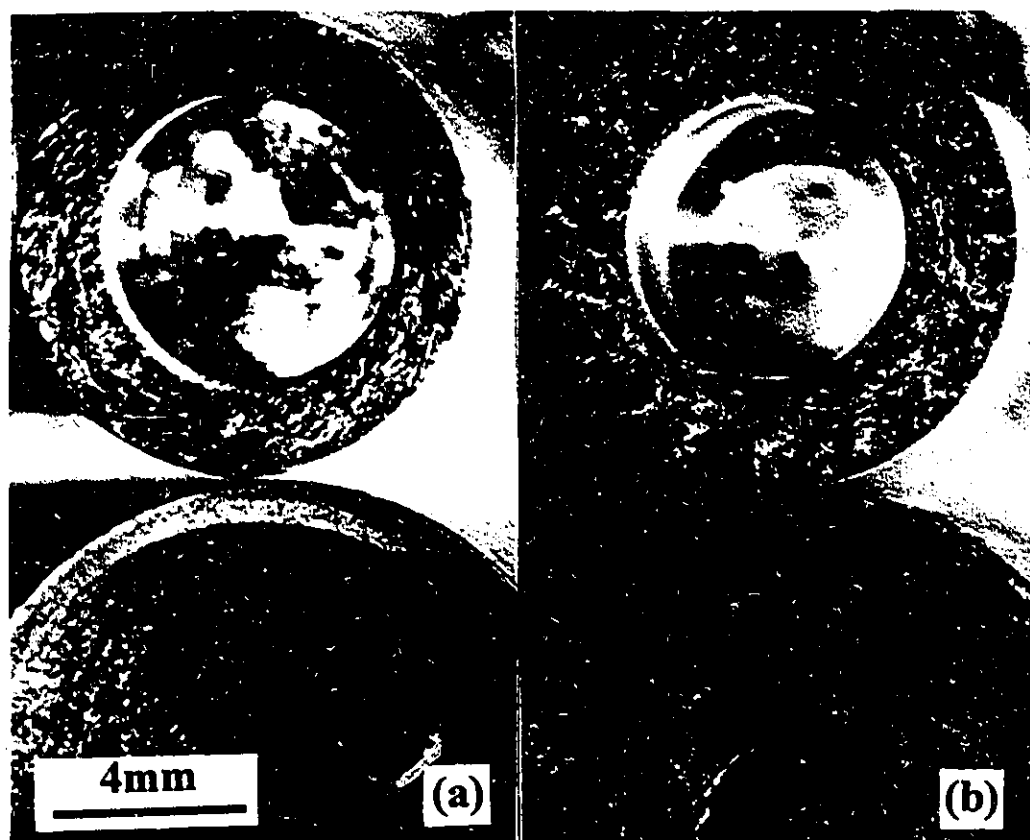


**Fig. 4.10. Optical micrographs of worn surfaces of samples (top) and counterfaces (bottom) after sliding at room temperature for Al6061 (a) and Al6061-20%Al<sub>2</sub>O<sub>3</sub> (b). (Load=10N, sliding speed=0.2m.s<sup>-1</sup>)**

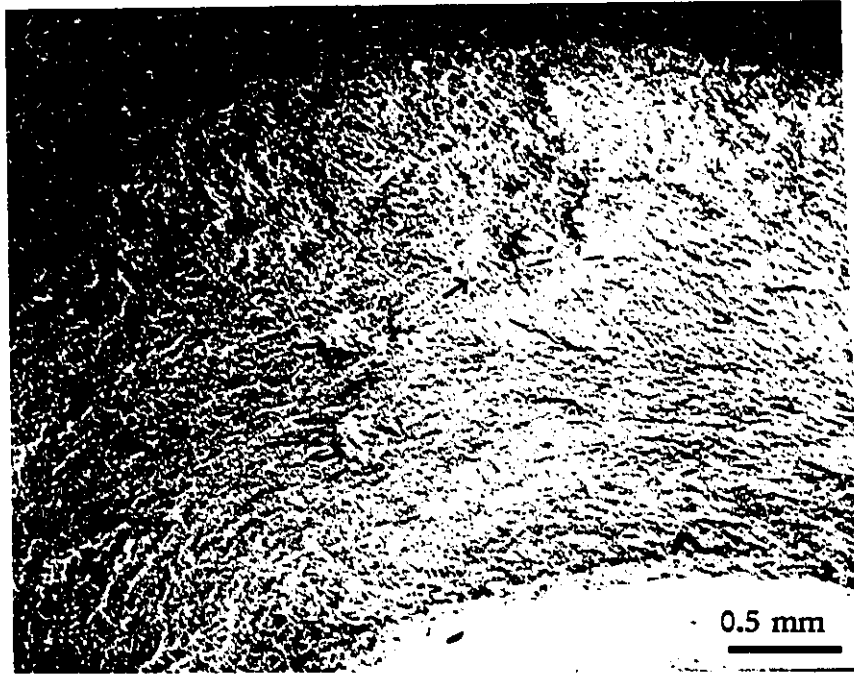


**Fig. 4.11.** Electron micrograph of worn surfaces of Al6061 after sliding at 25°C.

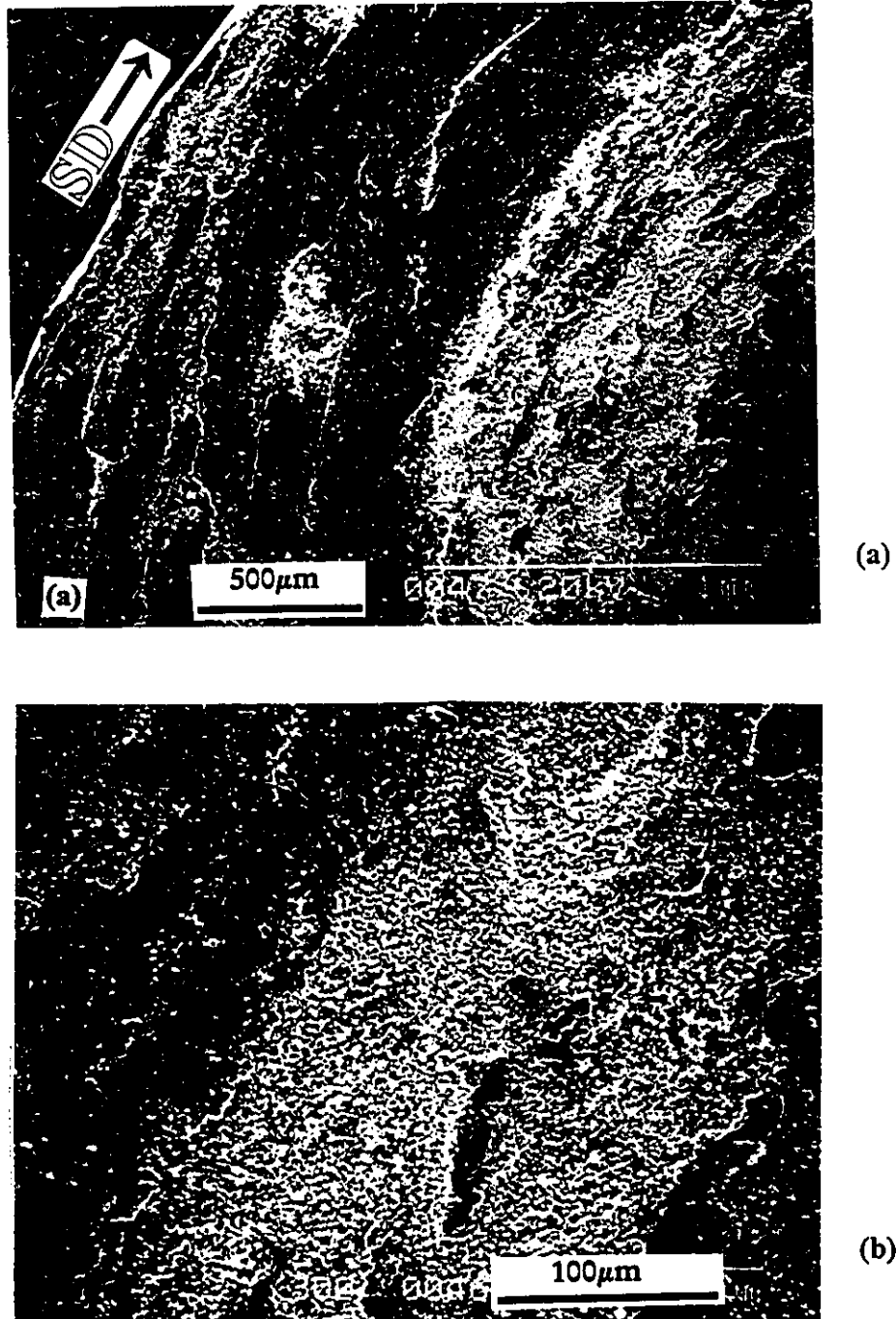


**Fig. 4.12. (a) SEM micrograph of worn surface of Al6061 specimen slid at 150°C under 10N load. The surface shows a smooth region and a region that appears light colored, (b) Details of the light colored region (c) region of the worn surface rich in debris containing iron and oxygen, and (d) EDS of the region shown in (b).**



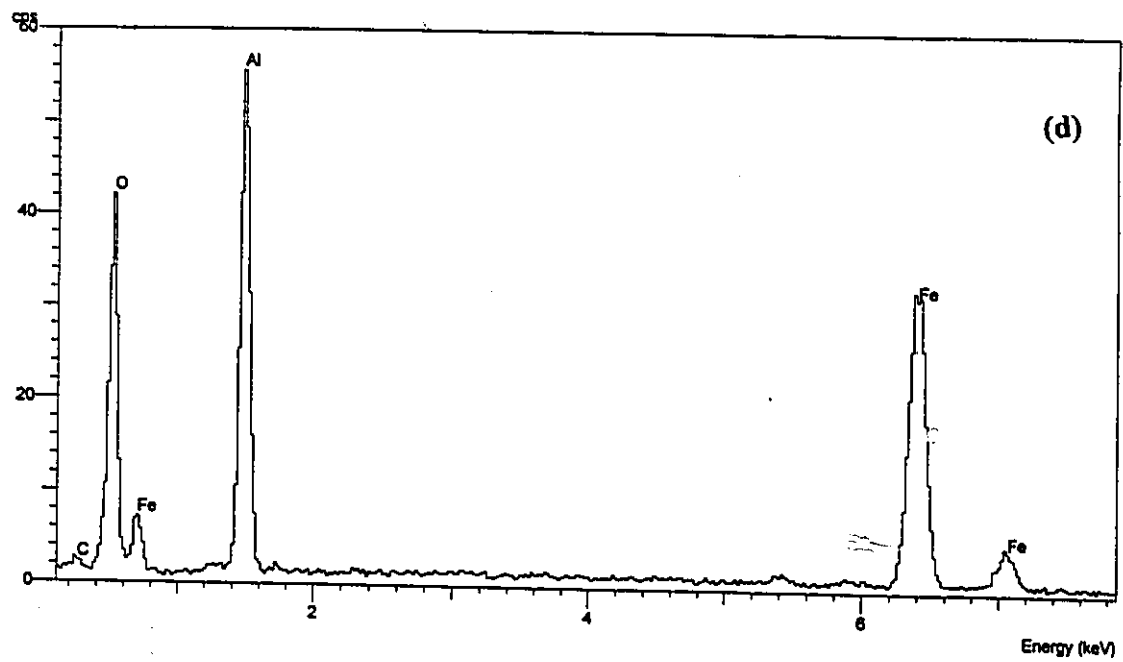
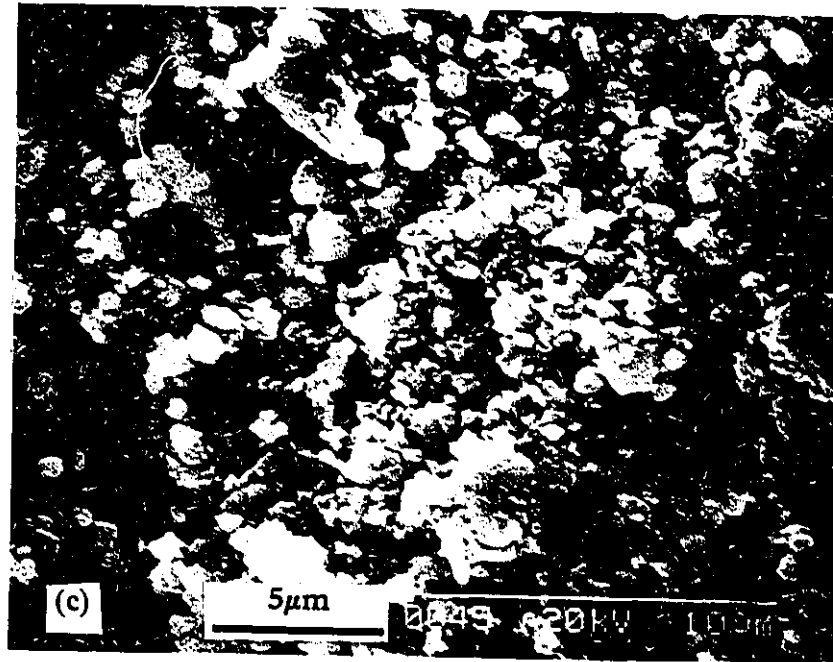
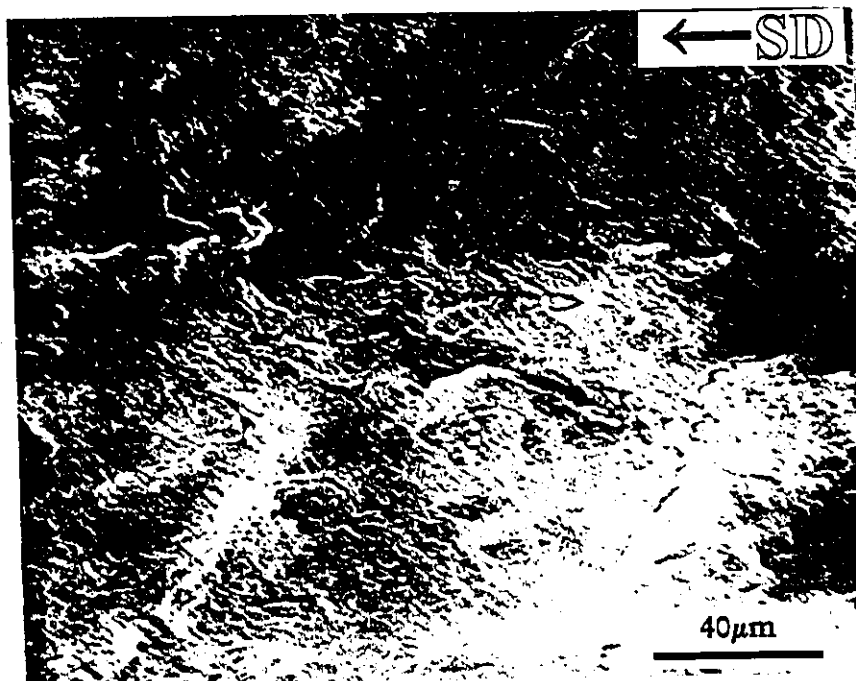


Fig. 4.12. Continued.



(a)

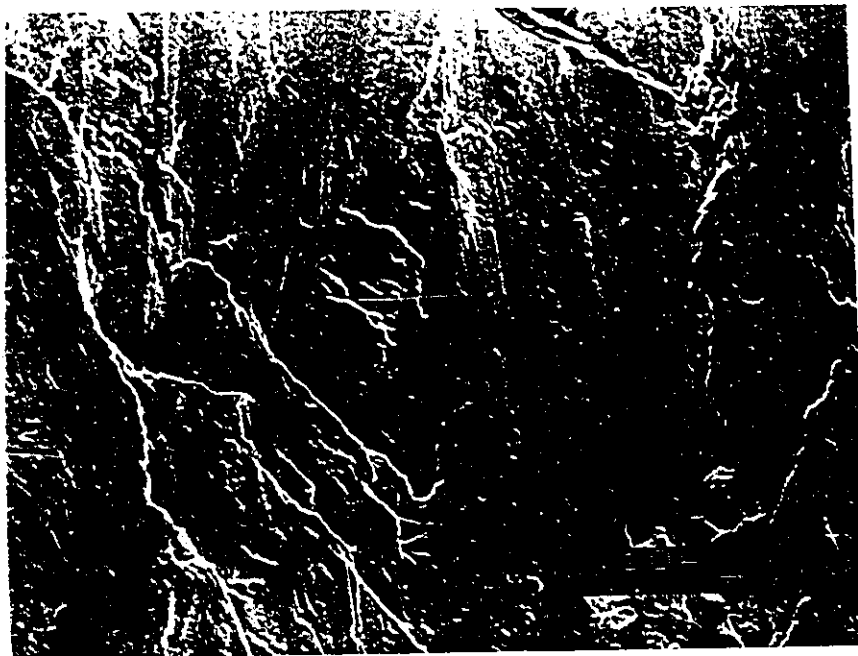


(b)

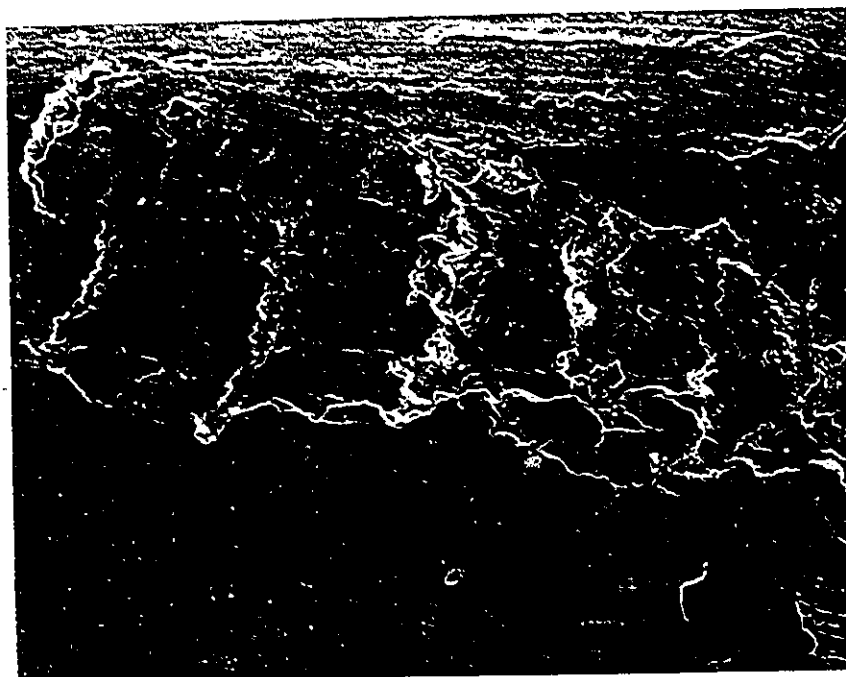
**Fig. 4.13. SEM observations on Al6061-20%Al<sub>2</sub>O<sub>3</sub> worn surfaces slid at 25°C at 10N load showing (a) elevated plateaus and pits, (b) surface cracks.**



**Fig. 4.14. Optical micrographs of worn surfaces of samples (top) and counterfaces (bottom) after sliding at 300°C under 10N load for Al6061 (a) and Al6061-20%Al<sub>2</sub>O<sub>3</sub> (b).**



(a)



(b)

**4.15. Electron micrograph of worn surface of specimen after sliding at 10N load**  
**(a) Al6061 at 200°C (sliding direction upward) and**  
**(b) Al6061-20%Al<sub>2</sub>O<sub>3</sub> at 350°C (sliding direction left to right).**

surface have smooth appearance and appear to be covered with oxides. Presence of deep pits at the surface indicate that the delamination may have occurred during the sliding process in which flakes of material are removed from the sliding surface. Higher magnification view of the pits in Fig. 4.13(b) shows high density of surface cracks.

#### 4.6.2. Severe Wear

Severe wear at elevated temperatures (Fig. 4.14) produced undulating and rougher surfaces than the mild wear. Extensive material transfer to the counterface has occurred in both the unreinforced as well as Al6061-20%Al<sub>2</sub>O<sub>3</sub> alloy and was readily evident to the unaided eye. The counterface surfaces have become rough and uneven and chunks of material, transferred from the specimen, can be seen sticking on the surface.

Worn surfaces of Al6061 after sliding in the severe wear regime appeared featureless at higher magnifications (Fig. 4.15(a)) except for the material flow marks in the direction of sliding. EDS analysis performed on specimen worn at elevated temperatures (severe wear regime) did not show the presence of iron on the sliding surfaces which was expected since aluminum transfer to the counterface essentially prevented direct contact between steel and aluminum.

Surfaces of the Al6061-20%Al<sub>2</sub>O<sub>3</sub> alloy slid in the severe wear regime (Fig. 4.15(b)) were mostly featureless except for shallow cracks normal to the sliding direction which were rather rare. These cracks appear to have been created by gauging of the specimen surface by the mounds of material left on the counterface surface. These mounds are created by the material transfer process in which chunks of aluminum are left sticking on to the steel surface (Fig. 4.14). Small fragmented alumina particles were occasionally found sticking on to the worn track.

### 4.7. Subsurface Characterization

#### 4.7.1. Mild Wear

Longitudinal cross-section of Al6061 specimen worn at 10N load at room temperature is shown in Fig. 4.16(a). The extrusion marks are normal to the contact surface in the base material. This is because the cylindrical specimen samples were machined from the extruded rods with sample axis parallel to the rod axis. The plastic deformation near the contact surface reorients these extrusion marks in the direction of sliding. The grain boundaries near the contact surface also get reoriented and bend towards the direction of sliding as a result of plastic deformation. However, the depth of the plastic zone is limited to about 10  $\mu\text{m}$ . The extent of plastic deformation increased at higher loads. In the case of Al6061-20%Al<sub>2</sub>O<sub>3</sub> (Fig. 4.16(b)), very fine cracks open to the worn surface were frequently observed.

#### 4.7.2. Severe Wear

Al6061 worn at higher loads induced large scale plastic deformation below the contact surface. Extensive plastic flow leads to extrusion of the material out of the contact area (Fig. 4.17(a)). Grains in the subsurface deformed and assumed a tear drop shape (Fig. 4.17(b)) and the grain boundaries close to the contact surface became parallel to the sliding direction.

Large scale subsurface deformation was observed in the specimens tested in the severe wear regime at elevated temperatures. The micrograph in Fig. 4.18 (longitudinal cross-section, etched) shows that the recrystallization has occurred in Al6061 worn at 350°C under 10N load. The recrystallized grains are oriented along the sliding direction. The recrystallized grain size near the worn surface is approximately 5  $\mu\text{m}$  as compared to a grain size of 45  $\mu\text{m}$  in the bulk of the specimen. The recrystallized grains can be observed up to a depth of 400  $\mu\text{m}$  at 350°C.

In the case of Al6061-20%Al<sub>2</sub>O<sub>3</sub>, large scale plastic deformation and extrusion of material out of the contact surface took place during sliding in severe wear regime. Cross-section of the specimen worn at 300°C at 10 N is shown in Fig.4.19(a). In addition to extrusion of material, a layer appears to have formed at the contact surface of the Al6061-

20%Al<sub>2</sub>O<sub>3</sub> alloy. Higher magnification micrograph of the circled area (Fig 4.19(b)) indicates that the particulate damage below the worn surface took place. The damage layer contains both large as well as very fine comminuted Al<sub>2</sub>O<sub>3</sub> particles. Although considerable plastic flow (Fig. 4.19(a)) has occurred below this layer (to a depth of 400  $\mu$ m as indicated by the thickness of the extruded zone), the Al<sub>2</sub>O<sub>3</sub> particles remain largely unaffected so that there is a sharp boundary between the comminuted particle layer and the deformed material below. Subsequent etching of this section also showed that the plastic deformation occurred to a higher depth as compared to the depth of the comminuted Al<sub>2</sub>O<sub>3</sub> particle layer.

Fig. 4.20 depicts SEM observations on the transverse tapered (at 7° to the sliding direction) cross-section of the specimen worn at 350°C under 10N load. A layer approximately 100  $\mu$ m thick consisting of highly fragmented Al<sub>2</sub>O<sub>3</sub> particles is seen at the worn surface. The thickness of the layer varies greatly along the width of the specimen.

The severity of particle comminution in Al6061-20%Al<sub>2</sub>O<sub>3</sub> alloy specimens during severe wear is more clearly seen in Fig. 4.21, which is higher magnification view of the surface seen in Fig. 4.20. Large particles are absent altogether in the damage layer. The average particle size within this layer is about 1 $\mu$ m. There is a sharp boundary between the fragmented particle layer and the bulk of the specimen.

#### 4.7.3 Subsurface Hardness Measurements

The results of hardness measurements (Vickers, 50N load on the tapered section) in the subsurface after sliding under 10 N at different temperatures is shown in Fig. 4.22. Increase in hardness near the worn surface is evident in Al6061 specimen tested at room temperature. This can be attributed to the work hardening as a result of plastic deformation. Similarly, work-hardening increased the hardness near the contact surface, however, the overall hardness has decreased in comparison to the specimen tested at room temperature due to overaging at 200°C. The specimens worn at temperatures 300°C showed very low bulk hardness as a result of loss of precipitation strengthening (over-

ageing). For example, the specimen exposed to 300°C shows microhardness of 46 kg.mm<sup>-2</sup> as compared to 118 kg.mm<sup>-2</sup> in the peak aged condition.

The matrix microhardness values in the subsurface after sliding of Al6061-20%Al<sub>2</sub>O<sub>3</sub> (at elevated temperatures under 10N load) are presented in Fig. 4.22(b). Care was taken to avoid hitting the ceramic particles during indentation. However, the indentations were very close to the particles and thus the values presented here may slightly overestimate the matrix hardness. Sliding at room temperature shows a small increase in hardness below the contact surface. Sliding at elevated temperatures resulted in formation of thick layers at the surface which contained tiny fragmented Al<sub>2</sub>O<sub>3</sub> particles (Fig. 4.19 and 4.20). The fine distribution of these particles made it impossible to get the matrix hardness, and therefore, the hardness of the composite microstructure of these layers was measured. The hardness values obtained within these layers (at 200°C and 300°C) is thus considerably higher than the matrix hardness in the bulk where Al<sub>2</sub>O<sub>3</sub> particles were intact. Also, the tribo-layer (with very high density of fine Al<sub>2</sub>O<sub>3</sub> particles) hardness is considerably higher (≈200 kg.mm<sup>-2</sup>) than the hardness of the original Al6061-20%Al<sub>2</sub>O<sub>3</sub> alloy with large particles (134 kg.mm<sup>-2</sup>).

#### 4.8. Debris Analysis

Debris generated during the sliding wear was collected and examined visually as well as through XRD analysis. In the mild wear regime, the debris was in the form of fine black powder mixed with small metallic platelet. Results of XRD analyses performed on debris collected during sliding tests at 10N for Al6061 at room temperature and 150°C are given in Fig. 4.23. According to XRD analysis, it is composed of metallic Al and Fe as well as oxides (Al<sub>2</sub>O<sub>3</sub>, Fe<sub>2</sub>O<sub>3</sub>). Al<sub>2</sub>O<sub>3</sub> and Fe<sub>2</sub>O<sub>3</sub> peaks appear very close to each other and it was difficult to index Fe<sub>2</sub>O<sub>3</sub> as separate peaks. Debris from higher temperature(150°C) test contains higher proportion of oxides. However, the analysis grossly underestimates metallic Al content because large size debris particles are left out of the powder diffraction specimen which are known to consist of metallic Al. The results on Al6061-



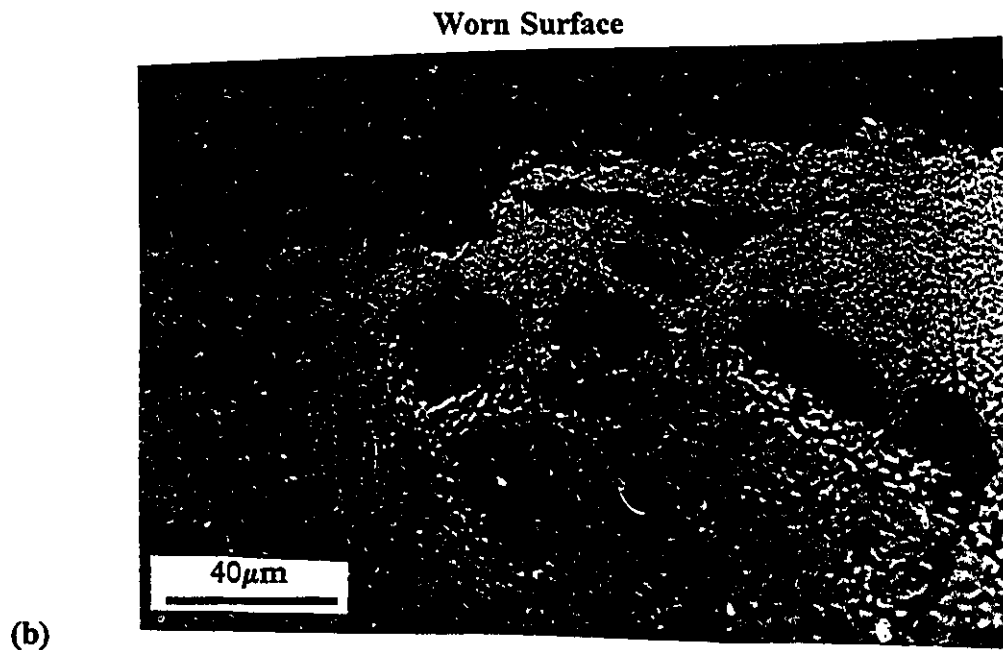
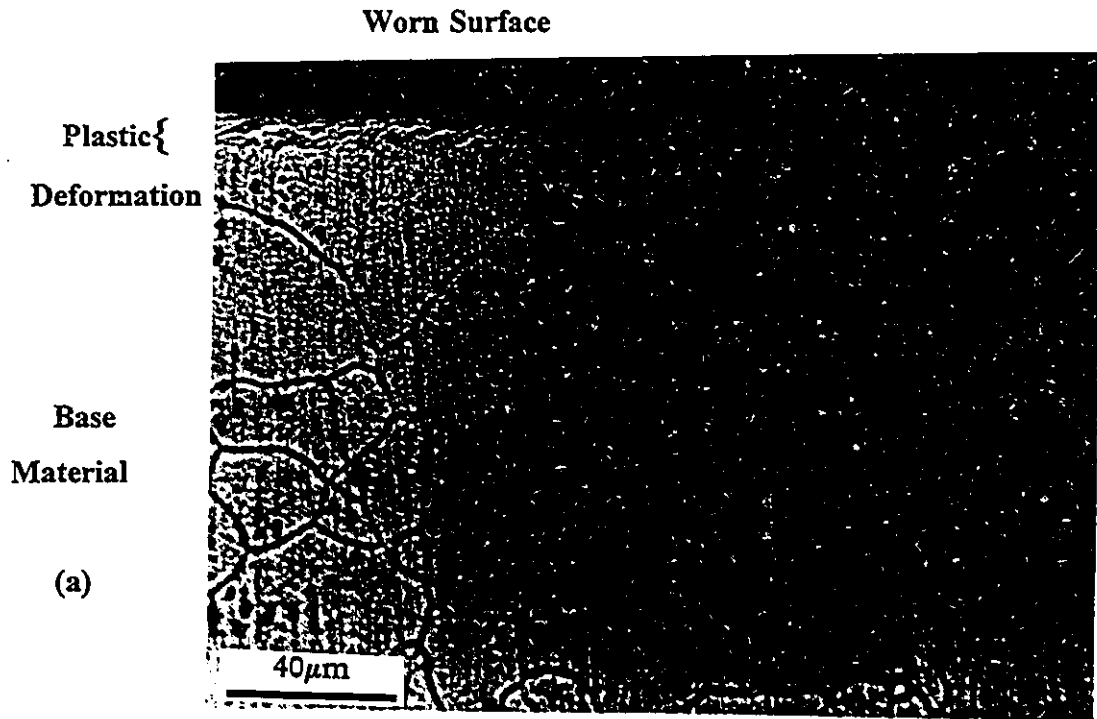


**Fig. 4.16. Longitudinal cross-section of Al6061 after sliding at 25°C under 10N load, (a) Al6061 and (b) Al6061-20%Al<sub>2</sub>O<sub>3</sub>. (sliding direction right to left)**

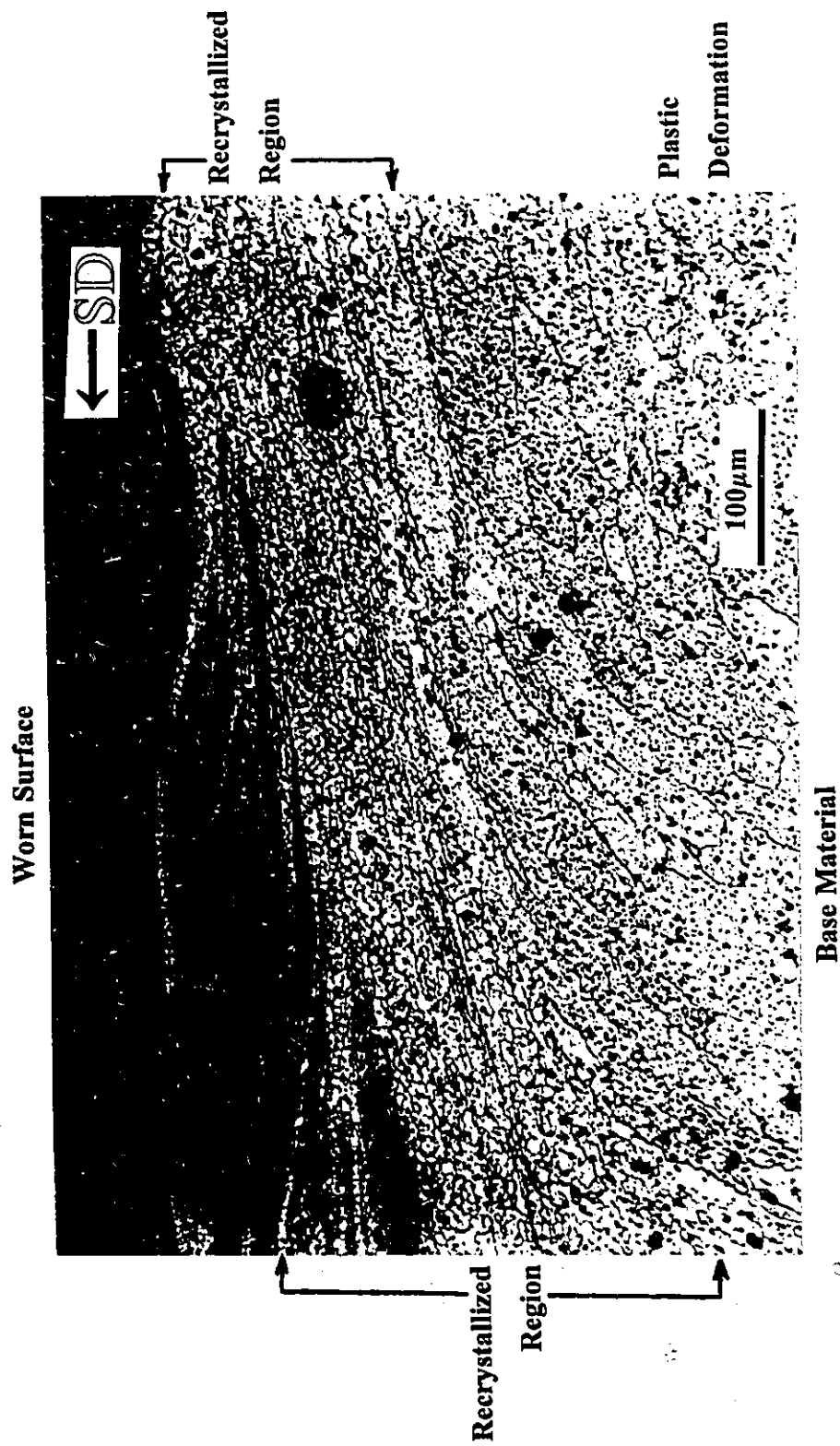
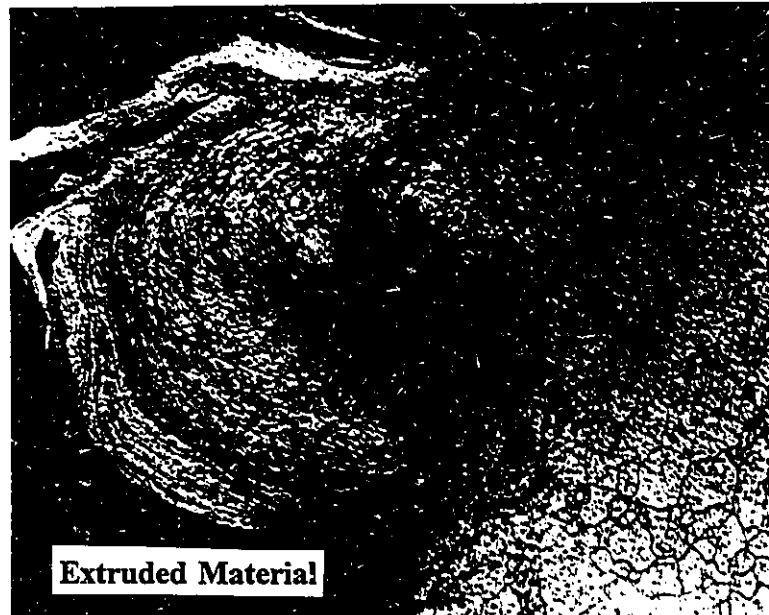


Fig. 4.17. Longitudinal cross-section of Al6061 worn at 350°C at 10N load showing recrystallised grains below the contact surface. SD is sliding direction.

Worn Surface



← SD

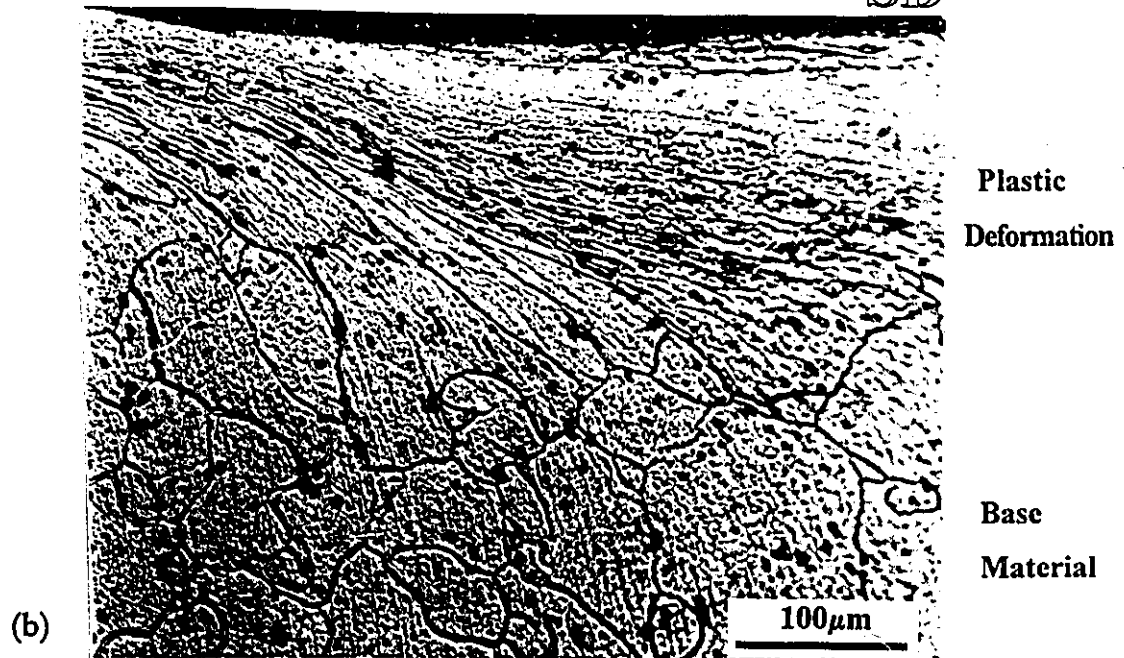


Fig. 4.18. Optical micrographs of transverse cross-section of Al6061 after sliding at 25°C, under 350N load, (a) Extrusion of material out of contact area and (b) plastic deformation below the contact surface. (sliding direction right to left).

Worn Surface

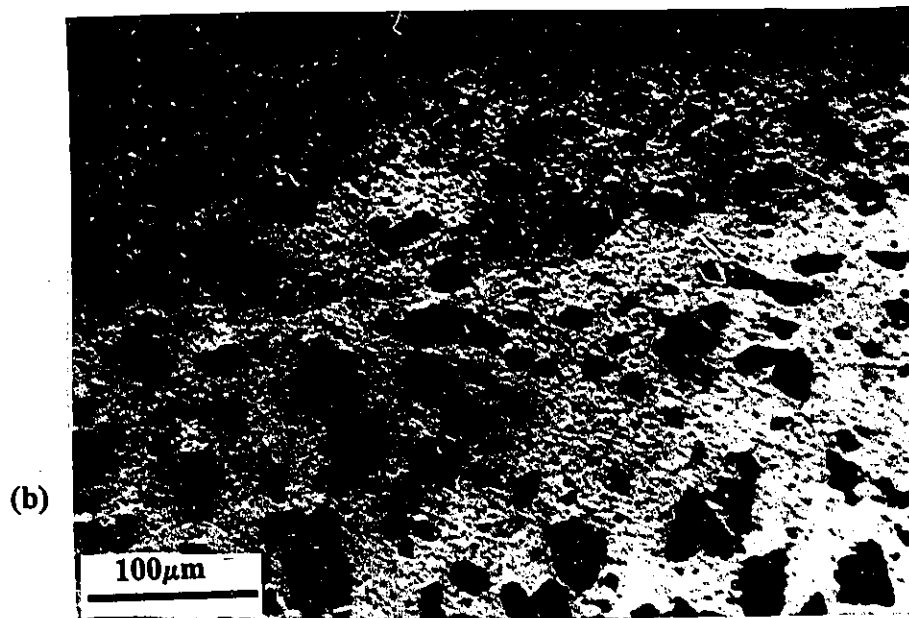
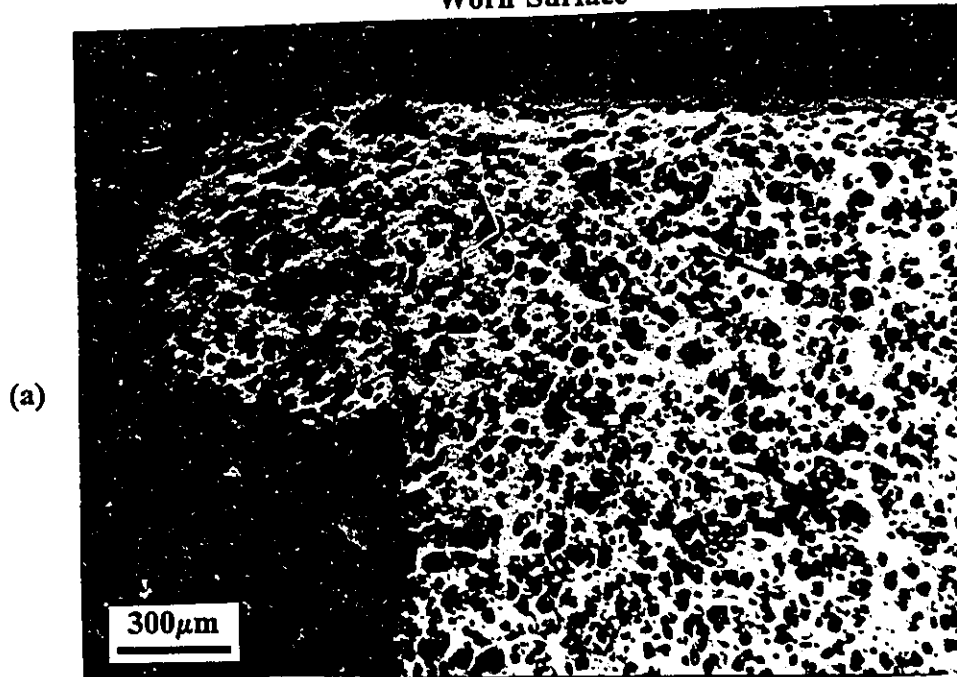
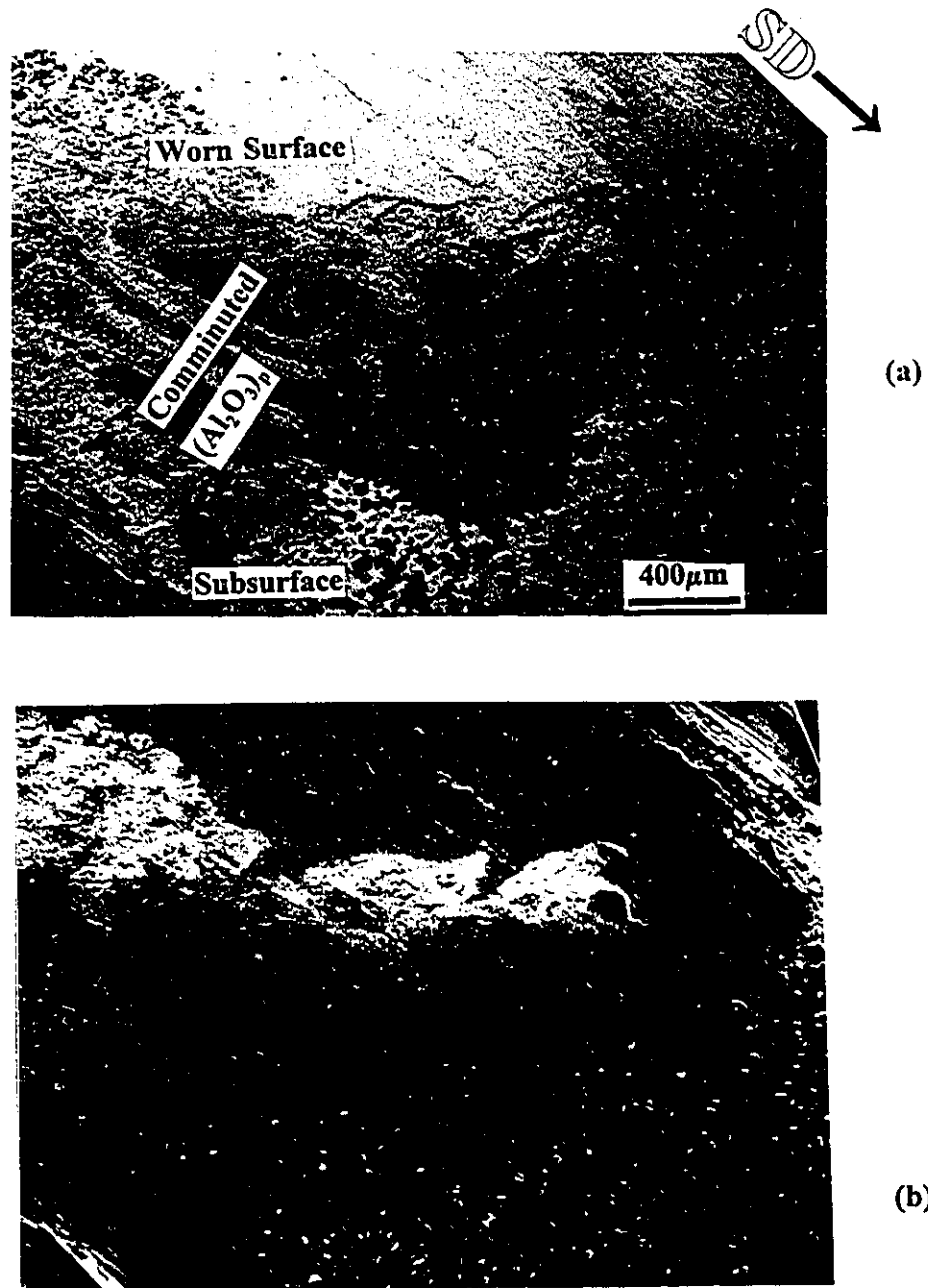


Fig. 4.19. Transverse cross-section of Al6061-20%Al<sub>2</sub>O<sub>3</sub> specimen after sliding at 300°C under 10N load depicting (a) material extrusion and formation of a layer below the contact surface and (b) particle comminution near the contact surface. (Sliding direction right to left)



**Fig. 4.20.** Transverse tapered section of Al6061-Al<sub>2</sub>O<sub>3</sub> after sliding at 350°C at 10N load. (a) secondary electron image (b) corresponding back scattered image.

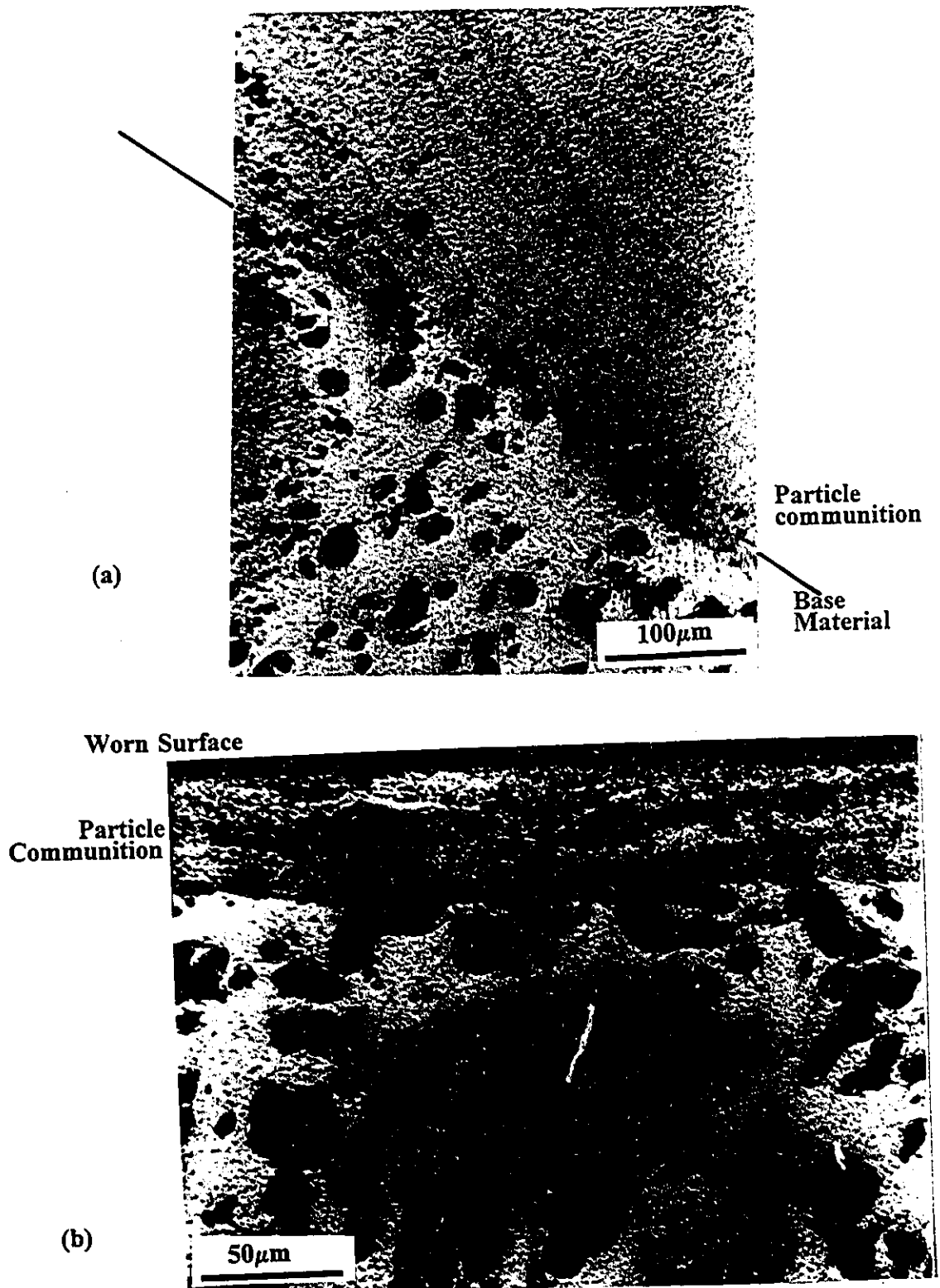
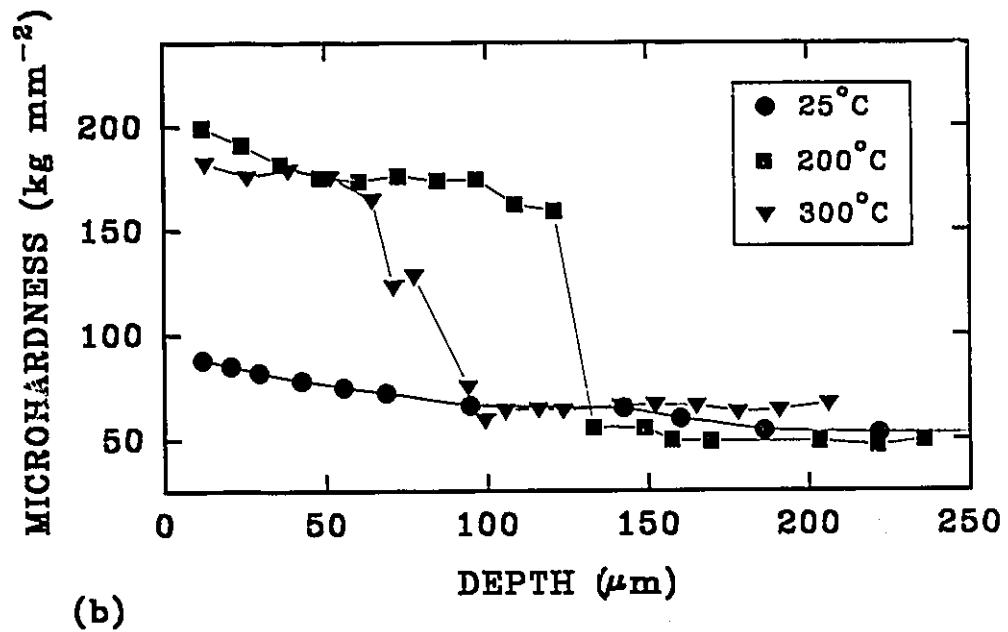
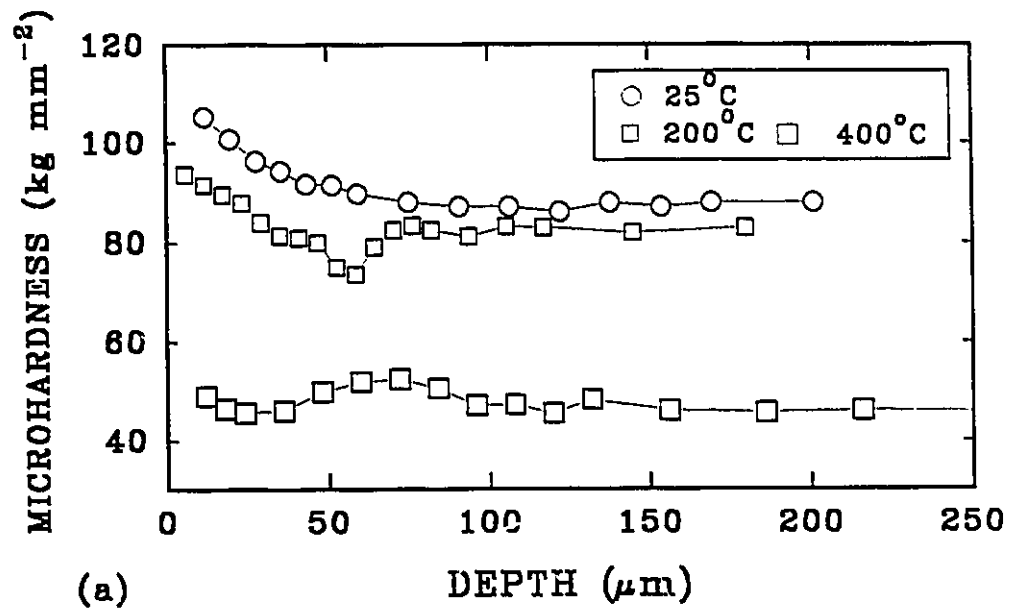


Fig. 4.21. Optical micrographs of Al6061-20%Al<sub>2</sub>O<sub>3</sub> specimen worn at (a) 10N load 350°C (tapered section), and (b) 250N load, 25°C indicating particle comminution.



4.22. Plot of hardness (Vickers, 50g load) measurements made in the subsurface after sliding at different temperatures. (a) Al6061 and (b) Al6061-20%Al<sub>2</sub>O<sub>3</sub>.

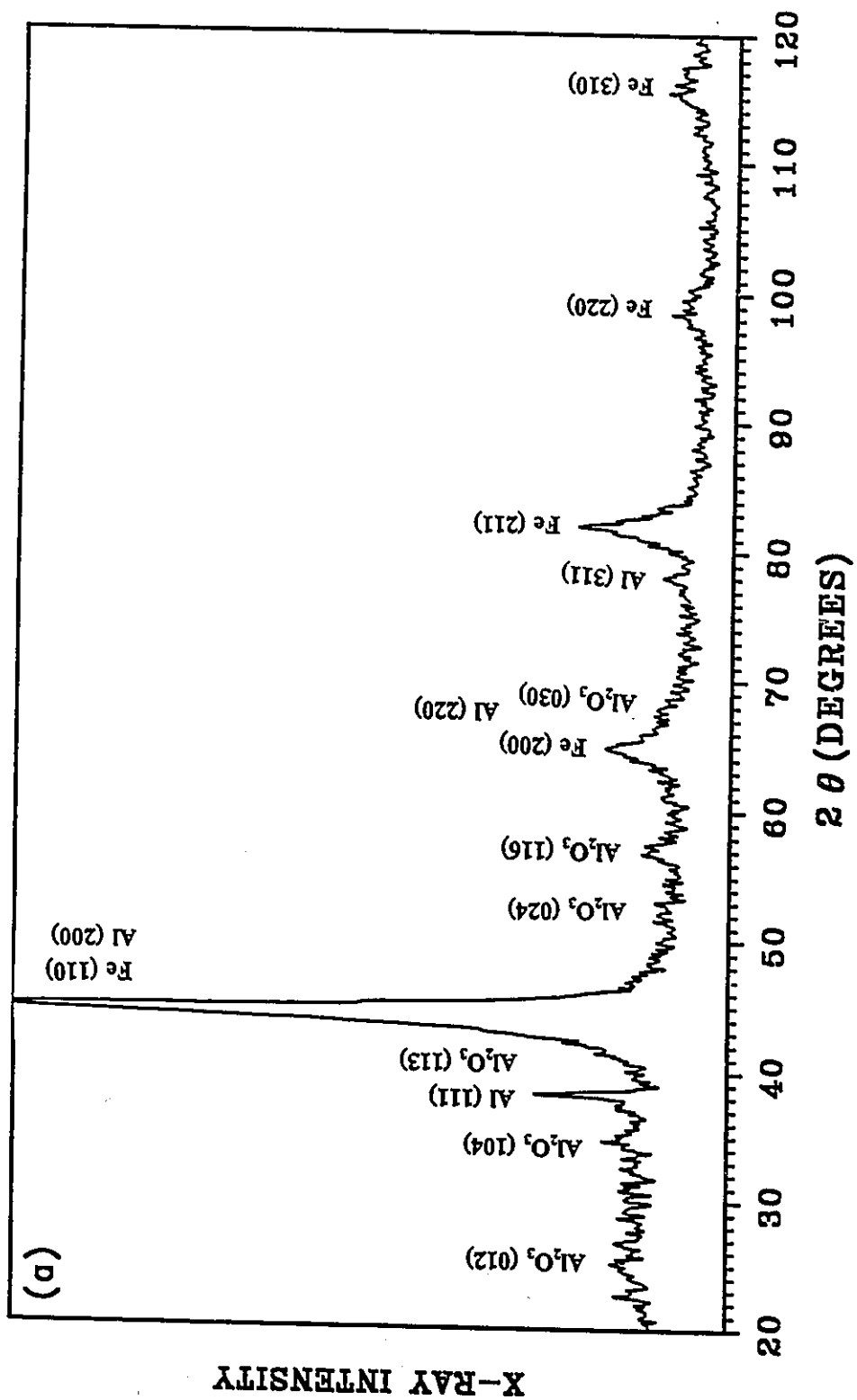


Fig. 4.23. XRD analysis of debris generated during sliding of Al6061 against SAE52100 at 10N load at (a) 25°C and (b) 150°C



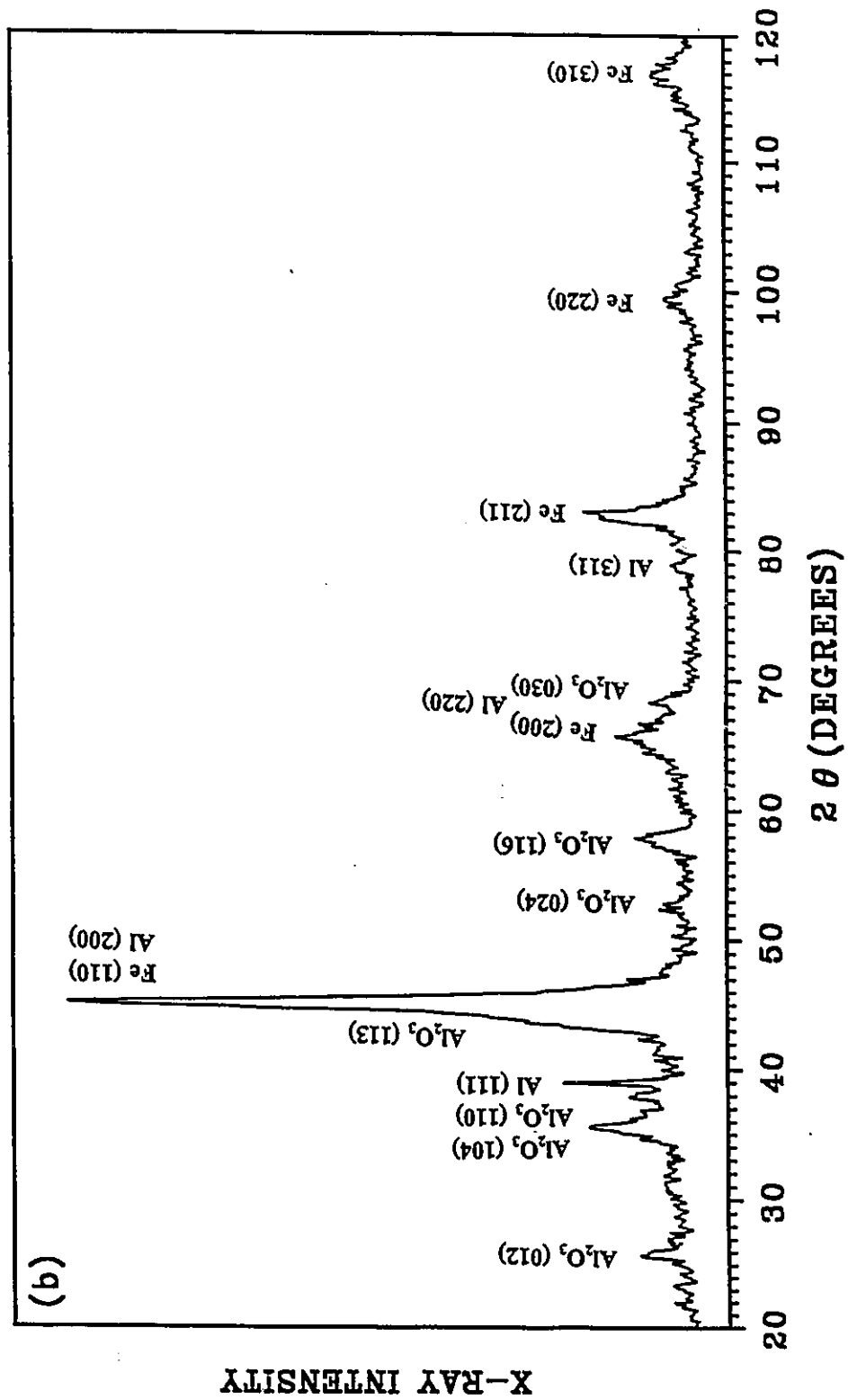


Fig. 4.23. Continued.

20%Al<sub>2</sub>O<sub>3</sub> were similar to those presented for the unreinforced alloy.

During severe at elevated temperatures, the debris consisted of only few large (mm size range) particles in the form of long arc shaped slivers. These particles could readily be identified as metallic aluminum pieces broken from the material extruded out of the contact area during sliding.

#### 4.9. Mechanical Behaviour

High temperature deformation behaviour of unreinforced Al6061 as well as Al6061-20%Al<sub>2</sub>O<sub>3</sub> alloy was studied through compression testing up to 500°C. Solid cylindrical specimen with height to diameter ratio of one were used for compression testing. Stress-strain plots for different test temperatures have been depicted in Fig. 4.24(a) and Fig. 4.24(b) respectively for the unreinforced and the reinforced 6061 alloy. True strain and true axial stress values during compression were calculated as:

$$\epsilon = \ln \frac{h_o}{h} \quad \dots\dots\dots (4.1)$$

$$\sigma = \frac{P}{A} = \frac{4P}{\pi d^2} = \frac{4Ph}{\pi d_o^2 h_o} \quad \dots\dots\dots (4.2)$$

where, P is the axial compression load, A is the instantaneous value of area of cross-section, h and d are the instantaneous values of the height and diameter during compression test while h<sub>o</sub> and d<sub>o</sub> are the original height and diameter of the compression specimen.

Fig. 4.24(a) shows curves for true plastic strain against true stress for the unreinforced alloy at different test temperatures. However, in the case of Al6061-20%Al<sub>2</sub>O<sub>3</sub>, the ceramic particles do not deform and the true plastic strain of the matrix,  $\epsilon_p^m$ , was corrected [80] as  $\epsilon_p^m = \epsilon_p^c / (1 - f_v)$ , where,  $\epsilon_p^c$  is the plastic strain in the composite and f<sub>v</sub> is the volume fraction of the reinforcing phase. Test temperatures are indicated

against each curve.

Several interesting observations can be made from these plots:

- 1) Both the alloys show high level of flow stress at lower temperatures. The flow stress at  $\epsilon=0.2$  is 435 MPa for Al6061 and 485 MPa for Al6061-20%Al<sub>2</sub>O<sub>3</sub>. At temperatures above 200°C the flow strengths of both alloys drop sharply.
- 2) The improvement in flow stress of the Al6061-20%Al<sub>2</sub>O<sub>3</sub> alloy over the unreinforced alloy (12% at room temperature) diminishes with increase in temperature and becomes negligible at temperatures above 230°C.
- 3) The initial work-hardening rate ( $d\sigma/d\epsilon$ ) of the Al6061-20%Al<sub>2</sub>O<sub>3</sub> is much higher than the Al6061 near yield point (low strains,  $<0.05$ ) but decreases to lower value than the unreinforced alloy at higher strains.
- 4) Both the alloys show work softening at higher temperatures.

The characteristics of room temperature flow curves of the two materials is compared in Fig. 4.25(a). The difference in flow stress is maximum at about 10% strain and is lower at both lower and higher strains. At the onset of yielding, the composite depicts much higher work-hardening rate,  $d\sigma/d\epsilon$ , (Fig. 4.25(b)) and therefore the flow curve of the composite rises more rapidly with strain than the unreinforced alloy. However, the composite work hardening rate decreases with strain faster the unreinforced alloy and thus the separation of the two curves decreases at high strains.

At temperatures above about 230°C both the materials show negative work hardening rates (work softening). Flow curves and the work-hardening rates of the two alloys are shown in Fig. 4.26. The work hardening rates of the composite are again higher at low strains and lower at higher strains as compared to the unreinforced alloy. Work

softening occurs in both the alloys. The work softening actually sets in at low strains typically below 5% plastic strain.

Flow stress of both the alloys at plastic strain of 1% and 20% is plotted against temperature in Fig. 4.27. Flow stresses of both the alloys decrease rapidly above 160°C. The flow stress of the composite, however, remains higher than the unreinforced alloy up to about 230°C. The difference in flow stress ( $\epsilon=0.2$ ) is about 50 MPa at room temperature, 35 MPa at 165°C but decreases to 10 MPa at 230°C and almost no difference at 400°C. The rate of decrease of flow stress ( $\epsilon=0.2$ ) with temperature has been plotted in Fig. 4.28. The maxima in the curves represent the temperature at which the flow stress falls most rapidly. These temperatures have been marked on the figure for both the alloys as  $T_d$ .  $T_d$  is 210°C for Al6061 and 235°C for Al6061-20%Al<sub>2</sub>O<sub>3</sub>.

The work hardening rates of both the alloys at two strain levels, 1% and 20% strain, are plotted in Fig. 4.29. Work hardening rates of these alloys drop sharply as the temperature is increased above room temperature. The work hardening rates become very low near the  $T_d$  temperature. Work softening occurs in both alloys at temperatures that exceed  $T_d$ .

Longitudinal cross-section of Al6061-20%Al<sub>2</sub>O<sub>3</sub> specimens tested in compression at room temperature and 200°C are given in Fig. 4.30. It was observed that all samples exhibited barrelling to a small extent at all temperatures due to frictional effects at the interface between specimen and the steel platens. Specimens tested at room temperature fractured at higher strains (above 50%) during compression. Particle damage appears to have occurred along the diagonals (45° to the compression axis) where maximum shear strains exist. The particle damage was not evident in the specimen tested at 200°C. The matrix strength decreased considerably at 200°C and the stress build up at the particles was not sufficient to fracture particles.

The particle fracturing is clearly evident in Fig. 4.31 in specimen compressed at

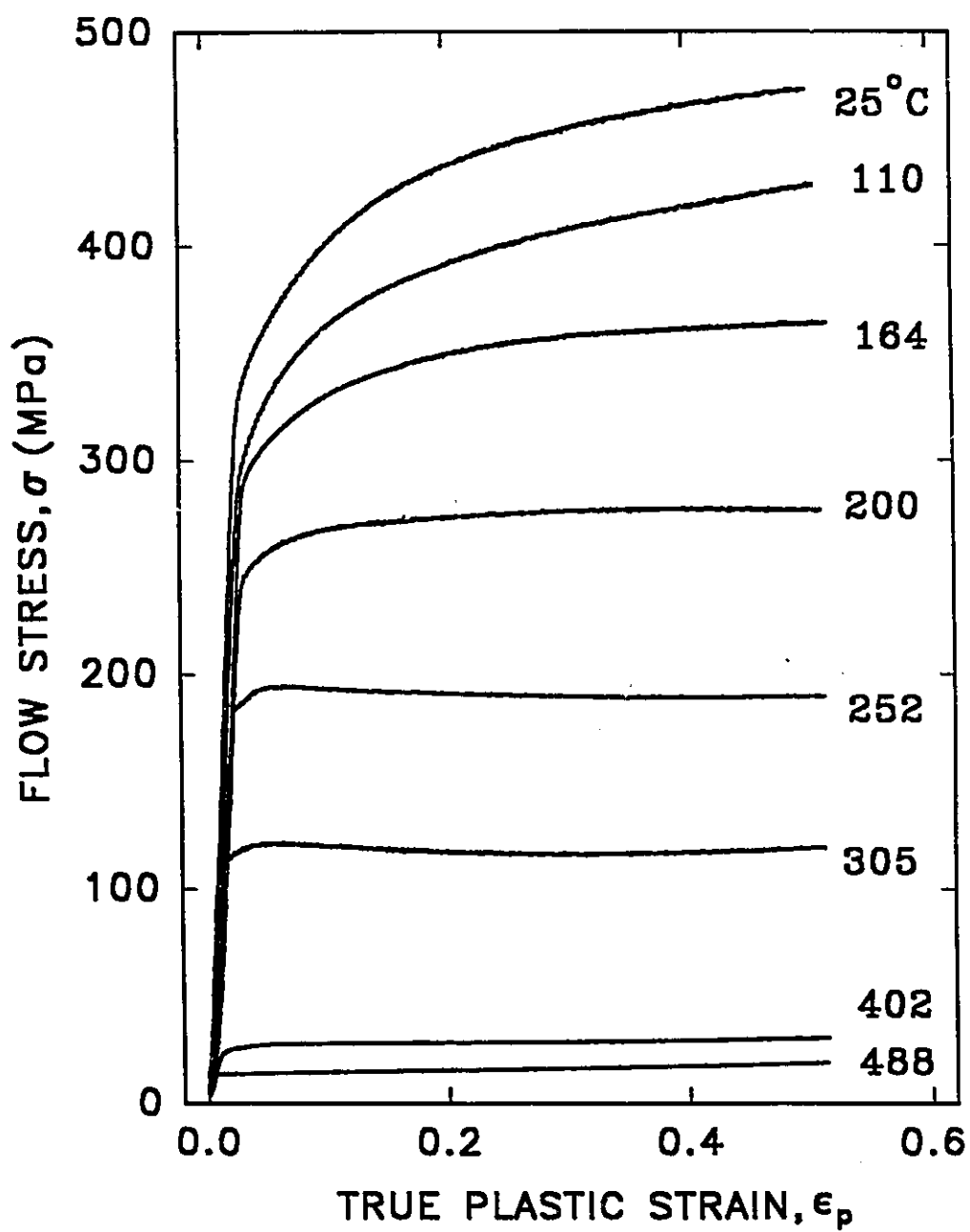


Fig. 4.24. Stress-strain plots for Al6061 (a), and Al6061-20%Al<sub>2</sub>O<sub>3</sub> (b) during compression at  $\dot{\epsilon} = 0.05 \text{ s}^{-1}$ . The test temperature is indicated against each curve.

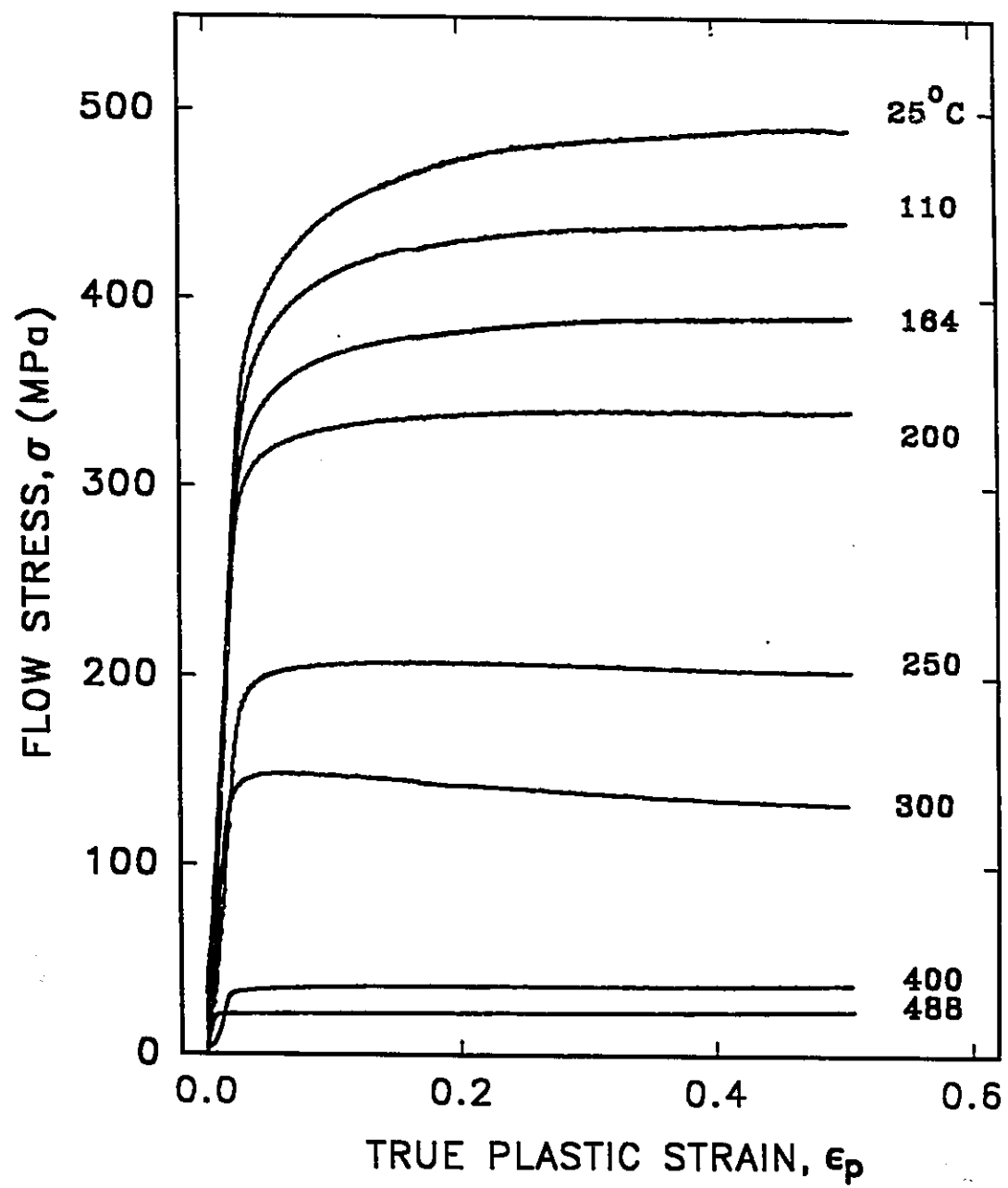


Fig. 4.24. Continued.

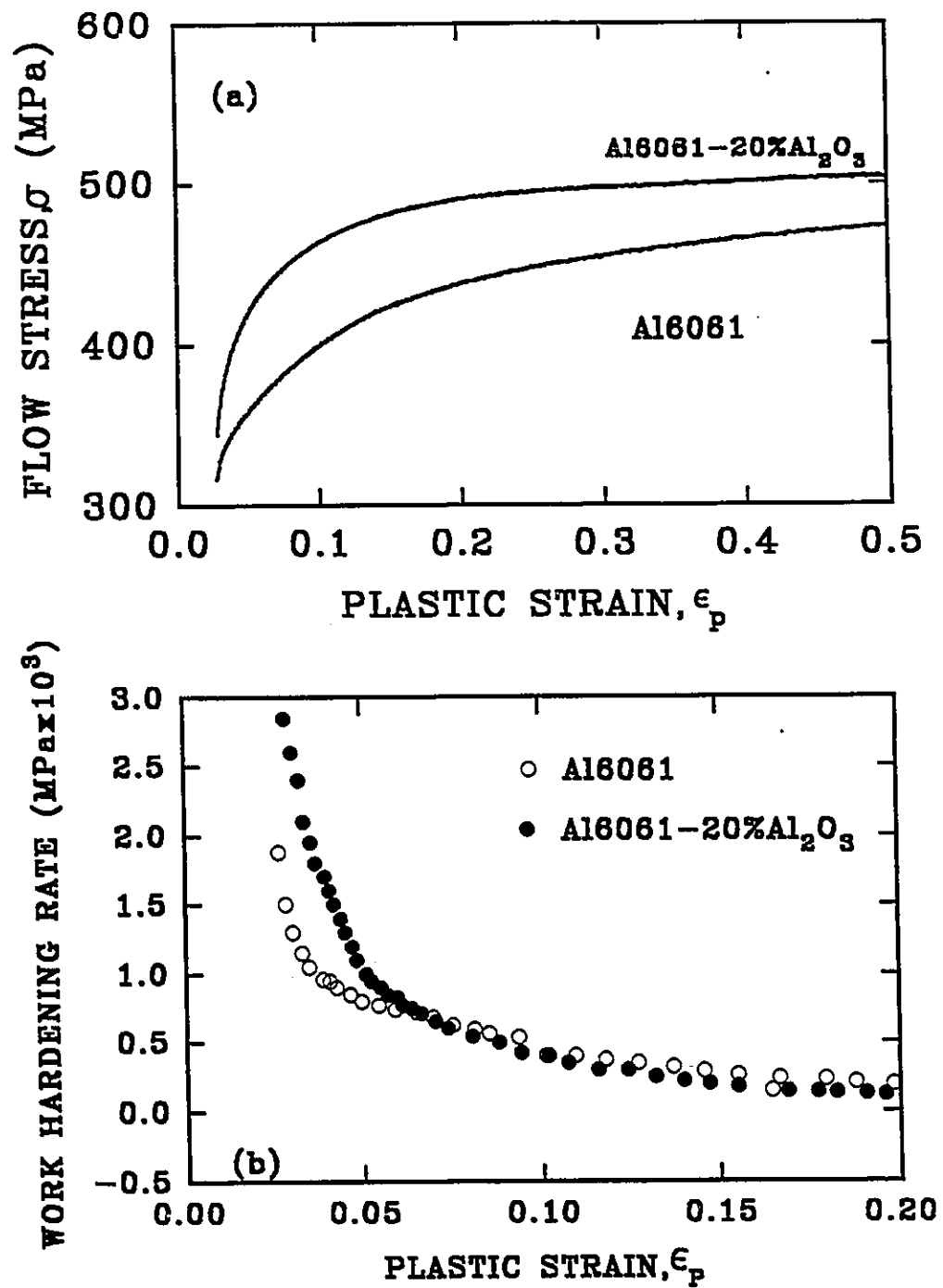


Fig. 4.25. Comparison of flow curves, (a) and work hardening rates (b) for Al6061 and Al6061-20%Al<sub>2</sub>O<sub>3</sub> during compression testing at room temperature.

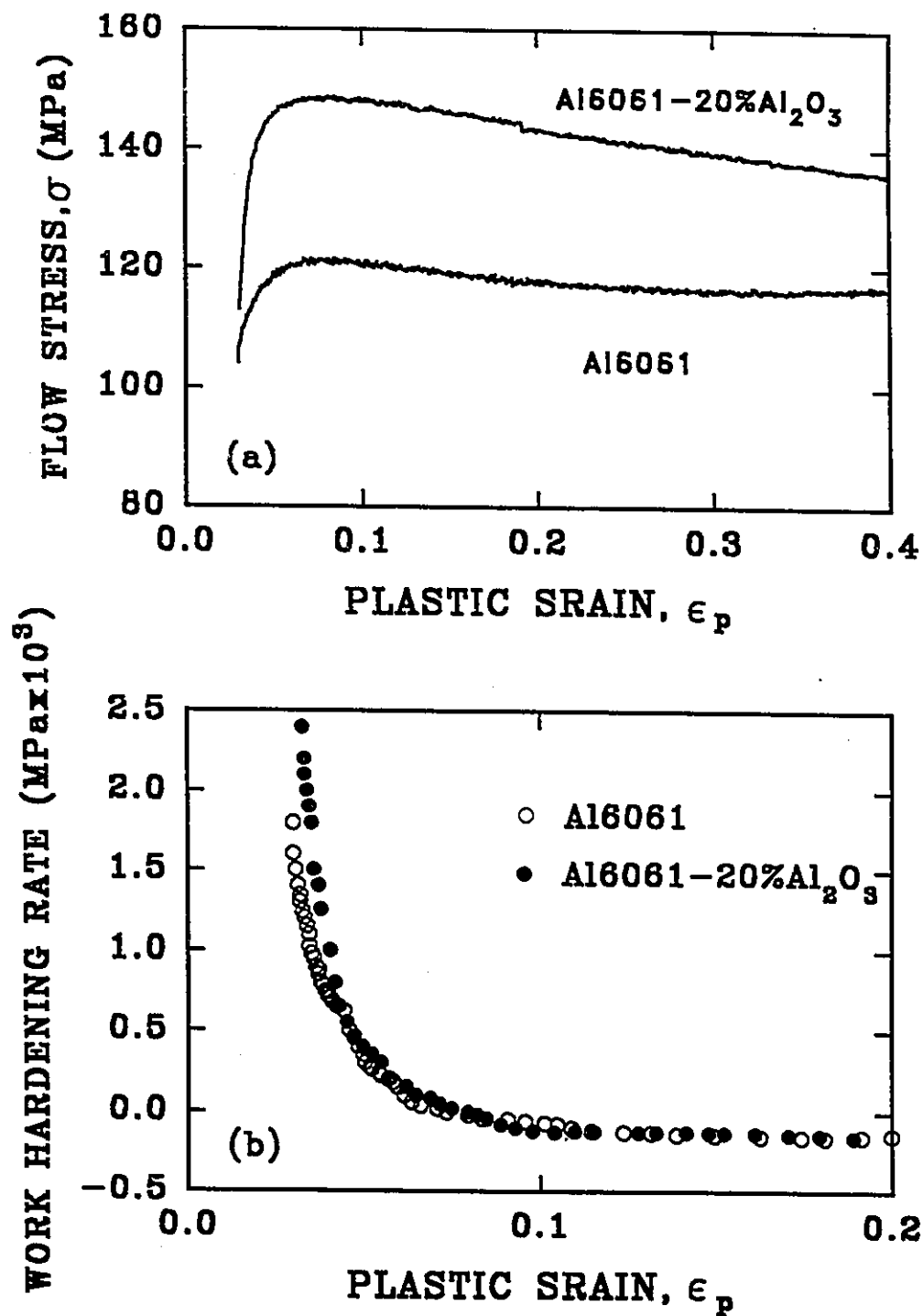


Fig. 4.26. Comparison of flow curves (a) and work hardening rates (b) for Al6061 and Al6061-20%Al<sub>2</sub>O<sub>3</sub> during compression testing at 300°C.



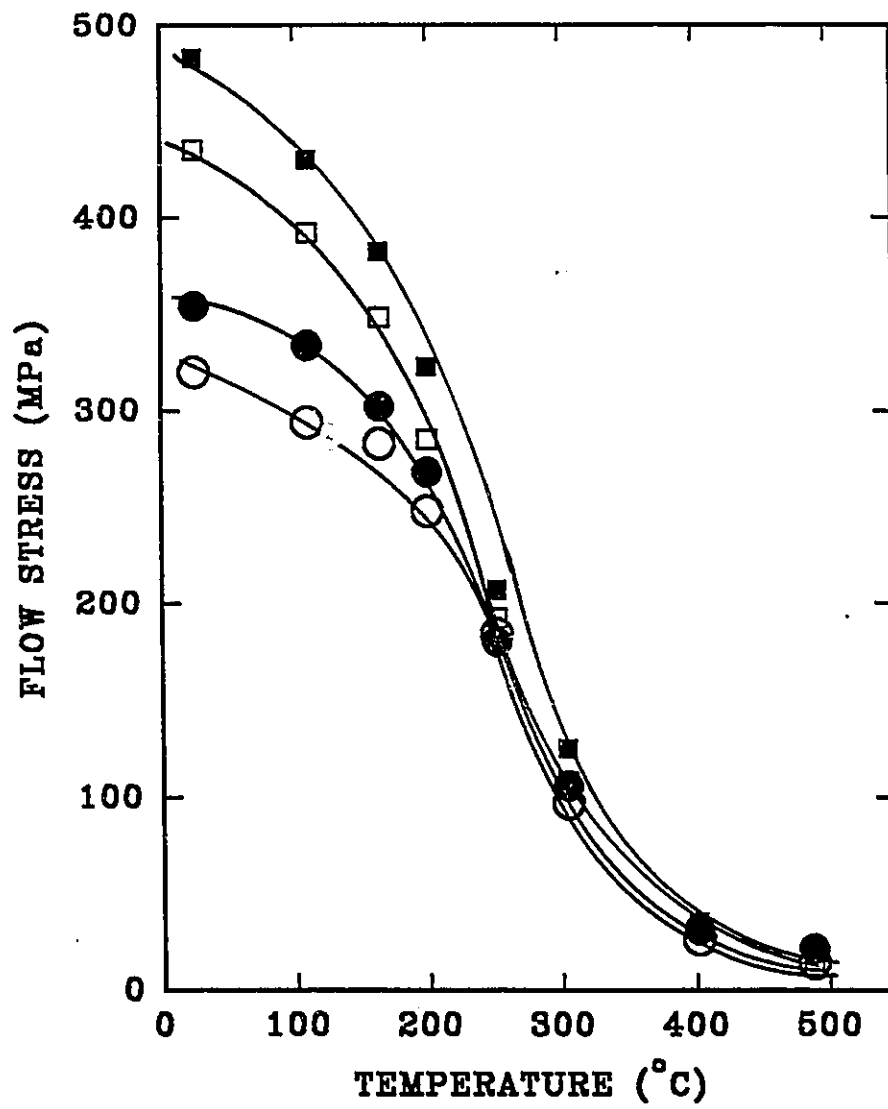


Fig. 4.27. Plots of flow strength of  
 Al6061 at  $\epsilon=0.01$  ( ○ ) and  $\epsilon=0.2$  ( □ );  
 Al6061-20%Al<sub>2</sub>O<sub>3</sub> at  $\epsilon=0.01$  ( ● ) and  $\epsilon=0.2$  ( ■ ).

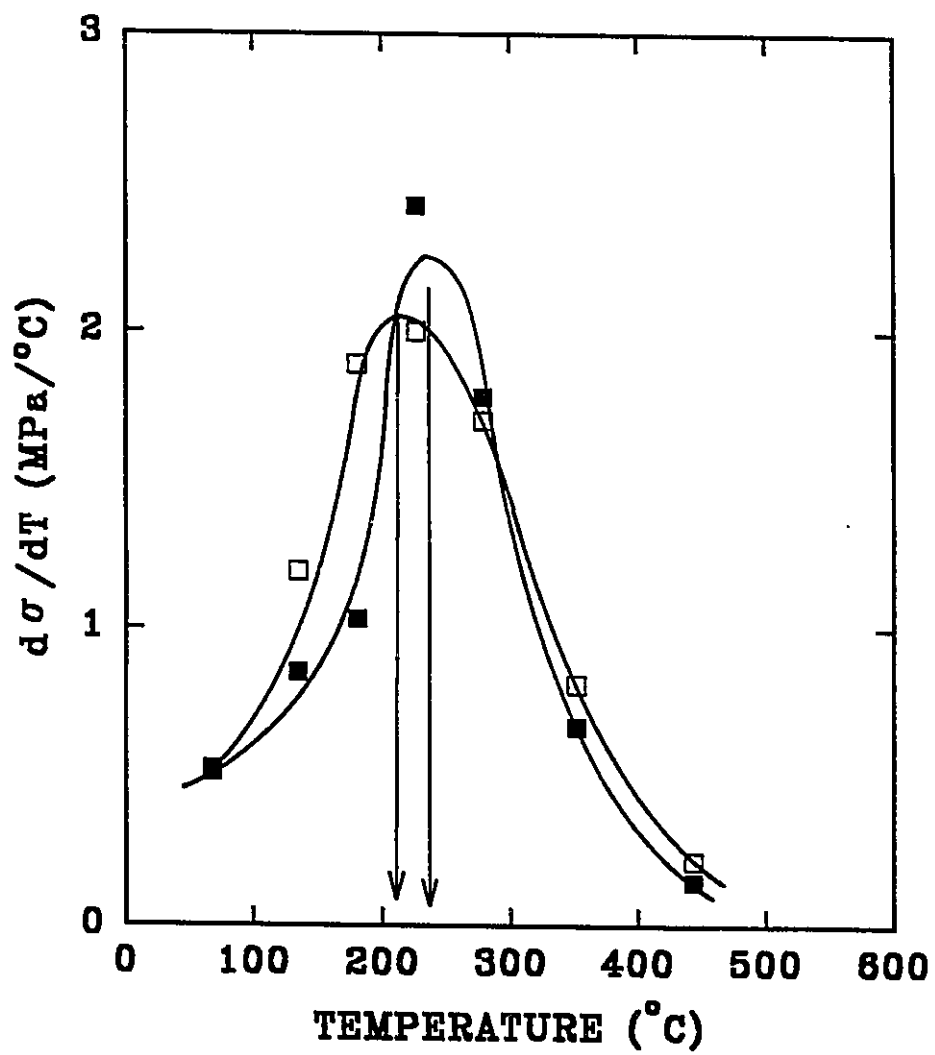


Fig. 4.28. Rate of decrease of flow strength  $\sigma$  vs temperature for Al6061 ( □ ) and Al6061-20%Al<sub>2</sub>O<sub>3</sub> ( ■ ). ( $\sigma$  = flow strength at  $\epsilon = 0.2$ )

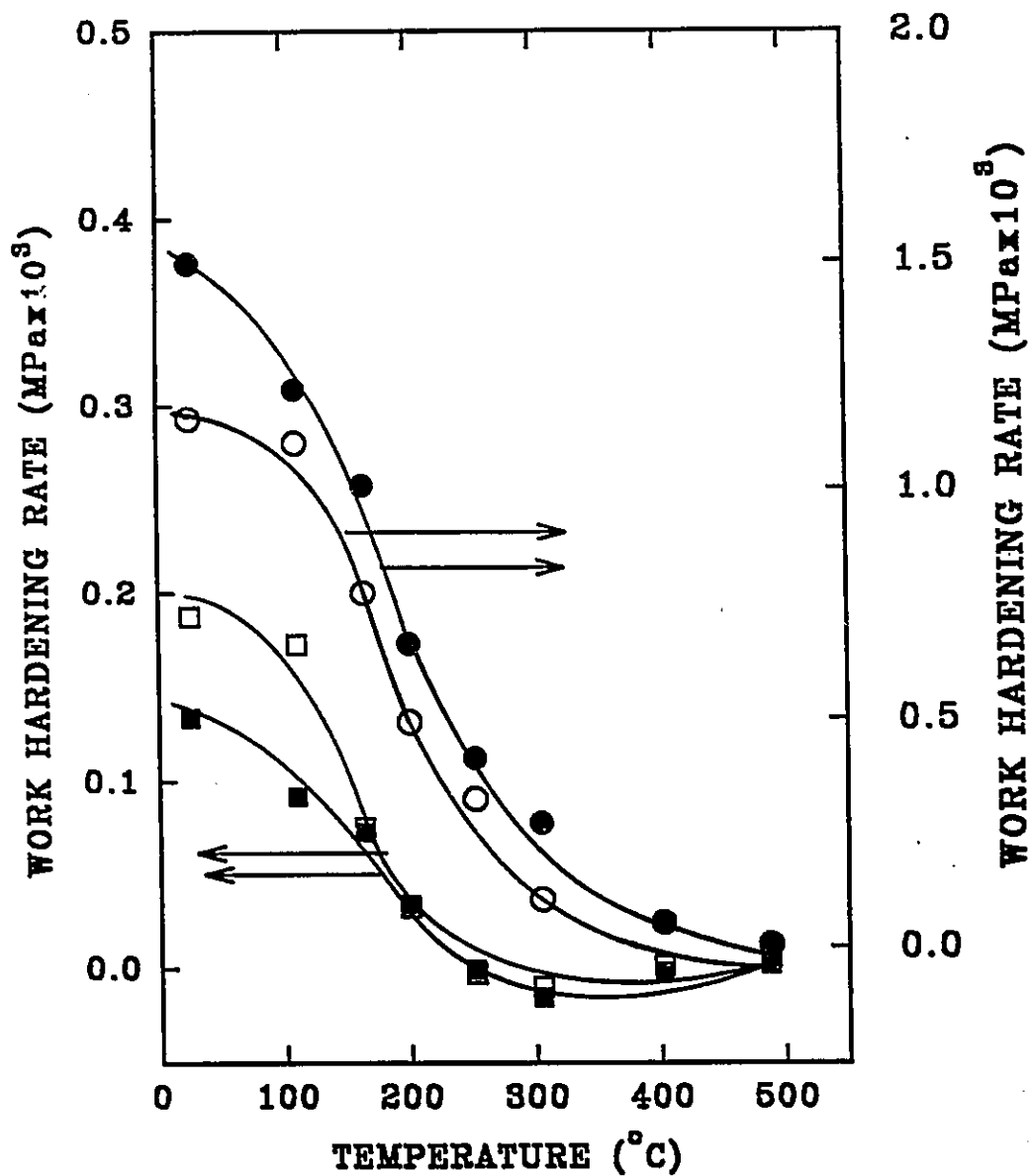


Fig. 4.29. Variation of work hardening rate with temperature for Al6061 at  $\epsilon=0.01$  (  $\bigcirc$  ) and  $\epsilon=0.2$  (  $\square$  ); Al6061-20%Al<sub>2</sub>O<sub>3</sub> at  $\epsilon=0.01$  (  $\bullet$  ) and  $\epsilon=0.2$  (  $\blacksquare$  ).

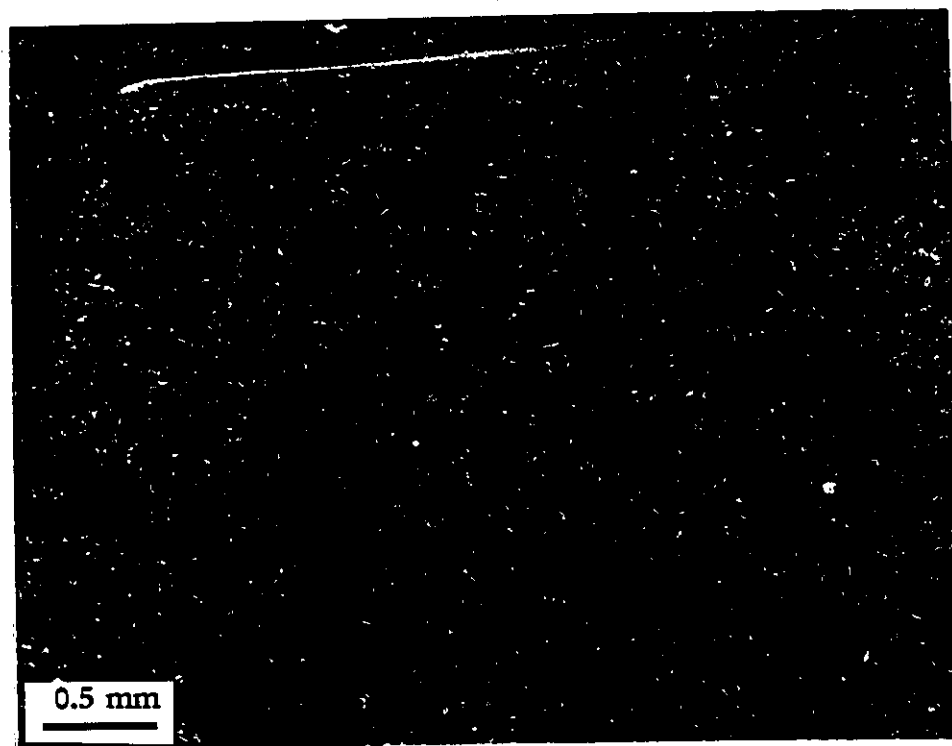


Fig. 4.30. Electron micrograph of longitudinal cross-section of Al6061-20%Al<sub>2</sub>O<sub>3</sub> specimen compressed to 50% engineering strain at room temperature.  $\dot{\epsilon} = 0.05 \text{ s}^{-1}$ .

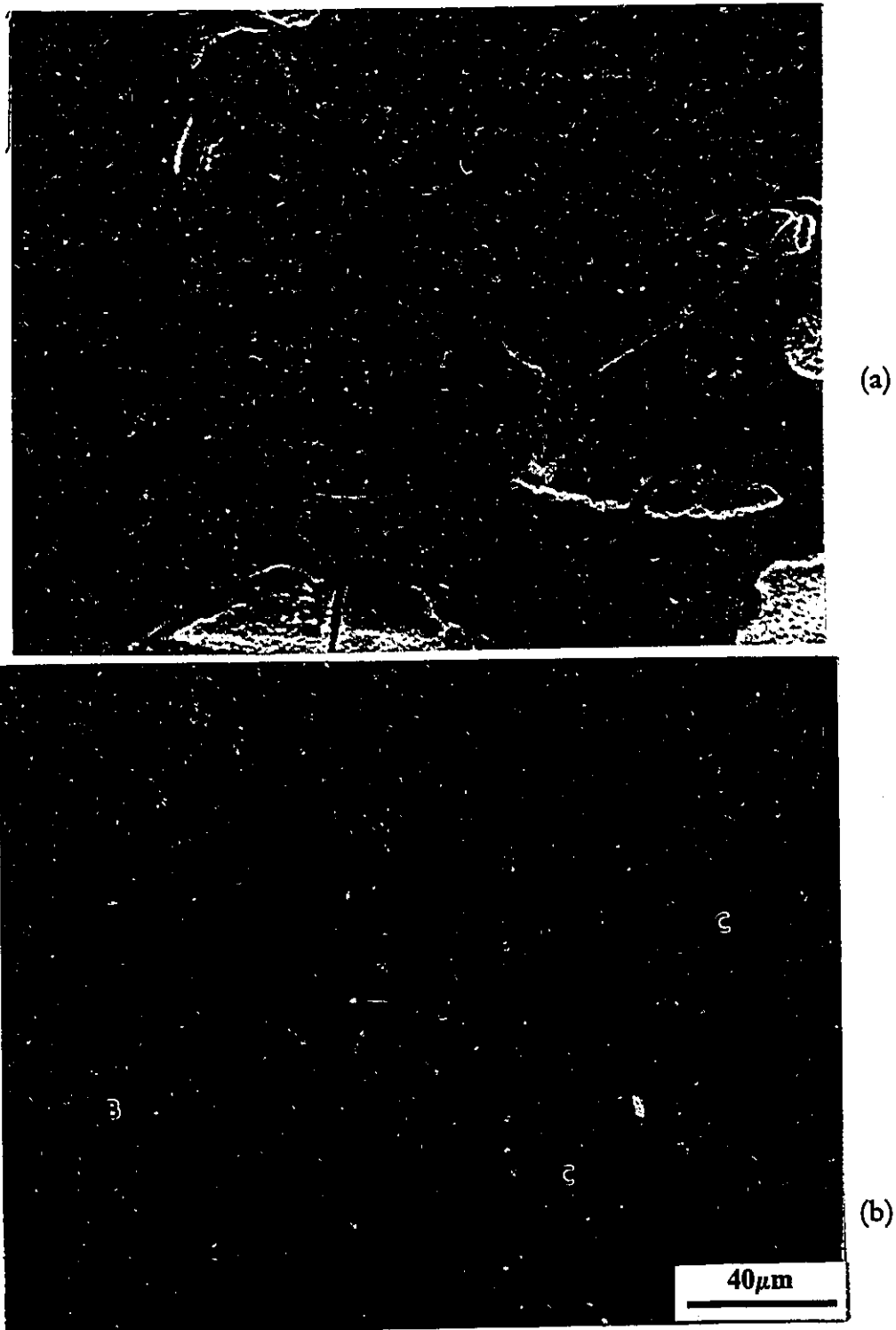


Fig. 4.31. (a) and (b) electron micrograph and (c) optical micrograph of cross-section of Al6061-20%Al<sub>2</sub>O<sub>3</sub> specimen compressed at room temperature to 50% engineering strain depicting particle damage.

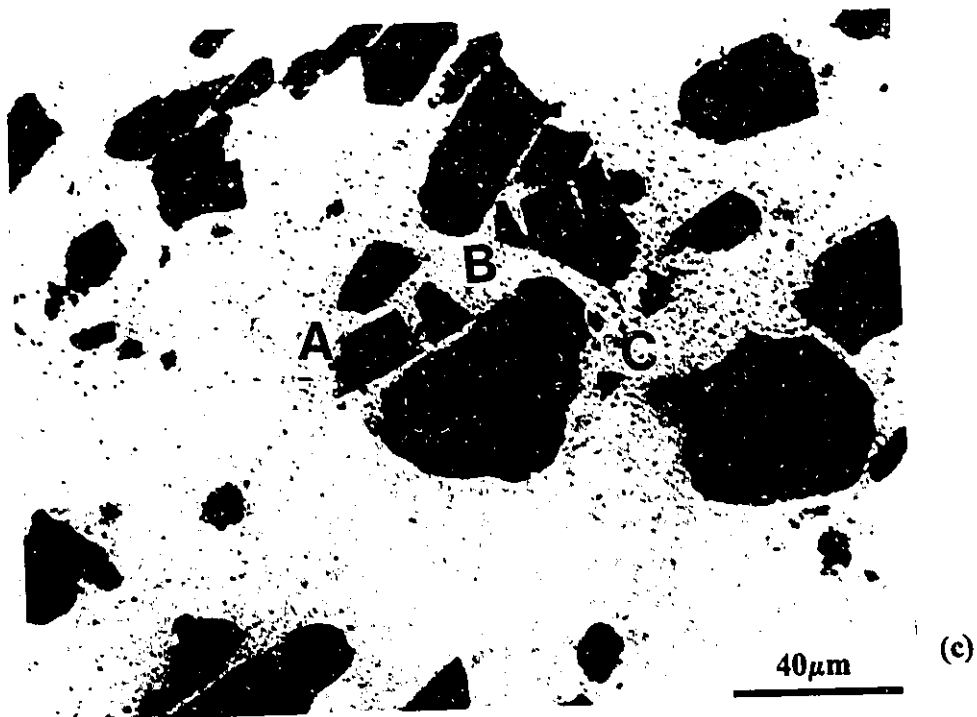


Fig. 4.31. Continued.

room temperature. Fragments from the broken particles were redistributed in the matrix. Three important observations have been highlighted on the micrographs:

- (A) Large particles and particles with large aspect ratios fracture more easily.
- (B) The broken parts move apart while the matrix moves in to fill the gap without leaving a crack (healing).
- (C) Fragmentation of large particles results in production of fine particles (comminution).

#### 4.10. Summary of the Results

The salient observations pertaining to elevated temperature sliding wear of Al6061 and Al6061-20%Al<sub>2</sub>O<sub>3</sub> at 10N load are presented in Table 4.2. In summary, the results indicate: Al6061 showed mild to severe wear transition on increasing the test temperature above 150°C. The transition temperature for the Al6061-20%Al<sub>2</sub>O<sub>3</sub> alloy was found to be 230°C but decreased to 200°C on increasing the load to 50N. In the mild wear regime, the wear rates of Al6061 decreased with an increase in sliding temperature and showed wear rates lower than the Al6061-20%Al<sub>2</sub>O<sub>3</sub> alloy. Wear rates of both the alloys increased rapidly once the temperature is raised beyond the transition temperature with reinforced alloy showing better wear resistance than the unreinforced alloy.

Wear rates measured from weight loss were similar to those obtained from specimen height change measurements in the mild wear regime. However, the wear rates from weight loss measurements, showed large decrease, a weight loss "well", at temperatures near the transition temperature.

Mild to severe wear transition was also observed on increasing the load at any given temperature for the Al6061-20%Al<sub>2</sub>O<sub>3</sub> alloy. The transition load decreased with increase in the sliding temperature. The transition loads are 350N, 200N and 50N for

sliding temperature of 25°C , 150°C and 200°C respectively. The wear rates decreased slightly just before the transition.

Al6061 surfaces were found to be covered with "protective" iron oxide layers during mild wear at low temperatures and helped to reduce wear rates and the coefficient of friction. Large plastic strains were evident near the contact surface of the specimens worn in the severe wear regime. The specimen worn at 350°C indicated that recrystallization occurred during the sliding process.

In the case of Al6061-20%Al<sub>2</sub>O<sub>3</sub> alloy, large plastic strains lead to formation of a hardened layer near the contact surface containing very fine distribution of severely fragmented hard particles thus improving the wear resistance of the composite at elevated temperatures.

Compression tests indicated large drop in flow strength and loss of work-hardening rates of both Al6061 and Al6061-20%Al<sub>2</sub>O<sub>3</sub> at temperatures above 150°C. Both alloys showed work-softening above 200°C.



**Table 4.2. Summary of observations on the high temperature sliding wear of Al6061 and Al6061-20%Al<sub>2</sub>O<sub>3</sub>.**

| <u>(a) Al6061</u>                             |  |  |
|---|--|--|
|   | Mild Wear  | Severe Wear  |
| Temperature range                             | 25-150°C (at 10N)  | >150°C (at 10N)  |
| Wear Rates (mm <sup>3</sup> m <sup>-1</sup> ) |  |  |
| Specimen                                      | 2x10 <sup>-3</sup> -4x10 <sup>-3</sup><br>Decrease slightly  | 1x10 <sup>-2</sup> -3x10 <sup>-1</sup><br>Rapid increase                             |
| Counterface                                   | Weight Loss  | Weight Gain  |
| Coefficient of friction (μ)                   | Decrease<br>0.5 (room temperature)-<br>0.35 (150°C)  | Increase<br>0.5-2.0  |
| Debris  | Mixed fine black powder<br>Metallic (Al and Fe)<br>Oxidized (Al <sub>2</sub> O <sub>3</sub> and Fe <sub>2</sub> O <sub>3</sub> ) | Large metallic<br>slivers of Al  |
| Worn Surfaces:<br>Specimen                    | Rough<br>Transfer layer<br>containing debris particles   | Smooth, uneven<br>No Fe transfer<br>Material extrusion<br>out of contact area        |
| Counterface                                   | Smooth<br>No aluminum transfer   | Uneven<br>Large scale Al transfer  |
| Subsurface                                    | Localized plastic deformation<br>within 10-20 μm depth   | Gross plastic deformation<br>Fine recrystallized grains<br>Dynamic recrystallization |

**Table 4.2. Continued.**

| <u>(b) Al6061-20%Al<sub>2</sub>O<sub>3</sub></u> |   |   |
|--|---|---|
|  | Mild Wear   | Severe Wear   |
| Temperature range                                | 25-250°C (at 10N)   | >250°C (at 10N)   |
| Wear Rates (mm <sup>3</sup> m <sup>-1</sup> )    |   |   |
| Specimen   | ≈5x10 <sup>-3</sup>   | 5x10 <sup>-2</sup> -2x10 <sup>-1</sup><br>Rapid increase  |
| Counteface                                       | Weight Loss   | Weight Gain   |
| Coefficient of friction (μ)                      | about 0.5   | 0.5-2.0   |
| Debris   | Mixed fine black powder<br>Metalic (Al and Fe)<br>Oxidized (Al <sub>2</sub> O <sub>3</sub> and Fe <sub>2</sub> O <sub>3</sub> ) | Large metallic<br>slivers of Al<br>and Al <sub>2</sub> O <sub>3</sub>   |
| Worn Surfaces<br>Specimen                        | Black<br>Transfer layer<br>containing debris particles  | Uneven<br>No Fe transfer<br>Extrusion of material<br>out of contact area  |
| Counterface                                      | Flat, smooth<br>No aluminum transfer  | Uneven<br>Large scale Al transfer   |
| Subsurface                                       | Little plastic deformation<br>Fine cracks near the contact<br>surface   | Gross plastic deformation<br>Hardened layers containing<br>communitied Al <sub>2</sub> O <sub>3</sub> particle. |

## B. DISCUSSION OF THE RESULTS

Both Al6061 and Al6061-20%Al<sub>2</sub>O<sub>3</sub> show transition from mild wear to severe wear on increasing either the test temperature or the applied normal load. During mild wear, material loss occurs through generation and removal of discrete debris particles. The wear rates are measured through two different techniques viz. the specimen height change and the specimen weight loss. Both techniques yield similar values for the wear rates near room temperature. Near the transition temperature, however, the wear rates obtained from height change are appreciably higher than those obtained from weight loss measurements. This is because the wear rates obtained from weight loss show a "well" prior to transition to severe wear. Near the transition temperature the wear rates drop sharply by more than an order of magnitude. Thus there is clearly a change in mechanism for wear at the transition temperature from the one in which the material loss is in the form of loose debris particles detached from the surface to the one in which generation of debris is essentially suppressed, and, wear is caused by extrusion of the subsurface material and material transfer to the counterface surface.

Severe wear results in a large reduction in the specimen height due to plastic flow (extrusion) of the material out of the contact area. The extruded material does not separate physically from the test specimen (Figs. 4.18 and 4.19). However, at high temperatures, well into the severe wear, the weight loss increases again due to gross material transfer to the counterface and breaking of the edges of the extruded material at large sliding distances resulting in removal of big metallic slivers.

Load and sliding speed dependent mild to severe wear transitions in aluminum alloys and aluminum matrix composites have been reported by Alpas and Zhang [64,65] and Wang and Rack [66]. Alpas and Zhang [64,65] have indicated that the transition occurs when the sliding surfaces reach a critical temperature under increased frictional heating generated by increasing the applied load. There are other ways to increase the temperature of the sliding surfaces beside increase in the applied load: for example,

increase in sliding speed thus increasing the rate of friction heating or by lowering the thermal conductivity of the counterface which decreases the rate of dissipation of frictional heat.

Martinez et al. [8] have reported temperature driven mild to severe wear transition during reciprocating sliding of a high silicon aluminum alloy (containing large silicon particles) as well as a Al-7Si-SiC composite. They have used load of 25N and obtained a transition temperature of 110°C for the Al-20Si alloy and 150°C for the reinforced alloy. Lower transition temperatures reported by these authors could be due to higher loads (or pressure) used in their investigation. However, direct comparison is difficult due to a different wear set up employed in the present study.

Temperature dependent transition from mild to severe wear is evident in both Al6061 and Al6061-20%Al<sub>2</sub>O<sub>3</sub> in Fig. 4.2. The transition temperature depends on the applied load and decreases with increase in load applied. The mild to severe wear transition, for given sliding temperature, can also be affected through increase in applied load (Figs. 4.4 and 4.5). Increase in ambient temperature lowers the critical load at which the transition occurred.

The severe wear of these materials can be related to their deformation behaviour at elevated temperatures, e.g., decrease in flow stress and work hardening rates. In this section an attempt has been made to model severe wear as a thermally activated deformation process. The effect of temperature on the wear of both the alloys is further discussed in terms of formation of surface layers and subsurface microstructural changes during sliding.

#### 4.11. Role of Plastic Deformation During Severe Wear

The onset of severe wear at elevated temperatures in case of both unreinforced as well as reinforced alloy was accompanied by gross plastic deformation in the subsurface

(Figs. 4.17-4.20) and large scale material transfer to the counterface surface (Fig. 4.14). The specimen wear took place by the displacement of the material out of the contact area as seen in Fig. 4.18, in a way similar to the hot extrusion of metals. The flow stress of the material is thus expected to have important influence on the severe wear of aluminum alloys.

The coefficient of friction during severe wear remains high (Fig. 4.15). The subsurface material during high temperature wear is subjected to shear stresses due to frictional drag in addition to the normal compression load. The softer the material near the contact region becomes, the easier it will be to displace it out and hence the wear rates will increase with temperature. The hardness or the flow strength of the material near the surface is thus expected to play important role during severe wear process.

At and near ambient temperatures the composite has significantly higher flow strength in comparison to the unreinforced alloy (Fig. 4.5 ). Higher composite strength can be attributed to higher dislocation density due to difference in CTE (coefficient of thermal expansion), higher work hardening rate as well as to the geometrical constraint of the hard rigid particles during plastic flow [20,21].

As the test temperature increases the matrix flow strength decreases, initially due to loss of precipitation strengthening, and then, large increase in the rate of dynamic recovery in aluminum alloys which is expected to take place at relatively low temperatures,  $T/T_m=0.4$  [22]. The geometrical constraint offered by the reinforcement itself depends upon the matrix strength [20] and decreases significantly with matrix softening. The work hardening rates of both the alloys decreased rapidly when the temperature exceeds 160°C. With increase in temperature, therefore, the difference in the flow strength of the reinforced and the unreinforced alloy decreases.

The transition temperature for Al6061 is 150°C which coincides well with the observation that flow stress and the work hardening rate of the alloy drops sharply above

150°C. However, the transition temperature for the composite was found to be considerably higher (230°C). Firstly, the flow stress of the composite remains higher than the unreinforced alloy up to 230°C. Secondly, particle comminution during sliding results in formation of hardened layers at the surface. This process of particles fracturing and redistribution of particles near the contact surface increases the local hardness of the material adjacent to the contact surface. This results in a virtual work hardening which discourages the transfer process and delays the onset of severe wear.

The material factors which effect the transition temperature ( $T_c$ ), for mild to severe wear transition, for given set of experimental sliding conditions (applied load, sliding speed, sliding geometry etc.) can be summarized as:

- (i) flow stress of the material at the test temperature,
- (ii) work hardening rate of the alloy,
- (iii) Surface conditions, e.g., oxidation of the specimen or counterface steel surface (lowers adhesion, increases  $T_c$ ),
- (iv) the formation of transfer layers on the sliding surfaces.

Fig. 4.32 shows the plots of flow strength at plastic strain of 20% ( $\epsilon_p=0.2$ ) of both unreinforced as well as the composite against the temperature of compression testing. The wear rates of both the alloys have also been plotted for comparison. The flow strength of the unreinforced alloy is maintained at high levels only up to about 160°C. At the same time, the alloy shows good wear resistance in this temperature range. Above this temperature the flow strength drops rapidly. The alloy flow strength is about 350MPa at 160°C (80 % of the room temperature strength) and 110MPa (25% of the room temperature strength) at 300°C. The wear rates of the unreinforced alloy, on the other hand, increase sharply in this temperature range. The wear rates are 3000% higher at

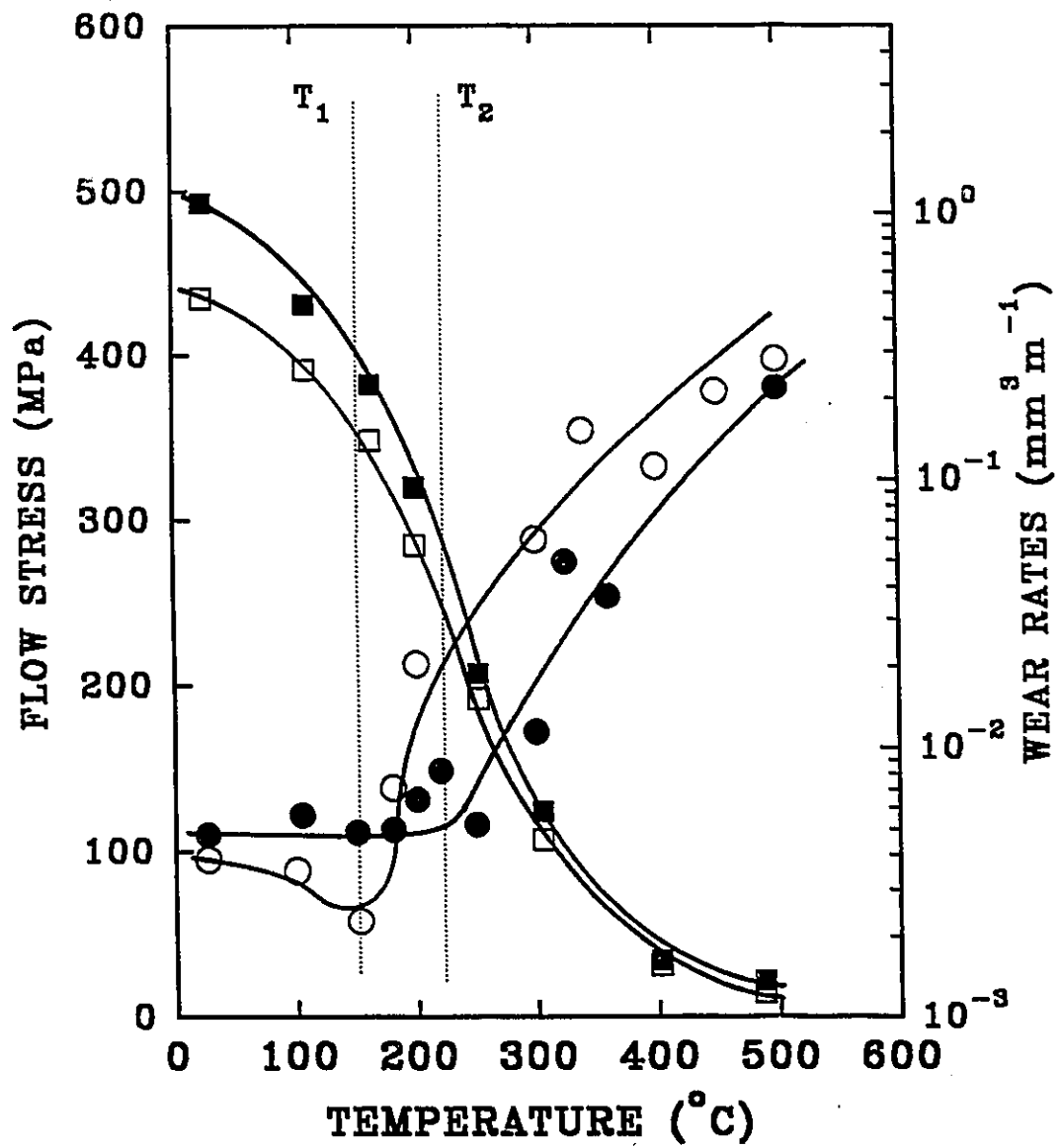


Fig. 4.32. Flow strength of Al5061 ( □ ) and Al5061-20%Al<sub>2</sub>O<sub>3</sub> ( ■ ) at  $\epsilon = 0.2$  plotted against temperature. Wear rates at 10 N load for Al5061 ( ○ ) and Al5061-20%Al<sub>2</sub>O<sub>3</sub> ( ● ) are shown for comparison. Wear rates obtained from specimen height change measurements.

300°C as compared to those at 150°C. The composite depicts a similar correlation between the flow strength and the wear rates. However, the transition to severe wear in the composite is delayed to higher temperature and, therefore, to lower level of bulk flow strength.

Work hardening behaviour of the two materials is different at low temperatures. Work hardening rate of composite is very high at low strains but decreases at large strains (>10% true strain). The unreinforced Al6061 shows high work hardening rates up to high strain levels. The work hardening rates of both the alloys decrease significantly with temperature at temperatures above 150°C and exhibit work softening above 230°C. Work hardening rate can strongly influence the depth of plastic zone and the microstructure developed below the contact surface as well as the material transfer to the counterface during sliding.

At low temperatures, work hardening increases the flow stress of the material near the contact surface, and the shear stresses are better transferred to the material below. The strain gradient is less steep below the contact surface. However, due to high flow stress, the depth of the plastic zone is limited. This can lead to strain localization or shear band formation at a certain distance below the contact surface [102]. This leads to crack nucleation at the structural discontinuities such as second phase precipitates or ceramic particles in case of the composite alloy. The depth of these bands has been found to be small and same as that of material transferred to the counterface [45-47] and can be related to the microstructural features of debris particles.

At elevated temperatures, the work hardening rates of the aluminum alloys are low. The material near the contact surface remains soft and experiences much higher strains than the material below yielding very steep strain gradients. Very high strain rates in this region and high temperature can lead to dynamic recrystallization which can result in total loss of work hardening and even work softening (Fig. 4.26). These conditions are ideal for gross extrusion of the material out of the contact area.



#### 4.12. A Phenomenological Model of Severe Wear

The preceding discussion make it clear that the wear of Al6061 and Al6061-20%Al<sub>2</sub>O<sub>3</sub> at elevated temperature is dominated by plastic deformation process. The wear of both the alloys occur through extrusion of the specimen material. At these temperatures, thermally activated deformation processes are expected to control the flow behaviour of both the alloys. Both the flow strength and the work hardening rates of the material near the contact surface will become time dependent properties. Thus the plastic flow controlled severe wear can be modelled as a hot deformation process. Both, hot deformation and high temperature severe wear involves high plastic strains at high strain rates. The relevant equation [101] which relates the strain rate ( $\dot{\epsilon}$ ), temperature (T) and the stress ( $\sigma$ ) is,

$$\dot{\epsilon} = B(\sinh \alpha \sigma)^{n'} \exp\left(-\frac{Q}{RT}\right) \dots\dots\dots (4.3)$$

where, B,  $\alpha$  and  $n'$  are constants, Q is the activation energy for hot deformation of the material, R is gas constant and T is the absolute temperature in °K. This equation is known [101] to give most satisfactory fit for the experimental data for hot deformation of metals at high strain rates and is therefore relevant to modelling of severe wear.

The strain rate ( $\dot{\epsilon}$ ) in equation (4.3) can be related to the volumetric wear rate ( $\dot{w}$ ) as follows:

The volumetric wear rates ( $\dot{w}$ ) during high temperature tests were measured from the rate of reduction in specimen height as,

$$\dot{w} = \frac{dw}{ds} = \frac{A dh}{ds} = \frac{A dh}{v dt} \dots\dots\dots (4.4)$$

where,  $w$  is the volumetric wear corrected for the counterface effect,  $s$  is the sliding distance,  $A$  is the contact area,  $v$  is sliding speed,  $dh$  is reduction in sample height at any time in a small interval of time  $dt$ .

The plastic flow of the test material during sliding occurs only in a narrow zone with depth,  $h_o$ , (about 400  $\mu\text{m}$ ) below the contact surface. Although, during sliding, the apparent area of the sliding surfaces increase (Fig. 4.14.), the material displaced out of the contact area do not support load. Therefore, the stress acting on the sliding surfaces remain constant during the wear run. Thus, during steady state sliding, the value of  $h_o$  is independent of sliding distance. During sliding, this zone deforms at a constant deformation rate of  $dh/dt$ , so that the strain rate experienced by this zone ( $\dot{\epsilon}$ ), is constant and can be written as,

$$\dot{\epsilon} = \frac{1}{h_o} \frac{dh}{dt} \quad \text{.....} \quad (4.5)$$

Combining equations (4.4) and (4.5),

$$\dot{w} = \frac{A h_o}{v} \dot{\epsilon} \quad \text{.....} \quad (4.6)$$

or, 
$$\dot{w} = k \dot{\epsilon} \quad \text{.....} \quad (4.7)$$

where,  $k (=A h_o/v)$  is a constant.

Thus, equation (4.3) can be re-written for the plastic deformation controlled wear as,

$$\dot{w} = B' (\sinh \alpha \sigma)^{n'} \exp\left(-\frac{Q}{RT}\right) \quad (4.8)$$

According to equation (4.8), the log-log plot of wear rates ( $\dot{w}$ ) vs reciprocal of absolute

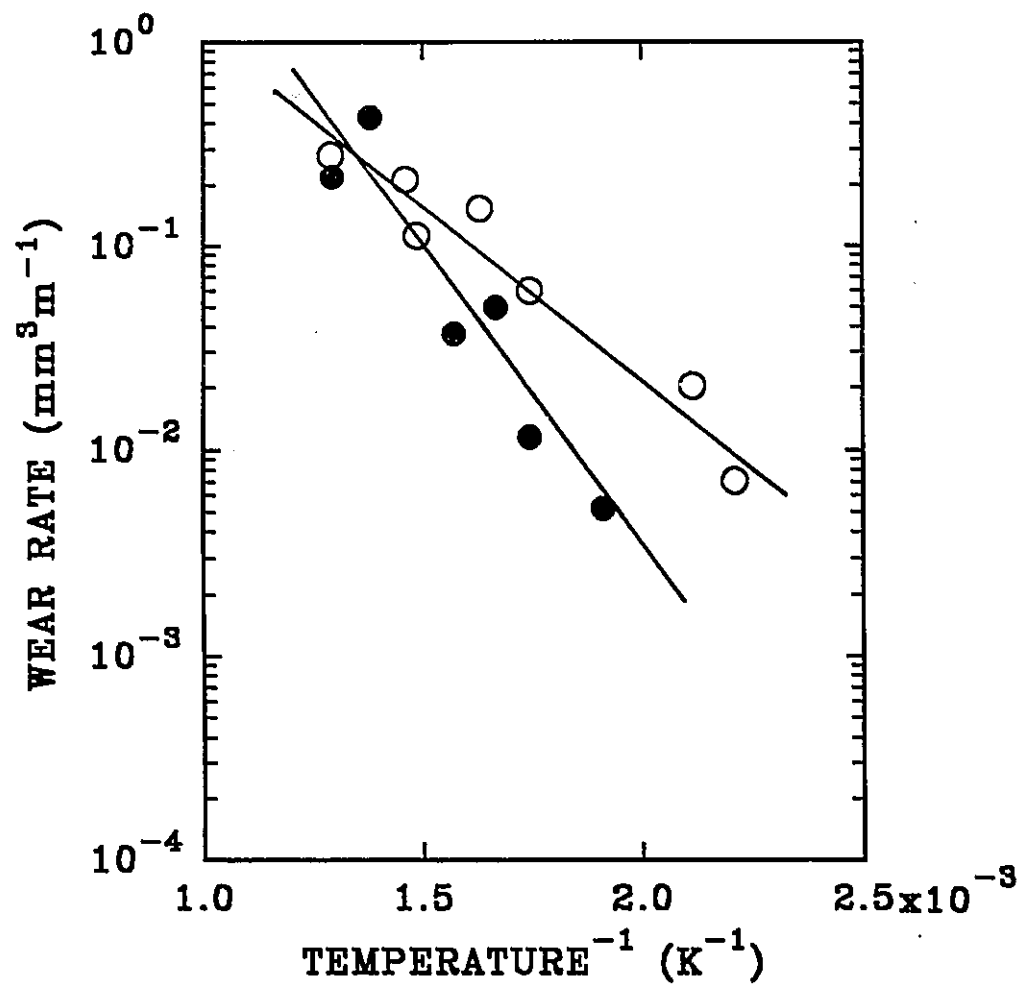


Fig. 4.33. Wear rates vs  $1/T$  plots for Al6061( ○ ) and Al6061-20%Al<sub>2</sub>O<sub>3</sub> ( ● ). The wear rates obtained from specimen hight change measurements at 10N load.

temperature ( $1/T$ ) should yield a straight line from which activation energy for the plastic deformation during high temperature wear can be obtained.

The wear rates of Al6061 and Al6061-20%Al<sub>2</sub>O<sub>3</sub> at  $\sigma = 0.24$ MPa which correspond to 10N (Fig. 4.2), have been plotted on log scale against  $1/T$  in Fig. 4.33. The high temperature wear data easily fits into a straight line. The slope of this line represents the value for  $Q/R$  from which activation energy,  $Q$ , for the deformation during wear can be obtained.

The wear data of Al6061-20%Al<sub>2</sub>O<sub>3</sub> at 10N ( $\sigma = 0.24$  MPa) in the temperature range 300°C to 500°C yields an activation energy of 60 kJ mole<sup>-1</sup>. On the other hand, at the same applied stress, Al6061 data in the temperature range 200°C to 500°C gives a best fit for a smaller activation energy of 34 kJ mole<sup>-1</sup>. Higher activation energy for the composite implies higher difficulty to plastic flow controlled wear at low temperatures. Higher temperatures will be required in the case of the composite to attain the same strain rates, and therefore, the same wear rates as unreinforced Al6061 alloy.

The activation energies determined for the two materials above are, however, significantly lower than those determined from hot deformation studies employing compression tests or torsion tests [101] which give the activation energies in the range of 120 kJ mole<sup>-1</sup> to 200 kJ mole<sup>-1</sup>. The deformation during sliding wear is clearly more complex than encountered during uniaxial compression or simple shear in torsion tests. The plastic deformation in sliding occurs under the tangential friction force with superimposed normal load. The value of the tangential force depends upon the surface conditions and varies with sliding distance (Fig. 4.8) and temperature (Fig. 4.9).

#### 4.12. Changes in Subsurface Microstructure and Mechanical Properties During Severe Wear

The phenomenological model can explain wear-deformation relationship up to a certain point. Microstructural analyses is required to rationalize wear processes at high temperatures.

##### 4.12.1. Al6061 Alloy

The temperature-time dependent microstructural changes are expected at temperatures above  $0.5T_m$  which is about  $150^{\circ}\text{C}$  ( $423\text{K}$ ) for aluminum alloys. Al6061 severe wear occurred in the temperature range of  $150^{\circ}\text{C}$  ( $0.5 T_m$ ) to  $500^{\circ}\text{C}$  ( $0.85T_m$ ). Recrystallised grains are seen in Fig.4.21 . The grain size in the recrystallized region is quite small, about  $1\mu\text{m}$ , as compared to  $31\mu\text{m}$  in the bulk specimen. These grains are oriented in the direction of sliding and appear to be the product of dynamic recrystallization during the sliding process.

The material below the contact surface undergoes large plastic strains during dry sliding process. The deformation energy is stored in the deformed material by increasing point defects and line defect density (dislocation density). At elevated temperature, this energy can be released either through dynamic recovery or dynamic recrystallization. The occurrence of dynamic recrystallization in aluminum and dilute aluminum alloys has been considered unlikely because of its high stacking fault energy (SFE) makes it very easy for dynamic recovery to occur. However, TEM investigations on deformed aluminum alloys have indicated that dynamic recrystallization can occur in dilute aluminum alloys. The appearance of large angle boundaries [102,103] and highly misoriented grains within the original bigger grains indicate that recrystallization does occur in aluminum alloy. TEM investigation by Xia and co-workers [85] of Al6061 as well as Al6061 reinforced with 15 vol.%  $\text{Al}_2\text{O}_3$  after hot torsion tests showed that both the alloys undergo dynamic recrystallization at elevated temperatures. The process of dynamic recrystallization is favoured by increasing the strain rate and the deformation temperature. The strain rates

close to contact surface could be extremely high. At elevated temperatures, due to low flow stress, the strain rates could be sufficiently high to result in dynamic recrystallization.

Several investigators have reported that the recrystallized material often with fine grain size is produced during sliding wear [104,105]. Dautzenberg et al. [107] have shown that the dynamic recrystallization occurred during room temperature sliding wear of copper and its alloys. Recrystallization at elevated temperature can result in total loss of work hardening and can result in dramatic increase in wear rates [45,104,105]. Kuo and Rigney [104] have reported recrystallization during ambient temperature sliding wear of a high purity aluminum alloy but it could not be established whether the recrystallization was dynamic (occurred during sliding) or meta-dynamic (occurred as soon as the test stopped).

#### 4.12.2. Al6061-20%Al<sub>2</sub>O<sub>3</sub> Alloy

A layer of highly fragmented particulate was observed on the Al6061-20%Al<sub>2</sub>O<sub>3</sub> worn specimens, Figs. 4.24 and 4.25. These layers start to form at temperatures lower than the transition temperature, at about 200°C but with smaller thicknesses of about 10-40  $\mu\text{m}$  and larger particle size in the layer. In the severe wear regimes (more than 300°C) these layers grow to more than 100  $\mu\text{m}$  depth and contain particles with a mean size of about 1  $\mu\text{m}$ . The comminution of the reinforcing ceramic particulate is often attributed to the large plastic strains near the sliding surfaces. Brechet et al. [90] have shown that the particulate size ( $D$ ) varies with plastic strain as  $\varepsilon = 1000 (D^{-3} - D_0^{-3})$ , where  $D$  and  $D_0$  are final and initial mean particle sizes. Plastic strains of the order of  $10^3$  would be required to achieve the final particle size of 1  $\mu\text{m}$  observed in these layers which appears to be rather high value. However, surface shear strain values between 10 to 100 have been reported for the dry sliding wear of aluminum and copper alloys [68,106,107]. It is also conceivable that the particles become crushed at the sliding surface

and then mix with the subsurface material.

Al6061-20%Al<sub>2</sub>O<sub>3</sub> particles after fragmentation, redistribute themselves below the contact surface. More or less uniform distribution of fine particles could be observed in Fig. 4.25. The particle density then becomes much higher (about 10-100 times) more than in the bulk alloy. Geometrical constraint imposed by the large ceramic particles is a large component of strength increase in composites at room temperature. However, this is not the case at elevated temperature. Due to matrix softening, this improvement is lost. Fine distribution of fragmented particles in the subsurface is expected to give hardening as a result of interaction of the particles with dislocations. It is evident from Fig. 4.26(b) that these layers composed of finely distributed Al<sub>2</sub>O<sub>3</sub> particles are very hard (VHN=200 kg.mm<sup>-2</sup>) which implies that once formed the layers may help to increase the wear resistance and delay the severe wear up to a certain temperature of 300°C. At higher temperatures, this effect is limited by the loss of matrix strength.

#### 4.13. Effect of Temperature on Mild Wear of Al6061 and Al6061-20%Al<sub>2</sub>O<sub>3</sub>

Wear rates of both Al6061 and Al6061-20%Al<sub>2</sub>O<sub>3</sub> were found to be low in the mild wear regime at low temperatures. The wear rates of unreinforced Al6061 wear slightly lower than the composite. The wear rates of Al6061 and to a certain degree for Al6061-20%Al<sub>2</sub>O<sub>3</sub> decreased with temperature up to the transition temperature. At the same time the coefficient of friction decreased with increase in test temperature (Fig. 4.9). Wear debris consist of mixture of fine powder and metallic platelets of aluminum.

Wear behaviour of a material is intimately dependent on the nature of the contacting counter body. In the present investigation, steel wear appears to have strong influence on the mild wear of both the materials. The wear rates of steel remained high at room temperature against the composite due to abrasive action by Al<sub>2</sub>O<sub>3</sub> particles. It

has been shown that the steel oxidation helps reducing the friction and wear during dry sliding. Oxide debris containing  $\text{Fe}_2\text{O}_3$  and  $\text{Fe}_3\text{O}_4$  acts as solid lubricants.  $\text{Fe}_2\text{O}_3$  has hard rhombohedral (haematite) structure which forms at lower temperatures acts as third-body abrasive. At higher temperatures, formation of  $\text{Fe}_3\text{O}_4$ , a more ductile spinel magnetite is favoured which acts as lubricant.  $\text{FeO}$  (soft wustite) is stable only above  $570^\circ\text{C}$  [108]. The presence of fine oxides results in smooth friction trace (Fig. 4.8) at elevated temperatures below the transition temperature, where, considerable steel wear occurred.

The worn surfaces were found to be covered with Fe rich layer. The wear debris transfers and gets compacted on the specimen surface (Fig. 4.12). These layers are expected to lower friction and give improved wear resistance by lowering adhesion through limiting the extent of metal to metal contact during sliding. These layers increase the surface hardness and abrade the counterface surface.

Mild wear of aluminum alloys and aluminum matrix composites have been shown to occur through delamination and abrasion [64-68]. Al6061-20% $\text{Al}_2\text{O}_3$  specimen worn in the mild wear regime showed cracks on the worn surfaces (Figs. 4.13 and 4.16). Aluminum alloys containing large ceramic particles are more prone to delamination due to ease of nucleation and propagation of delaminating cracks along the particle matrix interface. During sliding, fragmented alumina particles often appear between the sliding surfaces and act as third body abrasive. The composite, therefore, shows higher wear rates than the unreinforced alloy in the mild wear regime and the wear rates do not decrease with temperature.

A summary of important findings of this study on high temperature wear of Al6061 and Al6061-20% $\text{Al}_2\text{O}_3$  is given in Tables 4.3(a) and 4.3(b).



**Table. 4.3. High temperature wear characteristics of Al6061 and Al6061-20%Al<sub>2</sub>O<sub>3</sub>.**

| <b>(a) Al6061</b>  |  |  |
|--|--|--|
|  | <b>Mild Wear</b>                                     | <b>Severe Wear</b>   |
| Temperature Range  | 25-150°C (at 10N)                                    | >150°C (at 10N)  |
| Wear rates (mm <sup>3</sup> m <sup>-1</sup> )                      | 2x10 <sup>-3</sup> -4x10 <sup>-3</sup><br>Decrease   | 1x10 <sup>-2</sup> -3x10 <sup>-1</sup><br>Rapid increase           |
| Coefficient of friction ( $\mu$ )                                  | 0.5 (room temperature)-<br>0.35 (150°C)              | 0.5-2.0  |
| Flow strength (MPa)<br>( $\epsilon=0.2$ )                          | 435 (room temperature)                               | 285 (200°C)  |
| Work hardening rate,<br>$d\sigma/d\epsilon$ , $\epsilon=0.2$ (MPa) | 185 (room temperature)                               | 32 (200°C)   |
| Wear Mechanisms  | Delamination<br>Abrasion<br>Oxidation of counterface | Extrusion<br>Gross material transfer<br>to the counterface surface |
| Activation energy for<br>wear process                              | ---  | 34 kJ mole <sup>-1</sup>   |
| Subsurface Changes in<br>(i) Microstructure:                       | Plastic deformation                                  | Large plastic deformation<br>Recrystallization<br>Grain refinement |
| (ii) Mechanical properties<br>(expected)                           | Work-hardening                                       | Work Softening   |

| <b>(b) Al6061-20%Al<sub>2</sub>O<sub>3</sub></b> |                                 |   |
|--|---------------------------------|---|
|  | <b>Mild Wear</b>                | <b>Severe Wear</b>  |
| Temperature Range                                | 25-230°C (at 10N)               | >230°C (at 10N)   |
| Wear rates (mm <sup>3</sup> m <sup>-1</sup> )    | ≈5x10 <sup>-3</sup><br>Decrease | 5x10 <sup>-2</sup> -2x10 <sup>-1</sup><br>Rapid increase  |
| Coefficient of friction (μ)                      | ≈0.5                            | 0.5-2.0   |
| Flow strength (MPa)<br>(ε=0.2)                   | 490 (room temperature)          | 205 (250°C)   |
| Work hardening rate<br>dσ/dε, ε=0.2 (MPa)        | 135 (room temperature)          | -1 (250°C)  |
| Wear Mechanisms                                  | Delamination<br>Abrasion        | Extrusion<br>Material transfer<br>to the counterface surface  |
| Activation energy for<br>wear process            | ---                             | 60 kJ mole <sup>-1</sup>  |
| Subsurface Changes in<br>(i) Microstructure:     | Subsurface cracks               | Large plastic deformation<br>Comminution of Al <sub>2</sub> O <sub>3</sub><br>particles                         |
| (ii) Mechanical properties<br>(expected)         | Work-hardening                  | Work Softening<br>Hardening from Al <sub>2</sub> O <sub>3</sub><br>particle fragmentation<br>and redistribution |

# **Ti<sub>50</sub>Ni<sub>47</sub>Fe<sub>3</sub> INTERMETALLIC ALLOY**

### A. EXPERIMENTAL RESULTS

#### 5.1 Thermo-mechanical Treatment

The Ti<sub>50</sub>Ni<sub>47</sub>Fe<sub>3</sub> alloy was melted in an arc furnace in argon atmosphere as described in section 3.1.2. The cast alloy was cold worked by rolling (30% reduction in thickness) and annealed (850°C, 2 h) to modify and homogenize the cast structure. Annealed alloy was soft with microhardness of only 205 kg.mm<sup>-2</sup>. Tensile testing revealed that the alloy is ductile and showed tensile elongation up to 20%, however, the yield strength was low (410 MPa). The alloy thus needed to be strengthened through thermo-mechanical treatment by cold rolling and annealing.

Effect of cold working on the mechanical properties was investigated first. Ti<sub>50</sub>Ni<sub>47</sub>Fe<sub>3</sub> sheets were annealed (850°C, 1 h) and cold-rolled to give different percentages of cold-work up to 45% reduction in thickness. These results are shown in Fig. 5.1. The cold working increases the yield strength as well as tensile strength appreciably, however, the ductility shows a concomitant decrease. Cold rolling to 45% reduction in thickness increases the yield strength to 1200 MPa and tensile strength to above 1500 MPa. At the same time, the ductility of the intermetallic drops to 4% elongation. It is clear from Fig. 5.1 that the intermetallic alloy has not exhausted its work hardening ability after cold working up to 45% and further hardening is expected at larger deformations.

In a second set of experiments, highly deformed alloy was annealed to improve its ductility. The cold-worked sheets after 40% reduction in thickness were given a short time anneal at 450°C and 500°C. Then tensile tests were carried out on the annealed

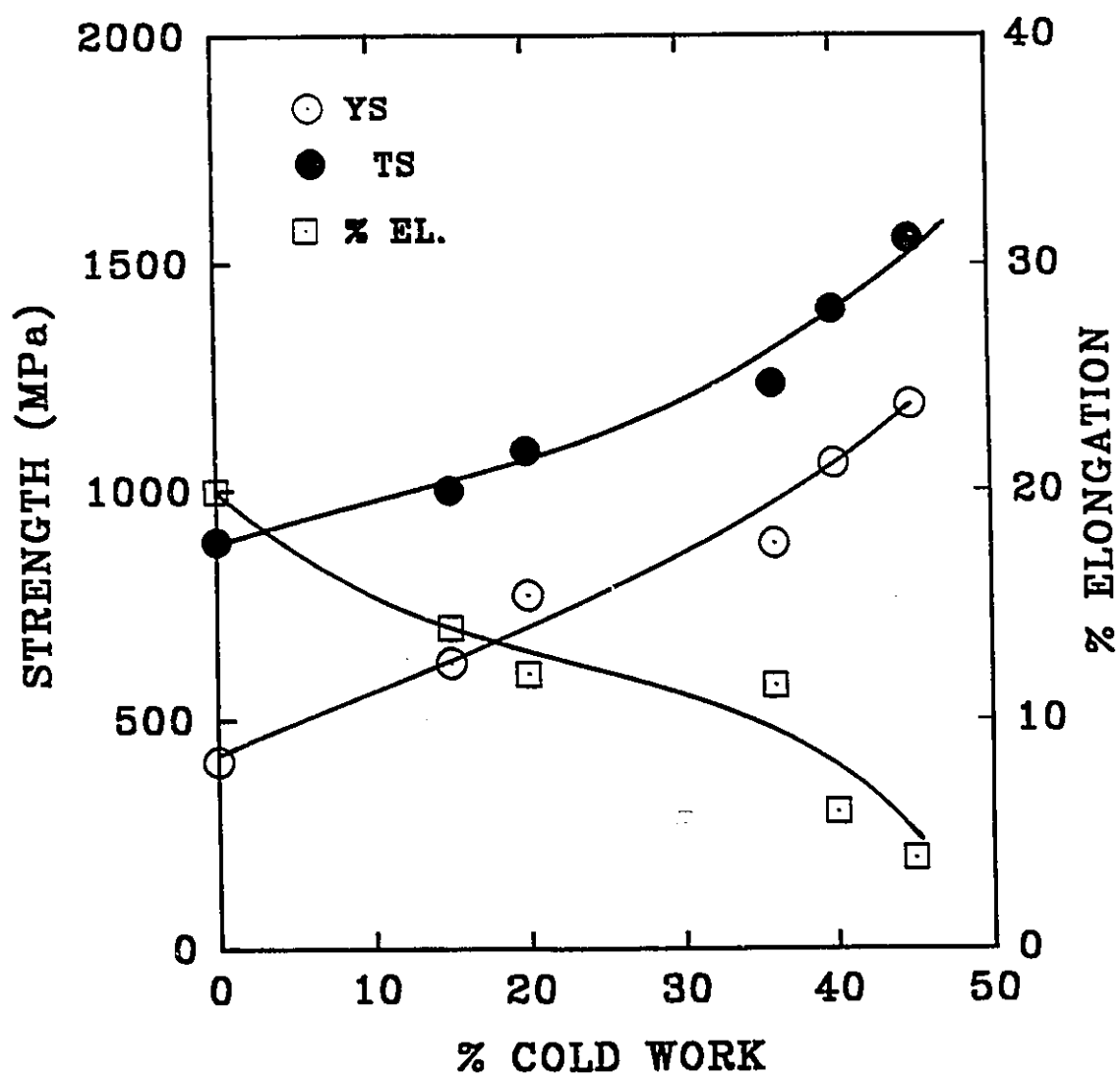


Fig. 5.1. Effect of cold work on the yield strength (YS), tensile strength (TS), and ductility (% elongation) of  $\text{Ti}_{50}\text{Ni}_{47}\text{Fe}_3$ .

**Table 5.1 Effect of thermomechanical treatment on the yield strength (YS) tensile strength (TS) and ductility (% elongation) of  $\text{Ti}_{50}\text{Ni}_{47}\text{Fe}_3$ .**

| Heat treatment after<br>40% CW by rolling | YS<br>(MPa) | TS<br>(MPa) | Ductility<br>(% el.) |
|---|-------------|-------------|----------------------|
| none                                      | 1110        | 1450        | 4                    |
| 450°C, 5 min.                             | 1080        | 1290        | 6                    |
| 450°C, 10 min.                            | 830         | 1100        | 15                   |
| 450°C, 100 min.                           | 659         | 968         | 17                   |
| 500°C, 5 min.                             | 765         | 1132        | 14                   |
| 500°C, 10 min.                            | 708         | 1097        | 18                   |
| 850°C, 60min.                             | 410         | 970         | 20                   |

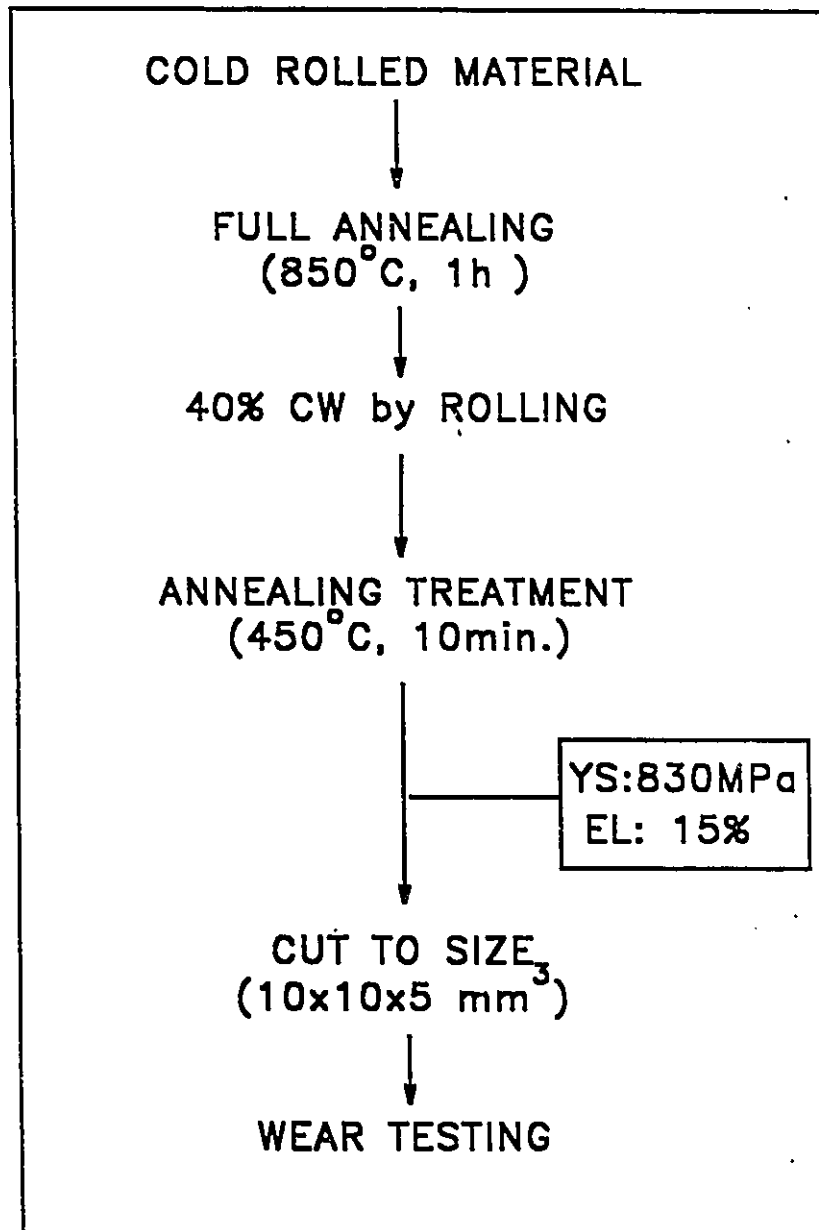


Fig. 5.2. Outline of the thermo-mechanical treatment given to  $\text{Ti}_{50}\text{Ni}_{47}\text{Fe}_3$  prior to wear testing.

samples with the objective of determining the optimum combination of yield strength and ductility. The results of tensile tests are listed in Table 5.1. These short anneals were effective in recovering the ductility of the alloy without adversely affecting the strength of the alloy. From Table 5.1., it is evident that a 10min. anneal at 450°C gives the best combination of strength and ductility (yield stress of 830 MPa and tensile elongation of 15%). Hence, this particular thermo-mechanical treatment, shown in Fig. 5.2 was given to the  $\text{Ti}_{50}\text{Ni}_{47}\text{Fe}_3$  alloy before the sliding wear tests.

## 5.2. Wear Rates at Room Temperature

### 5.2.1. Volume Loss vs of Sliding Distance Curves

$\text{Ti}_{50}\text{Ni}_{47}\text{Fe}_3$  alloy was given a thermo-mechanical treatment as outlined in Fig. 5.2, consisting of 40% cold-work by rolling followed by an isothermal heating at 450°C for 10 minutes. The dry sliding wear tests were performed using a block-on-ring type test machine (section 3.3). The tests were performed at different loads within the 2-400N load range at a constant sliding speed of 0.4 m.s<sup>-1</sup>. One test was done at each load to measure weight loss from the sample as a function of sliding distance. The test was interrupted at regular intervals and the weights of both the block and the ring were measured. The weight loss was converted to volumetric wear loss using the density of each material (Table 3.1) and is plotted against sliding distance in Fig. 5.3.

In Fig. 5.3(a), the volumetric wear loss of the  $\text{Ti}_{50}\text{Ni}_{47}\text{Fe}_3$  alloy as a result of dry sliding tests conducted at a constant sliding speed of 0.4 m.s<sup>-1</sup> is plotted against the sliding distance for different applied loads. The wear rates of the intermetallic alloy (average slope of the volume loss curves) are high in the beginning but stabilize to lower values at longer sliding distances. This behaviour is observed at all load levels between 2-400 N, however, this is not self evident for low load tests due to very low wear rates. The corresponding wear losses of the SAE 52100 steel are shown in Fig. 5.3(b). These plots differ in an important aspect from those of the  $\text{Ti}_{50}\text{Ni}_{47}\text{Fe}_3$  in that the wear rates do not decrease with sliding distance but continuously increase up to the longest sliding distance

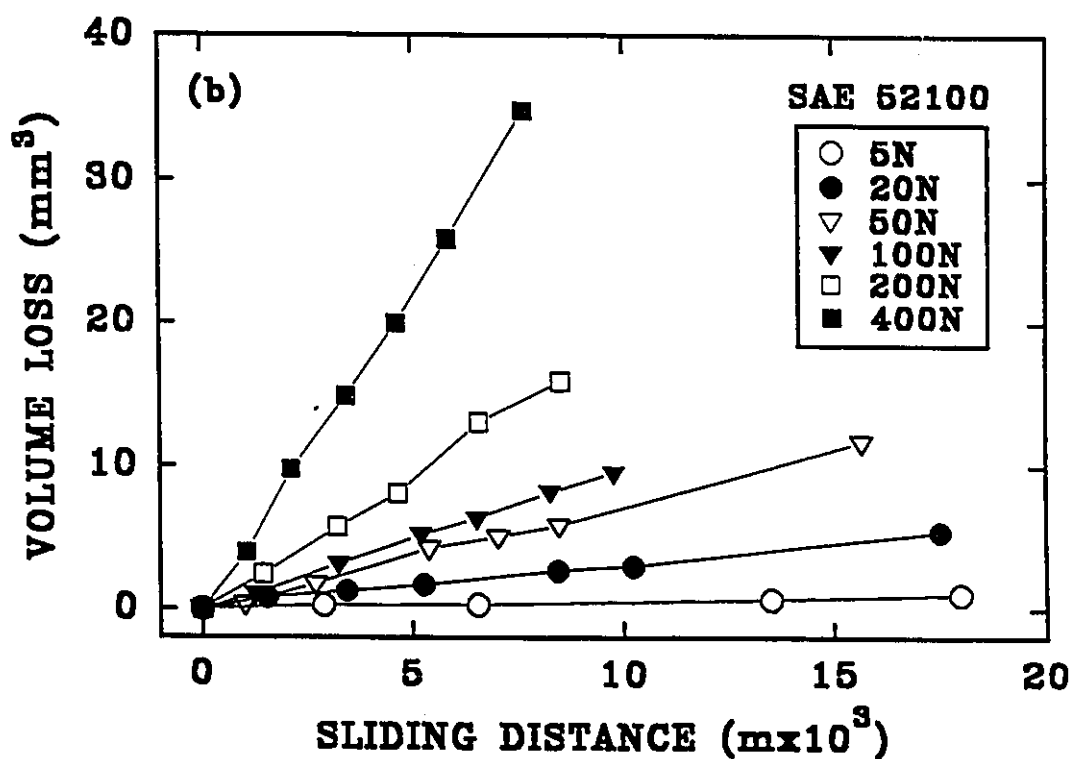
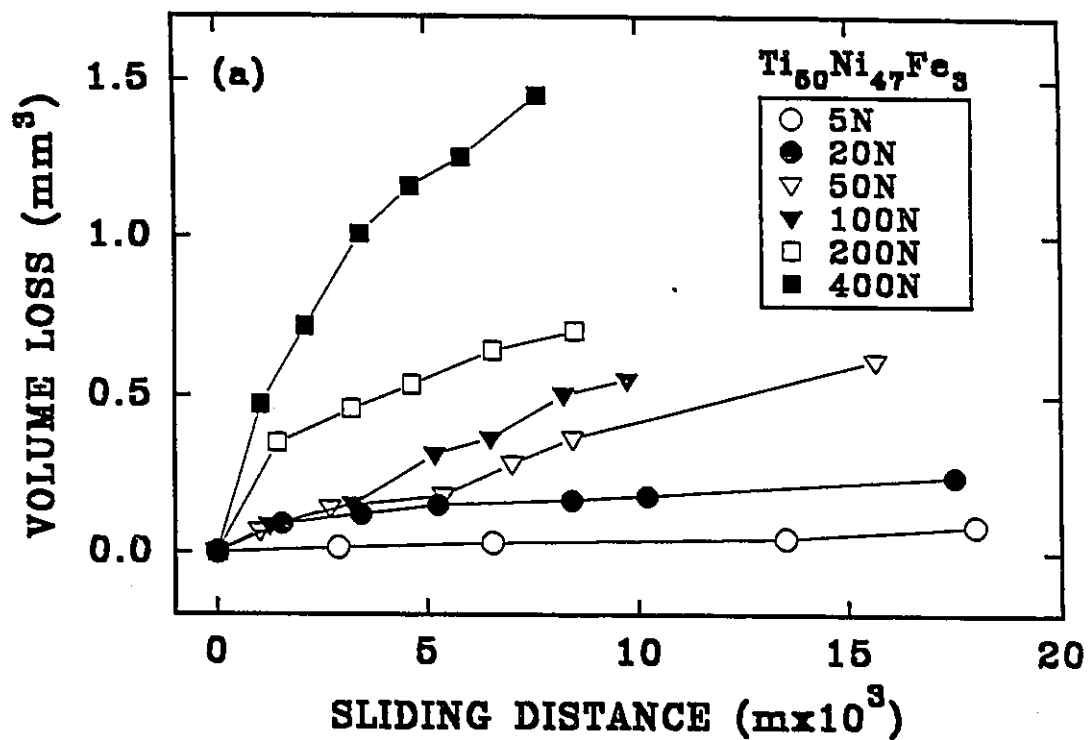


Fig. 5.3. Volumetric wear plots of (a)  $\text{Ti}_{50}\text{Ni}_{47}\text{Fe}_3$  alloy (b) SAE 52100 bearing steel at various applied loads. (sliding speed of  $0.4\text{ms}^{-1}$ ).



used.

### 5.2.2. Wear Rate vs Load

The average slopes of the volume loss versus sliding distance curves are plotted against the applied load in Fig. 5.4. The salient observation which can be made from these plots is that the wear rates of  $\text{Ti}_{50}\text{Ni}_{47}\text{Fe}_3$  alloy are only about 2 to 5% of those of the SAE 52100. These results were unexpected since the hardened bearing steel SAE 52100 (quenched and tempered) is almost three times harder (VHN 870  $\text{kg.mm}^{-2}$ ) in comparison to the intermetallic alloy (VHN 330  $\text{kg.mm}^{-2}$ ).

The  $\text{Ti}_{50}\text{Ni}_{47}\text{Fe}_3$  alloy shows two distinct wear regimes. At low loads, marked as regime I in Fig. 5.4, the wear rates are very low (e.g.  $1 \times 10^{-6} \text{ mm}^3\text{m}^{-1}$  at 2N and  $5 \times 10^{-6} \text{ mm}^3\text{m}^{-1}$  at 7N) but increase rather rapidly with load. The slope of the wear rate curve decreases with increasing load before reaching a steady value at the transition to regime II. Typical wear rates are  $1.5 \times 10^{-5} \text{ mm}^3\text{m}^{-1}$  at 20 N and  $1 \times 10^{-4} \text{ mm}^3\text{m}^{-1}$  at 200 N in this regime. The slope of the wear rate versus load curve of the  $\text{Ti}_{50}\text{Ni}_{47}\text{Fe}_3$  remains constant in the entire load range of 10-400 N such that the wear rates,  $W$ , in this regime obey a power law expression of the form

$$W = K P^n$$

where  $P$  is applied normal load,  $K$  is the wear constant, and  $n$  is defined as the wear exponent. The wear rate curve for the steel has a shape similar to that of  $\text{Ti}_{50}\text{Ni}_{47}\text{Fe}_3$  except for high loads ( $>200 \text{ N}$ ), at which the wear rates accelerate and, thus, show another transition which is labelled as regime III in Fig. 5.4. The wear data of the  $\text{Ti}_{50}\text{Ni}_{47}\text{Fe}_3$  as well as the SAE 52100 for regime II fitted to the above expression show that the wear rates of the intermetallic vary as  $1.4 \times 10^{-6} P^{0.8}$  while the wear rates of the steel increase according to  $2.7 \times 10^{-5} P^{0.8}$  within the load range of 10N to 200N. Both  $\text{Ti}_{50}\text{Ni}_{47}\text{Fe}_3$  and SAE 52100 show similar values for the wear exponent. However, the wear constant,  $K$ , for the steel is 20 times higher than for the intermetallic alloy. This means that the load dependence of wear rates is same for both the materials which implies that the same wear

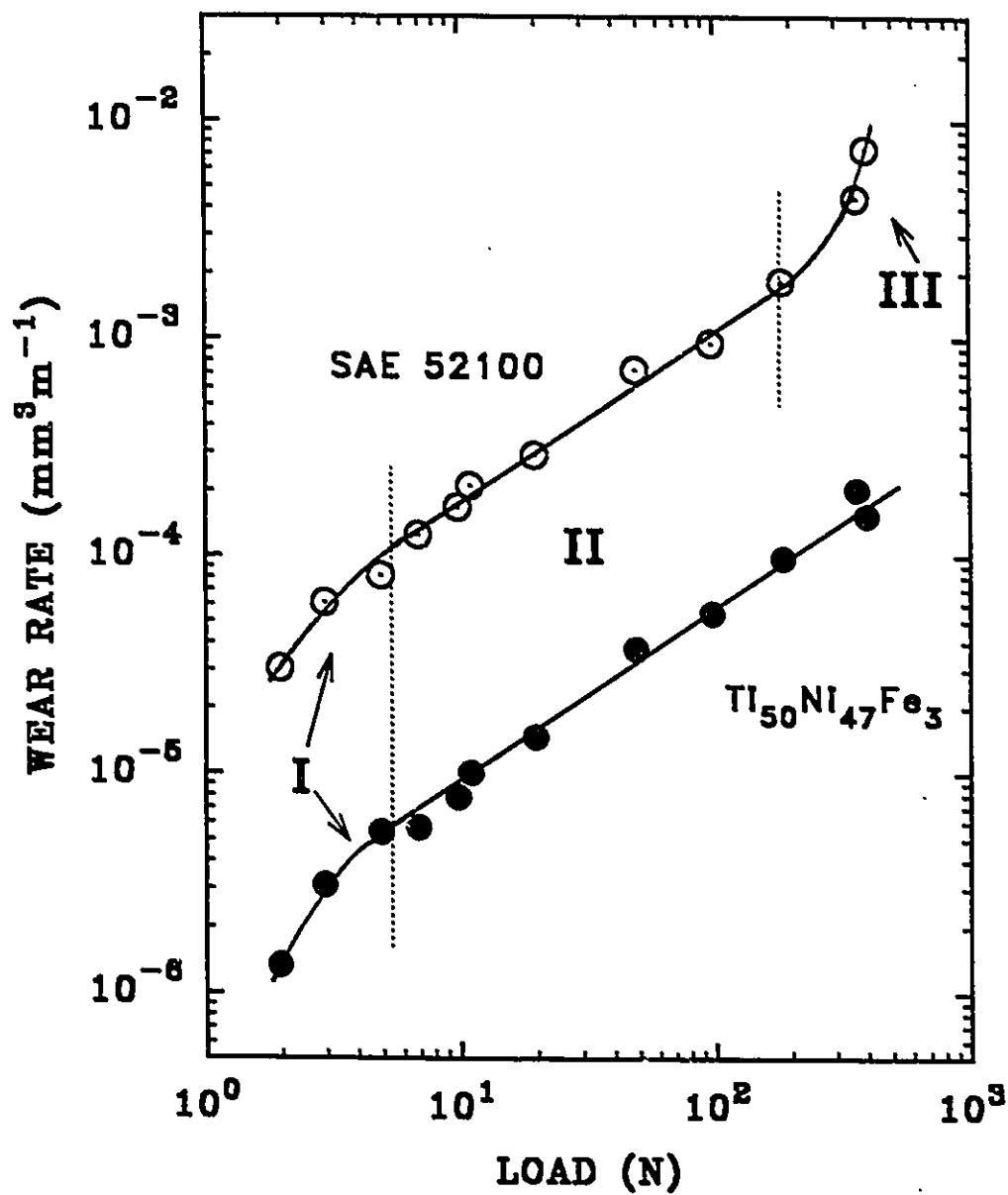


Fig. 5.4. Wear rates of  $\text{Ti}_{50}\text{Ni}_{47}\text{Fe}_3$  and SAE 52100 steel plotted against load. (sliding speed  $0.4 \text{ ms}^{-1}$ )

mechanism operates in both  $\text{Ti}_{50}\text{Ni}_{47}\text{Fe}_3$  and steel under the sliding conditions employed here. The absolute wear rates for the steel are, however, much higher indicating that the mechanism operates faster in steel.

### 5.2.3. Effect of Sliding Speed

The effect of sliding speed was investigated for the wear regime II (Fig. 5.4), which dominates the wear behaviour of the  $\text{Ti}_{50}\text{Ni}_{47}\text{Fe}_3$  as well as the SAE 52100. The experiments were carried out at a constant applied load of 20N. The results of these tests are shown in Fig. 5.5. Several interesting observations can be made from the wear plots of both alloys.

(1) Sharp transitions in the wear rates of both materials are self evident. The  $\text{Ti}_{50}\text{Ni}_{47}\text{Fe}_3$  alloy undergoes a mild to severe wear transition at critical sliding speed of  $2.7 \text{ m.s}^{-1}$ . The transition for the steel is from high wear rates to low wear and occurs at sliding speed of  $2.5 \text{ m.s}^{-1}$ .

(2) At low sliding speeds, from  $0.04 \text{ m.s}^{-1}$  to  $2.7 \text{ m.s}^{-1}$ , the wear rates of the  $\text{Ti}_{50}\text{Ni}_{47}\text{Fe}_3$  are very low (characteristic of regime II of Fig. 5.4.) and increase gradually with the sliding speed (e.g.  $1.5 \times 10^{-5} \text{ mm}^3\text{m}^{-1}$  at  $0.4 \text{ m.s}^{-1}$  to  $2.0 \times 10^{-5} \text{ mm}^3\text{m}^{-1}$  at  $2.7 \text{ m.s}^{-1}$ ). However, the wear rates rise sharply by a factor of 10 (to  $2 \times 10^{-4} \text{ mm}^3\text{m}^{-1}$ ) when the sliding speed is increased to  $3.0 \text{ m.s}^{-1}$ . This mild to severe wear transition of the  $\text{Ti}_{50}\text{Ni}_{47}\text{Fe}_3$  occurs within a very narrow range of sliding speed ( $2.7 - 3.2 \text{ m.s}^{-1}$ ). Further increase in the sliding speed further increases the wear rates but only slightly (to  $2.5 \times 10^{-4} \text{ mm}^3\text{m}^{-1}$  at  $5.3 \text{ m.s}^{-1}$ ).

(3) The SAE 52100 bearing steel, in contrast to  $\text{Ti}_{50}\text{Ni}_{47}\text{Fe}_3$ , shows a sharp fall in the wear rate at a critical sliding speed of  $2.5 \text{ m.s}^{-1}$ . The wear rates of the steel drop by a factor of 20 from  $6 \times 10^{-4} \text{ mm}^3\text{m}^{-1}$  to  $3 \times 10^{-5} \text{ mm}^3\text{m}^{-1}$  on increasing the sliding speed above  $2.5 \text{ m.s}^{-1}$ . The wear rates of the steel continue to decrease as the sliding speed is increased beyond this transition speed.

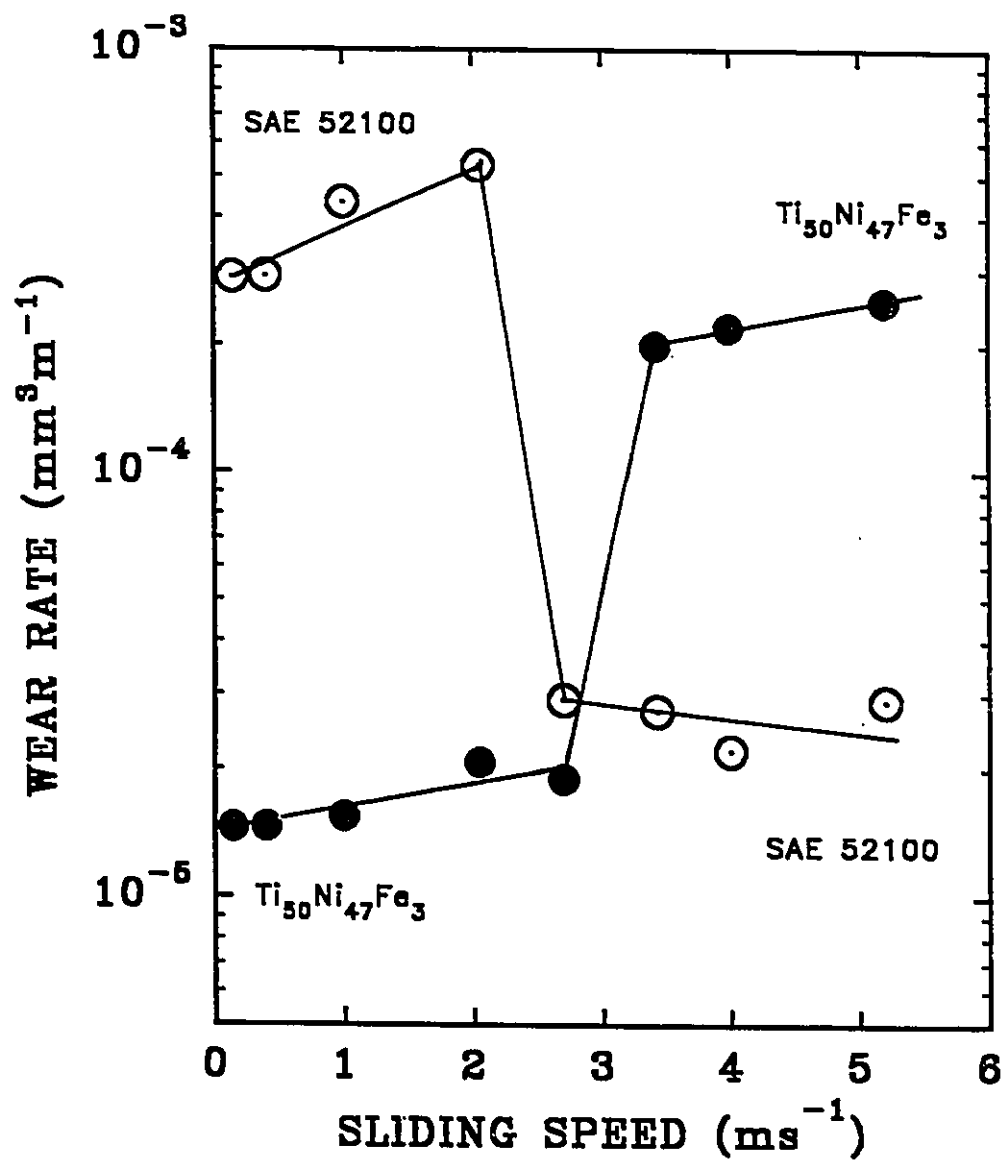


Fig. 5.5. Wear rates of  $\text{Ti}_{50}\text{Ni}_{47}\text{Fe}_3$  and SAE 52100 plotted against sliding speed (applied load is 20N).

(4) It can be noted that the wear transition in the SAE 52100 (high to low wear rates) occurs at a lower sliding velocity with respect to the mild to severe wear transition speed of the  $\text{Ti}_{50}\text{Ni}_{47}\text{Fe}_3$ . At the sliding speed of  $2.7 \text{ m.s}^{-1}$  both the  $\text{Ti}_{50}\text{Ni}_{47}\text{Fe}_3$  specimen and the steel counterface show excellent wear resistance.

### 5.3. Wear Rates at Elevated Temperature

High temperature sliding wear of  $\text{Ti}_{50}\text{Ni}_{47}\text{Fe}_3$  alloy was investigated in the temperature range 25-520°C using a pin on disk wear geometry (Fig. 3.7). Testing conditions employed were: sliding speed  $0.4 \text{ m.s}^{-1}$ , sliding distance of  $10^4 \text{ m}$  and an applied load of 15N. The wear rates were obtained from the specimen weight loss measured at the end of the wear test. The wear rates of both the pin ( $\text{Ti}_{50}\text{Ni}_{47}\text{Fe}_3$ ) and the disk (SAE 52100) have been plotted against temperature in Fig. 5.6.  $\text{Ti}_{50}\text{Ni}_{47}\text{Fe}_3$  alloy shows an unusual behaviour at elevated temperatures. The following observations can be made regarding high temperature wear behaviour of  $\text{Ti}_{50}\text{Ni}_{47}\text{Fe}_3$  sliding against SAE52100:

(1) The intermetallic wear rates at room temperature are lower ( $6 \times 10^{-6} \text{ mm}^3 \text{ m}^{-1}$ ) than those observed during block on ring testing ( $9 \times 10^{-6} \text{ mm}^3 \text{ m}^{-1}$ ) under the same load and sliding speed.

(2) The wear rates slightly decrease with increase in test temperature up to 200°C. Wear rates drop sharply above 200°C. Between 250°C and 350°C, the wear rates were so low that no measurable weight loss occurred after a sliding distance of  $10^4 \text{ m}$ .

(3) Above 350°C, the wear rates of the intermetallic increase sharply with temperature. The wear rates of  $\text{Ti}_{50}\text{Ni}_{47}\text{Fe}_3$  increased from  $<10^{-7} \text{ mm}^3 \text{ m}^{-1}$  at 350°C to  $2.3 \times 10^{-4} \text{ mm}^3 \text{ m}^{-1}$  at 510°C.

(4) SAE 52100 depicts entirely different wear behaviour. The wear rates increase with increasing temperature up to a maximum at 350°C. At higher temperatures ( $>350^\circ\text{C}$ ), the

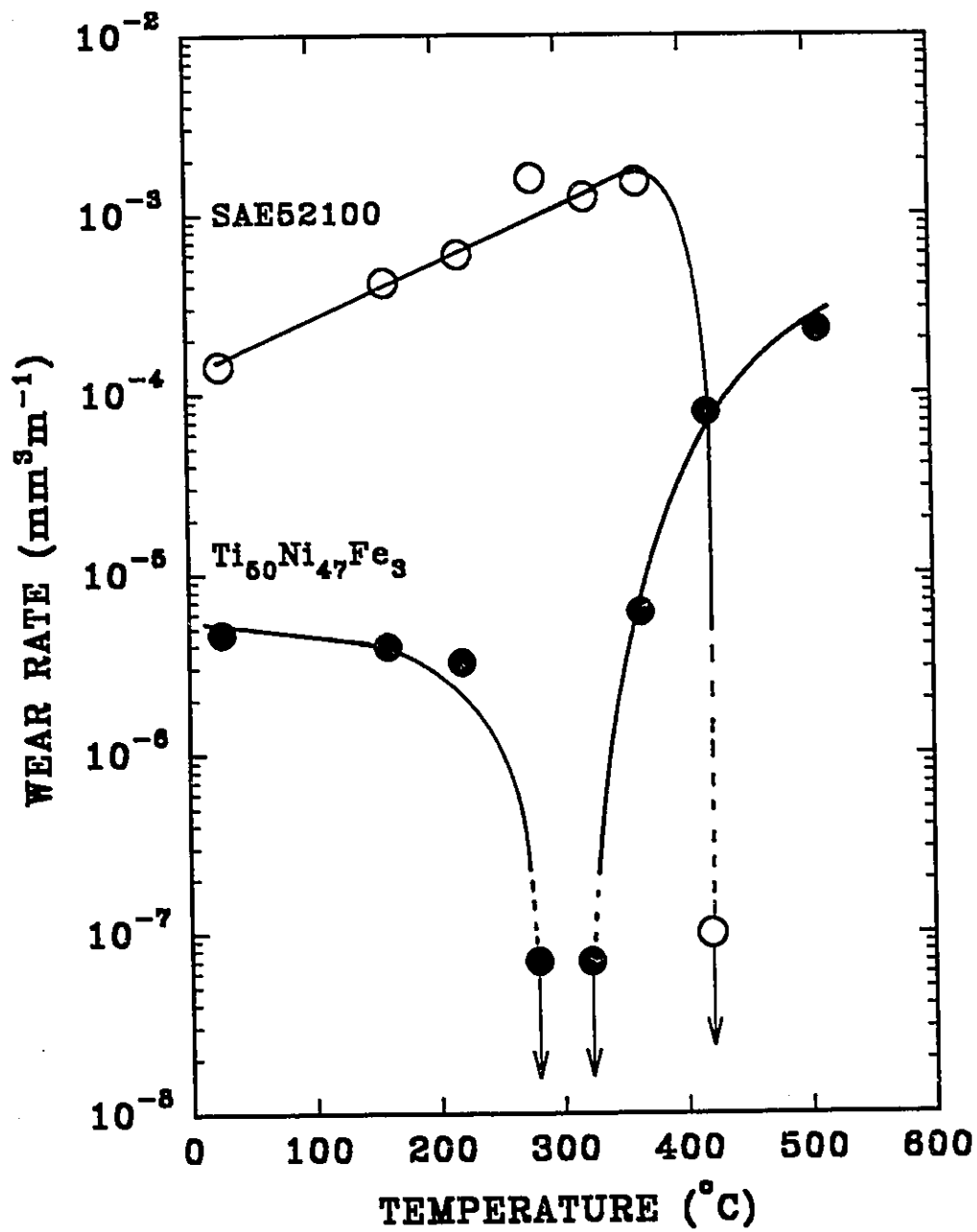


Fig. 5.6. Effect of temperature on the sliding wear of  $\text{Ti}_{50}\text{Ni}_{47}\text{Fe}_3$  alloy against SAE52100 steel.

steel wear rates start to drop rapidly and shows weight gain at and above 400°C due to material transfer from  $\text{Ti}_{50}\text{Ni}_{47}\text{Fe}_3$  pin to the 52100 disc.

Wear behaviour similar to that shown by the  $\text{Ti}_{50}\text{Ni}_{47}\text{Fe}_3$  (a decrease in wear with temperature and then an increase) has been reported by Berns and Fisher [44] for the high temperature abrasion wear of cobalt based alloys. Lancaster [52] has also indicated decrease in wear rate with temperature for leaded brass sliding against hard steel. The decrease in wear at elevated temperatures has been attributed to the formation of tribo-layers (in particular oxide layers) on the sliding surfaces. At higher temperatures, material loses its strength and shows severe wear.

#### 5.4. Friction Behaviour

Friction measurements were performed on the high temperature wear machine using pin on disc wear setup. Friction measurements were made under 15N load and at sliding speed of 0.4 m.s<sup>-1</sup>. The frictional traces of the wear run at different temperatures are given in Fig. 5.7. The wear run was noisy and the friction trace more spread out at room temperature. The oscillations in the friction force (normalized as T/P) at room temperature has maximum amplitude of about 2. With the increasing temperature wear tests became smoother and the amplitude of oscillations drops to a minimum at 320°C to a value of 0.4. The average value of the coefficient of friction as well as the maximum and minimum values are plotted against the test temperature in Fig. 5.8. The coefficient of friction shows a drop with increasing temperature up to 350°C. Further increase in temperature led to higher coefficient of friction. However, the wear runs remained more or less smooth up to 500°C.

#### 5.5. Wear Debris

The wear debris produced during wear tests was examined by metallography as well as X-ray diffraction analysis (XRD), and found to vary markedly in colour and composition with the applied load. At low loads (<50N) and low speed (0.4 m.s<sup>-1</sup>) the

wear debris were reddish brown and became increasingly darker with increasing load. At loads above 200N, the black powdery debris were mixed with metallic particles. XRD analyses results of wear debris generated at low speed  $0.4 \text{ m.s}^{-1}$  at 10N and 400N load are depicted in Fig 5.9(a) and 5.9(b), respectively. The debris contained mainly iron oxides at low loads and iron oxides plus metallic iron at high loads.

At high sliding speeds ( $4.2 \text{ m.s}^{-1}$ , load 20N), the debris were mainly metallic but mixed with fine oxidised powdery debris. XRD analysis (Fig. 5.10) showed that the debris is composed of metallic  $\text{Ti}_{50}\text{Ni}_{47}\text{Fe}_3$  (B2 phase),  $\text{Ni}_3\text{Ti}$  and oxides of  $\text{Ti}_{50}\text{Ni}_{47}\text{Fe}_3$  constituents.

Four types of wear debris were observed for the ambient temperature were testing:

- (1) Reddish fine powder, mainly  $\text{Fe}_2\text{O}_3$  (wear regime I, Fig. 5.4)
- (2) Dark brown, fine powder containing  $\text{Fe}_2\text{O}_3$  and  $\text{Fe}_3\text{O}_4$ , (wear regime II, Fig. 5.4)
- (3) Fine black powder mixed with metallic debris having metallic iron,  $\text{Fe}_2\text{O}_3$  as well as  $\text{Fe}_3\text{O}_4$ . (wear regime III, Fig. 5.4)
- (4) Large metallic ( $\approx 100 \mu\text{m}$ ),  $\text{Ti}_{50}\text{Ni}_{47}\text{Fe}_3$  plates, during severe wear (Fig. 5.4) at sliding speeds above  $3.0 \text{ m.s}^{-1}$ . The debris was composed of  $\text{TiNiO}_3$  and  $\text{TiO}$  in addition to  $\text{Ti}_{50}\text{Ni}_{47}\text{Fe}_3$ .

Pin on disc tests during elevated temperature sliding at 15N load produced fine powdery debris up to  $420^\circ\text{C}$  which were essentially similar to those produced in regime II at ambient temperature tests (types 1,2). At higher temperature mixed (powder and metallic debris) debris (types 3,4) were obtained. The amount of debris collected was not enough for carrying out an XRD analysis.



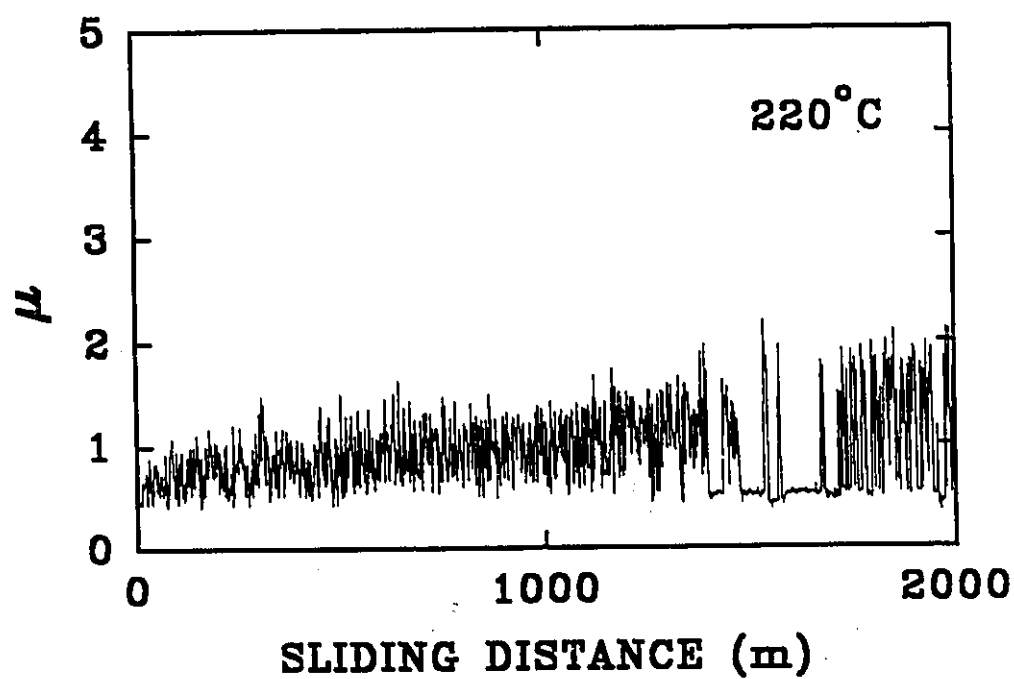
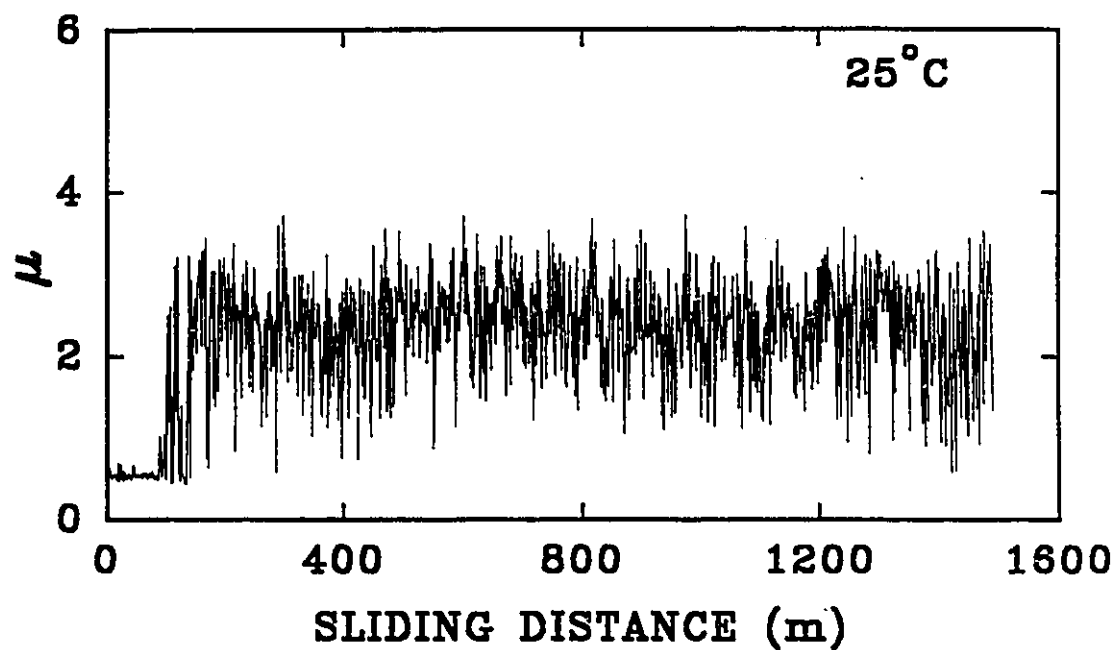


Fig. 5.7. Friction trace during wear run of  $\text{Ti}_{50}\text{Ni}_{47}\text{Fe}_3$  alloy against SAE 52100 at (a) 25°C, (b) 220°C, (c) 320°C and (d) 520°C. (Load 15N, sliding speed  $0.4 \text{ ms}^{-1}$ ).

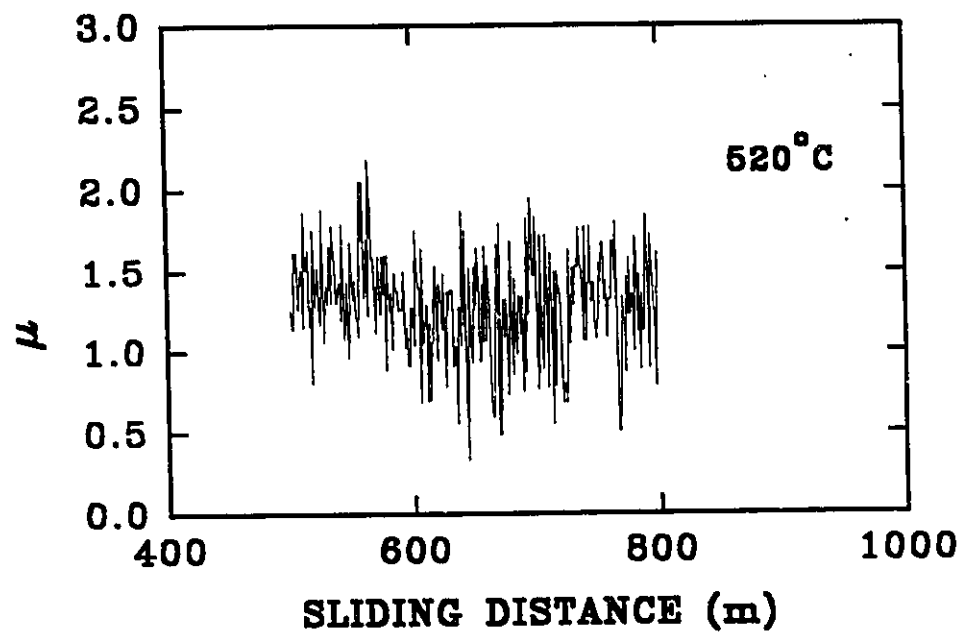
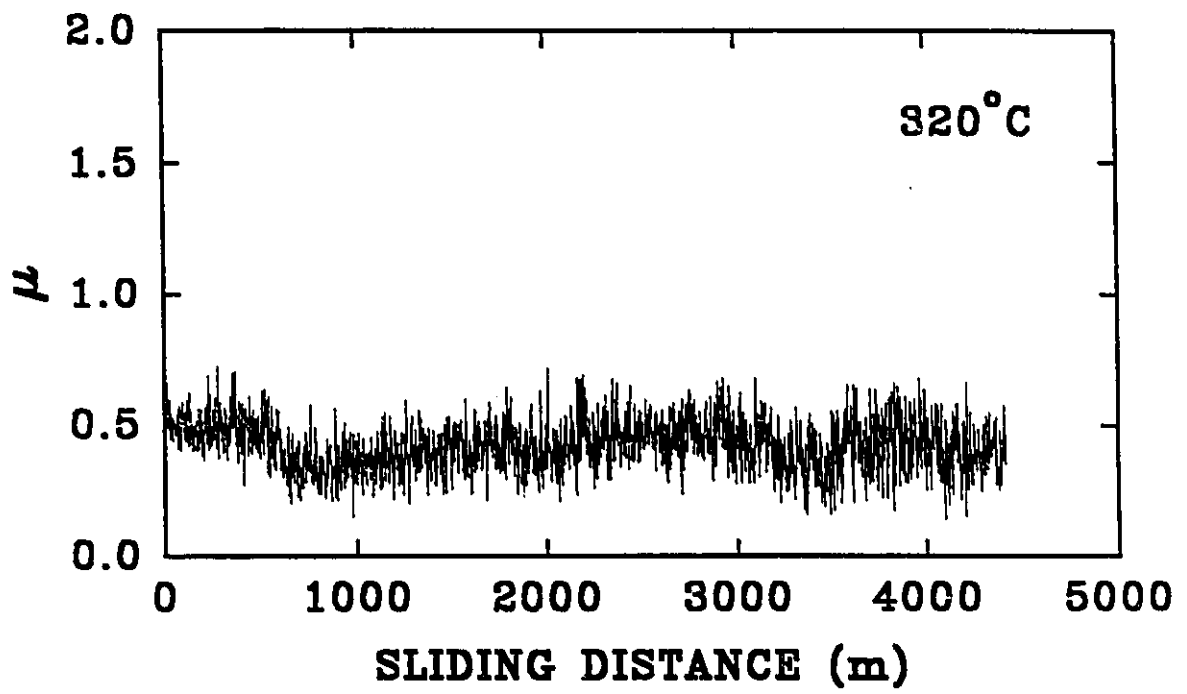


Fig. 5.7. Continued.

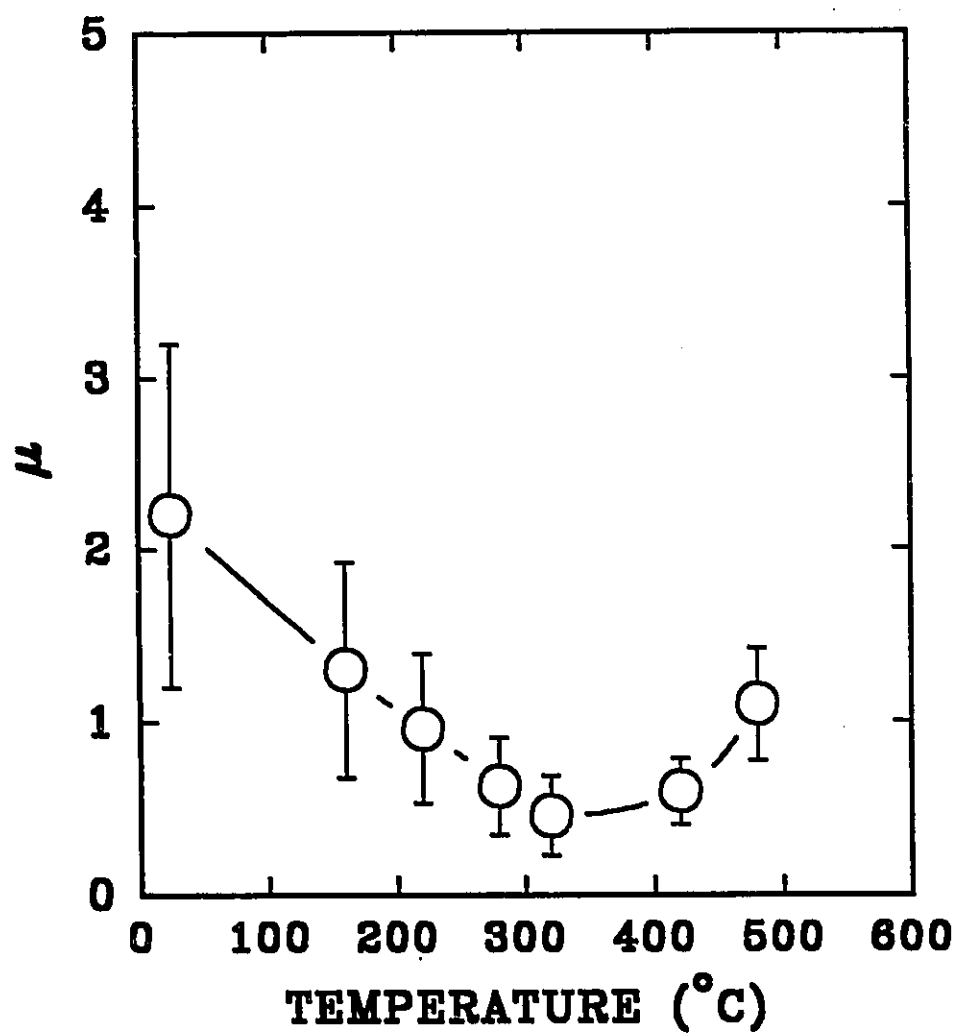


Fig. 5.8. Effect of temperature on the average coefficient of friction ( $\mu$ ) for  $\text{Ti}_{30}\text{Ni}_{47}\text{Fe}_3$  sliding against SAE52100 at 15N load. (Sliding speed  $0.4 \text{ ms}^{-1}$ ).

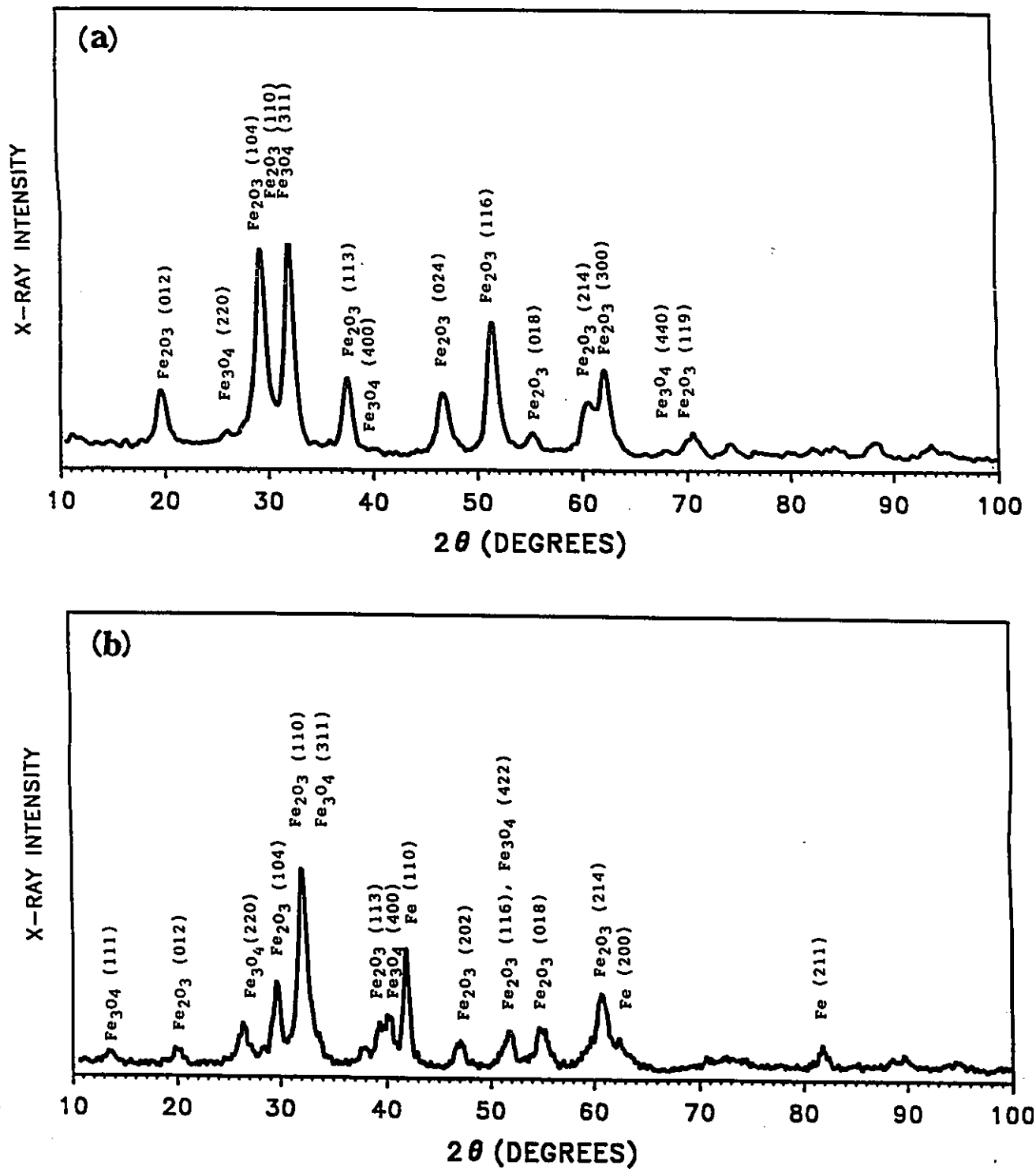


Fig. 5.9. XRD analysis of wear debris generated during sliding of Ti<sub>50</sub>Ni<sub>47</sub>Fe<sub>3</sub> against SAE52100 at (a) 10N load, and (b) 400N load. (sliding speed 0.4 ms<sup>-1</sup>)

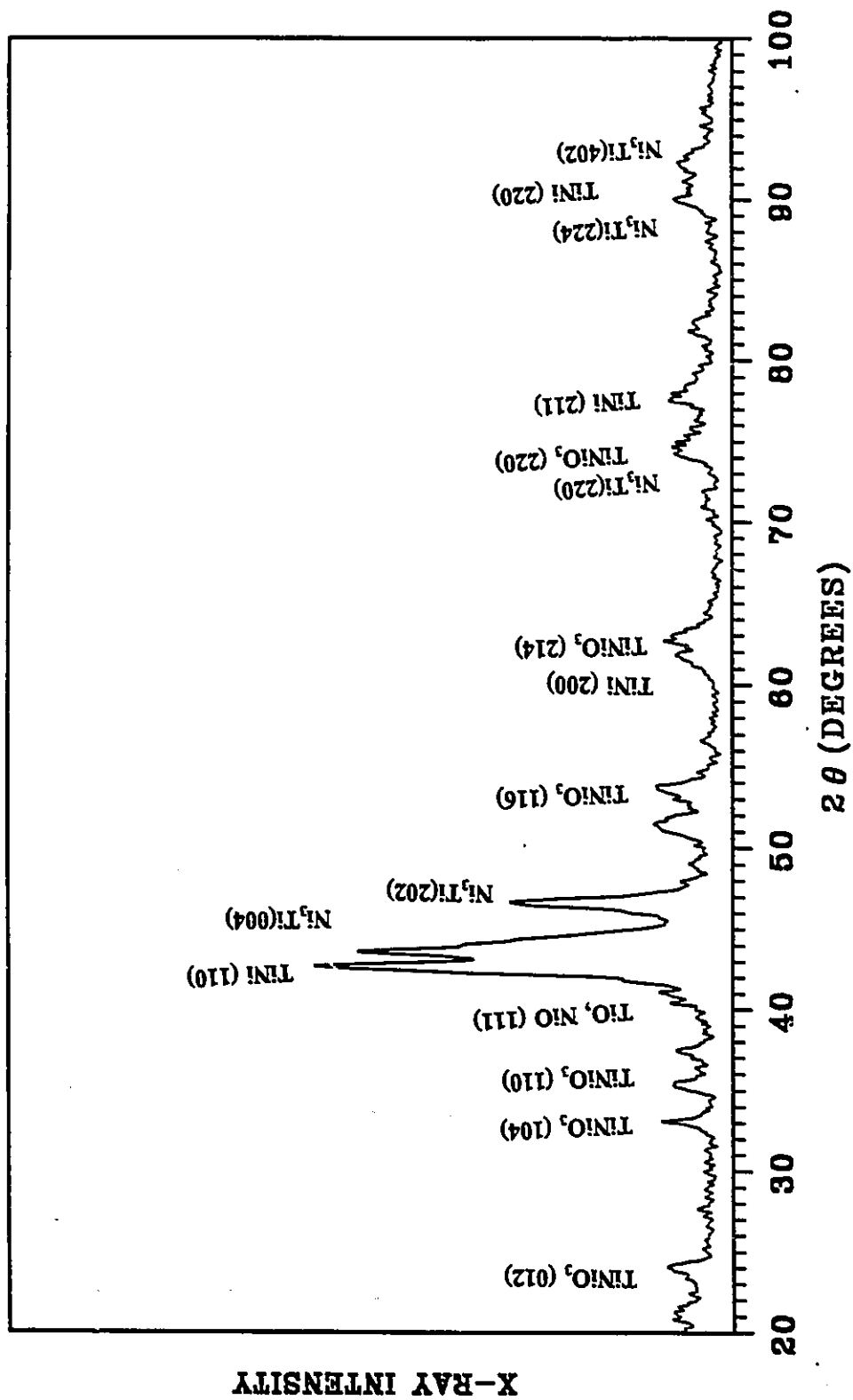


Fig. 5.10. XRD analysis of wear debris generated at sliding speed of  $4.2 \text{ ms}^{-1}$  under 20N load at room temperature.

## 5.6. Worn Surfaces

### 5.6.1 Room Temperature Sliding

#### 5.6.1.1. Effect of Load

The visual examination of the worn surfaces of  $\text{Ti}_{50}\text{Ni}_{47}\text{Fe}_3$  blocks tested in wear regimes I and II (Fig. 5.4) revealed the presence of reddish-brown layers on the wear surfaces along with continuous grooves in the direction of sliding. The colour of the worn tracks matched with that of the debris produced. At low loads, the grooves formed on the surface were fine and shallow (Fig. 5.11(a)) and the wear track was covered completely with a brown layer. At high loads (Fig. 5.11(b)), deep and wide grooves developed on the worn surface which were covered with a black layer. The change was gradual over the entire load range.

SEM micrograph (Fig. 5.12(a)) of worn surface of a specimen worn at 10N load (sliding speed  $0.4 \text{ m.s}^{-1}$ ) shows that the wear surface is uniformly covered with what appears as fine compacted powder. Energy dispersive X-ray (EDS) analysis (Fig. 5.12(b)) showed that an iron rich surface layer has developed on the wear track. The amount of iron on the surface increased with load and sliding distance. At high loads, the layer appears (Fig. 5.13(a)) discontinuous and smeared along the grooves on the worn surface. EDS (Fig. 5.13(b)) shows that the thickness of this iron rich layer is higher at high loads. Since no Ti or Ni peaks could be observed, the layer thickness is greater than the sampling depth of EDS which is about  $6\text{-}8 \mu\text{m}$ . At 10N load (Fig. 5.12), Ti peak shows significantly high intensity indicating lower thickness of the transfer layer.

XRD analysis was performed on the worn surfaces after the tests to ascertain the nature of phases formed on the surface of  $\text{Ti}_{50}\text{Ni}_{47}\text{Fe}_3$  alloy during sliding against steel counterface and the results are shown in Fig. 5.14. The worn surface after sliding at high loads ( $400\text{N}$ ,  $0.4 \text{ m.s}^{-1}$ ) at room temperature was covered with iron ( $\alpha\text{-Fe}$ ) as well as oxidation products of steel ( $\text{Fe}_2\text{O}_3$  and  $\text{Fe}_3\text{O}_4$ ).

The worn surfaces of the steel ring were always found to be shiny at low sliding speeds regardless of applied load used. However, shallow grooves formed in the sliding direction during sliding. The electron micrograph (Fig. 5.15) shows that the surface within these grooves has a polished appearance. EDS results did not show evidence for the material transfer from  $\text{Ti}_{50}\text{Ni}_{47}\text{Fe}_3$  to the steel within the range of applied loads and sliding speeds used in this study.

#### 5.6.1.2. Effect of Sliding Speed

Surfaces of the specimen slid at sliding speeds greater than  $4 \text{ m.s}^{-1}$  had more metallic appearance compared to those worn at a sliding speed of  $0.4 \text{ m.s}^{-1}$  (Fig. 4.11). Low magnification optical micrograph of a specimen tested at a sliding speed of  $4.2 \text{ m.s}^{-1}$  is shown in Fig. 5.16. The grooves on the surface, parallel to the sliding direction formed with width narrower than at low sliding speeds (Fig. 5.11(a)). EDS analysis indicated that the iron transfer to the intermetallic block did not occurred at sliding speeds higher than  $2.6 \text{ m.s}^{-1}$ . XRD analysis done on a specimen worn under severe wear (not presented) conditions at higher sliding speeds ( $4.2 \text{ m.s}^{-1}$ , 20N) indicated the presence of  $\text{TiNiO}_3$ ,  $\text{Ni}_3\text{Ti}$  and  $\text{TiO}$  in addition to  $\text{Ti}_{50}\text{Ni}_{47}\text{Fe}_3$  (TiNi, B2) phase on the wear track.

The worn surfaces under different sliding conditions can be summarized as:

- 1) At low sliding speeds ( $<3.6 \text{ m.s}^{-1}$ ) and low loads ( $<50\text{N}$ ), the worn surfaces were uniformly covered with compacted fine oxide ( $\text{Fe}_2\text{O}_3$  and  $\text{Fe}_3\text{O}_4$ ) debris.
- 2) At low sliding speeds ( $<3.6 \text{ m.s}^{-1}$ ) and high loads ( $>50\text{N}$ ), the worn surfaces had deep grooves and were covered with thicker transfer layer composed of compacted wear debris ( $\text{Fe}_2\text{O}_3$  and  $\text{Fe}_3\text{O}_4$  and Fe).
- 3) At high sliding speeds ( $>3.6 \text{ m.s}^{-1}$ ) at 20N load, the wear track appeared metallic with no transfer layer.

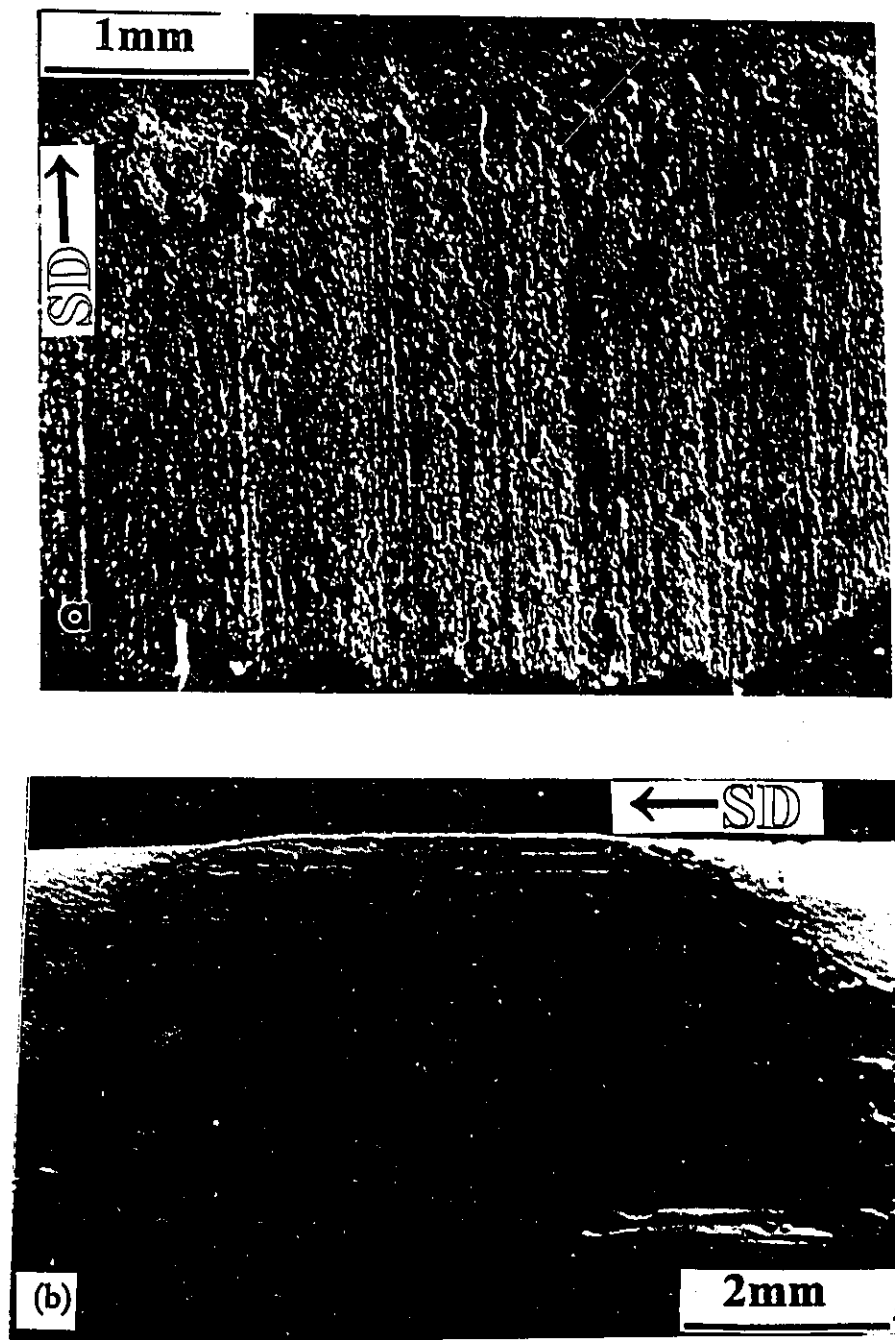


**Fig. 5.11.** Low power optical micrographs of worn surfaces of  $\text{Ti}_{50}\text{Ni}_{47}\text{Fe}_3$  alloy at (a) 10N load, depicting presence of grooves and fine wear debris (b) 400N load showing deep grooves. (sliding speed  $0.4 \text{ ms}^{-1}$ ).



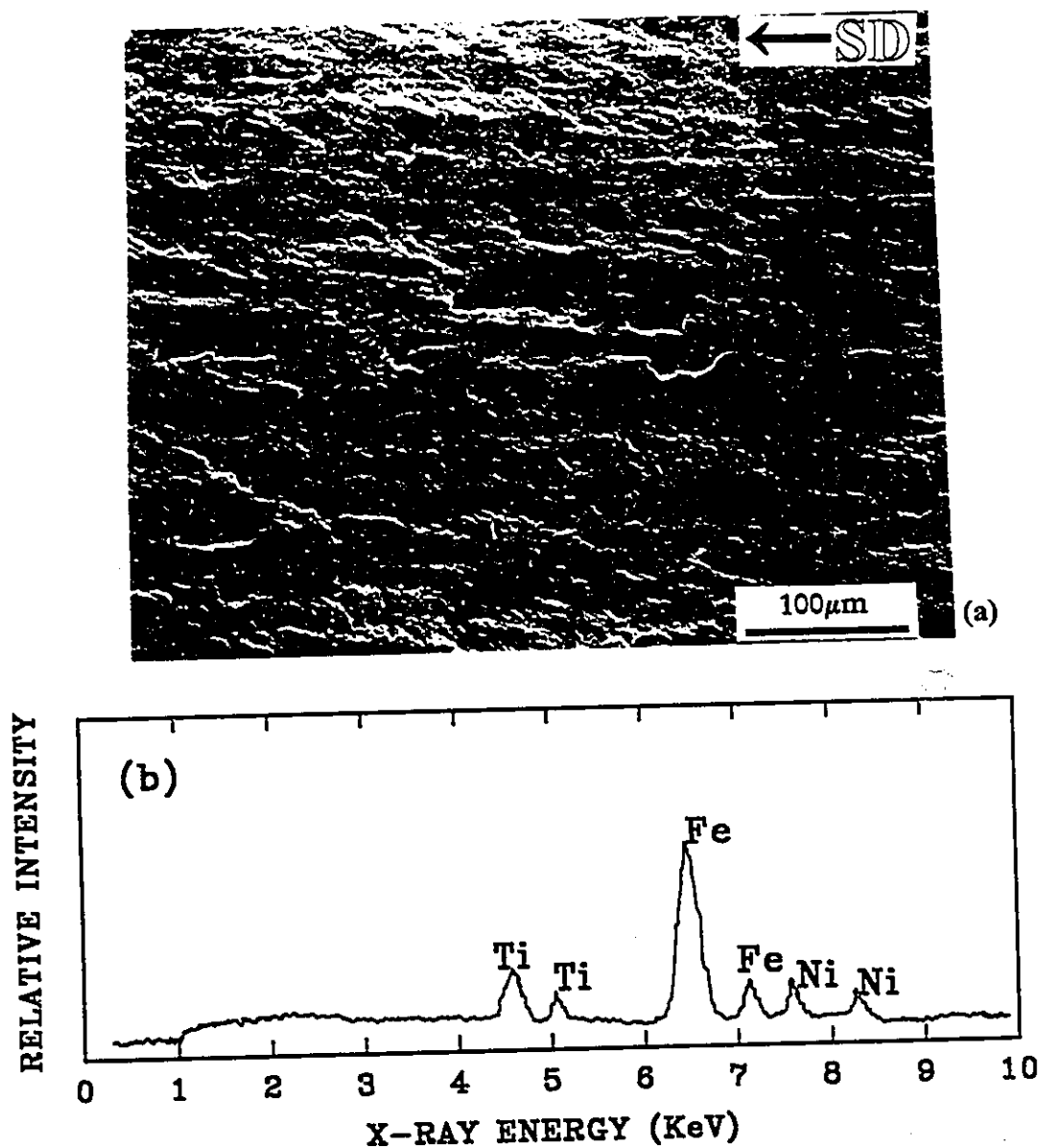


Fig. 5.12. (a) Electron micrograph of the worn surface of  $\text{Ti}_{50}\text{Ni}_{47}\text{Fe}_3$  alloy after sliding against SAE 52100 at 10N and sliding speed of  $0.4 \text{ m.s}^{-1}$ . The surface is uniformly covered by a layer of compacted wear debris. (b) Energy dispersive X-ray analysis (EDS) performed on the wear tracks indicating the presence of large amount of iron on the worn surface.

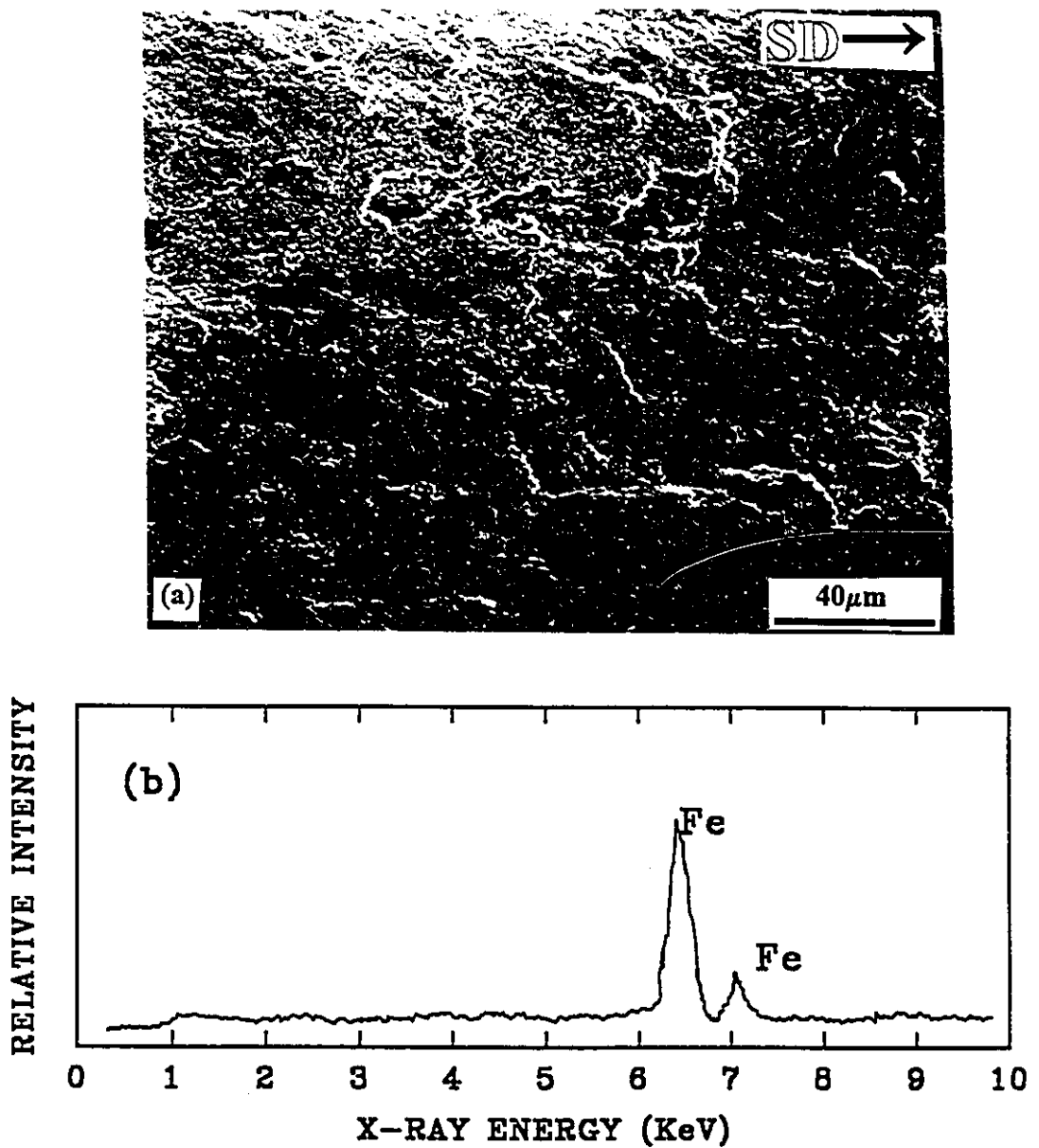


Fig. 5.13. (a) Electron micrograph of the worn surface  $\text{Ti}_{50}\text{Ni}_{47}\text{Fe}_3$  alloy after sliding against SAE 52100 at 400N load at sliding speed of  $0.4 \text{ ms}^{-1}$  depicting presence of oxide layer (sliding direction right to left). (b) EDS analysis of the wear track indicating thick iron rich layer on the surface.

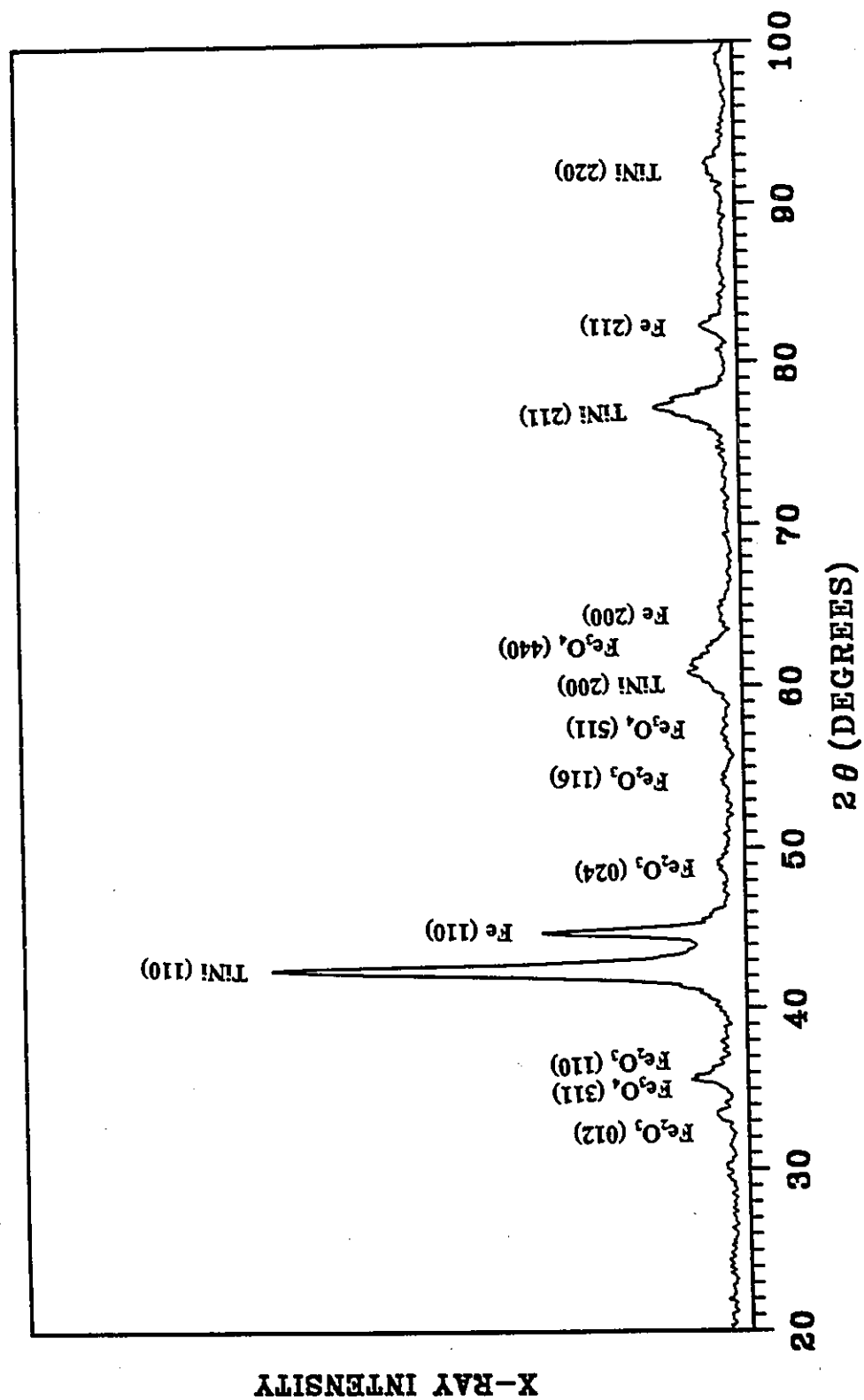
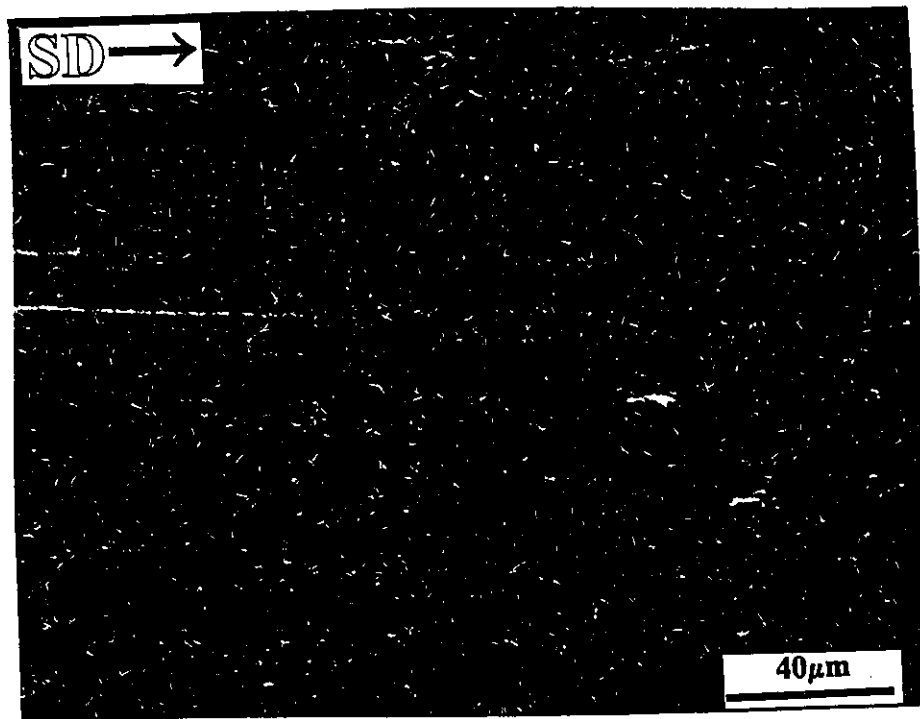
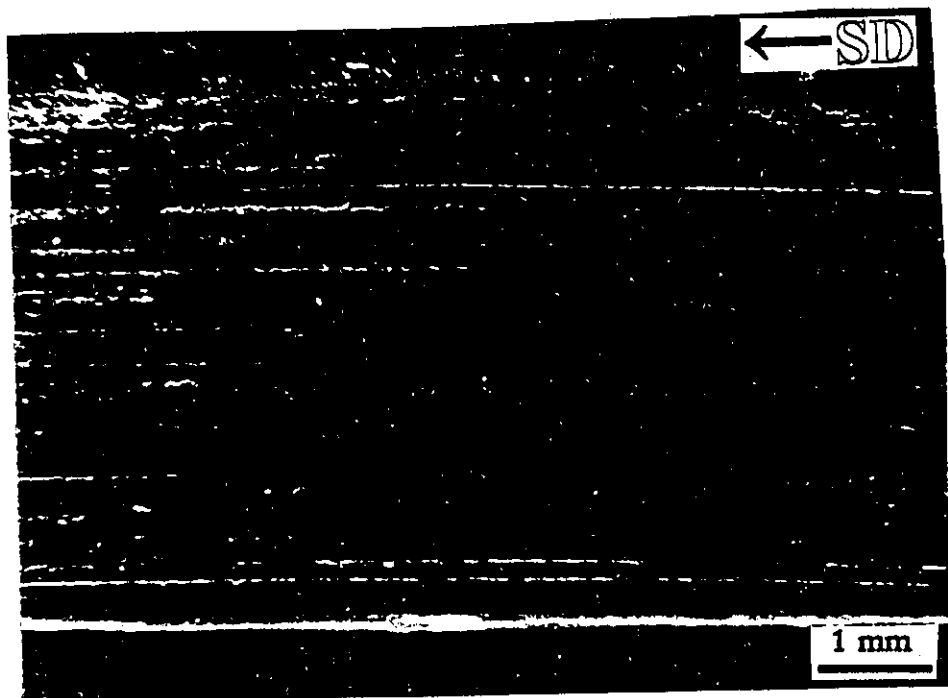


Fig. 5.14. X-ray diffraction analysis (XRD) performed on the worn surface of  $\text{Ti}_{50}\text{Ni}_{47}\text{Fe}_3$  after sliding at 400N load (sliding speed  $0.4 \text{ ms}^{-1}$ ).



**Fig. 5.15.** Surface morphology of SAE 521000 steel ring after sliding at 400 N load. Note the polished appearance of the surface. (sliding speed  $0.4 \text{ m.s}^{-1}$ ).



**Fig. 5.16.** Optical micrograph of the worn surface of  $\text{Ti}_{50}\text{Ni}_{47}\text{Fe}_3$  alloy after sliding against 52100 steel at sliding speed of  $4.2 \text{ m.s}^{-1}$  under 20 N load.

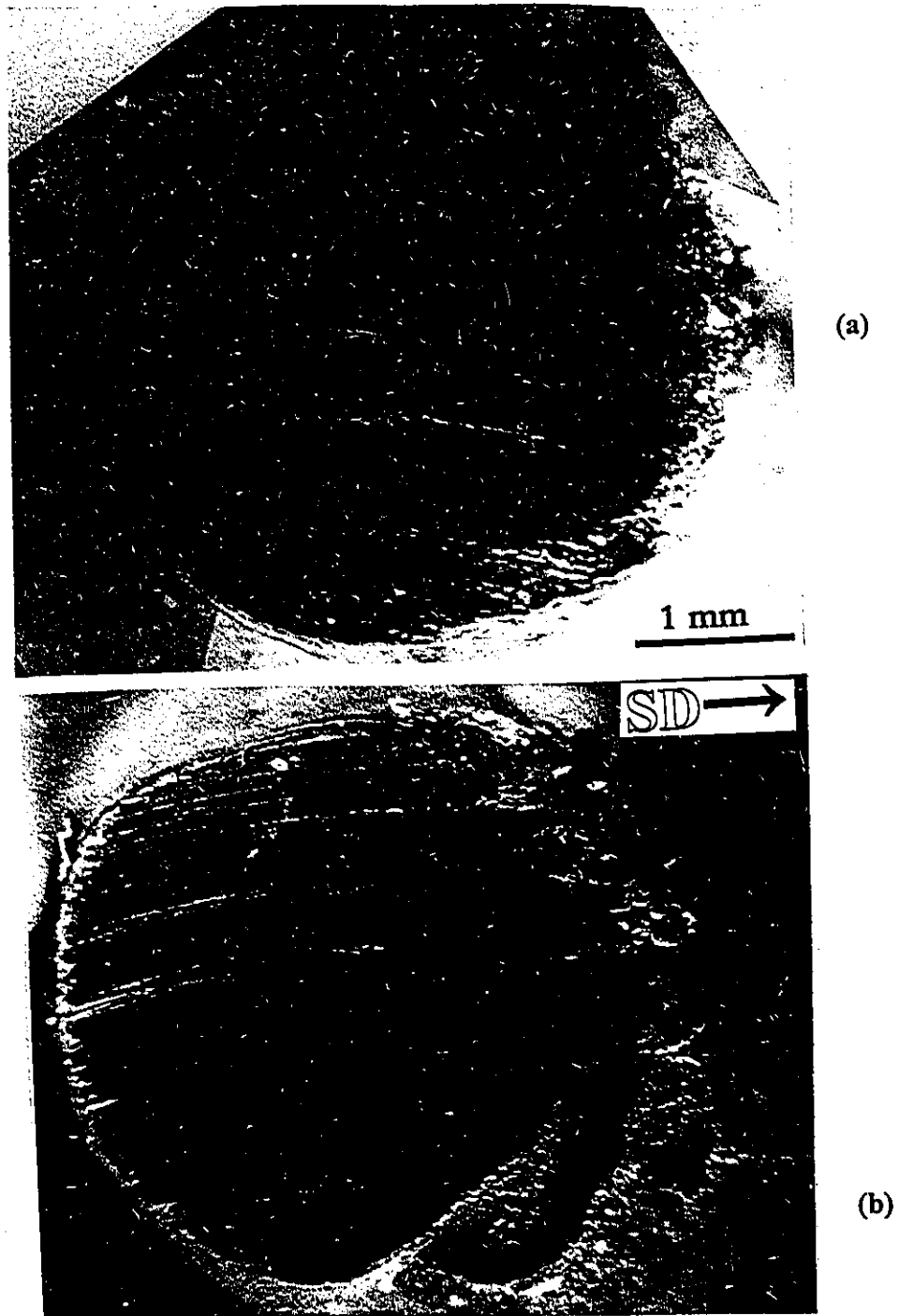


**Fig. 5.17.** Optical micrographs of the worn surfaces of  $\text{Ti}_{50}\text{Ni}_{47}\text{Fe}_3$  pins after sliding at (a) 480°C and (b) 520°C showing smooth and flattened surface. Material displaced in the direction of sliding forms a burr at the exit end.

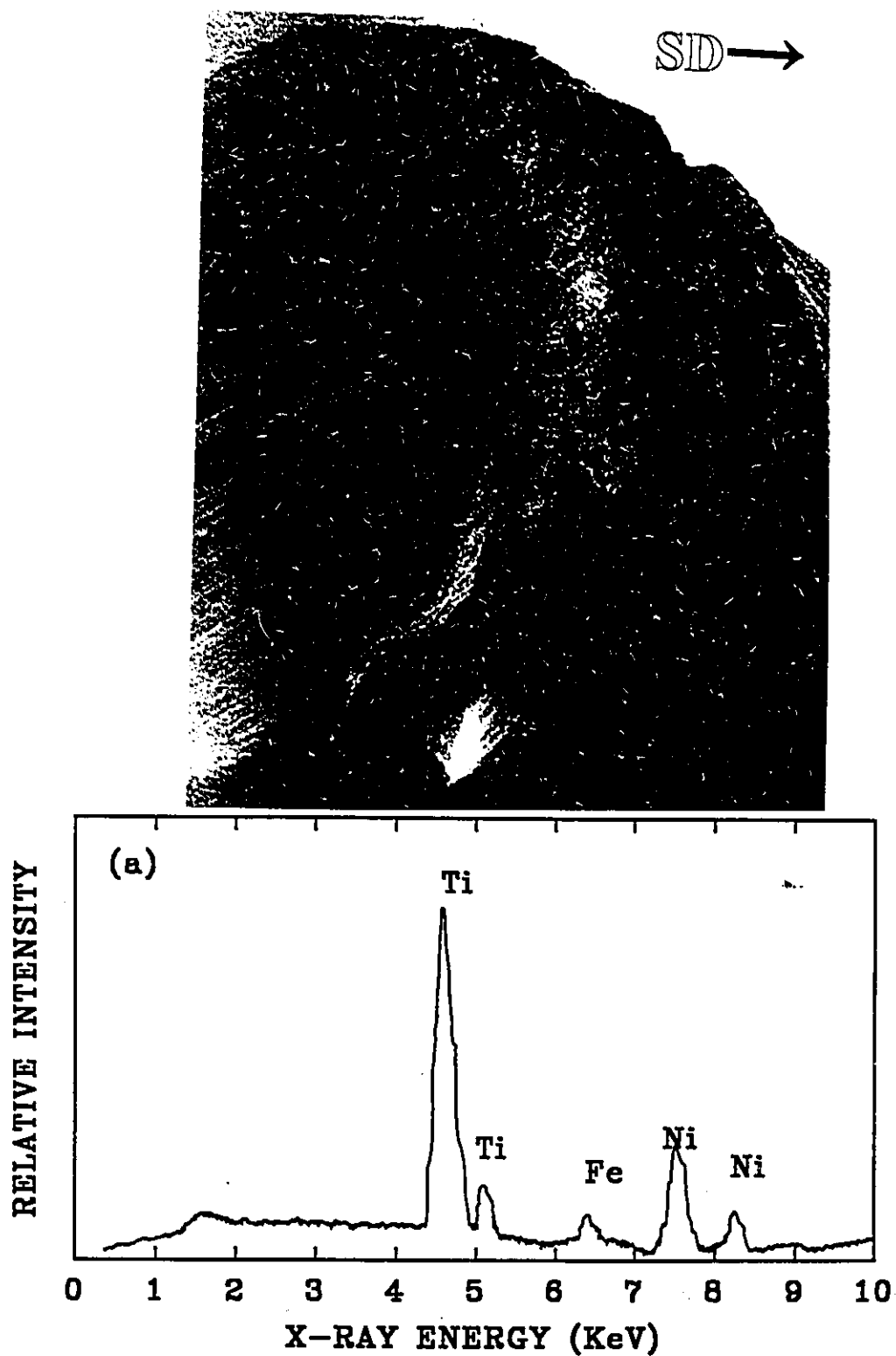


Fig. 5.18. Electron micrograph of the worn  $\text{Ti}_{50}\text{Ni}_{47}\text{Fe}_3$  pin after sliding at  $520^\circ\text{C}$ , (b) EDS analysis done on the worn track. (load 15N, sliding speed  $0.4 \text{ ms}^{-1}$ ).

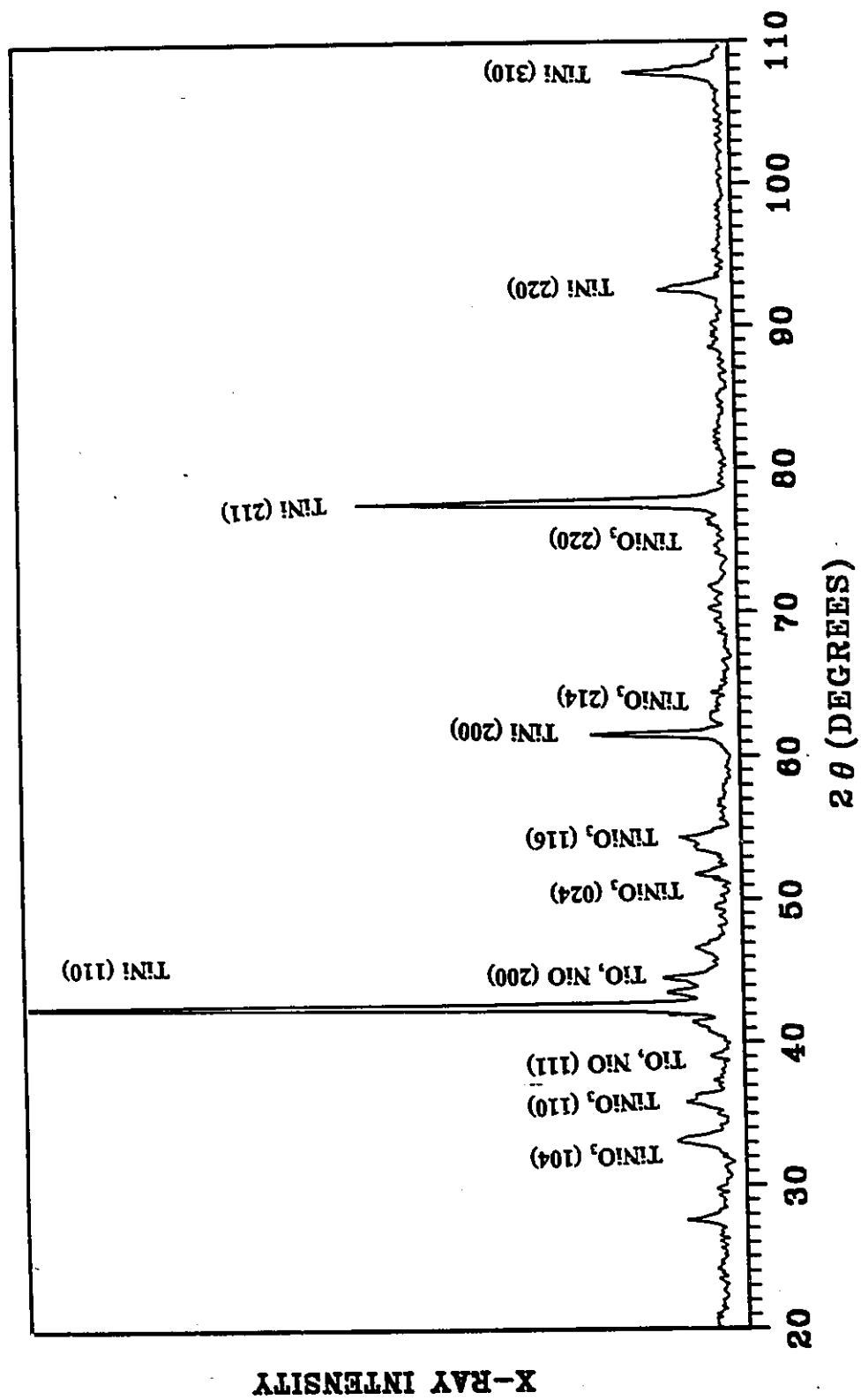
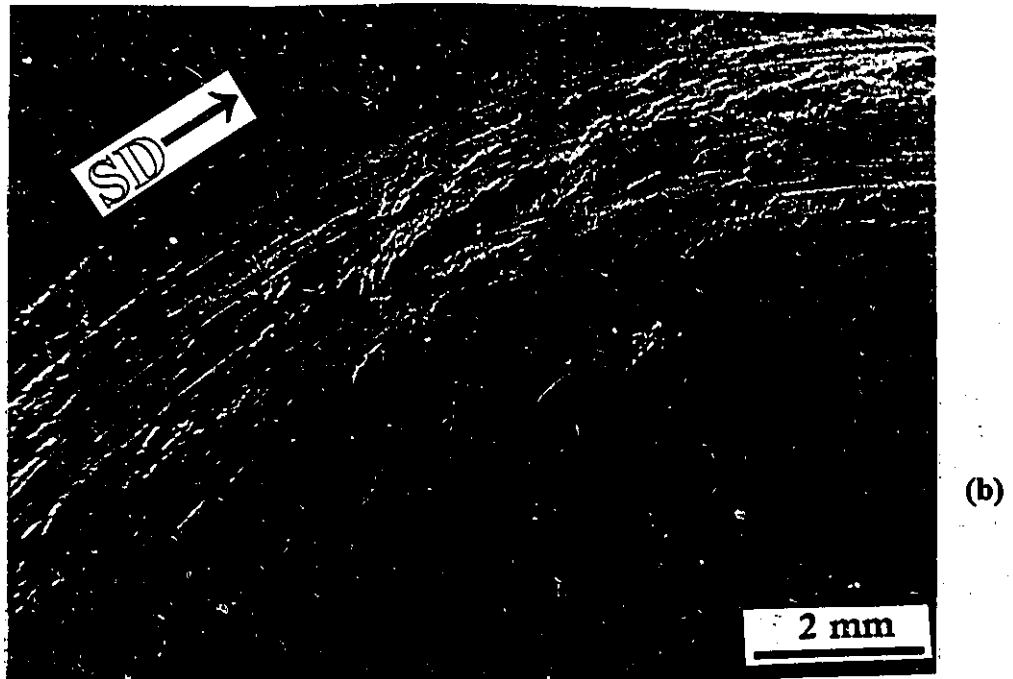
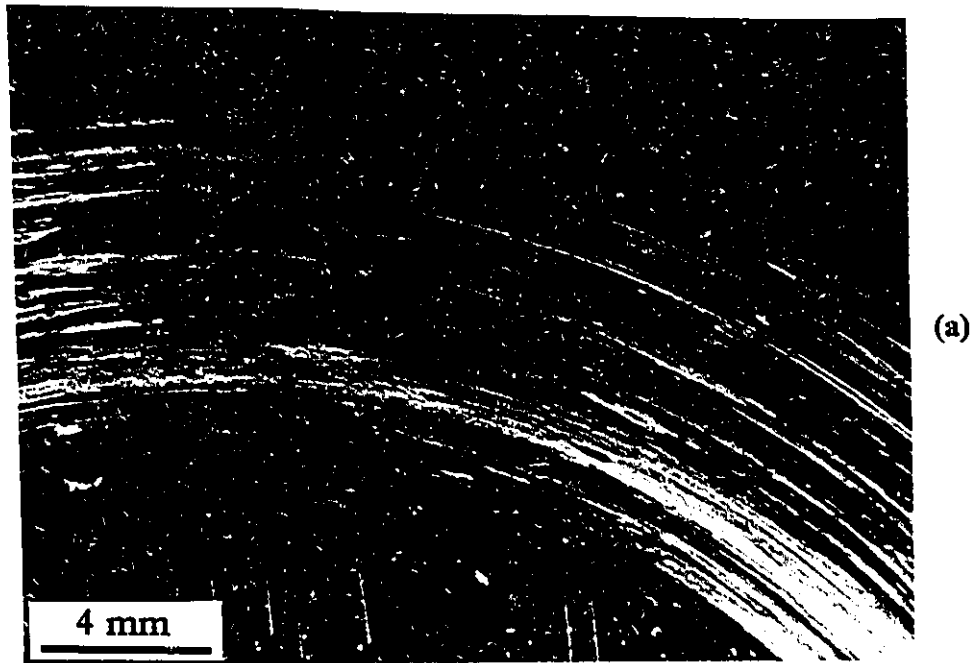
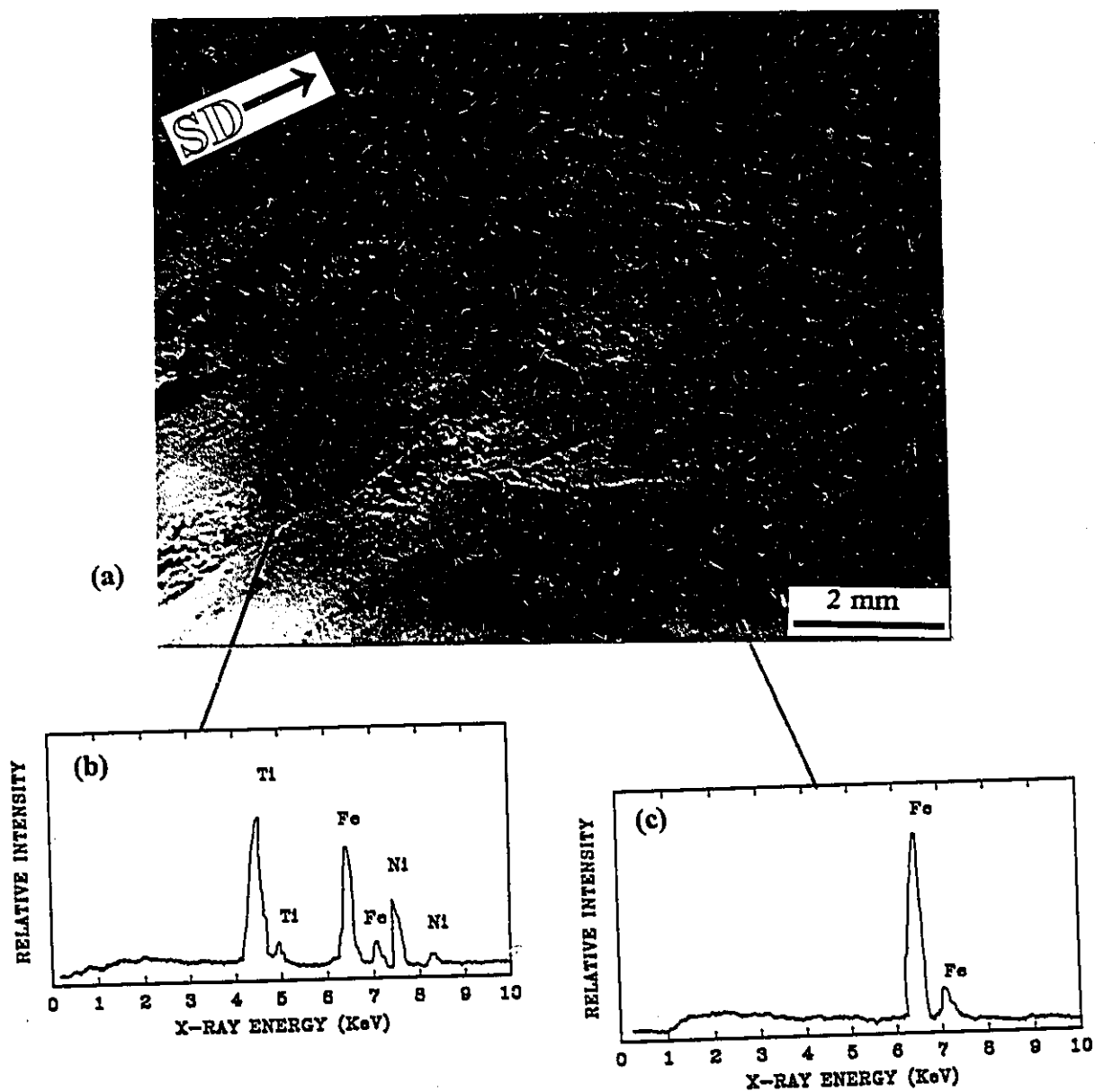


Fig. 5.19. XRD analysis performed on the wear track of  $\text{Ti}_{50}\text{Ni}_{47}\text{Fe}_3$  worn at  $520^\circ\text{C}$ . (Load 15N, sliding speed  $0.4 \text{ ms}^{-1}$ ).



**Fig. 5.20. Wear track on the surface of SAE 52100 disc (optical) after sliding at 15 N load at (a) 220°C showing deep groove, and (b) 480°C showing  $\text{Ti}_{50}\text{Ni}_{47}\text{Fe}_3$  specimen material transfer to the counterface surface.**





**Fig. 5.21. (a) Electron micrograph of wear track on the surface of SAE52100 after sliding at 520°C showing extensive specimen material transfer. EDS analysis results (b) inside the wear track, and (c) outside the wear track.**

### 5.6.2. Elevated Temperature Sliding

The worn surfaces of the  $\text{Ti}_{50}\text{Ni}_{47}\text{Fe}_3$  at low temperatures ( $<200^\circ\text{C}$ ) had the appearance (covered with black oxides) similar to those slid at room temperature at the same sliding speed. At temperatures between  $280\text{--}350^\circ\text{C}$ , the  $\text{Ti}_{50}\text{Ni}_{47}\text{Fe}_3$  surfaces suffered little damage other than disc material (native iron, oxidized iron) transferred to the specimen surface.

During severe wear at elevated temperatures ( $>350^\circ\text{C}$ ), the worn surfaces became increasingly smoother on increasing the test temperature beyond  $350^\circ\text{C}$ . Optical micrographs in Fig. 5.17(a) and (b) show the worn surface of intermetallic pins tested at  $480^\circ\text{C}$  and  $510^\circ\text{C}$ , respectively. The worn surface became flattened due to plastic flow of the material in the direction of sliding. Much of this extruded out material formed a burr at the leading end of the pin (Fig. 5.18(a)). The worn surfaces appeared to be covered with "glaze", a smooth and shiny oxide layer. EDS analysis performed showed little or no steel transfer from the disc to the intermetallic pin (Fig. 5.18(b)). XRD analysis of the pin surface slid at  $510^\circ\text{C}$  is given in Fig. 5.19. The results indicate that the worn surface is covered with oxides ( $\text{NiTiO}_3$  and  $\text{TiO}$ ).

The wear tracks on the counterface SAE52100 disc after sliding at  $200^\circ\text{C}$  and  $420^\circ\text{C}$  are shown in Fig. 5.20. A deep scar on the disc has been cut by the intermetallic pin (Fig. 5.20(a)) at  $200^\circ\text{C}$ . On the other hand, at  $420^\circ\text{C}$  (Fig. 5.20(b)), a large amount of pin material can be seen sticking on the disc surface. SEM micrograph and EDS analysis (Fig. 5.21) done on inside of the wear track shows that extensive material transfer from pin to the disc occurred during sliding at  $510^\circ\text{C}$  and was smeared along the wear track.

## 5.7. Subsurface Characterization

### 5.7.1. Room Temperature

#### 5.7.1.1. Mild Wear (Regime II, load: 20-400N, sliding speed: 0.4 ms<sup>-1</sup>)

The optical micrograph (Fig. 5.22) of a cross-section parallel to the sliding direction shows that extensive plastic deformation took place below the contact surface during sliding. In a deformation zone of about 100 $\mu$ m deep, the grains are elongated towards the sliding direction. No evidence of subsurface cracking or delamination could be observed.

The worn specimen cut and polished at a taper angle of 1-2° to the surface was also investigated. A "finger like" morphology, consisting of features elongated in the direction of sliding developed right below the worn surface as shown in Fig. 5.23(a). Microhardness (Vickers) measurements taken on the taper sections showed that the mechanically mixed layers ("fingers") have hardness values ranging from 500 to 800 kg.mm<sup>-2</sup> as compared to 350-400 kg.mm<sup>-2</sup> for the material outside them (Fig. 23(b)). The fingers were found to be resistant to abrasive wear. Metallographic polishing on wet cloth with 0.05 $\mu$ m Al<sub>2</sub>O<sub>3</sub> powder removed the material from the surrounding region at a faster rate than the fingers and therefore the fingers appear as elevated plateaus. Monitoring the size of the micro-hardness indentations before (Fig. 5.23(b)) and after the polishing (Fig. 5.24(a)) also confirmed that the material removal rate from the fingers was much lower.

Fig. 5.24(a) shows the detailed morphology of fingers. The layers appear to have a layered structure and have a clear interface with the surrounding base material. The compacted oxide layer found to be present at all loads at low sliding speeds (Fig. 5.13) was still sticking, in patches, on the polished surface within the fingers (Fig. 5.24(b)). The oxide layer appears to be well adhered to the material below. The layer fractured under the microhardness indentation but did not flake off indicating brittle nature of the layer and good adhesion with the subsurface.

These "fingers" form directly below the grooves on the worn surface. The fingers were found to penetrate to a depth of about 80-100  $\mu\text{m}$  below the surface and according to the EDS analysis (Fig. 5.25), they are composed of a mixture of Ti, Ni and Fe. Iron consistently exhibited the strongest intensity throughout the layer. Fig. 5.25 shows dark veins running parallel to the surface at a depth of about 40  $\mu\text{m}$  within the mechanically mixed layer. The veins were observed to be made up of iron and presumably of iron oxides ( $\text{Fe}_2\text{O}_3$  and  $\text{Fe}_3\text{O}_4$ ).

#### 5.7.1.2. Severe Wear (Load:20N, Sliding Speed: 2.7 $\text{m.s}^{-1}$ -6.0 $\text{m.s}^{-1}$ )

The specimen tested at sliding speeds higher than 2.6  $\text{m.s}^{-1}$  (in the severe wear regime, Fig. 5.5) revealed the presence of numerous but very fine cracks normal to both the sliding direction and the sliding surfaces (Fig. 5.26). In addition to these normal cracks, delamination cracks parallel to the wear surface were frequently observed. Such delamination cracks are clearly evident in the electron micrograph in Fig. 5.26(a). on a longitudinal cross-section of a specimen tested at a sliding speed of 4  $\text{ms}^{-1}$ . The same cross-section shown in optical micrograph in Fig.5.26(b) reveals fine normal cracks along with long parallel cracks clearly capable of generating large metallic debris obtained during severe wear at high sliding speeds.

#### 5.7.2. Elevated Temperature

Sliding at elevated temperatures ( $>400^\circ\text{C}$ ) resulted in large plastic deformation below the sliding surfaces and extrusion of the intermetallic in the direction of sliding. Longitudinal cross section of  $\text{Ti}_{50}\text{Ni}_{47}\text{Fe}_3$  pin worn at  $520^\circ\text{C}$  is shown in Fig. 5.27. The specimen material plastically flows (extrudes) in the direction of sliding and gets mushroomed at the exit end. The worn surface (Fig. 5.27(a)) of the pin is covered with a thick layer of oxides which according to XRD analysis (Fig. 5.19) are  $\text{TiNiO}_3$  and  $\text{TiO}$ . The oxide thickness on the pin surface varied with location. The thickness was minimum ( $\approx 1\mu\text{m}$ ) at the leading end and increased towards the exit end. The oxide thickness near the exit end was found to be 5-10  $\mu\text{m}$ . The subsurface was free of cracks except very close

Worn Surface

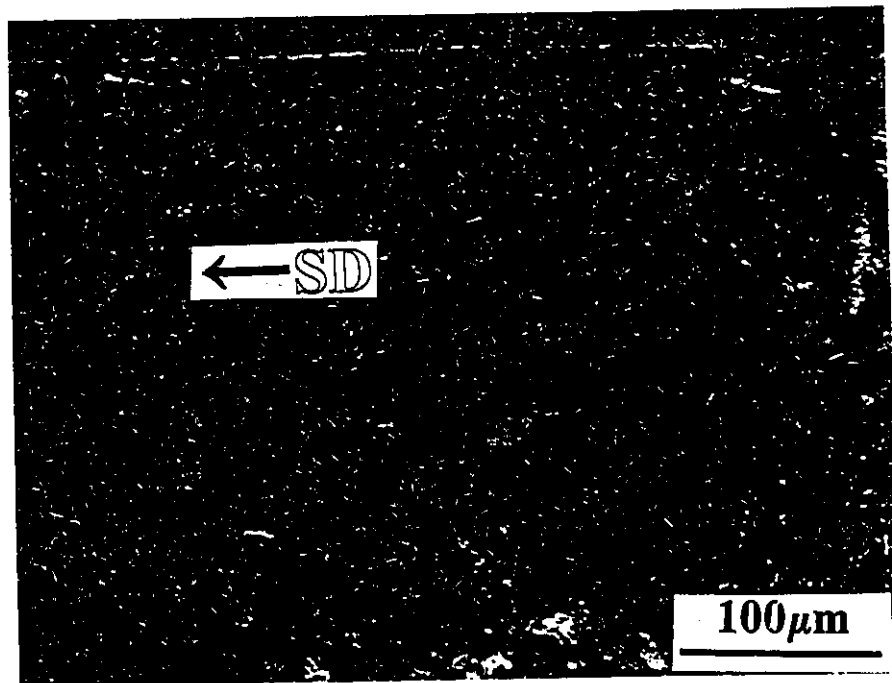


**Fig. 5.22. Longitudinal cross-section (etched) through the worn surface revealing the extent of plastic deformation during wear of  $\text{Ti}_{50}\text{Ni}_{47}\text{Fe}_3$  at 400 N load. (sliding speed  $0.4 \text{ m.s}^{-1}$ ).**

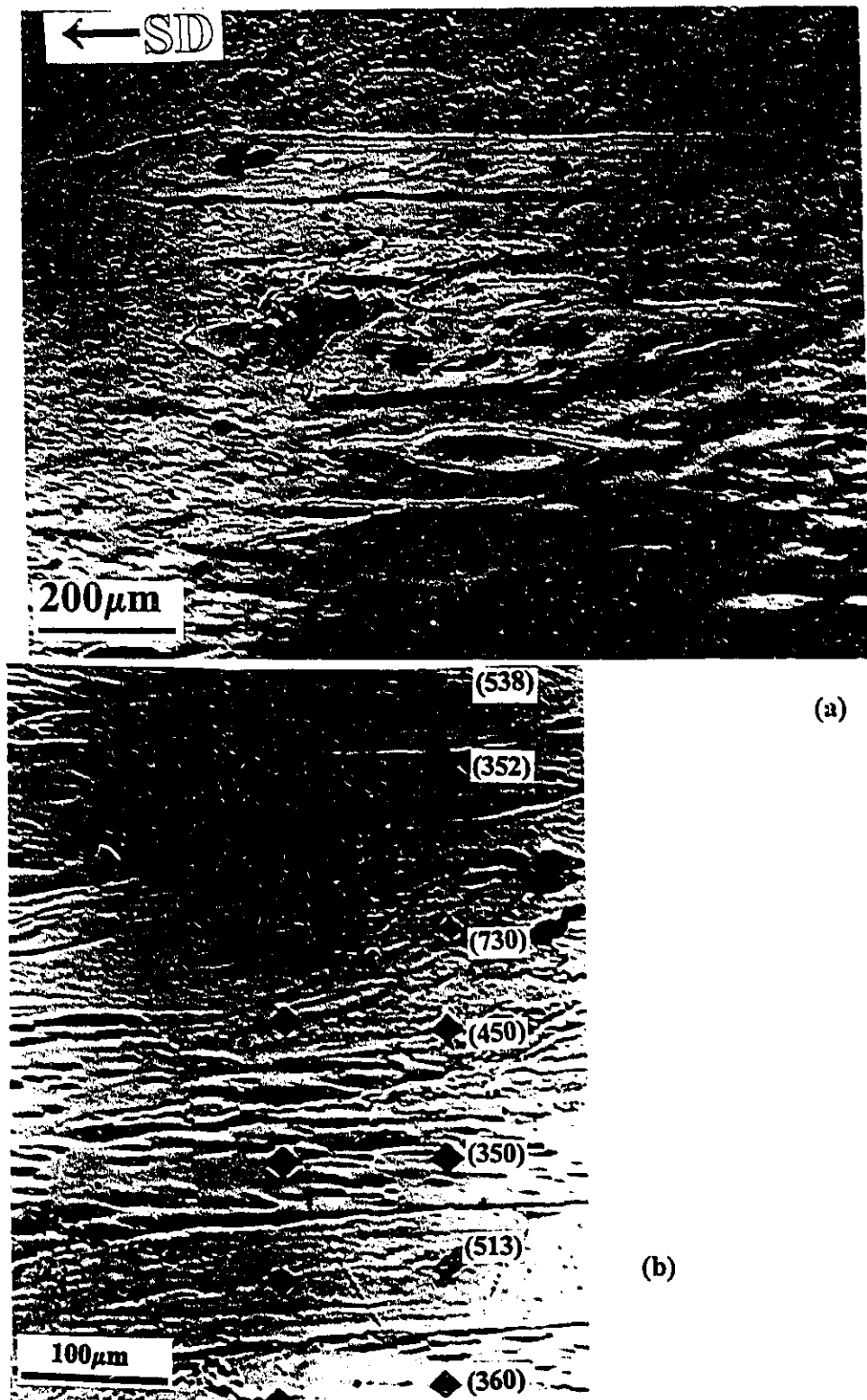
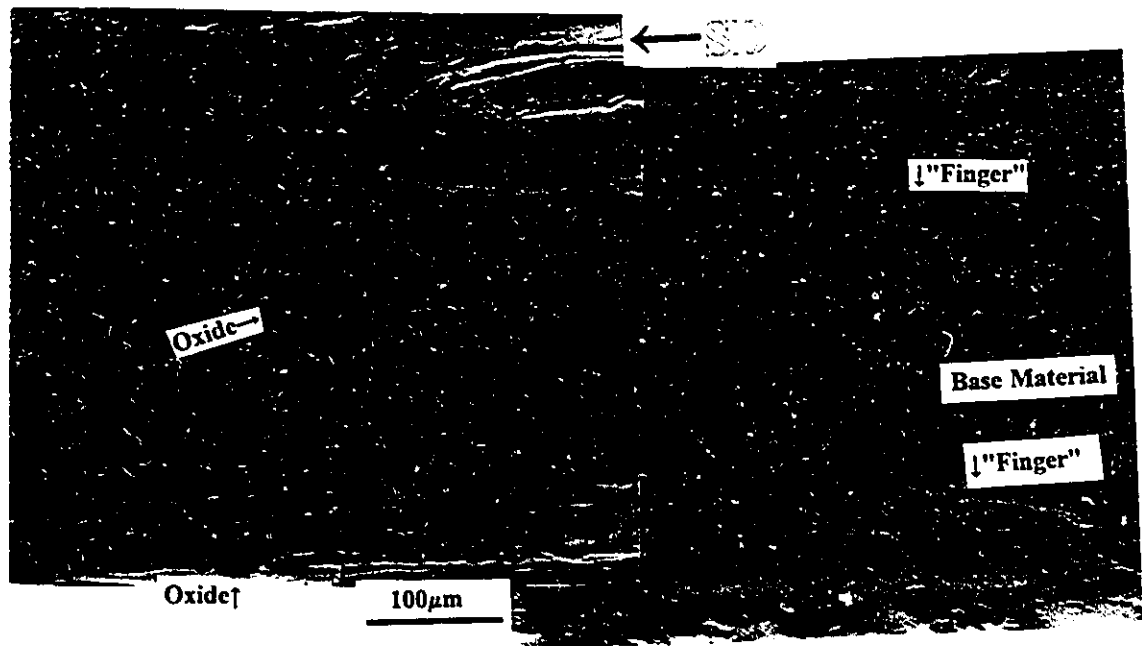


Fig. 5.23. Longitudinal tapered section of  $\text{Ti}_{50}\text{Ni}_{47}\text{Fe}_3$  tested under 400N load (1-2° to the worn surface), depicting; (a) "finger" type morphology below the contact surface; (b) microhardness values obtained at various locations at the surface in (a).



(a)



(b)

**Fig. 5.24. (a) Detailed morphology of fingers, (b) presence of oxide transfer layer adhered to the finger surface, the layer fractures under the hardness indentation.**

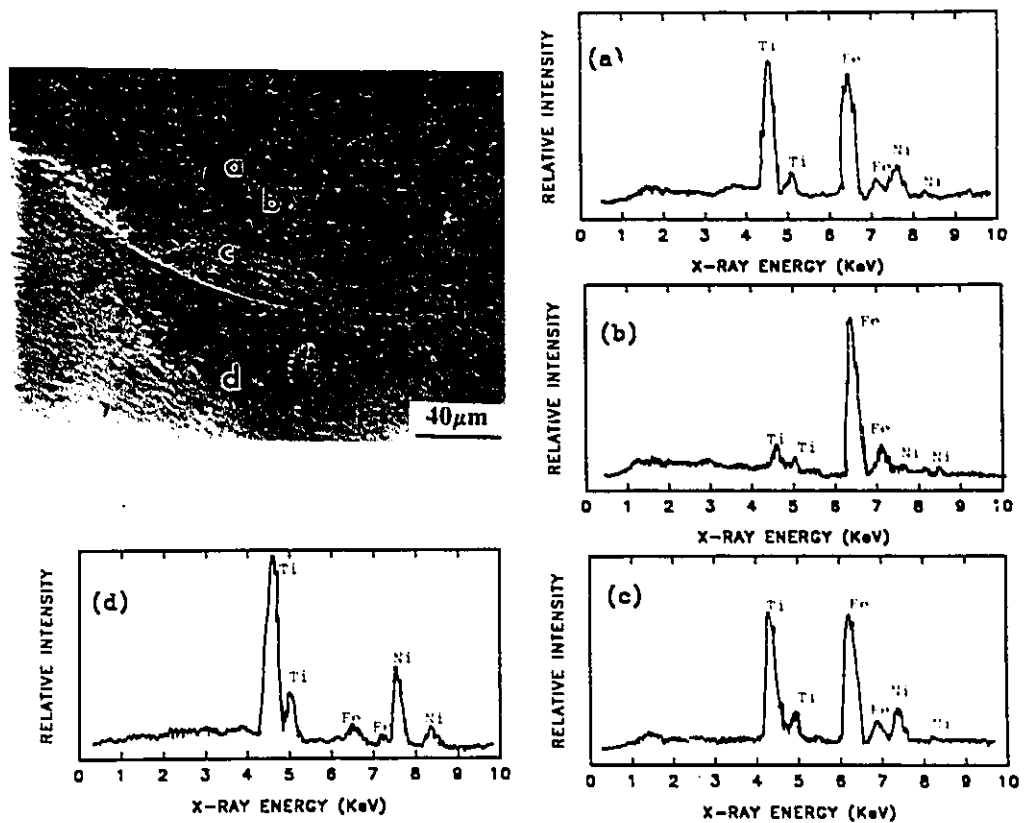
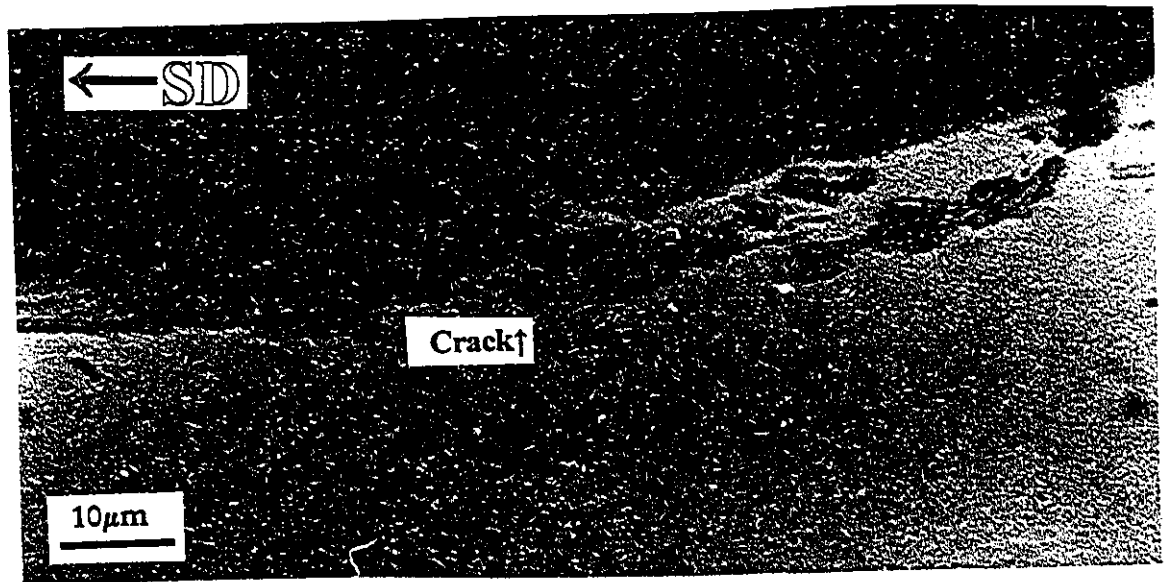
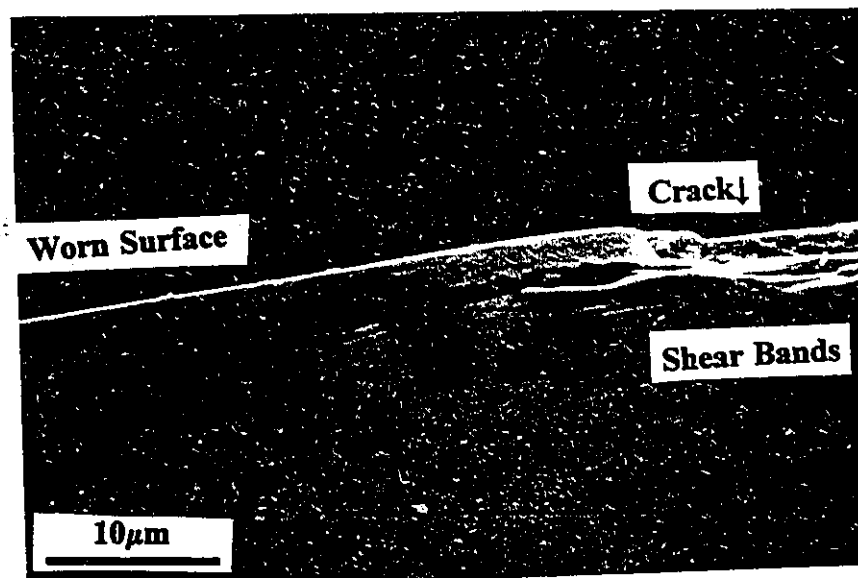


Fig. 5.25. Transverse cross-section of  $\text{Ti}_{50}\text{Ni}_{47}\text{Fe}_3$  after sliding at 400 N load at sliding speed of  $0.4 \text{ m.s}^{-1}$  and EDS analysis across the mechanically mixed layer. Locations where the analysis was performed are indicated by letters a-d.





(a)



(b)

Fig. 5.26. Longitudinal section of  $\text{Ti}_{50}\text{Ni}_{47}\text{Fe}_3$  after sliding at a speed of  $4.2 \text{ m.s}^{-1}$  at 20 N load, depicting subsurface cracking, (a) optical, (b) electron micrograph.

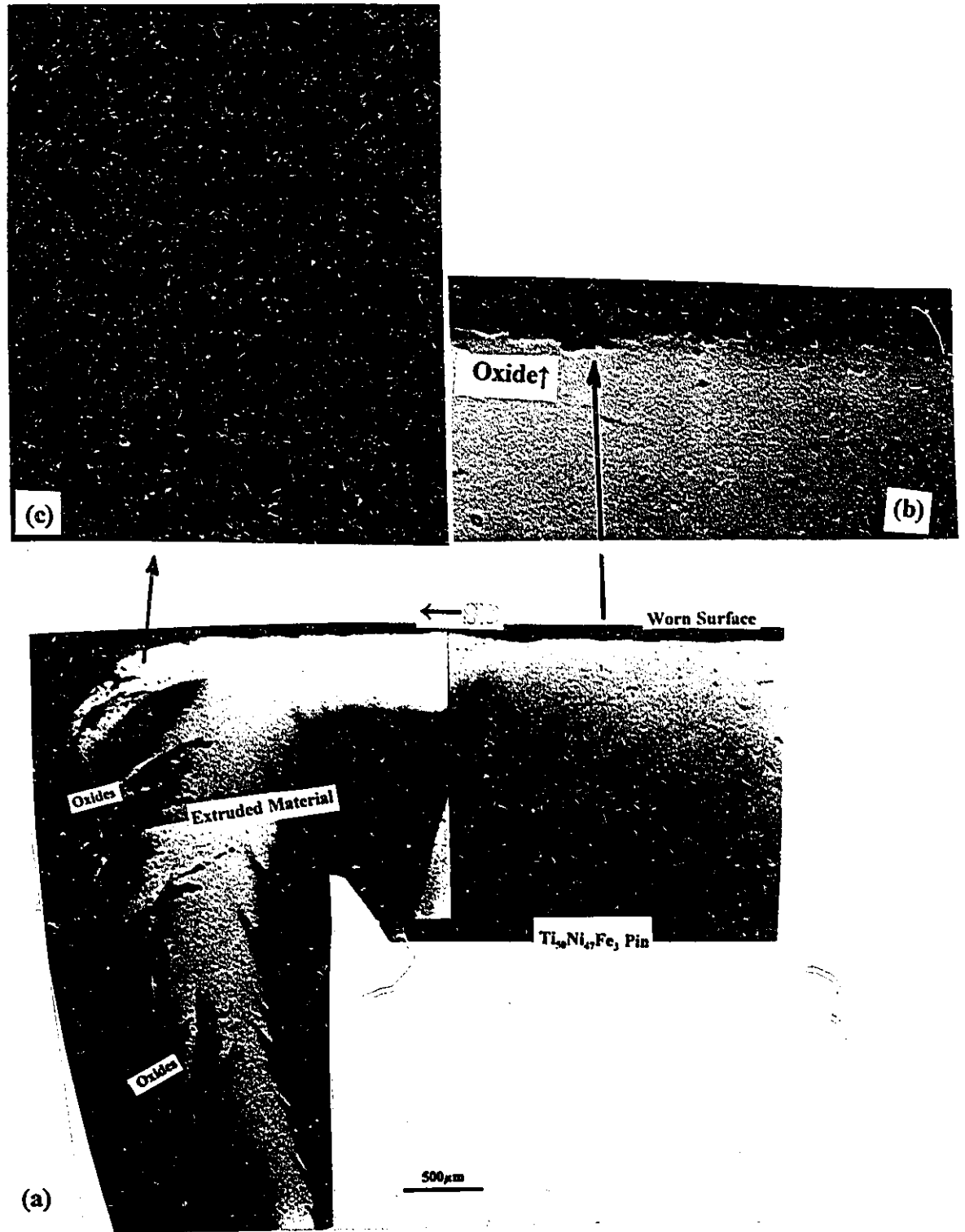
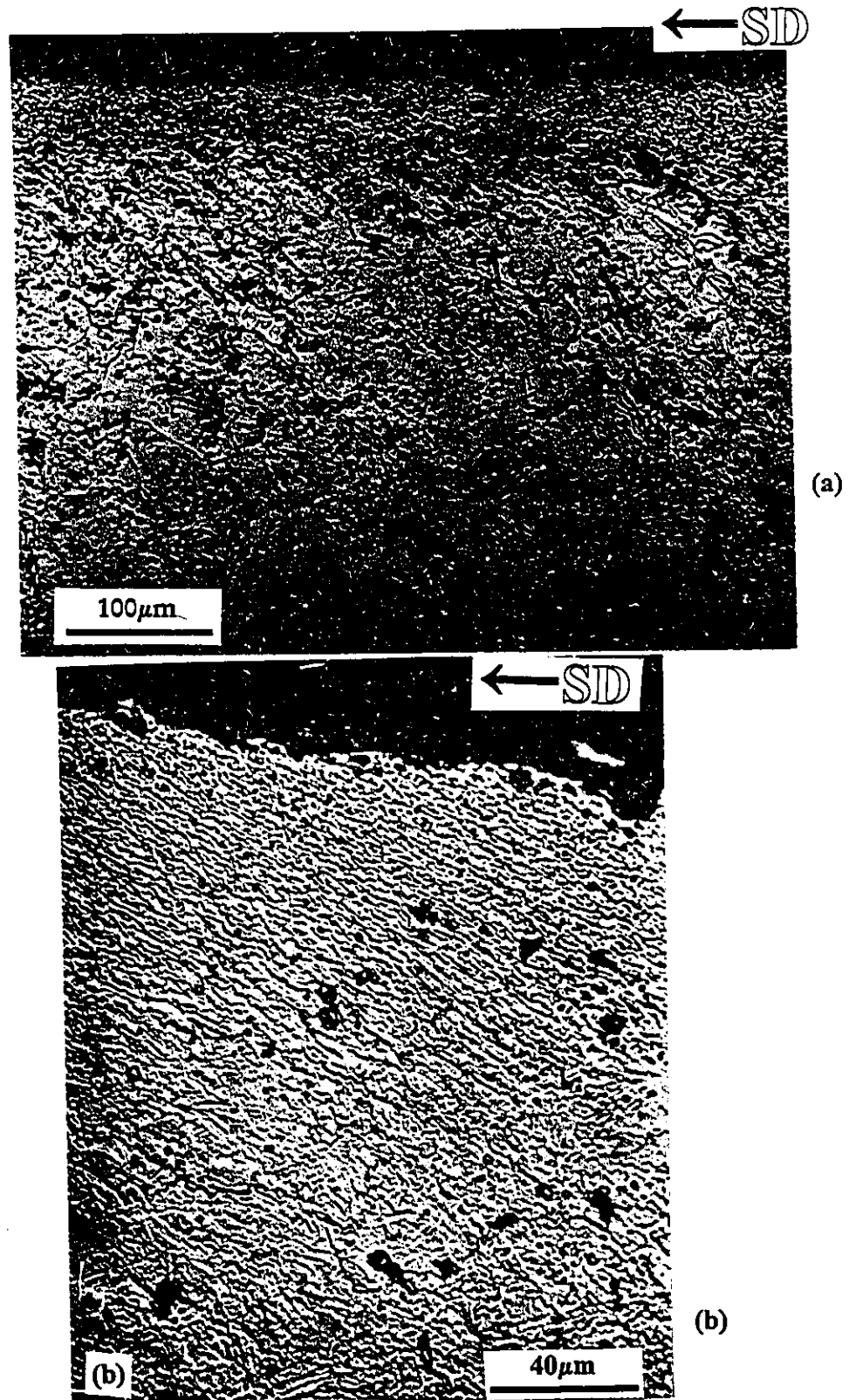


Fig. 5.27. (a) Longitudinal cross-section of  $\text{Ti}_{50}\text{Ni}_{47}\text{Fe}_3$  after sliding at  $520^\circ\text{C}$  at 15N load, showing material displacement out of the contact area, (b) a thin oxide layer on the worn surface and (c) large amount of oxide present on the extruded material.



**Fig. 5.28. Longitudinal cross-section (etched) of  $\text{Ti}_{50}\text{Ni}_{47}\text{Fe}_3$  after sliding at 520°C at 15N load (a) depicting extensive plastic deformation below the contact surface, (b) showing recrystallised grains near the contact surface.**

to the exit end where small normal cracks could be observed. The debris particle appears to be generated very close to or outside of the exit end.

The pin material extruded out at the exit end is covered with significantly thicker oxide layer (Fig. 5.27(c)). It appears that the oxide formed at the contact surface is continuously driven out due to plastic flow below the contact surface. Cracks are evident within the platelet type morphology of the extruded material.

Chemical etching of the longitudinal section shown in Fig. 5.27 revealed extensive plastic deformation below the contact surface (Fig. 5.28(a)). Recrystallized grains are evident in Fig. 5.28(b) near the contact surface.

## 5.8. Summary of Observations

One of the most important results obtained in the present study is that the intermetallic  $\text{Ti}_{50}\text{Ni}_{47}\text{Fe}_3$  shows 2-5% as much wear as steel during dry sliding wear against the SAE 52100 steel although the intermetallic has a lower bulk hardness ( $300 \text{ kg.mm}^{-2}$ ) in comparison to that of the SAE 52100 bearing steel ( $900 \text{ kg.mm}^{-2}$ ).

The worn surfaces of  $\text{Ti}_{50}\text{Ni}_{47}\text{Fe}_3$  are severely deformed during sliding at high loads ( $>20\text{N}$ , sliding speed  $0.4 \text{ m.s}^{-1}$ ). The surfaces were covered by an iron rich layer which consisted of compacted oxide particles. Metallography indicated that beneath the oxide layer are finger like features which are mechanically mixed tribo-layers composed of iron (possibly  $\text{Fe}_2\text{O}_3$  and  $\text{Fe}_3\text{O}_4$ ) and Ti and Ni compounds.

The intermetallic showed a transition to severe wear when the sliding speed was increased beyond  $2.7 \text{ m.s}^{-1}$ . Numerous fine cracks normal to the sliding surfaces as well as large cracks parallel to the wear surface were observed at higher sliding speeds. The counterface steel showed mild oxidational wear to severe oxidational wear at a lower sliding speed ( $2.5 \text{ m.s}^{-1}$ ).

The wear rates of the intermetallic slowly decreased when temperature was increased above room temperature up to 200°C. Further increase in temperature resulted in sharp fall in wear of  $\text{Ti}_{50}\text{Ni}_{47}\text{Fe}_3$ . Above 350°C, transition to severe wear occurred and the wear rates accelerated rapidly. Elevated temperature severe wear was characterised by: material transfer from intermetallic pin to 52100 disc, large scale plastic deformation (100-1000% near the contact surface) in the subsurface, recrystallization and grain refinement near the contact surface, and glazed reflective appearance of the worn surface of the pin.

A general summary of important results is given in Table 5.2.

Table 5.2. Summary of wear behaviour of  $Ti_{50}Ni_{47}Fe_3$  during sliding against SAE52100 steel.

| (a) Effect of load         |                                  | Regime I   | Regime II   | Regime III  |
|----------------------------|----------------------------------|--|---|---|
| Applied load               |                                  | 5-20N  | 20-200N   | 200-400N  |
| Wear rates<br>( $mm^3/m$ ) | $Ti_{50}Ni_{47}Fe_3$<br>SAE52100 | $1 \times 10^{-6}$ - $1 \times 10^{-5}$<br>$2 \times 10^{-5}$ - $2 \times 10^{-4}$ | $1 \times 10^{-5}$ - $1 \times 10^{-4}$<br>$2 \times 10^{-4}$ - $2 \times 10^{-3}$      | $> 2 \times 10^{-3}$  |
| Worn<br>surface            | $Ti_{50}Ni_{47}Fe_3$             | .smooth<br>.reddish brown (oxide) layer<br>.no plastic deformation                 | .shallow groves<br>.dark brown (oxide) layer<br>.plastic deformation<br>.Hardened layer | .rough with deep groves<br>.black layer (Fe rich)<br>.heavy plastic deformation<br>.formation of hardened fingers |
|                            | SAE52100                         | .smooth and shinny   | .fine groves, shinny  | .uneven shinny  |
| wear debris                |                                  | .fine powder<br>.reddish brown<br>.oxide ( $Fe_2O_3$ )                             | .fine powder<br>.dark brown<br>.oxide ( $Fe_2O_3, Fe_3O_4$ )                            | .black and mixed<br>.large metallic Fe and<br>.fine oxide ( $Fe_2O_3$ and $Fe_3O_4$ )                             |
| Subsurface                 | $Ti_{50}Ni_{47}Fe_3$             | .No plastic Deformation  | .Plastic Deformation<br>.Oxide layer on the surface<br>.Mechanically mixed layer        | .Large plastic Deformation<br>.Thick oxide layer<br>.Mechanically mixed layer<br>"Finger" morphology              |

Table 5.2. Continued.

| (b) Effect of sliding speed.             |   |  |
|--|---|--|
|  | Mild Wear   | Severe Wear  |
| Sliding speed                            | $<2.5 \text{ ms}^{-1}$  | $>2.7 \text{ ms}^{-1}$   |
| Wear rates<br>( $\text{mm}^3/\text{m}$ ) | $\text{Ti}_{50}\text{Ni}_{47}\text{Fe}_3$<br>SAE52100<br>$1 \times 10^{-5} - 2 \times 10^{-5}$<br>$3 \times 10^{-4} - 6 \times 10^{-4}$ | $2 \times 10^{-4} - 3 \times 10^{-4}$<br>$3 \times 10^{-5} - 2 \times 10^{-5}$                 |
| Worn surfaces                            | $\text{Ti}_{50}\text{Ni}_{47}\text{Fe}_3$<br>.reddish brown<br>.Fine groves<br>.subsurface deformation<br>.hardened layer               | .black patches<br>.rough with deep groves<br>.minimal deformation<br>.subsurface cracks        |
| Wear debris                              | .fine powder<br>.reddish brown<br>.iron oxides ( $\text{Fe}_2\text{O}_3, \text{Fe}_3\text{O}_4$ )                                       | .large( $\approx 100 \mu\text{m}$ )<br>.metallic ( $\text{Ti}_{50}\text{Ni}_{47}\text{Fe}_3$ ) |
| Subsurface                               | $\text{Ti}_{50}\text{Ni}_{47}\text{Fe}_3$<br>No subsurface cracks   | .Extensive cracking<br>.Cracks normal to as well as parallel to worn surface                   |

Table. 5.2. Continued.

| (c) Effect of temperature. |   | 25°C-250°C   | 250°C -350°C   | 350°C -520°C   |
|----------------------------|---|--|--|--|
| Wear rates                 | Ti <sub>50</sub> Ni <sub>47</sub> Fe <sub>3</sub> | 5x10 <sup>-6</sup> -3x10 <sup>-6</sup>   | Negizable  | 6x10 <sup>-6</sup> -2x10 <sup>-4</sup>   |
|                            | SAE52100  | 1.5x10 <sup>-4</sup> -6x10 <sup>-4</sup>   | ~1.5x10 <sup>-3</sup>  | Weight gain  |
|                            |   | 1.0-1.5  | 0.5  | 0.5-1.0  |
| Wear Debris                | Ti <sub>50</sub> Ni <sub>47</sub> Fe <sub>3</sub> | .Fine powder<br>.Brown-black<br>.Oxidised (Fe <sub>2</sub> O <sub>3</sub> and Fe <sub>3</sub> O <sub>4</sub> ) | .Mixed,<br>.Small metallic (Fe) and<br>black oxidised powder | .Large metallic  |
|                            |   |  |  |  |
|                            |   |  |  |  |
| Worn Surfaces              | Ti <sub>50</sub> Ni <sub>47</sub> Fe <sub>3</sub> | .Iron(oxide) transfer  | .Extensive Iron transfer                                     | .small iron transfer<br>.Smooth reflective "glaze"<br>.Oxidised (TiNiO <sub>3</sub> , TiO) |
|                            |   |  |  |  |
|                            |   |  |  |  |
| Subsurface Deformation     | 52100   | .Deep groove along wear track<br>.Shiny and Smooth   | .Deep groove<br>.Oxidised and smooth                         | .Intermetallic transfer<br>.Rough and uneven   |
|                            | Ti <sub>50</sub> Ni <sub>47</sub> Fe <sub>3</sub> | No data  | No data  | .Extensive plastic   |
|                            |   |  |  | .Recrystallization<br>.Grain Refinement<br>.Oxide layer                                    |



## B. Discussion of the Results

### 5.9. Room Temperature Wear

#### 5.9.1. Effect of Load

The wear rates of the intermetallic at low sliding speeds against hardened SAE 52100 steel depicted as regime I in Fig. 5.4 can be termed as "ultra-mild". The wear rates of  $\text{Ti}_{50}\text{Ni}_{47}\text{Fe}_3$  are only 3% of those of the hard counterface 52100 steel. This is surprising because the bulk hardness of  $\text{Ti}_{50}\text{Ni}_{47}\text{Fe}_3$  is only  $300 \text{ kg.mm}^{-2}$  as compared to  $870 \text{ kgmm}^{-2}$  for the hardened (Q&T) 52100 steel. However, examination of worn surfaces revealed the presence of oxide transfer layers (Fig. 5.12) on the worn surfaces. Formation of this type of layers has been shown to improve the wear resistance of various iron and nickel alloys [53,108,109]. Presence of these oxide layers reduces the coefficient of friction and the sliding damage by reducing adhesion as less metal to metal contact takes place.

The wear rates decreased progressively during the wear run. In the beginning of the wear process,  $\text{Ti}_{50}\text{Ni}_{47}\text{Fe}_3$  makes direct contact with the steel ring and therefore shows high wear rates (Fig. 5.3(a)). When a layer of iron oxides starts to form on the surface of the  $\text{Ti}_{50}\text{Ni}_{47}\text{Fe}_3$ , the wear rates show a decrease with increasing sliding distance until this layer reaches an equilibrium thickness to give steady low wear rates.

In wear regime II (Fig. 5.4) i.e. at loads  $>20\text{N}$ , the  $\text{Ti}_{50}\text{Ni}_{47}\text{Fe}_3$  wear rates remain 20-50 times lower than the counterface 52100. The intermetallic, however, shows better wear resistance than in the wear regime I (low loads). The wear of the intermetallic now increased at a lower rate on increasing the applied load than during the wear regime I. This can be attributed to three factors: (i) increase of surface hardness due to work hardening of  $\text{Ti}_{50}\text{Ni}_{47}\text{Fe}_3$  due to large plastic strains near the contact surface, (ii) formation of thicker transfer layer, and (iii) formation very hard (hardness up to  $800 \text{ kg.mm}^{-2}$ )

mechanically mixed layers below the wear track. These factors result in formation of four zone morphology below the contact surface (Fig. 5.29)

Sliding at high loads resulted in formation of deep grooves on the wear track. These wear tracks were covered with a thick transfer layer (Zone 4 in Fig. 5.29). The transfer has higher thickness now (Fig. 5.13) as compared to that observed at low loads (Fig. 5.12). The transfer layer had the same colour and composition as the wear debris. XRD analysis (Fig. 5.14.) of the wear track showed that the surface layer contained iron and its oxides ( $\text{Fe}_2\text{O}_3$  and  $\text{Fe}_3\text{O}_4$ ). The thicker transfer layer is expected to give better protection to the specimen surface during sliding.

In addition to the transfer layers, sliding at high loads in regime II led to formation of very hard (Fig. 5.23) metallic layers below the transfer layer. EDS showed presence of large amount of iron (Zone 3 in Fig. 5.29). These layers give finger like features below the wear surface. The mechanically mixed layers were found to be more resistant to abrasive wear than the base alloy and are therefore, expected to improve the sliding wear of the intermetallic. However, they are expected to play a more important role, which is to support the transfer layer.

The transfer layers have been shown to be dynamic in nature. The layer is disrupted, gets removed and reforms continuously in the course of sliding. Removal of the layer at times allows metal to metal contact between the intermetallic and hard steel. The intermetallic will then undergo adhesive wear due to very low hardness of  $\text{Ti}_{50}\text{Ni}_{47}\text{Fe}_3$  alloy. However, due to very low wear rates of the intermetallic, XRD did not reveal in what form (metallic or oxidized) the wear debris particles are generated. Increase of applied load in wear regime I, will disrupt the layer more often and, therefore, results in large increase in the wear rates of the intermetallic. At high loads (regime II) large plastic deformations result in formation of hard mechanically mixed layer, which reduces the sliding wear damage whenever the transfer layer is disrupted.

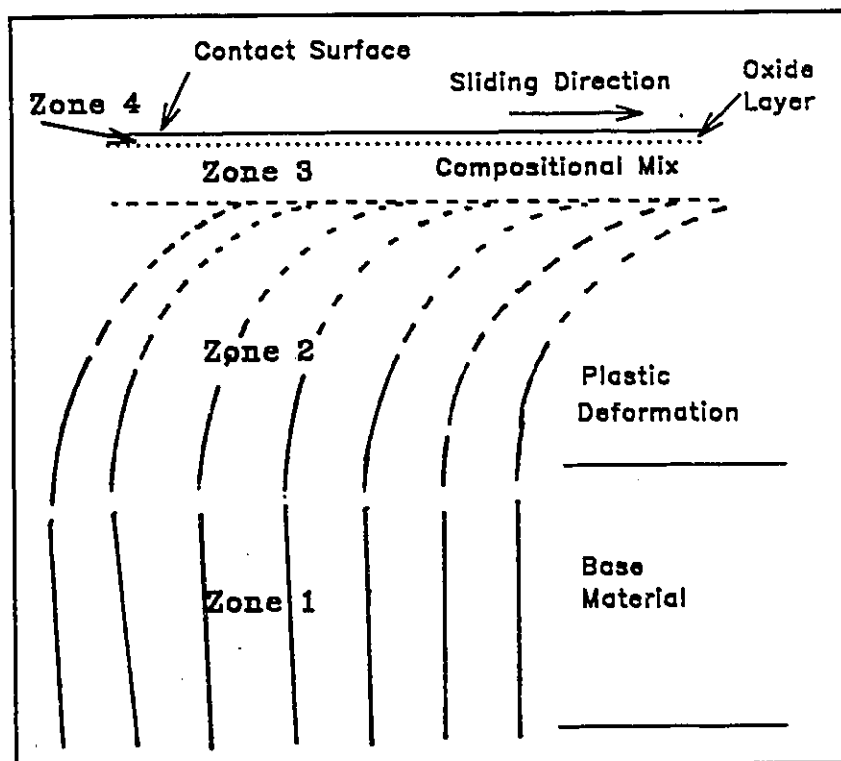


Fig. 5.29. Subsurface changes in  $\text{Ti}_{20}\text{Ni}_{47}\text{Fe}_3$  after sliding against SAE52100 during mild wear at room and elevated temperatures (schematic).

In ductile materials, wear processes generate large plastic strains beneath the contact surfaces [107]. It is shown by cold rolling experiments (Fig. 5.1) that  $\text{Ti}_{50}\text{Ni}_{47}\text{Fe}_3$  can considerably work-harden at high strains. Subsurface examination of the specimen tested in regime II revealed large plastic deformations (Fig. 5.22) in the subsurface region and is depicted as Zone 2 in Fig. 5.29. In fact, the microhardness measurements taken on the contact surface in locations outside the mechanically mixed finger like features, indicate that the surface hardness of  $\text{Ti}_{50}\text{Ni}_{47}\text{Fe}_3$  can reach up to  $400 \text{ kgmm}^{-2}$  an increase of about 30% relative to the bulk hardness. Thus, the hardening of the contact surfaces during wear is expected to increase the wear resistance of  $\text{Ti}_{50}\text{Ni}_{47}\text{Fe}_3$ . It is important to note that the cold worked intermetallic material can retain its strength at elevated temperatures (Table. 3.1), so that, work hardened zone below the contact surface is not expected to work-soften while the contact surface temperature increases during the sliding process.

#### 5.9.2. Effect of Sliding Speed

The wear of  $\text{Ti}_{50}\text{Ni}_{47}\text{Fe}_3$  can be described as mild at low sliding speeds and severe at high sliding speeds (greater than  $3.0 \text{ m.s}^{-1}$ ) as indicated by the shape of the wear rate versus the sliding velocity plot of Fig. 5.5. At low sliding speeds, the low wear rates of this alloy can be attributed to the work hardening of the surface layers and the formation of a hardened wear resistant layer which consists of iron oxides and the base alloy. However, above a critical sliding speed of about  $3.0 \text{ m.s}^{-1}$ , the tribo-layers cease to form. Metallographic examination of the subsurface region showed no sign of formation of finger like features or iron oxide veins at high sliding speeds. Instead, cracks emanating from the bottom of the surface grooves running normal to the wear surface were observed. The wear process, under these conditions, produces metallic debris in the  $100 \mu\text{m}$  size range.

The  $\text{Ti}_{50}\text{Ni}_{47}\text{Fe}_3$  alloy is softer (hardness  $300 \text{ kg.mm}^{-2}$ ) as compared to the SAE 52100 alloy (hardness  $900 \text{ kg.mm}^{-2}$ ) and is expected to wear at a higher rate once the protective surface layers stop to form. Fig. 5.26 shows that severe delamination occurs at

high sliding speeds. It appears that the ductility of  $\text{Ti}_{50}\text{Ni}_{47}\text{Fe}_3$  is adversely effected by the high strain rates caused by high sliding speeds. This could also be the result of thermal fatigue due to higher temperature gradients and thermal cycling of the unprotected surface. Formation of martensite (under high stresses and strains at the contact surface) can be a plausible explanation for the above behaviour. Stress-strain curves for the  $\text{Ti}_{50}\text{Ni}_{47}\text{Fe}_3$  alloy determined at room temperature did not show any martensite transformation strains. The  $M_s$  temperature of  $\text{Ti}_{50}\text{Ni}_{47}\text{Fe}_3$  is about  $-140^\circ\text{C}$ , whereas, the temperature near the contact surface at sliding speed of  $0.4 \text{ m.s}^{-1}$  and 20N load was experimentally measured to be  $170^\circ\text{C}$  after only 10 minutes of sliding by inserting a thin ungrounded thermocouple just below the contact surface. Under these conditions formation of martensite is highly unlikely. It has been shown [110,111] that the stress required for martensite formation increases at the rate of  $11.54 \text{ MPa/K}$  as the temperature is raised above the  $M_s$  temperature. XRD analysis on the wear debris collected at sliding speed of  $0.4 \text{ m.s}^{-1}$  did not indicate the existence of martensite. This, however, cannot rule out the possibility of having the stress induced martensite during the course of the sliding wear. The martensite at that temperature being pseudo-elastic (sliding temperature,  $T_s > A_f$ ) will transform back to the austenite phase once the stress is removed. Thus increasing the sliding speed and, therefore, the temperature, cannot be expected to result in such a transition.

The wear of the SAE 52100 steel undergoes a change in wear mechanism at a sliding speed of  $2.6 \text{ m.s}^{-1}$ . At this sliding speed, the steel appears to undergo a transition from mild oxidative type wear to severe oxidative wear, resulting in a large drop in its wear rates. Such a transition has been related to the formation of an oxide layer on the steel surface itself [2,112,113], when the temperature of the steel is sufficiently high to reform oxide at a rate faster than it is removed. Increase in the sliding speed increases the surface temperature and therefore the oxidation rate of the iron.

## 5.10. High Temperature Wear

### 5.10.1. Mild Wear

The  $\text{Ti}_{50}\text{Ni}_{47}\text{Fe}_3$  alloy maintains its superior wear resistance against steel up to  $350^\circ\text{C}$ . The wear rates decrease slowly with temperature above room temperature up to  $200^\circ\text{C}$ . Further increase in temperature reduced the wear rates more sharply and wear loss is negligible in the temperature range  $250\text{--}350^\circ\text{C}$  (Fig. 5.6).

The counterface wear appears to exert a significant influence on the wear behaviour of the intermetallic. The steel oxidation helps reducing the friction and wear during dry sliding by:

- (1) Oxide debris ( $\text{Fe}_2\text{O}_3$  and  $\text{Fe}_3\text{O}_4$ ) acts as solid lubricants (specially  $\text{Fe}_3\text{O}_4$ ) [112,113].  $\text{Fe}_2\text{O}_3$  has hard rhombohedral (haematite) structure which forms at lower temperatures can act as third-body abrasive, while at higher temperatures, formation of  $\text{Fe}_3\text{O}_4$ , a more ductile spinel magnetite is favoured.  $\text{FeO}$  (soft wustite) is stable only above  $570^\circ\text{C}$  [119] and therefore is not expected to form below  $250^\circ\text{C}$ . XRD results (Fig. 5.10) showed that mainly oxide debris ( $\text{Fe}_2\text{O}_3$  and  $\text{Fe}_3\text{O}_4$ ) are generated during sliding at ambient temperature.
- (2) The debris transfers and gets compacted on the specimen surface (Figs. 5.12 and 5.13). Such layers have been shown to be highly wear resistant [51,52,93,113] and protect the specimen surface against sliding damage.
- (3) Mixing of fine debris with the subsurface material of the specimen gives mechanically mixed material with much higher hardness [112-115]. Such a process has clearly occurred in wear regime II during ambient temperature wear at high loads (Fig. 5.25).

Oxidational rate of steel is thus expected to have important influence on the

Ti<sub>50</sub>Ni<sub>47</sub>Fe<sub>3</sub> wear. Dynamic oxidation rates (during sliding) have been found to be much higher than during static conditions. Several attempts have been made to model the oxidative wear of steel [40-43,50,51]. The steel oxidation is believed to follow, like static oxidation, the Arrhenius equation,

$$k_p = A \exp (-Q/RT) \quad \text{.....} \quad (3.1)$$

where,  $k_p$  is the parabolic rate constant for the growth of oxide film,  $T$  is the absolute temperature and  $R$  is the gas constant. Higher oxidation rate during sliding is usually attributed to higher value of  $A$  during sliding. However, there is no universal agreement on the activation energy for oxidation. Earlier studies indicated similar values of activation energy under dynamic and static conditions. Recent calculations by Quinn [50] put this value between 40 and 50 kJ mole<sup>-1</sup>, about half the value during static oxidation. During Ti<sub>50</sub>Ni<sub>47</sub>Fe<sub>3</sub> alloy wear testing, at low temperatures, only the steel wore and the intermetallic showed insignificant wear loss.

At elevated temperatures the steel wear rates are expected to be controlled by the oxidation rate and in fact the wear rate of steel (Fig. 5.6.) did increase exponentially. This should provide more favourable conditions for the formation of transfer (oxide) layer on the intermetallic surface and thus reduce its wear rate.

#### 5.10.2. Severe Wear

At temperatures above 350°C, the Ti<sub>50</sub>Ni<sub>47</sub>Fe<sub>3</sub> showed transition to severe wear. The steel wear rates decrease rapidly and showed weight gain. There are two factors which are important here. Firstly, as the test temperatures is increased the steel starts to form an oxide layer on its surface. This layer at low temperatures is not protective and merely contributes to the oxidational wear of the steel. However, with increase in ambient temperatures, the layer becomes thick and protects the steel surface resulting in a drop in the steel wear rates.

Secondly, the intermetallic is expected soften near the transition temperature. Results presented in Table. 3.1. as well as those of Moberly et al. [12] indicate that the

intermetallic starts to soften near 400°C about  $0.4T_m$ . The recrystallization temperature for the  $Ti_{50}Ni_{47}Fe_3$  alloy has been reported to be 467°C [114]. Sliding at 520°C resulted in recrystallization and grain refinement near the contact surface. Thus at elevated temperatures, the intermetallic is expected to have very low strength. Recrystallization can lead to work softening during plastic deformation. This results in material transfer from pin to the hard steel counterface disc. This leads to self-mated sliding (intermetallic/intermetallic) with uneven surfaces and, therefore, results in large increase in coefficient of friction. The  $Ti_{50}Ni_{47}Fe_3$  thus undergoes extensive sliding damage due to gross plastic deformation in the subsurface which results in extrusion of the pin material outside the contact geometry. The surface oxidation of the intermetallic was observed (Fig. 5.27) but was continuously displaced out of the contact area along with the plastically deforming subsurface material.

## 5.11. Formation of Tribo Layers

The  $Ti_{50}Ni_{47}Fe_3$  showed excellent wear resistance during mild wear at room temperature and elevated temperatures (up to 350°C). The superior wear behaviour of the intermetallic can be rationalized in terms of formation of highly wear resistant tribo-layers on its surface during sliding against SAE52100 steel.

### 5.11.1. Transfer Layers

Surface and subsurface examination of the worn surfaces indicate the formation of iron rich tribo-layers on the worn surfaces of the intermetallic alloy. The top-most layer had the same colour as oxide wear debris (brown colour at low loads and black at high loads). Optical microscopy (Figs. 5.11 and 5.24) clearly indicate that an oxide layer forms on the wear surface during the wear process. Scanning electron microscopy and EDS (Figs 5.12, 5.13) further revealed that these layers consist of compacted wear debris containing mainly iron (oxides). Since intermetallic wear rates are only 2-5% of that of the steel, these layers therefore, contained metallic constituents mainly from the counterface. XRD analysis of the worn surface also confirmed the presence of iron oxides



( $\text{Fe}_2\text{O}_3$  and  $\text{Fe}_3\text{O}_4$ ) on the wear track.

At low loads the oxide layers covered the surface more or less uniformly, although, the thickness was small. High loads, according to EDS results, led to the formation of thicker layers within the grooves on the wear track. The oxide layer in Fig. 5.24 shows that the layers are well adhered to the surface and are brittle and will fracture due to strains in the subsurface.

Increase in ambient temperature favoured the formation of these layers and led to the improvement of the wear resistance of both aluminum as well as the intermetallic alloy. Temperatures higher than  $420^\circ\text{C}$  led to the formation of glazed appearance of surfaces. The XRD results (Fig. 5.19.) indicate that the surface oxidation had occurred.

The presence of the oxide layers lower the wear rates as well as coefficient of friction considerably [2,112] owing to lower adhesion and junction growth. Formation of these layers is promoted by dynamic (tribological) oxidation [113]. Quantitative modelling [106] of the friction behaviour of such oxide bearing surfaces showed that the coefficient of friction of the sliding system is a function of oxide coverage fraction over the contacting surface [108].

Formation of these transfer layers can be explained as a four step process. The steel wear occurs mainly through generation of iron oxide debris by the process of metal transfer or delamination. These debris particles get repeatedly fragmented and the fine particles generated become adherent to the intermetallic specimen surface and agglomerate. Further sliding results in compression and compaction of the agglomerated clusters to form well adhered layer. Sliding at high loads produces deep grooves where debris can collect and agglomerate and thus favours the formation of thicker oxide layer (Fig 5.31) at the bottom of the grooves. At elevated temperatures sintering of the oxides during compaction would lead to the formation of durable layers and reduce the wear rates (Fig. 5.7).

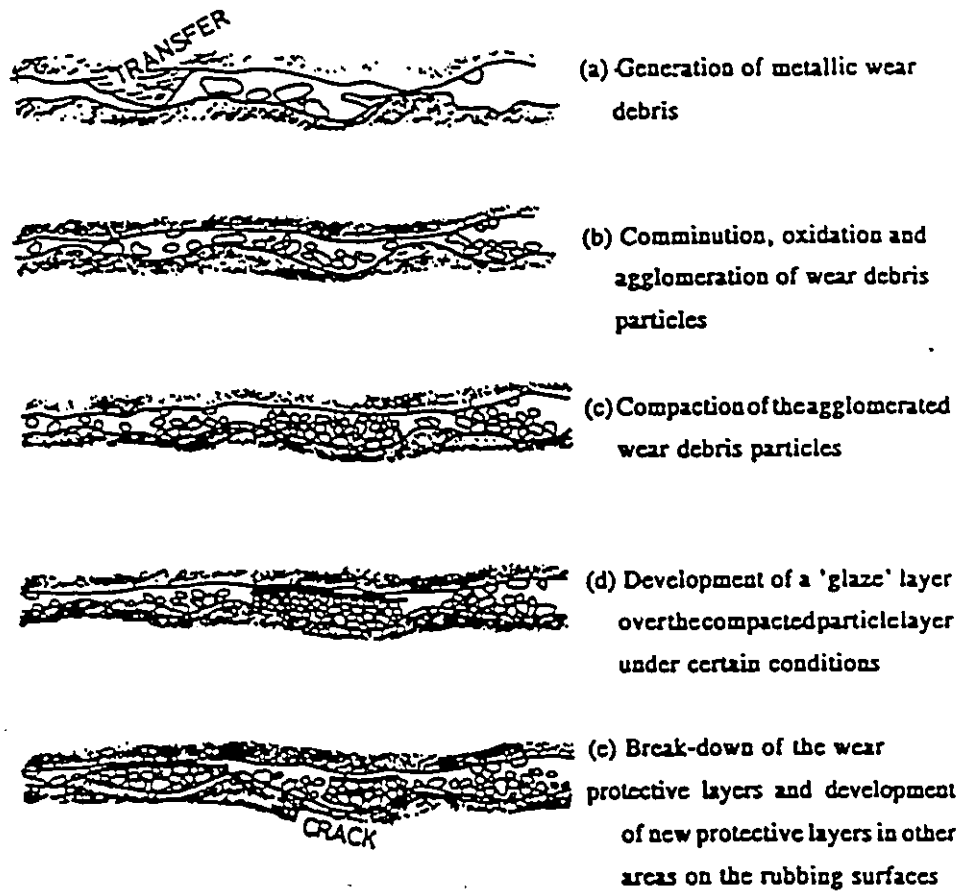


**Fig. 5.30. A model for development of transfer layers from wear debris particles (schematic). After Jiang et al. [109].**

### 5.11.2. Mechanically Mixed Layers

Below the transfer layer (compacted oxide debris) a hardened layer with very high iron contents was observed. These layers in some specimens worn at high loads gave finger like feature below the contact surface (Fig. 5.23.). High hardness values (Fig. 5.23(b)) recorded in these mechanically mixed layers may be attributed to a structure which consists of a mixture of iron and/or iron oxide with the base material. Due to very high hardness, these layers demonstrate much better wear and abrasion behaviour and more importantly provide support to the formation of transfer layers with high wear resistance.

Formation of mechanically mixed layers on the worn surfaces have been reported by several researchers [115,116]. TEM examination by Rainforth et al. [116] showed that the submicroscopic iron oxide particles penetrate up to a depth of several tens of microns and intimately mixed with the base material. This is in agreement with the observation that the layers of a mechanical mixture of iron oxides and intermetallic compounds have penetrated into the  $\text{Ti}_{50}\text{Ni}_{47}\text{Fe}_3$  up to a depth of about  $80\mu\text{m}$  (Figs. 5.25).

Formation of these mechanically mixed layers can be explained as follows: initially only transfer layer (iron + iron oxide) forms on the surface and increases the surface hardness of the intermetallic. Further sliding will make it sink into the subsurface which has significantly lower hardness. Don et al. [117] have indicated that, whenever the surface hardness (H) is greater than the hardness of the base material (h), i.e.  $H/h > 1.2$ , the hardened layer will penetrate and sink into the subsurface region. Sliding at high loads result in large scale plastic deformation near the contact surface (Fig. 5.22) which would induce mechanical mixing of this penetrated transfer layer with the base alloy. This intimate mixing of base alloy with oxide would result in very fine composite structure (metal/oxide) with very high hardness as have been seen in Fig. 5.23.

## Chapter 6

### CONCLUSIONS AND RECOMMENDATIONS FOR FUTURE WORK

The aim of this study was to understand the elevated temperature wear behaviour of two technologically important classes of materials viz. metal matrix composites (MMCs) and intermetallics due to their potential applications at high temperatures. Sliding wear of an aluminum matrix composite Al6061-20%Al<sub>2</sub>O<sub>3</sub> as well as unreinforced 6061 alloy was studied against 52100 steel in the temperature range 25°C to 500°C in a high temperature wear machine. High temperature compression testing of both the alloys was carried out to understand the role of plastic deformation during their elevated temperature wear. The intermetallic selected for this work was Ti<sub>50</sub>Ni<sub>47</sub>Fe<sub>3</sub>. The ambient temperature sliding wear of this alloy was studied as function of sliding distance, load and sliding speed against 52100 steel. High temperature wear of the intermetallic was studied in the temperature range 25°C -520°C. Detailed analyses of wear debris, worn surfaces and subsurfaces were done in all the cases to understand the wear mechanisms operating under different sliding conditions.

#### A. Conclusions

##### On Al6061 and Al6061-20%Al<sub>2</sub>O<sub>3</sub>

1. Al6061 alloy and the particulate reinforced Al6061-20%Al<sub>2</sub>O<sub>3</sub> composite show a mild to severe wear transition when the test temperature is increased above a certain temperature. This transition occurred at 180°C for Al6061 and at a higher temperature of 250°C for the reinforced alloy. During constant temperature tests on Al6061-20%Al<sub>2</sub>O<sub>3</sub>, similar mild to severe transition could be obtained on increasing the applied load. The load required for transition to occur decreased with increase in test temperature.

2. At elevated temperatures the reinforced alloy exhibits better wear resistance than Al6061. Increasing the load increased the wear rates at any given temperature.
3. The mild to severe wear transition corresponds to a temperature range where the flow strength of each material is low with respect to room temperature strength (70% for Al6061 and 57% for Al6061-20%Al<sub>2</sub>O<sub>3</sub>) and the alloys undergo work softening in compression.
4. In the mild wear regime at low temperatures, the wear rates of both the alloys are similar. Oxidation of the steel counterface and deposition of oxide debris on the contact surfaces strongly influence the wear rates.
5. Severe wear at high temperature occurs by extrusion of material out of the contact area through plastic deformation near the contact surface. Extensive material transfer to the counterface results in large increases in friction and accelerates the sliding wear damage.
6. Severe wear at high temperature can be modelled as a hot deformation process. The model indicated that the activation energy for the sliding wear at stress of 0.24 MPa (10N load) is 34 kJ mole<sup>-1</sup> for Al6061 in the temperature range of 200-450°C and 60 kJ mole<sup>-1</sup> for Al6061-20%Al<sub>2</sub>O<sub>3</sub> in the temperature range of 250-450°C.
7. Microstructural changes including recrystallization of deformed grains and comminution of Al<sub>2</sub>O<sub>3</sub> particles take place near the contact surface. Redistribution of fragmented particles and higher particle density lead to hardening of the near surface region and improved the wear resistance of the composite at elevated temperatures.

#### On $\text{Ti}_{50}\text{Ni}_{47}\text{Fe}_3$

1. The intermetallic alloy,  $\text{Ti}_{50}\text{Ni}_{47}\text{Fe}_3$ , can be strengthened through a thermo-mechanical treatment (45% cold work followed by annealing at 450°C for 10 min) to obtain an optimum combination of yield strength (830 MPa) and ductility (15% elongation).
2. The strengthened  $\text{Ti}_{50}\text{Ni}_{47}\text{Fe}_3$  alloy shows excellent wear resistance when tested for dry sliding wear against SAE 52100 steel. The wear rates of the intermetallic are 20 to 50 times lower than those of the steel counterface.
3. The excellent wear resistance of the  $\text{Ti}_{50}\text{Ni}_{47}\text{Fe}_3$  alloy can be attributed to the formation of protective tribo-layers on the surface and work hardening of the alloy below the contact surfaces. The top layer consisted of compacted oxide debris ( $\text{Fe}_2\text{O}_3$  and  $\text{Fe}_3\text{O}_4$ ). Beneath this layer formed finger like feature with very high hardness. These features are the result of mechanical mixing of oxides with the subsurface material.
4. The  $\text{Ti}_{50}\text{Ni}_{47}\text{Fe}_3$  alloy undergo a transition to severe wear on increasing the sliding speed beyond 3.0 m/s while the counterface experiences a transition from high wear rates to low wear rates at 2.5 m/s due to change in wear mechanism from mild oxidational wear to severe oxidational wear. At high speeds, the tribo-layers disappear and the  $\text{Ti}_{50}\text{Ni}_{47}\text{Fe}_3$  shows severe delamination wear.
5. The wear rates of the  $\text{Ti}_{50}\text{Ni}_{47}\text{Fe}_3$  alloy decrease on increasing the ambient temperature above room temperature and becomes insignificant near 300°C. However, further increase in temperature results in mild to severe wear transition. The transition for the intermetallic occurs near 400°C.
6. The severe wear of the  $\text{Ti}_{50}\text{Ni}_{47}\text{Fe}_3$  alloy at elevated temperatures occurs by

transfer to the counteface and gross plastic deformation (extrusion) in the direction of sliding. Oxidation of the intermetallic results in formation of glaze at the sliding surfaces but does not improve its wear resistance.

### General Conclusions

1. Wear rates of both Al6061 and  $\text{Ti}_{50}\text{Ni}_{47}\text{Fe}_3$  decreased with temperature during mild wear at low temperatures. Similarly, the friction coefficient of both the alloys showed a decrease in the same temperature range.
2. Oxidative wear of steel had an important influence on the mild wear of all the three alloys. Increase in temperature improves the friction and wear because of:  
(i) fine iron oxide debris acts as solid lubricants, (ii) the debris forms a protective layer on the specimen surface and (iii) mixing of debris with the subsurface material increases the hardness of sliding surfaces.
3. The mild to severe wear transition in all the three materials was similar despite wide difference in the nature of these materials. On increase of ambient temperature, the transition occurs when the material flow strength decreases to very low value or work softens due to dynamic recrystallization.

### **B. Recommendations For Future Work**

1. Both Al6061 and Al6061-20%Al<sub>2</sub>O<sub>3</sub> show low wear rates in the mild wear regime at low temperatures. The wear rates decreased with temperature in this regime. Wear rates determined through weight loss measurements showed large decrease especially near the transition temperature. Generation of cracks near the contact surface, and therefore, production of debris particles at the sliding surfaces is suppressed near 200°C. Friction and wear of both the materials need to be investigated further in this temperature range. In particular, the effect of sliding speed should be studied to arrive at sliding conditions where these materials show

the optimum wear resistance. This type of study is also important to address the problem of surface cracking of the composite during hot extrusion process.

2. Oxidation of steel strongly influenced the elevated temperature wear of all the materials. Sliding against an inert counterface, for instance a ceramic, would yield different results and is expected to throw more light on the elevated temperature tribological behaviour of these materials. Pure alumina ( $\text{Al}_2\text{O}_3$ ) or zirconia toughened alumina can be used for this purpose. This will make it easier to delineate the role of mechanical properties of the test material in its high temperature wear characteristics.
3. Material hardness and ductility play important role in wear of materials. Both hardness and ductility of  $\text{Ti}_{50}\text{Ni}_{47}\text{Fe}_3$  alloy can be varied to a great extent through thermo-mechanical treatment. This provides an opportunity to study the relative role of these parameters in the sliding wear of metallic materials.
4. Large decrease in wear rates of the intermetallic is an important finding of this work. Further work needs to be carried out on intermetallics with better elevated temperature strength. Nickel aluminide ( $\text{NiAl}$ ) as well as titanium aluminide ( $\text{TiAl}$ ) are good candidates for such an investigation. The strength of these intermetallic alloys shows positive temperature dependence, that is, the strength increases with increase of temperature. Similarly, the ductility and toughness of these alloys improve at high temperatures. Thus these intermetallics are excellent candidates for investigation of high temperature wear. High strength steels are not ideally suited as counterface material at elevated temperatures due to their high wear rates. Instead, high performance ceramics (for example alumina) should be used as counterface.



## REFERENCES

1. Quin, T. F. J., *Journal of applied Physics*, 33 (1962) 13.
2. Welsh, N.C., *Journal of Applied Physics*, 28 (1957) 960.
3. Lampman, S.R., *Advanced Materials and Processes*, 5 (1991) 17.
4. Rohatagi, P., *Journal of Metals*, April 1991, 10.
5. Lloyd, D.J., *International Materials Reviews*, 39 (1994) 1.
6. Ibrahim, I.A., F.A. Mohamad and E.J. Lavernia, *Journal of Material Science*, 26 (1991) 1137.
7. Fishman, S.G., *Journal of Metals*, 38 (1986) 26.
8. Martinez, M.A., A. Martin, and Llorca J., *Scripta Metallurgica et Materialia*, 28 (1993) 207.
9. Watanabe, A., Y. Sugai, T. Tsuzimura, K. Takao, E. Nishii, T. Khikawa, *Proceedings conference RASELM 1991, Japan Inst. Light Metals, Tokyo (1991)* 329.
10. Ellis, B.D., M.F. Gittos and P.L. Threadgill, *Materials World*, August 1994, 415.
11. Wayman, C.M., *Journal of Metals*, 6 (1980) 129.
12. Moberly, W.J., J. L. Proft, T. W. Duerig and R. Sinclair, *Acta Metallurgica et Materialia*, 38 (1990) 2601.
13. *Standard Terminology Relating to Erosion and Wear*, G40, *Annual book of ASTM Standards*, ASTM, pp. 45.
14. Burwell, J.T. and C.D. Strang, *Journal of Applied Physics*, 23 (1952) 18.
15. Finkin, E.F., *Materials in Engineering Applications*, 1 (1979) 154.
16. Archard, J.F. and W. Hirst, *Proceedings Royal Society*, A236 (1956) 397.
17. Archard, J.F., Jr. *Appl. Physics*, 24 (1953) 981.
18. Suh, N.P., *Wear* 25, (1973) 111.
19. Suh, N.P., *wear, Wear*, 44 (1977) 1.
20. Heilmann, P., W.A.T. Clarck, D.A. Rigney, *Acta Metallurgica*, 31 (1983) 1293.
21. Fleming, J.R., N.P. Suh, *Wear*, 44 (1977) 39.
22. Kimura, Y., in *Fundamentals of Friction and Wear of Materials*, ed. D.A. Rigney

- ASM, Materials Park (1981) 187.
23. Ritchie, R.O., in Fundamentals of Tribology, N.P. Suh and N. Saka eds., MIT, 1978, 127.
  24. Rosenfield, A.R., Wear, 72 (1981) 245.
  25. Alpas, A.T., and J.D. Embury, Wear 146 (1991) 285.
  26. Rosenfield, A.R., Wear 116 (1987) 317.
  27. Zhang, J. and A.T. Alpas, Materials Science and Engineering, A160 (1993) 25.
  28. Rice, J.R. and D.M. Tracy, Journal of the Mechanics and Physics of Solids, 17 (1969) 201.
  29. Lim C.S. and M.F. Ashby, Acta Met., 35 (1987) 1.
  30. Yust, C.S., International Metals Review, 30 (1985) 141.
  31. Rigney, D.A., Annual Review of Materials Science, 18 (1988) 141.
  32. Zum Gahr, K.H., Elsevier, New York, 1987.
  33. Akagaki, T. and D.A. Rigney, Wear, 141 (1991) 353.
  34. Ludema, K.C., Sliding and Abrasive Wear, ASM handbook 'Friction and Wear Applications', 18 (1992) 1.
  35. Lancaster, J.K., Tribology International, 23 (1990) 371.
  36. Ruff, A.W., Wear of Materials, ASME (1989) 717.
  37. Uetz, U. and K. Sommer, Wear, 43 (1977) 375.
  38. Hutchings, I.M., Tribology: Friction and Wear of Engineering materials; CRC Press, England (1992) 93.
  39. Uetz, H. and J. Fohl, Wear, 49 (1978) 253.
  40. Quinn, T.F.J, Tribology International, 16 (1983) 257.
  41. Quinn, T.F.J, Tribology International, 16 (1983) 305.
  42. Ashby, M.F., J. Abulawi and H.S. Kong, STLE Tribology Transactions, October 1991.
  43. Archard, J.F. and R.A. Rowntree, Wear, 128 (1988) 1.
  44. Blok, H., Wear, 6 (1993) 483.
  45. Ling, F.F. and E. Saibal, Wear 1(1957) 80.
  46. Waterhouse, R.B. and D.E. Taylor, ed. N.S. Stoloff, High Temperature Materials,

- Vol. 4., No. 1, Freund Publishing Telavive, (1978) 259.
47. Berns, H. and A. Fischer, *Wear*, 162-164 (1993) 441.
  48. Fisher, A., *Wear*, 152 (1992) 151.
  49. Arnell, R.D., P.B. Davis, J. Halling and T.L. Whomæs, *Tribology: Principles and Design Applications*, Macmillan, London (1991) 97.
  50. Quinn, T.F.J., *Wear*, 175 (1994) 199.
  51. Earles, S. and Tenwick N., *Wear*, 19 (1972) 287.
  52. Buckley, D.H. and Johnson R.L., *Lubrication conference*, American Society of Lubrication Engineers, New York, October (1969) 93.
  53. Waterhouse, R.B., D.E. Tayler, *Review on High temperature Materials*, ed. N.S. Stoloff, Freud Publishing, Televive, Vol.4, (1978) 259.
  54. Stott, F.H., D.S. Lin, G.C. Wood, C.W. Stewenson, *Wear*, 36 (1976) 147.
  55. Lancaster, J.K., *Proceedings Royal Society A*, vol. 273 (1960) 467.
  56. Clarck, W.T., *Proc. Inst. Mech. Engrs.*, 182, Pt.3N (1967-68) 97.
  57. Duncckley, P.M., T.F.J. Quinn and J. Salter, *ASLE Trans.*, 19, 3, (1975) 221.
  58. Lee, C.S., Y.H. Kim, K.S. Khan, *Journal of Materials Science*, 27 (1992) 793.
  59. Park, H.C., *Scripta Metallurgica et Materialia*, 27 (1992) 465.
  60. Rohatgi, P., S. Ray and Y. Liu, *International Materials Reviews*, 37 No.3, (1992).
  61. Wilson, S., A. Ball, in *Tribology of Composite Materials*, eds. P.K. Rohatgi, P.J. Blan and C.S. Yust, ASM International, Materials Park, OH, (1991) 123.
  62. Rauta, V., M. Saynatzoki, *Tribologia*, vol. 10, No.4 (1991) 48.
  63. Modi, O.P, B.K. Prasad, A.H. Yegneswaran, M.L. Vaidya, *Materials Science and Engineering*, A151 (1992) 253.
  64. Alpas, A.T. and J. Zhang, *Wear* 155 (1992) 83.
  65. Alpas, A.T. and J. Zhang, *Scripta Metallurgica et Materialia*, 26 (1992) 505.
  66. Wang, A. and H.J. Rack, *Materials Science and Engineering*, A147 (1991) 211.
  67. Parmila Bai, B.N., B.S. Ramasesh, M.K. Surappa, *Wear* 157 (1992) 294.
  68. Zhang, J. and A.T. Alpas, *Materials Science and Engineering*, A161 (1993) 273.
  69. Nesarikar, A.R., S.N. Tiwari, E.E. Graham, *Materials Science and Engineering*, A147 (1991) 191.

70. Saka, N., D.P. Karalekas, *Wear of materials* 1985, ASME (1985) 784.
71. Scott, W., *The tribological Behaviour of aluminum matrix composites*, PhD thesis, University of Capetown, (1993) 138.
72. Suzuki, Y., and T. Kuroyanagi, *Titanium Zirconium*, 27 (1979) 67.
73. Shida, Y. and Y. Sugimoto, *Wear*, 146 (1991) 219.
74. Moine, P., O. Popoola, J.P. Villain, *Scripta Metallurgica*, 20 (1986) 305.
75. Clayton, P., *Wear*, 162-164 (1993) 202.
76. Moupin, H.E., R.D. Wilson, J.A. Hawk, *Wear*, 162-164 (1993) 432.
77. McDanel, D.L., *Metallurgical Transactions*, 16A (1985) 1105.
78. Humphreys, F.J., H. basu and M.R. Djazeb: in 'Metal matrix composites - processing, microstructure and properties', 12th Risø Int. Symp. on Metallurgy and Materials Science, eds. N. Hansen et al., Risø National Laboratory, Roskilde, Denmark, (1991) 51.
79. Christman, T., A. Needleman, and S. Suresh, *Acta Metallurgica et Materialia*, 37 (1989) 3029.
80. Taya, M., K.E. Lulay, and D.J. Lloyd, *Acta Metallurgica et Materialia*, 39 (1991) 73.
81. Levi, A. and J.M. Papazian, *Acta Metallurgica et Materialia*, 39 (1991) 2255.
82. Zedall, M.S., Gilman P.S. and S.K. Das, 'High performance Composites for the 1990s' eds. S.K. Das et al, The Metallurgical Society of AIME, Warrendale, PA, (1990) 61.
83. Corbin, S.F. and D.S. Wilkinson, *Acta Metallurgica et Materialia*, 42 (1994) 1329.
84. Sakaris, P. and H.J. McQueen, in *Aluminum Alloys: their physical and mechanical properties (ICAA3)*, eds. L. Arnberg et al, Vol. 1, Trondheim, Norway, (1992) 554.
85. Xia X., P. Skaris and H.J. McQueen, *Materials Science and technology*, 10 (1994) 487.
86. Edelson, B.I. and W.M. Baldwin Jr, *Transactions American Society of Metals*, 55 (1962) 230.
87. Hunt, W.H., O. Richmond and R.D. Young, 6th International Conference on Composite Materials, eds. F.I. Mathews et al., Vol. 2, Elsevier, Amsterdam,

- 1988, pp. 209.
88. Lloyd, D.J., *Acta Metallurgica*, 39 (1991) 59.
  89. Yang, J., C. Cady, M.S. Hu, F. Zok, R. Mehrabian, *Acta Metallurgica et Materialia*, 38 (1990) 2613.
  90. Brechet, Y., J. Newell, S. Tao and J.D. Embury, *Scripta Metallurgica et Materialia*, 28 (1993) 47.
  91. Zhao, D., Tuler F.R. and D.J. Lloyd, *Acta Metallurgica et Materialia*, 42 (1994) 2525.
  92. Cai, B.C., D. Kuhlmann-Wilsdorf and R.B. Nelson, *Materials Science and Engineering*, A138 (1991)33.
  93. Stoloff, N.S., *Metallurgical Transactions*, 24A (1993) 561.
  94. Gupta, S.P. and A. A. Johnson, *Trans. Japan Inst. Metals*, 14 (1973) 292.
  95. Tuominen, S.M. and R. J. Biermann, *Journal of Metals*, 2 (1988) 32.
  96. Madan Gopal, K., J. Singh and S. Banerjee, *Scripta Metallurgica et Materialia*, 25 (1991) 2153.
  97. Goo, E. and R. Sinclair, *Acta Metallurgica*, 33 (1985) 1717.
  98. Goo, E., T. Duerig, K. Melton and R. Sinclair, *Acta Metallurgica*, 33 (1985) 1725.
  99. Park, K.T. and E. Goo, *Acta Metallurgica et Materialia*, 12 (1991) 3027.
  100. Melton, K.N. and O. Mercier, *Acta Metallurgica*, 27 (1979) 137.
  101. Honeycombe, R.W.K., *The Plastic Deformation of Metals*, Second Edition, Edward Arnold, London, (1984) 394.
  102. Sheppard, T., Parson N.C. and M.A. Zaidi, *Metals Science*, 17 (1983) 481.
  103. Gudmundsson H., D. Brooks and J.A. Vert, *Acta Metallurgica*, 39 (1991) 19.
  104. Kuo, S.M. and D.A. Rigney, *Materials Science and Engineering*, A157 (1992) 131.
  105. Dautzenberg, J.H., *Wear*, 60 (1980) 401.
  106. Moore, M.A., R.C.D. Richardson and D.G. Atwood, *Metallurgical Transactions*, 3 (1972) 2485.
  107. Dautzenberg, J.H. and J.H. Zatt, *Wear* 23 (1973) 9.
  108. Stott, F.H., J. Glascott and G.C. Wood, *Wear*, 97 (199) 93.
  109. Jiang, J., F.H. Stott and M.M. Stack, *Wear* 176 (1994) 185.

110. Takei, F., T. Miura, S. Mmiyazaki, S. Kimura, K. Otsuka and Y. Suzuki, Scripta Metallurgica, 17 (1983) 987.
111. Madangopal, K., G.R. Krishnan and S. Banerjee, Scripta Metallurgica, 22 (1988) 1593.
112. Kato, H., T. S. Eyre and B. Ralph, Acta Metallurgica et Materialia, 42 (1994) 1703.
113. Bulpet, R., T.S. Eyre, B. Ralph, Wear, 162-164 (1993) 1051.
114. Sullivan, J.L. and N.W. Granville, Tribology International, 17 (1984) 63.
115. Ludema, K.C., Wear, 100 (1984) 315.
116. Liu Y. and P.G. McCormick, ISIJ International, 29 (1989) 417.
117. Heilmann, P., J. Don, T. C. Sun, D. A. Rigney and W. A. Glaeser, Wear, 91 (1983) 171.
118. Rainforth, W.M., R Stevens and J. Nutting, Philosophical Magazine, A66 (1992) 621.
119. Don, J., T. C. Sun and D. A. Rigney, Wear, 91 (1983) 191.

## VITA AUCTORIS

NAME: Jugraj Singh  
PLACE OF BIRTH: Ambala (Haryana), India  
YEAR OF BIRTH: 1964  
EDUCATION: Benares Hindu University, Varanasi, India  
1983-1987 B. Tech.

University of Windsor, Windsor, Ontario, Canada  
1992-1994 M.A.Sc.

## LIST OF PUBLICATIONS FROM THIS THESIS:

1. Singh, J. and A.T. Alpas, Elevated Temperature Wear of Al6061 and Al6061-20%Al<sub>2</sub>O<sub>3</sub>, *Scripta Metallurgica et Materialia*, accepted December 1994, in press.
2. Singh, J., and A.T. Alpas, High-temperature Wear of Al6061 and Al6061-20%Al<sub>2</sub>O<sub>3</sub>, Proceedings of the International Symposium on *Recent Developments in Light Metal Alloys*, M. Gilbert, P. Tremblay and E. Ozberk, eds., Met. Soc. of CIM, Toronto (1994) 149-160.
3. Singh, J. and A.T. Alpas, Wear Mechanisms in a Ti<sub>50</sub>Ni<sub>47</sub>Fe<sub>3</sub> Intermetallic Alloy, *Wear*, accepted October 1994, in press.